

(10)

**EFFECT OF STATE OF STRESS ON VELOCITY OF  
LOW-AMPLITUDE COMPRESSION WAVES PROPAGATING  
ALONG PRINCIPAL STRESS DIRECTIONS IN DRY SAND**

S. E. Kopperman, K. H. Stokoe II  
and D. P. Knox

a report on research  
sponsored by  
United States Air Force  
Office of Scientific Research  
Bolling Air Force Base

DTIC  
ELECTE  
OCT 19 1982  
S H

AD A120425

Qualified requestors may obtain additional copies from  
the Defense Technical Information Service.

**Conditions of Reproduction**

Reproduction, translation, publication, use and disposal  
in whole or in part by or for the United States  
Government is permitted.

UNCLASSIFIED

SECURITY CLASSIFICATION OF THIS PAGE (When Data Entered)

REPORT DOCUMENTATION PAGE		READ INSTRUCTIONS BEFORE COMPLETING FORM
1. REPORT NUMBER <b>AFOSR-TR- 82-0907</b>	2. GOVT ACCESSION NO. <b>AD-A220425</b>	3. RECIPIENT'S CATALOG NUMBER
4. TITLE (and Subtitle)  EFFECT OF STATE OF STRESS ON VELOCITY OF LOW-AMPLITUDE COMPRESSION WAVES PROPAGATING ALONG PRINCIPAL STRESS DIRECTIONS IN DRY SAND		5. TYPE OF REPORT & PERIOD COVERED ANNUAL 1 Oct 79 - 31 Dec 81
		6. PERFORMING ORG. REPORT NUMBER
7. AUTHOR(s)  STEWART E. KOPPERMAN, KENNETH H. STOKOE, II, and DAVID P. KNOX		8. CONTRACT OR GRANT NUMBER(s)  AFOSR-80-0031
9. PERFORMING ORGANIZATION NAME AND ADDRESS  UNIVERSITY OF TEXAS AT AUSTIN DEPARTMENT OF CIVIL ENGINEERING AUSTIN, TX 78712		10. PROGRAM ELEMENT, PROJECT, TASK AREA & WORK UNIT NUMBERS  61102F 2307/C1
11. CONTROLLING OFFICE NAME AND ADDRESS  AIR FORCE OFFICE OF SCIENTIFIC RESEARCH/NA BOLLING AFB, DC 20332		12. REPORT DATE February 1982
		13. NUMBER OF PAGES 288
14. MONITORING AGENCY NAME & ADDRESS (if different from Controlling Office)		15. SECURITY CLASS. (of this report) <b>UNCLASSIFIED</b>
		15a. DECLASSIFICATION/DOWNGRADING SCHEDULE
16. DISTRIBUTION STATEMENT (of this Report)  Approved for Public Release; Distribution Unlimited.		
17. DISTRIBUTION STATEMENT (of the abstract entered in Block 20, if different from Report)		
18. SUPPLEMENTARY NOTES		
19. KEY WORDS (Continue on reverse side if necessary and identify by block number)  COMPRESSION WAVES                      BIAXIAL TESTING SEISMIC VELOCITY                      LOW AMPLITUDE BODY WAVES CONSTRAINED MODULUS                  STRESS HISTORY DAMPING                                  STRUCTURAL ANISOTROPY TRIAxIAL TESTING		
20. ABSTRACT (Continue on reverse side if necessary and identify by block number)  Little research has been performed in which the effect of biaxial and triaxial states of stress on the propagation velocity of compression and shear waves has been investigated. Therefore, a triaxial testing device was constructed, and an initial test series was performed to determine the relationship between propagation velocities and state of stress in a dry sand. The testing device was constructed of reinforced steel and was designed to hold a cubic soil sample measuring 7 ft (2.1 m) on a side. Rubber membranes		

DD FORM 1 JAN 73 1473

EDITION OF 1 NOV 65 IS OBSOLETE

UNCLASSIFIED

SECURITY CLASSIFICATION OF THIS PAGE (When Data Entered)

UNCLASSIFIED

SECURITY CLASSIFICATION OF THIS PAGE(When Data Entered)

were placed between the soil and three mutually perpendicular walls of the cube, corresponding to the three principal planes. The membranes were filled with water and pressurized to achieve the desired state of stress, either isotropic, biaxial, or triaxial. Waves were generated at sources contacting the soil surface and extending outside the cube. The waves were monitored by accelerometers placed in the soil sample. The accelerometer records were recorded on digital oscilloscopes for determination of velocities. Stress and strain measuring devices were also placed in the soil. The effects on compression of the sample were determined. Structural anisotropy caused a variation between principal stress axes of about ten percent in velocity at a given pressure. Stress history resulted in no noticeable variation in P-wave velocity and, therefore, was neglected. Biaxial and triaxial loading results lead to the same conclusion, namely that the velocity of compression waves propagating along principal stress directions in dry sand as low-amplitude body waves depends only on the stress in the direction of wave propagation. This conclusion is important in that compression wave velocity has been assumed to depend primarily on the mean effective principal stress in the past.

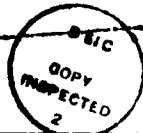
Accelerometer

THIS COPY  
THIS TAB  
Unmeasured  
Justification

By  
Distribution/  
Availability Codes

Dist Avail an. Special

A



UNCLASSIFIED

SECURITY CLASSIFICATION OF THIS PAGE(When Data Entered)



EFFECT OF STATE OF STRESS ON VELOCITY OF LOW-AMPLITUDE  
COMPRESSION WAVES PROPAGATING ALONG PRINCIPAL  
STRESS DIRECTIONS IN DRY SAND

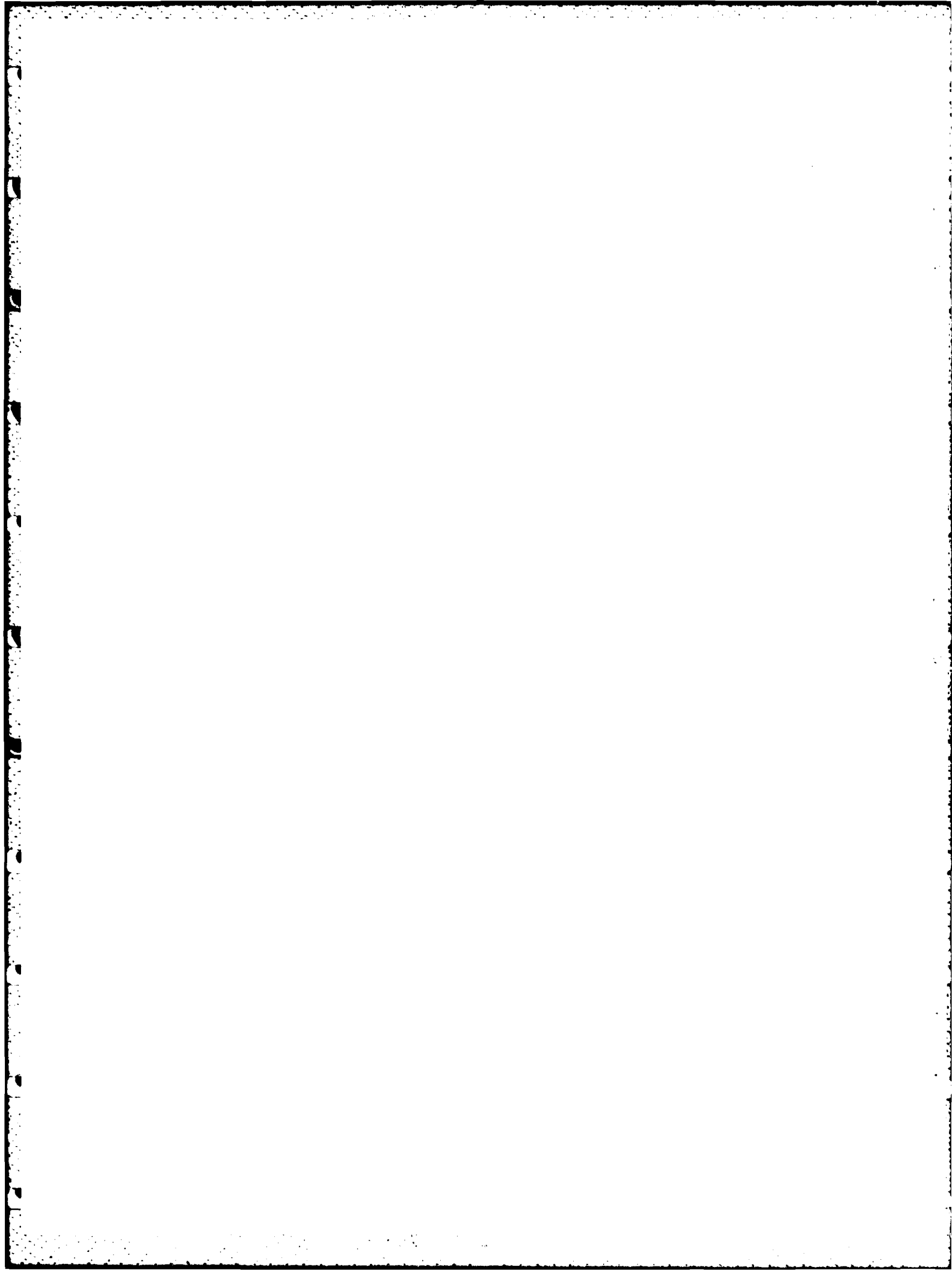
S. E. Kopperman, K. H. Stokoe, II,  
and D. P. Knox

AIR FORCE OFFICE OF SCIENTIFIC RESEARCH (AFSC)  
NOTICE OF TRANSMITTAL TO DTIC  
This technical report has been reviewed and is  
approved for public release IAW AFR 190-12.  
Distribution is unlimited.  
MATTHEW J. KEMPER  
Chief, Technical Information Division

a report on research  
sponsored by  
United States Air Force  
Office of Scientific Research  
Bolling Air Force Base

February, 1982

Geotechnical Engineering Report GR82-22  
Geotechnical Engineering Center  
Civil Engineering Department  
The University of Texas at Austin  
Austin, Texas



## ACKNOWLEDGEMENTS

The authors wish to acknowledge the following people for their valuable assistance in this project:

- Dr. Jose M. Roesset for his assistance and advice,
- Ms. Sarah C. Clark for her excellent typing and aid in the completion of this report on time,
- geotechnical engineering graduate students at The University of Texas at Austin, all of whom helped in some manner, especially Joe Baka, J. Scott Heisey, Juan Bernal, Jimmy Allen, and Augusto Canales,
- Dr. Roy E. Olson and Dr. Stephen G. Wright, members of the graduate faculty at The University of Texas at Austin,
- the staff and faculty of the Phil Ferguson Laboratory, Ba'cones Research Center, The University of Texas at Austin, especially Mr. George Moden and Mrs. Laurie Golding,
- the technical staff of the Department of Civil Engineering, The University of Texas at Austin, especially James Stewart and Marvin Howse,
- the Engineering Machine Shop, especially Mr. Terry Rose who constructed the cube,
- Mr. W. Howell, who aided in the structural design of the cube, and
- the United States Air Force Office of Scientific Research (AFOSR), Bolling Air Force Base, Washington, D.C., for supporting this research under grant AFOSR 80-0031A. Major John J. Allen was the project manager.

## ABSTRACT

Little research has been performed in which the effect of biaxial and triaxial states of stress on the propagation velocity of compression and shear waves has been investigated. Therefore, a triaxial testing device was constructed, and an initial test series was performed to determine the relationship between propagation velocities and state of stress in a dry sand. The testing device was constructed of reinforced steel and was designed to hold a cubic soil sample measuring 7 ft (2.1 m) on a side. Rubber membranes were placed between the soil and three mutually perpendicular walls of the cube, corresponding to the three principal planes. The membranes were filled with water and pressurized to achieve the desired state of stress, either isotropic, biaxial, or triaxial. Waves were generated at sources contacting the soil surface and extending outside the cube. The waves were monitored by accelerometers placed in the soil sample. The accelerometer records were recorded on digital oscilloscopes for determination of velocities. Stress and strain measuring devices were also placed in the soil.

The portion of the research presented herein focuses on the effect of the states of stress on compression wave velocity. The effect of shear waves is analyzed by Knox, et al (1982). The effects on compression wave velocity of structural anisotropy and stress

history of the sample were also determined. Structural anisotropy caused a variation between principal stress axes of about ten percent in velocity at a given pressure. Stress history resulted in no noticeable variation in P-wave velocity and, therefore, was neglected.

Biaxial and triaxial loading results lead to the same conclusion, namely that the velocity of compression waves propagating along principal stress directions in dry sand as low-amplitude body waves depend only on the stress in the direction of wave propagation. This conclusion is important in that compression wave velocity has been assumed to depend primarily on the mean effective principal stress in the past.

## TABLE OF CONTENTS

	Page
ACKNOWLEDGEMENTS . . . . .	i
ABSTRACT . . . . .	ii
TABLE OF CONTENTS . . . . .	iv
LIST OF TABLES . . . . .	ix
LIST OF FIGURES . . . . .	xi
LIST OF SYMBOLS . . . . .	xviii
 CHAPTER 1. INTRODUCTION . . . . .	 1
CHAPTER 2. REVIEW OF LITERATURE . . . . .	4
2.1 INTRODUCTION . . . . .	4
2.2 TESTING DEVICES . . . . .	4
.1 Resonant Column Method . . . . .	6
.2 Pulse Method . . . . .	7
.3 Cyclic Method . . . . .	10
2.3 EFFECT OF ISOTROPIC CONFINEMENT . . . . .	12
.1 Effective Mean Confining Pressure . . . . .	13
.2 Stress History . . . . .	13
.3 Strain Amplitude . . . . .	13
.4 Frequency . . . . .	16
.5 Other Factors . . . . .	16
.6 Summary . . . . .	16
2.4 EFFECT OF BIAxIAL CONFINEMENT . . . . .	17
2.5 SUMMARY . . . . .	18

	Page
CHAPTER 3. TRIAXIAL TESTING DEVICE . . . . .	21
3.1 INTRODUCTION . . . . .	21
3.2 STRUCTURE OF THE CUBE . . . . .	23
.1 Design Considerations . . . . .	23
.2 Cube Construction . . . . .	24
.3 Special Features of the Cube Structure . . . . .	31
3.3 LOADING SYSTEM . . . . .	
.1 Membrane Operation . . . . .	
.2 Membrane Characteristics . . . . .	
.3 First-Design Membranes . . . . .	
.4 Final Membrane Design . . . . .	
.5 Hydraulic Loading of Membranes . . . . .	
3.4 EXCITATION PORTS . . . . .	46
.1 Wave Generation . . . . .	49
.2 Soil Anvil Contacts . . . . .	49
.3 Additional Design Considerations . . . . .	52
.4 Preliminary Testing for Anvil-Base Design . . . . .	52
3.5 MONITORING AND RECORDING SYSTEM . . . . .	55
.1 Accelerometers . . . . .	55
.2 Recording Devices . . . . .	61
3.6 STRESS MEASUREMENT . . . . .	63
3.7 STRAIN MEASUREMENT . . . . .	65
3.8 TEST SAMPLE . . . . .	68
.1 Soil-Cube Boundary . . . . .	68
.2 Sand Placement . . . . .	69
.3 Density Measurement of Sample . . . . .	71
3.9 SUMMARY . . . . .	71

	Page
CHAPTER 4. ENGINEERING PROPERTIES OF SOIL . . . . .	73
CHAPTER 5. TESTING PROGRAM AND PROCEDURES . . . . .	75
5.1 INTRODUCTION . . . . .	75
.1 Isotropic Confinement . . . . .	75
.2 Confinement with Constant Mean Effective Principal Stress . . . . .	81
.3 Confinement with Varying Mean Effective Principal Stress . . . . .	83
5.2 TESTING PROCEDURE . . . . .	86
.1 Sample Construction . . . . .	87
.2 Placement of Electronics . . . . .	95
.3 Loading the Soil . . . . .	112
.4 Problems in Use of Stress and Strain Measuring Devices . . . . .	115
.5 Dynamic Testing . . . . .	119
5.3 SUMMARY AND CONCLUSIONS . . . . .	121
CHAPTER 6. ISOTROPIC CONFINEMENT . . . . .	123
6.1 INTRODUCTION . . . . .	123
6.2 DATA ANALYSIS . . . . .	124
.1 Determination of Velocity . . . . .	125
.2 Determination of Predominant Frequency . . . . .	128
.3 Determination of Particle Amplitude . . . . .	130
.4 Determination of Strain Amplitude . . . . .	131
.5 Determination of Wavelengths . . . . .	132
6.3 DIRECT AND INTERVAL VELOCITIES . . . . .	134
.1 Short versus Long Interval Measurements. . . . .	140
.2 Statistical Presentation . . . . .	143
6.4 EFFECT OF STRESS HISTORY . . . . .	146
6.5 EFFECT OF STRUCTURAL ANISOTROPY . . . . .	150
6.6 EFFECT OF ISOTROPIC CONFINEMENT . . . . .	155
6.7 SUMMARY AND CONCLUSIONS . . . . .	158



	Page
CHAPTER 7. BIAXIAL CONFINEMENT . . . . .	160
7.1 INTRODUCTION . . . . .	160
7.2 TESTING WITH A VARIABLE EFFECTIVE MEAN PRINCIPAL STRESS . . . . .	161
.1 Notation for Stresses . . . . .	162
.2 Effect of Principal Stress in Direction of Wave Propagation . . . . .	164
.3 Effect of Principal Stress Perpendicular to Wave Propagation . . . . .	171
.4 Effect of Stress History . . . . .	175
.5 Effect of Structural Anisotropy . . . . .	177
.6 Effect of Lateral Pressure Coefficient on P-wave Velocity . . . . .	182
7.3 TESTING WITH A CONSTANT EFFECTIVE MEAN PRINCIPAL STRESS . . . . .	185
7.4 SUMMARY AND CONCLUSIONS . . . . .	188
CHAPTER 8. TRIAXIAL CONFINEMENT . . . . .	191
8.1 INTRODUCTION . . . . .	191
8.2 TESTING WITH A VARIABLE EFFECTIVE MEAN PRINCIPAL STRESS . . . . .	193
.1 Effect of Principal Stress in Direction of Wave Propagation . . . . .	194
.2 Effect of Principal Stress Perpendicular to Wave Propagation . . . . .	198
.3 Effect of Stress History . . . . .	202
.4 Effect of Structural Anisotropy . . . . .	202
.5 Effect of Lateral Pressure Coefficient on P-wave Velocity . . . . .	205
8.3 TESTING WITH A CONSTANT EFFECTIVE MEAN PRINCIPAL STRESS . . . . .	208
8.4 SUMMARY AND CONCLUSIONS . . . . .	212

	Page
CHAPTER 9. SUMMARY, CONCLUSIONS AND RECOMMENDATIONS FOR FUTURE WORK . . . . .	216
9.1 SUMMARY AND CONCLUSIONS . . . . .	216
.1 Triaxial Testing Device . . . . .	216
.2 Effect of the State of Stress on $V_p$ . . . . .	217
.3 Stress-Strain Measurements . . . . .	219
.4 Importance to Laboratory Testing and Constitutive Modeling . . . . .	220
9.2 RECOMMENDATIONS FOR FUTURE WORK . . . . .	220
APPENDIX A. ENGINEERING PROPERTIES OF SAND . . . . .	223
APPENDIX B. COMPUTER LISTING OF PROGRAM CUBE . . . . .	242
APPENDIX C. SAMPLE ISOTROPIC DATA . . . . .	247
APPENDIX D. SAMPLE BIAXIAL DATA . . . . .	253
APPENDIX E. SAMPLE TRIAXIAL DATA . . . . .	259
REFERENCES . . . . .	265

## LIST OF TABLES

Table		Page
2.1	Summary of Values of the Slope of the $\log V_p - \log \bar{\sigma}_0$ Relationship . . . . .	15
2.2	Effect of Stress Ratio on Compression Wave Velocity at a Mean Effective Principal Stress of 10 psi . . . . .	19
5.1	Pressure Loading Sequences . . . . .	76
5.2	Densities and Void Ratios of Sand at Various Elevations in the Cube . . . . .	96
5.3	Source-Accelerometer Distances Determined After Placement . . . . .	101
6.1	Average Interval Velocities and Standard Deviation For Repeated Isotropic States of Stress . . . . .	148
6.2	Constants for Equations 6.9 and 6.14 . . . . .	157
7.1	Comparison of Constants and Slopes for Equations Relating $V_p$ or $M$ to $\bar{\sigma}_0$ for Isotropic Confinement and to $\bar{\sigma}_a$ for Biaxial Confinement . . . . .	170
7.2	Comparison of $V_p$ for Isotropic and Biaxial Confinement States When $\bar{\sigma}_a$ was Constant and $\bar{\sigma}_c$ Varied . . . . .	176
7.3	Comparison of Constants of Eq. 7.3 or Mean P-Wave Velocity During Loading and Unloading Sequences in Biaxial Confinement . . . . .	179
7.4	Comparison of Constants for Equations or Mean $V_p$ for Isotropic and Biaxial Confinement with $\bar{\sigma}_1$ along the North-South Axis . . . . .	181
8.1	Comparison of Constants and Slopes for Equation Relating $V_p$ or $M$ to $\bar{\sigma}_0$ for Isotropic Confinement and to $\bar{\sigma}_a$ for Triaxial Confinement . . . . .	197

Table		Page
8.2	Comparison of $V_p$ for Isotropic and Triaxial Confinement States When $\bar{\sigma}_a$ was Constant and $\bar{\sigma}_{c2}$ Varied . . . . .	201
8.3	Comparison of Constants of Eq. 7.3 or Mean P-wave Velocity during Loading and Unloading Sequences in Triaxial Confinement . . . . .	203
8.4	Comparison of Constants for Equations or Mean $V_p$ for Isotropic and Triaxial Confinements with $\bar{\sigma}_1^p$ along the North-South Axis . . . . .	206
8.5	Comparison of Constants and Slopes for Equations Relating $V_p$ or $M$ to $\bar{\sigma}_0$ for Isotropic Confinement and to $\bar{\sigma}_a$ for Triaxial Confinement with a Constant Mean Effective Principal Stress . . . . .	211
C.1	Travel Time Data Sheet Determined from Sample Isotropic Data . . . . .	251
D.1	Travel Time Data Sheet Determined from Sample Biaxial Data . . . . .	257
E.1	Travel Time Data Sheet Determined from Sample Triaxial Data . . . . .	263

## LIST OF FIGURES

Figure		Page
2.1	Pulse Method Testing Device Used by Lawrence to Study Compression Waves (from Lawrence, 1963) . .	8
2.2	Pulse Method Testing Device used by Schmertmann (from Schmertmann, 1978) . . . . .	9
2.3	Pulse Method Testing Device Used by Roesler for Shear Wave Measurements (from Roesler, 1979) . . . .	11
2.4	Variation of Compression Wave Velocity with Confining Pressure (from Wilson and Miller, 1962) .	14
3.1	Schematic Diagram of Model Cube and Associated Systems . . . . .	22
3.2	Cut-Away, Isometric View of Triaxial Cube Showing Top Reinforcement Details . . . . .	25
3.3	Cross-Sectional View Along Central Vertical Plane in Triaxial Cube . . . . .	26
3.4	Cross-Sectional View Along Central Horizontal Plane in Triaxial Cube . . . . .	29
3.5	Isometric View of Triaxial Cube Showing Side Reinforcement Details . . . . .	30
3.6	Sand Filling Operation in Progress with Wood Scaffolding in Place . . . . .	33
3.7	Completed Cube Structure . . . . .	34
3.8	Exploded View of Triaxial Cube . . . . .	36
3.9	Construction of First-Design Membranes . . . . .	40
3.10	Membrane Used to Apply Load to Sand Sample in Cube .	45
3.11	Schematic of Air/Water System Used to Pressurize the Membranes . . . . .	47

Figure		Page
3.12	Panel Board Used to Pressurize Membranes in Cube . .	48
3.13	Excitation Hammer in Each Port of Triaxial Cube . .	50
3.14	Close-up View of Excitation Port Without Impulse Hammer . . . . .	51
3.15	Typical Travel Time Records for Surface Source and Embedded Receivers . . . . .	54
3.16	Schematic of Monitoring and Recording Systems . . .	56
3.17	Isometric View of 3-D Accelerometer Package . . . .	57
3.18	Three-Dimensional Accelerometer Block with Accelerometers Installed . . . . .	58
3.19	Accelerometer Being Placed into a 3-D Accelerometer Block . . . . .	60
3.20	Accelerometer Orientation in 3-D Packages Relative to Impulse of Source . . . . .	62
3.21	Soil Stress Cell and Control Unit (from Terra Technology literature) . . . . .	64
3.22	Typical 2-in. Diameter Soil Strain Gage . . . . .	66
3.23	Original Sand Placement System . . . . .	70
5.1	Variation in Confining Pressure Along each Axis of the Cube with Time . . . . .	80
5.2	Mohr-Coulomb Envelope for Biaxial Confinement with Constant Mean Effective Principal Stress . . .	82
5.3	Mohr-Coulomb Envelope for a Typical Test under Triaxial Confinement . . . . .	84
5.4	Rubber Membranes Being Attached to the North and West Faces of the Cube . . . . .	88
5.5	Layer of Oil Being Applied to Plastic Sheet on West Face of Cube . . . . .	89
5.6	Sand Being Air-Dried in Outdoor Storage Bin . . . .	92

Figure		Page
5.7	Location of Density Measurements Taken During Filling of Cube . . . . .	94
5.8	Location of Stress and Strain Measuring Devices in Cube When Looking West Through the Cube . . . . .	98
5.9	Horizontal Location of Stress and Strain Measuring Devices at Mid-Height of Cube . . . . .	99
5.10	Personnel Cage Used in Placement of Electronics into Sand During Filling Operation . . . . .	102
5.11	Placement of Total Stress Cells When the Cube was Half Filled . . . . .	103
5.12	Total Stress Cell for Vertical Stress Measurement Placed on Sand Surface During Building of Sample . .	104
5.13	Total Stress Cell for Horizontal Stress Measurement Placed on Sand Surface During Building of Sample . .	105
5.14	Wires from Stress Cells Fed Through East Wall of Cube . . . . .	106
5.15	Placement of Strain Sensors When the Cube was Partially Filled . . . . .	109
5.16	Horizontal Strain Sensors Placed in the Sand During the Building of the Sample . . . . .	110
5.17	Sand Surface upon Completion of Building of the Sample . . . . .	113
5.18	Stress-Strain Curves for Each Axis of the Cube Based on Strain Gages . . . . .	116
5.19	Stress-Strain Curves for Each Axis of the Cube Based on Water Flowing Into and Out of Membranes . .	118
5.20	Stress Cell Reading versus Pressure Determined by Panel Board Gage for Each Axis of the Cube . . . . .	120
6.1	Compression Wave Travel Time Determined from a Set of Three Accelerometer Records Along One Axis of the Cube . . . . .	126

Figure		Page
6.2	Determination of Particle Amplitudes and Predominant Period from a Typical Accelerometer Record . . . . .	129
6.3	Variation in Compression Wave Velocity in the Vertical Direction with Isotropic Confining Pressure	135
6.4	Variation in Direct and Interval Compression Wave Velocity Along the Vertical Axis of the Cube with Isotropic Confining Pressure . . . . .	136
6.5	Variation in Direct and Interval Compression Wave Velocity Along the North-South Axis of the Cube with Isotropic Confining Pressure . . . . .	137
6.6	Variation in Direct and Interval Compression Wave Velocity Along the East-West Axis of the Cube with Isotropic Confining Pressure . . . . .	139
6.7	Typical Set of Accelerometer Traces for the East-West Axis Before Sand Leakage from the East Port . . . . .	141
6.8	Typical Set of Accelerometer Traces for the East-West Axis After Sand Leakage from the East Port . . . . .	142
6.9	Comparison of the Variation of Interval Compression Wave Velocity for Long and Short Intervals with Isotropic Confining Pressure . . . . .	144
6.10	Compression Wave Velocity for the Short Interval Normalized to the Long-Interval Value along the Vertical Axis versus Isotropic Confining Pressure .	145
6.11	Variation in Compression Wave Velocity with Isotropic Confining Pressure for Propagation along Each Axis of the Cube . . . . .	147
6.12	Variation with Time of Interval Compression Wave Velocity along the Vertical Axis at 20 psi Normalized to the Average Interval Compression Wave Velocity . . . . .	151
6.13	Variation in Compression Wave Velocity with Isotropic Confining Pressure for the Three Cube Axes . . . . .	153



Figure		Page
7.1	Illustration of Notation Used to Describe State of Stress Relative to Wave Motions . . . . .	165
7.2	Effect of Major Principal Stress in Direction of Wave Propagation on Compression Wave Velocity for Biaxial Confinement . . . . .	166
7.3	Effect of Minor Principal Stress in Direction of Wave Propagation on Compression Wave Velocity for Biaxial Confinement . . . . .	167
7.4	Effect of Minor Principal Stress in Direction of Wave Propagation on Compression Wave Velocity for Biaxial Confinement . . . . .	168
7.5	Effect of Major Principal Stress Perpendicular to Wave Propagation on Compression Wave Velocity for Biaxial Confinement . . . . .	172
7.6	Effect of Major Principal Stress Perpendicular to Wave Propagation on Compression Wave Velocity for Biaxial Confinement . . . . .	173
7.7	Effect of Minor Principal Stress Perpendicular to Wave Propagation on Compression Wave Velocity for Biaxial Confinement . . . . .	174
7.8	Summary of Effect of Stress History on P-Wave Velocity . . . . .	178
7.9	Effect of Structural Anisotropy on Compression Wave Velocity for Biaxial Confinement . . . . .	180
7.10	Variation in Normalized P-Wave Velocity with Lateral Pressure Coefficient, $K_{13}$ , for Biaxial Loading . . . . .	183
7.11	Variation in Normalized P-Wave Velocity with Lateral Pressure Coefficient, $K_{ac}$ , for Biaxial Loading . . . . .	184
7.12	Effect of Principal Stress in Direction of Wave Propagation on Compression Wave Velocity for Biaxial Confinement with Constant Mean Effective Principal Stress . . . . .	187

Figure		Page
7.13	Variation in Normalized P-Wave Velocity with Lateral Pressure Coefficient, $K_{13}$ , for Biaxial Loading with Constant $\bar{\sigma}_0$ . . . . .	189
8.1	Effect of Intermediate Principal Stress in Direction of Wave Propagation on Compression Wave Velocity for Triaxial Confinement . . . . .	195
8.2	Effect of Intermediate Principal Stress Perpendicular to Wave Propagation on Compression Wave Velocity for Triaxial Confinement . . . . .	199
8.3	Effect of Intermediate Principal Stress Perpendicular to Wave Propagation on Compression Wave Velocity for Triaxial Confinement . . . . .	200
8.4	Effect of Structural Anisotropy on Compression Wave Velocity for Triaxial Confinement . . . . .	204
8.5	Variation in Normalized P-Wave Velocity with Lateral Pressure Coefficient, $K_{23}$ , for Triaxial Loading . . . . .	207
8.6	Effect of Principal Stress in Direction of Wave Propagation on Compression Wave Velocity for Triaxial Confinement with Constant Mean Effective Principal Stress . . . . .	210
8.7	Variation in Normalized P-Wave Velocity with Lateral Pressure Coefficient, $K_{13}$ , for Triaxial Loading . . . . .	213
8.8	Variation in Normalized P-Wave Velocity with Lateral Pressure Coefficient, $K_{23}$ , for Triaxial Loading . . . . .	214
A.1	Grain Size Analysis of Washed Mortar Sand . . . . .	224
A.2	Failure Envelopes for Loose and Dense Sand Samples from Consolidated, Drained Triaxial Tests . . . . .	228
A.3	Variation in Low-Amplitude Shear Modulus with Effective Confining Pressure . . . . .	232
A.4	Variation in Low-Amplitude Shear Wave Velocity with Effective Confining Pressure . . . . .	234

Figure		Page
A.5	Variation in Low-Amplitude Material Damping Ratio with Effective Confining Pressure . . . . .	235
A.6	Variation in Shear Modulus with Shearing Strain . .	238
A.7	Variation in Material Damping Ratio with Shearing Strain . . . . .	239
C.1	Accelerometer Records for Sample Isotropic Data . .	248
C.2	Accelerometer Records for Sample Isotropic Data . .	249
C.3	Accelerometer Records for Sample Isotropic Data . .	250
C.4	Output from Program CUBE for Isotropic Data . . . .	252
D.1	Accelerometer Records for Sample Biaxial Data . . .	254
D.2	Accelerometer Records for Sample Biaxial Data . . .	255
D.3	Accelerometer Records for Sample Biaxial Data . . .	256
D.4	Output from Program CUBE for Biaxial Data . . . . .	258
E.1	Accelerometer Records for Sample Triaxial Data . . .	260
E.2	Accelerometer Records for Sample Triaxial Data . . .	261
E.3	Accelerometer Records for Sample Triaxial Data . . .	262
E.4	Output from Program CUBE for Triaxial Data . . . . .	264

## LIST OF SYMBOLS

A	= peak particle amplitude
A	= constant
A <sub>1</sub>	= amplitude of accelerometer record
A <sub>2</sub>	= double amplitude of accelerometer record
B	= bulk modulus
$\bar{c}$	= apparent effective cohesion
C	= dimensionless constant
C <sub>1</sub>	= constant
C <sub>u</sub>	= coefficient of uniformity
d	= distance
dia	= diameter
D	= material damping ratio
D <sub>10</sub>	= effective grain size
e	= void ratio
E	= Young's Modulus
F(e)	= $0.3 + 0.7 e^2$
f	= wave frequency
f <sub>n</sub>	= natural frequency
G	= shear modulus
G <sub>max</sub>	= low-amplitude shear modulus
h	= height from water elevation in panel board accumulator to top of cube

ID	= inside diameter
k	= factor based on plasticity index
K	= lateral pressure coefficient
$K_{ac}$	= lateral pressure coefficient, defined as $\bar{\sigma}_a/\bar{\sigma}_c$
$K_{13}$	= lateral pressure coefficient, defined as $\bar{\sigma}_1/\bar{\sigma}_3$
$K_{23}$	= lateral pressure coefficient, defined as $\bar{\sigma}_2/\bar{\sigma}_3$
$l$	= length of resonant column specimen
m	= slope of $\log V_p - \log \bar{\sigma}_a$ relationship
M	= constrained modulus
max	= maximum value
min	= minimum value
n	= slope of $\log M - \log \bar{\sigma}_a$ relationship
OCR	= overconsolidation ratio
$P_a$	= atmospheric pressure
$P_a$	= pressure read on gage in panel board
$P_c$	= actual pressure at center of cube
$S_i$	= constant
SD	= standard deviation
t	= travel time
T	= period
$\dot{u}_p$	= particle velocity
V	= wave velocity
$V_c$	= compression-wave velocity through a rod
$V_p$	= compression-wave velocity for a body wave

xx

- $V_{P(EW)}$  =  $V_p$  along the east-west axis of the cube  
 $V_{P(NS)}$  =  $V_p$  along the north-south axis of the cube  
 $V_{P(V)}$  =  $V_p$  along the vertical axis of the cube  
 $V_s$  = shear-wave velocity  
 $W$  = weight of added mass in resonant column tests  
 $W_r$  = weight of rod (sample) in resonant column tests  
 $Z$  = particle acceleration
- $\beta$  =  $\omega_n l/V_c$   
 $\gamma$  = single-amplitude shear strain  
 $\gamma$  = density  
 $\delta$  = logarithmic decrement  
 $\epsilon$  = linear strain amplitude  
 $\Delta\epsilon$  = cyclic change in strain  
 $\lambda$  = wavelength  
 $\nu$  = Poisson's ratio  
 $\pi$  = 3.14159 . . .  
 $\rho$  = mass density  
 $\bar{\sigma}_a$  = effective principal stress in direction of wave propagation  
 $\bar{\sigma}_{a1}$  = effective major principal stress in direction of wave propagation  
 $\bar{\sigma}_{a3}$  = effective minor principal stress in direction of wave propagation  
 $\bar{\sigma}_b$  = effective principal stress in direction of particle motion  
 $\bar{\sigma}_{b1}$  = effective major principal stress in direction of particle motion

$\bar{\sigma}_{b3}$	= effective minor principal stress in direction of particle motion
$\bar{\sigma}_c$	= effective principal stress perpendicular to $\bar{\sigma}_a$ and $\bar{\sigma}_b$
$\bar{\sigma}_{c1}$	= effective major principal stress perpendicular to $\bar{\sigma}_a$ and $\bar{\sigma}_b$
$\bar{\sigma}_{c2}$	= effective intermediate principal stress perpendicular to $\bar{\sigma}_a$ and $\bar{\sigma}_b$
$\bar{\sigma}_{c3}$	= effective minor principal stress perpendicular to $\bar{\sigma}_a$ and $\bar{\sigma}_b$
$\bar{\sigma}_{EW}$	= effective principal stress along the east-west axis
$\bar{\sigma}_{NS}$	= effective principal stress along the north-south axis
$\bar{\sigma}_o$	= mean effective principal stress
$\bar{\sigma}_1$	= major principal stress
$\bar{\sigma}_2$	= intermediate principal stress
$\bar{\sigma}_3$	= minor principal stress
$\Delta\sigma$	= change in stress
$\bar{\phi}$	= effective friction angle
$\omega_n$	= natural circular frequency

## CHAPTER ONE

## INTRODUCTION

Little research has been performed in which the effect of biaxial and triaxial states of stress on the propagation velocity of compression and shear waves has been investigated. An understanding of this behavior is necessary in the prediction of ground response and soil-structure interaction under dynamic loading. In addition, this knowledge is necessary in the proper interpretation of laboratory and field seismic testing and their relationship to each other. Therefore, a triaxial testing device was constructed, and an initial test series was performed to determine the relationship between propagation velocities and state of stress in a dry sand.

The portion of the research presented herein focuses on the effect of the states of stress on compression wave velocity. The reader is directed to Knox, et al (1982) for that part of the research which is concerned with shear wave velocity. The triaxial testing device was jointly designed and constructed by Mr. Knox and the writer, and compression and shear testing was performed concurrently.

A major part of the effort in this phase of the research was the design and construction of the triaxial testing device, hereafter referred to as the cube. As detailed in Chapter 3, the



cube was constructed of reinforced steel and was designed to hold a cubic soil sample measuring 7 ft (2.1 m) on a side. Rubber membranes were placed between the soil and three mutually perpendicular walls of the cube which correspond to the three principal planes. The membranes were filled with water and pressurized to load the soil to any of the three desired states of stress: isotropic, biaxial, or triaxial. Excitation ports were constructed in the three walls of the cube which were not covered with membranes. These ports provided access for a source bearing directly against the soil with which seismic waves could be generated in the soil. Accelerometers buried in the sample monitored the propagation of waves through the sample. Accelerometer signals were recorded on digital oscilloscopes. From these records, compression wave velocity was determined.

Only one sample was tested. This sample was a dry sand sample. The properties of the sand are discussed in Chapter 4 and Appendix A. The sand was rained into the cube as described in Chapter 5. Raining of the sand was halted at predetermined elevations for placement of the accelerometers. Stress and strain measuring devices were also placed in the sand to observe the stress-strain properties under the loading. The loading sequence was chosen to include isotropic confinement, biaxial confinement with constant and varying mean effective principal stresses and triaxial confinement with constant and varying mean effective principal stresses. The relationship between P-wave velocity and confinement was determined for each type of loading. The variation in compression wave velocity

with isotropic, biaxial, and triaxial confinement states is presented in Chapters 6, 7 and 8, respectively.

The effects on compression wave velocity of structural anisotropy and stress history of the sample were also determined. These effects are most easily seen in the results presented in Chapter 6 for isotropic confinement. Structural anisotropy caused a maximum variation of about ten percent in velocity between the axes of propagation. Stress history resulted in no noticeable variation in P-wave velocity and so was neglected.

Biaxial and triaxial loading results lead to the same conclusion, namely that the velocity of compression waves propagating through sand as body waves depend only on the stress in the direction of wave propagation. This conclusion had not been previously discussed in the literature as shown by the literature review presented in Chapter 2. It had briefly been discussed by Schmertmann (1978) for the biaxial state, but never by anyone for a triaxial state of stress.

## CHAPTER TWO

### REVIEW OF LITERATURE

#### 2.1 INTRODUCTION

The purpose of this research is to determine, for a dry sand, the relationship between compression and shear wave velocities and the triaxial state of stress. The work presented herein deals only with compression wave velocities. The effect of isotropic confinement on compression wave (P-wave) velocity has been well documented (Hardin and Richart, 1963; Hardin and Drnevich, 1970; Hardin and Drnevich, 1972; Hardin, 1978; Schmertmann, 1978; Wilson and Miller, 1962; and Lawrence, 1963). However, little research has been performed investigating the effect of biaxial confinement on P-wave velocities, and there is an absence of work in the literature dealing with the effect of the triaxial state of stress on either compression or shear wave velocity. The following sections review pertinent literature dealing with P-wave velocity and state of confinement. Knox (1982) presents a similar discussion for shear wave velocity.

#### 2.2 TESTING DEVICES

A major part of the effort of past research has been in the design of devices to measure the dynamic shear modulus,  $G$ , or the constrained modulus,  $M$ , of soil. Compression wave velocity is

directly related to M as shear wave velocity to G as defined by the following equations:

$$G = \frac{\gamma}{g} V_s^2 \quad (2.1)$$

$$M = \frac{\gamma}{g} V_p^2 \quad (2.2)$$

where:  $\gamma$  = density of the soil,

$g$  = acceleration of gravity (32.2 ft/s or 9.8 m/s),

$V_s$  = shear wave velocity, and

$V_p$  = compression wave velocity in an infinite medium.

Since  $V_p$  is the compression wave velocity in an infinite medium, and dynamic laboratory testing is done on small cylindrical soil specimens (small relative to the compression wave lengths used to test the sample), the elastic, or Young's modulus,  $E$ , is generally determined in the laboratory. The relationship between  $E$  and compression wave velocity through a rod,  $V_c$ , is:

$$E = \frac{\gamma}{g} V_c^2 \quad (2.3)$$

A number of devices used to determine M or E are summarized below.

Three general methods exist for determination of dynamic soil properties: the resonant column method, the pulse method, and the cyclic method. More details may be found in Woods' (1978) state-of-the-art paper on laboratory and field testing for dynamic properties of soils.

### 2.2.1 Resonant Column Method

One of the most common laboratory devices for measuring the dynamic moduli and material damping of soils is the resonant column device. Determination of the dynamic properties of soil is based on the theory of wave propagation through an elastic rod which is typically confined in a fixed-free configuration. Compression or shear waves may be propagated through the soil depending upon the excitation system. Torsional excitation produces shear waves and longitudinal excitation produces compression waves. Generally, only shear wave velocity is measured under isotropic confinement. Biaxial cells permitting separate variation of axial load and cell pressure have been designed (Hardin and Black, 1966; Hardin and Drnevich, 1970). However, these cells have only been used to measure shear wave velocities.

To determine  $V_c$  in the resonant column method, the natural frequency,  $f_n$ , of a rod in a longitudinal motion is determined. The natural frequency is combined with system constants to obtain  $V_c$ . For a sample tested using a fixed-free configuration with an added mass on the free end, the equation used to determine  $V_c$  is (Richart, Hall and Woods, 1970):

$$V_c = \frac{2\pi f_n l}{\beta} \quad (2.4)$$

where:  $l$  = length of the specimen,

$\pi = 3.14159\dots$ , and

$\beta$  = term found by solving the following equation:

$$\beta \tan \beta = \frac{W_r}{W} \quad (2.5)$$

where:  $W_r$  = weight of the rod, and  
 $W$  = weight of the added mass.

### 2.2.2 Pulse Method

In the pulse method, the travel time,  $t$ , is measured for a disturbance to travel through a distance,  $d$ , from the source to receiver. Velocity,  $V$ , is simply determined as:

$$V = \frac{d}{t} \quad (2.6)$$

Piezoelectric crystals are generally used as sources and receivers in the pulse method. The source generates low intensity waves of ultrasonic frequency (500,000 Hz) which travel through the soil and are monitored by receiving crystals to determine the travel time. The orientation and type of crystal determines whether it will generate P- or S-waves. Lawrence (1963) used these crystals to generate one-dimensional dilatational waves through sand and glass-bead samples which were longitudinally loaded by a pair of pistons and then placed in a load frame as shown in Fig. 2.1.

A test chamber in which the pulse method was employed was used by Schmertmann (1978) to measure both shear and compression waves in dry sand. The steel chamber, shown in Fig. 2.2, was 4 ft (1.2 m) high by 4 ft (1.2 m) in diameter and had separate axial and lateral loading systems to permit isotropic and biaxial

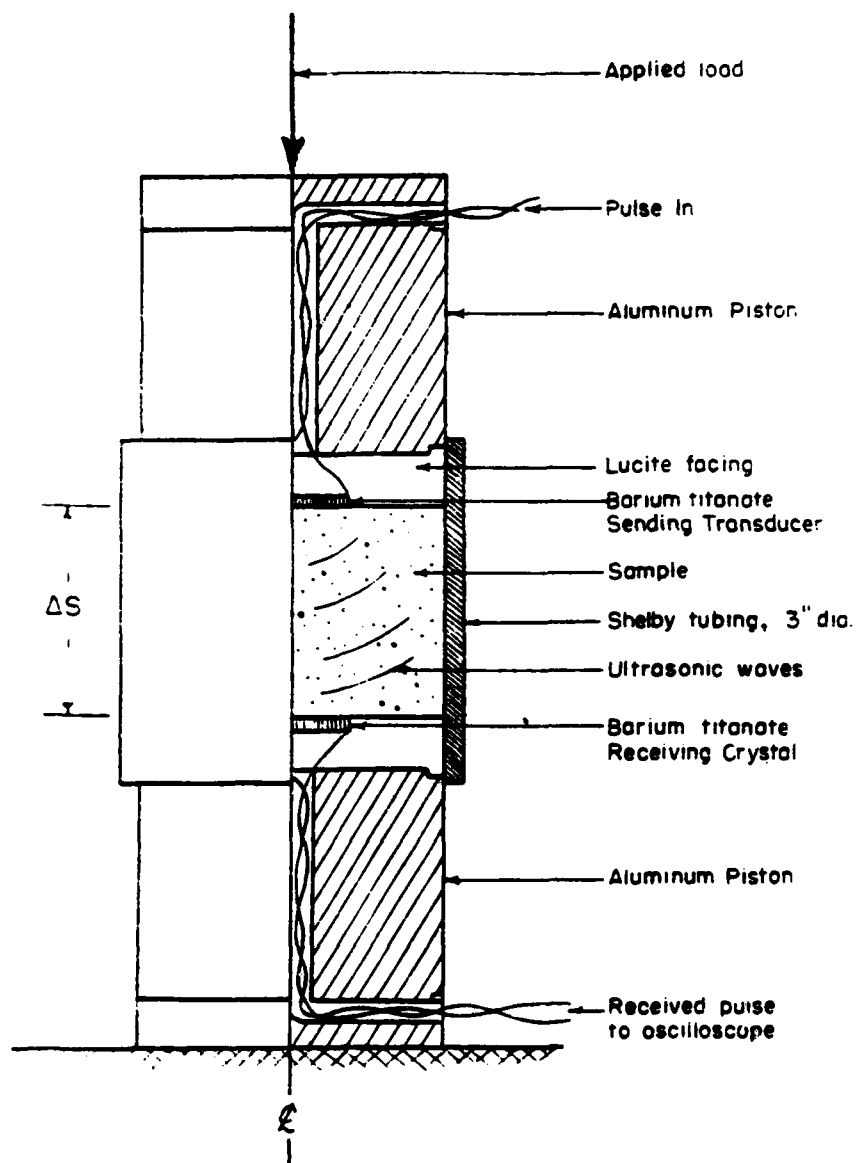
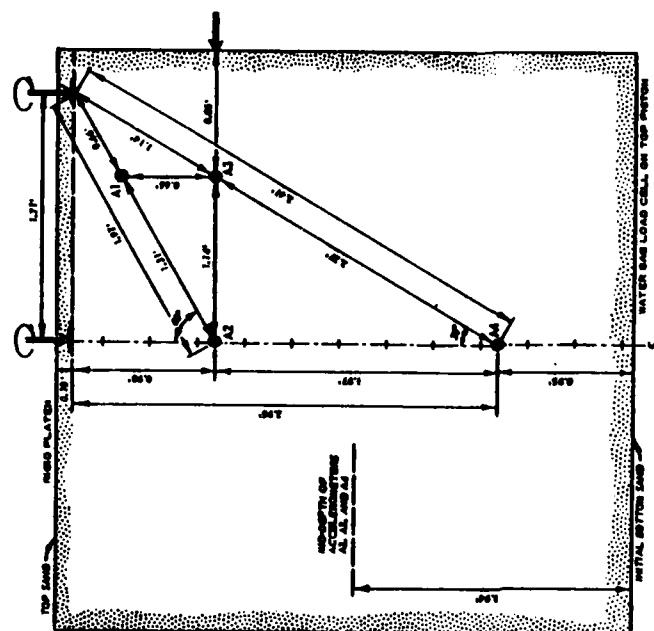
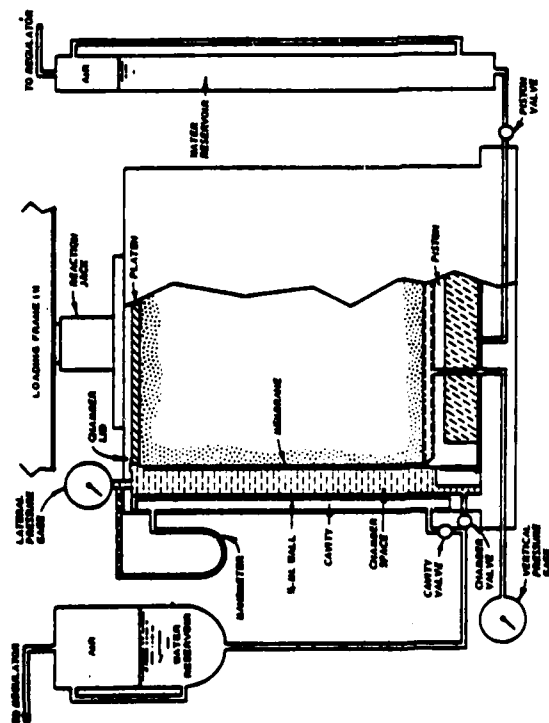


Fig. 2.1 - Pulse Method Testing Device Used by Lawrence to Study Compression Waves (from Lawrence, 1963)



b. Accelerometer Pattern in Plane Through Axis of Chamber



a. Schematic of Test Chamber and Loading System

Fig. 2.2 - Pulse Method Testing Device used by Schmertmann  
(from Schmertmann, 1978)

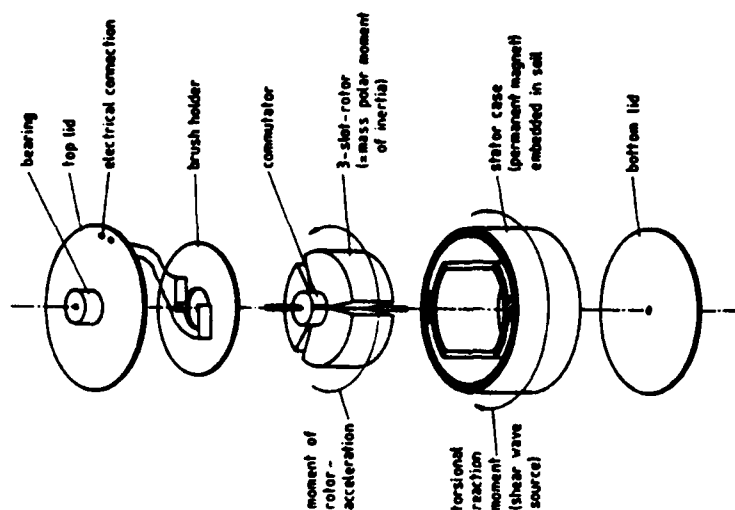


testing in the range of 5 to 20 psi (35 to 138 kPa). The large sample size was chosen to reduce boundary effects. The source for the waves was a circular disk which was buried in the surface of the sand and which extended outside the chamber for excitation. The disk was subjected to a downward motion to generate P-waves. Travel times used to compute  $V_p$  were determined using accelerometers buried in the sand.

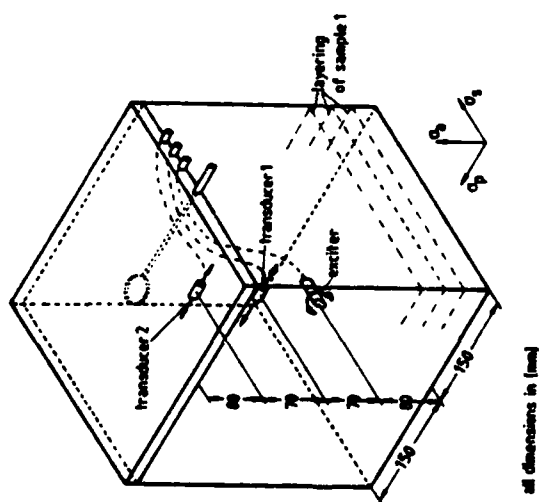
Roesler (1979) also used the pulse method to generate and record waves in soil. As shown in Fig. 2.3, Roesler's sample was a cube of sand measuring 30 cm (11.4 in.) on a side. Isotropic and biaxial states of stress were induced by evacuating the sample to an isotropic loading pressure and then applying an optional axial load. By keeping the sand cube evacuated, it was stable enough to be rotated allowing the axial load to be oriented along any of the three axes of the cube to study the effect of structural anisotropy. However, Roesler only used his device to study shear waves.

### 2.2.3 Cyclic Method

There are several types of cyclic test devices. The first is the torsional shear device, such as that used by Hardin and Drnevich (1970) to reduce the boundary condition problems associated with cyclic simple shear devices. However, this type of apparatus was only used for shear wave determination under isotropic loading and, therefore, is not discussed here. Another type is the cyclic simple shear device. This device is used for measuring



b. Shear Wave Exciter



a. Cubical Sand Sample showing  
Exciter and Transducers

Fig. 2.3 - Pulse Method Testing Device Used by Roesler for Shear Wave Measurements (from Roesler, 1979)

G at small strains under biaxial states of stress. Since this device is used only for G, hence shear waves, it is not discussed here.

The third type of cyclic test device is the cyclic triaxial testing device. This device is used for compression wave determination. In the cyclic triaxial device, the change in strain  $\Delta\epsilon$ , is typically measured for a cycling change in stress,  $\Delta\sigma$ . The elastic modulus is then determined by the following equation:

$$E = \frac{\Delta\sigma}{\Delta\epsilon} \quad (2.7)$$

The compression wave velocity can then be determined using Eq. 2.3. The shear modulus is often calculated from the elastic modulus using:

$$G = \frac{E}{2(1 + \nu)} \quad (2.8)$$

where:  $\nu$  = Poisson's ratio.

In using this equation, the assumption is made that the same factors influence both G and  $\nu$ , and therefore, both  $V_s$  and  $V_p$ .

### 2.3 EFFECT OF ISOTROPIC CONFINEMENT

The effect of isotropic confinement on P-wave velocity has been well documented. Using resonant column and cyclic triaxial devices, Hardin and others (Hardin and Richart, 1963; Hardin and Drnevich, 1970; Hardin and Drnevich, 1972; Hardin, 1978; and Silver and Park, 1975) analyzed the various parameters affecting wave

velocity under isotropic confinement. Their findings are summarized below.

#### 2.3.1 Mean Effective Principal Stress

Compression wave velocity has been shown to increase with increasing mean effective principal stress,  $\bar{\sigma}_0$ , in a linear fashion on a logarithmic plot as shown in Fig. 2.4. The slope of this relationship, as found by several authors, is listed in Table 2.1. From their findings, P-wave velocity is approximately proportional to the 1/5 to 1/4 power of the mean effective principal stress.

#### 2.3.2 Stress History

Stress history produces only a small decrease in P-wave velocity in sands. The decrease of about one to four percent from a virgin specimen is believed to be caused by the microscopic rounding of sand grains under loading (Hardin and Richart, 1963). The total effect of stress history is small enough to be neglected in sands.

#### 2.3.3 Strain Amplitude

The effect of strain amplitude on wave velocity is significant if the strains exceed 0.001 percent. Figure A.6, in Appendix A, shows the effect of strain amplitude on G which is typically assumed to be similar to the effect that strain amplitude would have on E and, therefore, on compression wave velocity. An increase in strain from 0.001 percent to 0.1 percent results in a three-fold decrease in wave velocity. However, all testing performed in this

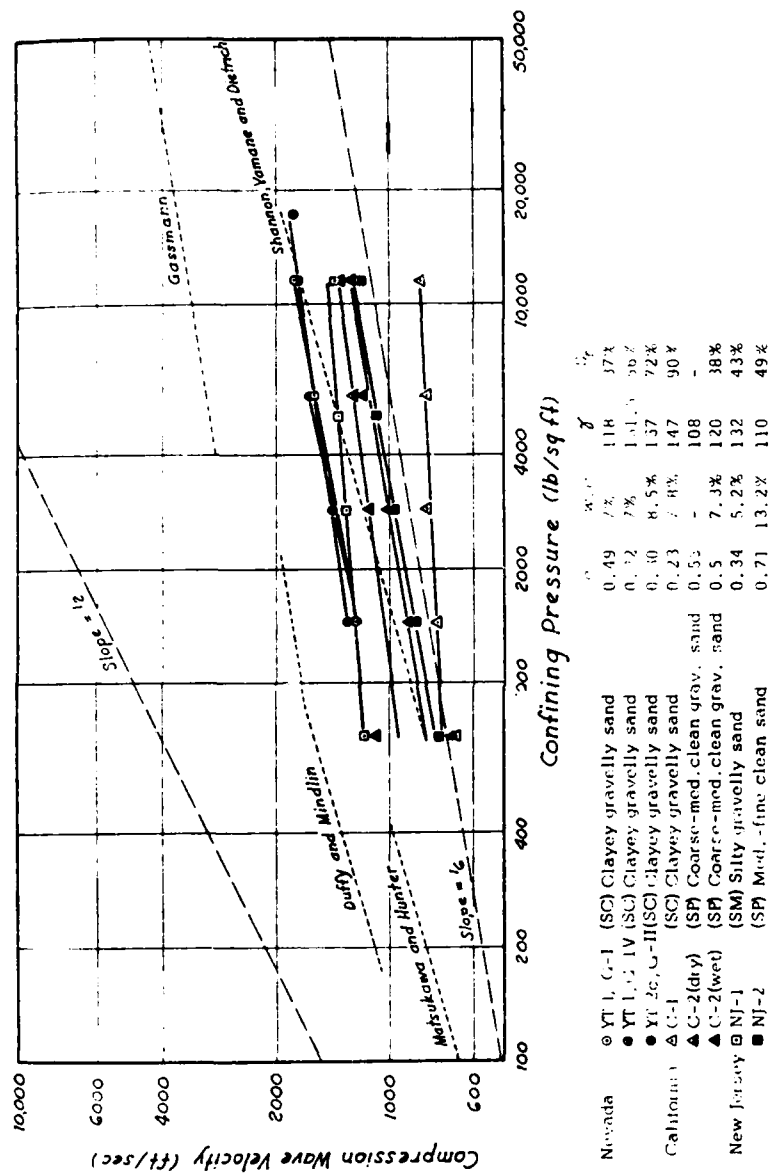


Fig. 2.4 - Variation of Compression Wave Velocity with Confining Pressure  
(from Wilson and Miller, 1962)

TABLE 2.1

Summary of Values of the Slope of the  
 $\log V_p - \log \bar{\sigma}_o$  Relationship

Reference (1)	Slope (2)
Hardin and Richart (1963)	
< 14 psi	0.25 to 0.33
> 14 psi	0.20 to 0.25
Schmertmann (1978)	0.20
Wilson and Miller (1962)	0.20 to 0.25
Lawrence (1963)	0.20 to 0.25

study was in the low-amplitude (small-strain) range where strain amplitudes are less than 0.001 percent. Thus, modulus is independent of strain amplitude in this strain range, and strain amplitude can be neglected as shown in Fig. A.6.

#### 2.3.4 Frequency

The frequency of the seismic wave can affect wave velocity. However, this effect is small in sand in the range of 200 to 2500 Hz (Hardin and Richart, 1963). Testing was conducted within this range, and therefore frequency was neglected.

#### 2.3.5 Other Factors

A number of other factors such as void ratio, degree of saturation, grain size characteristics, temperature, secondary effects, and soil structure can affect  $V_p$ . However, these effects did not enter this study because they either were constant or did not exist.

#### 2.3.6 Summary

Hardin (1978) summarized important factors affecting S-wave velocity into one equation expressed in terms of shear modulus at small strains,  $G_{max}$ , as:

$$G_{max} = \frac{A \text{OCR}^k}{0.3+0.7e^2} p_a^{1-n} \frac{\sigma_o}{\sigma_o}^n \quad (2.9)$$

where:  $A$  = constant (dimensionless),

OCR = overconsolidation ratio,

$k$  = function of soil plasticity ( $k = 0$  for sands),

$e$  = void ratio,

$P_a$  = atmospheric pressure, in units of  $G_{\max}$ ,

$n$  = slope of  $\log G_{\max} - \log \bar{\sigma}_o$ , and

$\bar{\sigma}_o$  = mean effective principal stress, in units of  $G_{\max}$ .

Using identities between  $G_{\max}$  and the elastic constrained modulus,  $M$ ,

Hardin rewrote the equation:

$$M = \frac{(1 - \nu) S_i \text{OCR}^k}{(1 + \nu)(1 - 2\nu)F(e)} P_a^{1-n} \bar{\sigma}_o^n \quad (2.10)$$

where:  $\nu$  = Poisson's ratio,

$F(e)$  = function of void ratio ( $F(e) = 0.3 + 0.7e^2$ ), and

$S_i$  = constant.

Since the P-wave velocity is related to  $M$  by Eq. 2.2 and  $V_s$  to  $G$

by Eq. 2.1, Hardin made the assumption that the above factors have

the same effect on  $V_p$  as they do on  $V_s$  (assuming  $\nu$  independent of  $\bar{\sigma}_o$ ).

## 2.4 EFFECT OF BIAXIAL CONFINEMENT

The majority of the research into the effect of biaxial confinement has concentrated on S-wave velocities rather than P-wave velocities. Although some devices were capable of generating compression waves (Section 2.2), few results on P-wave velocity were published.



Schmertmann (1978) used both compression wave velocity, and shear wave velocity in his study of bulk modulus. The bulk modulus,  $B$ , is defined as:

$$B = \frac{\gamma}{g} (V_p^2 - \frac{4}{3} V_s^2) \quad (2.11)$$

As described in Section 2.2, Schmertmann measured travel times between an impulse source and accelerometer receivers in a test chamber. Both isotropic and biaxial loading was possible. Under isotropic loading, he found that  $V_p$  was slightly faster in the horizontal direction than in the vertical direction. He suggested structural anisotropy formed during sand placement was the cause for the difference.

Under biaxial loading, Schmertmann found significant variation in P-wave velocity with a change in the stress ratio while keeping the mean effective principal stress constant. As shown in Table 2.2, there was little change (3 percent) in  $V_p$  in the horizontal direction as the stress ratio was varied. However, the P-wave velocity of wave propagating in the vertical direction increased with the increased stress. He concluded that P-wave velocities were greater in the direction of major principal stress.

## 2.5 SUMMARY

Most of the research previously performed to study the effect of state of stress on P-wave velocity has concentrated on isotropic confinement. Investigators have shown that P-wave

TABLE 2.2

Effect of Stress Ratio on Compression Wave Velocity  
 at a Mean Effective Principal Stress of 10 psi  
 (from Schmertmann, 1978)

Direction of Propagation	Stress Ratio ( $\sigma_3/\sigma_1$ )	Compression Wave* Velocity, fps
(1)	(2)	(3)
Vertical	1	1455
	1/3	1621
Horizontal	1	1506
	1/3	1460

\*Based on an average of two densities.

velocity varies with approximately the  $1/5$  to  $1/4$  power of the mean effective principal stress.

Schmertmann (1978) and Hardin (1978) studied the effect of biaxial confinement on  $V_p$ . Schmertmann noted that the major principal stress influenced the P-wave velocity, but Hardin based his equations on the mean effective principal stress, assuming that if this stress was constant, then the velocity did not vary.

A number of factors influence P-wave velocity in addition to state of stress. These factors include stress history, structural anisotropy, void ratio, temperature, strain amplitude, frequency, degree of saturation, and grain size characteristics. Most of the factors were constant in this study or were not within the scope of the study and, as such, were neglected.

### CHAPTER THREE

#### TRIAXIAL TESTING DEVICE

##### 3.1 INTRODUCTION

Much of the effort in this project was necessarily directed toward the design, fabrication, and readiness for testing of the triaxial cube and associated equipment. This chapter discusses the design of the triaxial cube and associated equipment and reviews the development and evolution of each system within the triaxial testing device.

The triaxial cube is essentially a steel box with interior dimensions of 7 ft (2.1 m) on a side. Equipment associated with the cube is used to: 1. place the sand in a uniform state within the cube, 2. pressurize the sand mass to a desired stress state, 3. excite compression or shear waves in the sand, 4. monitor and digitally record these waveforms, and 5. monitor the stress and strain throughout the sand sample during testing. A schematic drawing of the cube and its associated systems is shown in Fig. 3.1. The cube and associated equipment are located at the Phil M. Ferguson Structural Engineering Laboratory at the Balcones Research Center of The University of Texas at Austin.

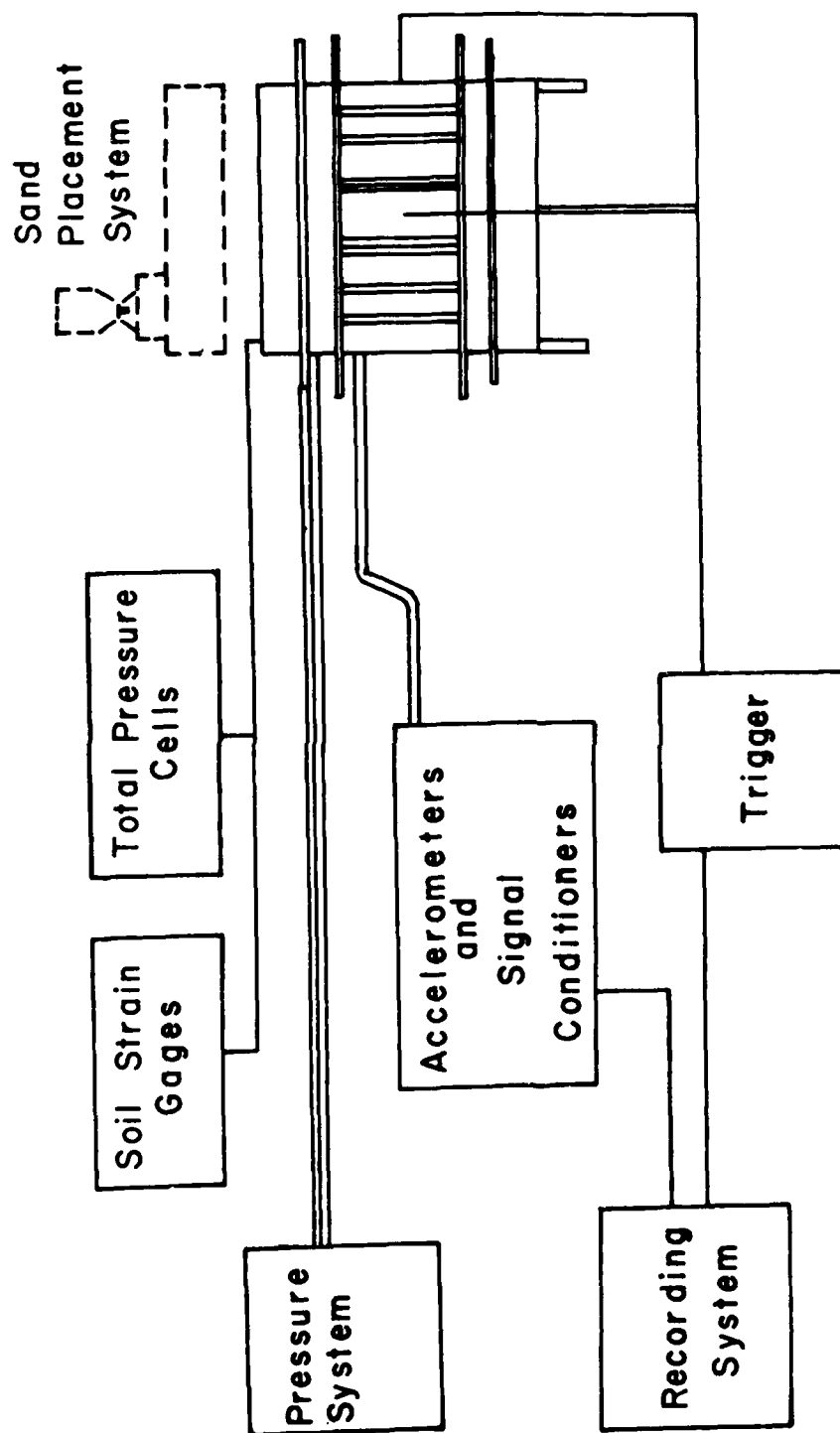


Fig. 3.1 - Schematic Diagram of Model Cube and Associated Systems

## 3.2 STRUCTURE OF THE CUBE

### 3.2.1 Design Considerations

The cube was planned to provide a cubic sample, 7 ft (2.1 m) on a side, through which wave propagation tests could be performed. It was desired to form as large a sample as practical in order to obtain a central portion of sand which would be relatively free of any boundary effects. One boundary effect results from the loading system creating uncertain stresses in the sand along the sides and especially in the corners of the cube. The dimensions selected for the cube provide a central, 4-ft (1.2 m) cubic portion of sand which is considered free from edge effects.

In its simplest form, the cube was initially envisioned as a large box composed of interconnected steel plates approximately 7 ft (2.1 m) square. However, subsequent calculations showed that a plate thickness of 12 in. (30.5 cm) would be required to restrict the bending of the plates to an acceptable value under the desired maximum working pressure of 50 psi (340 kPa). Plates of this size were impractical because of high fabrication costs and excessive weight. A compromise between reduced plate thickness and substantial reinforcement was chosen to reduce the cost of the material and weight of the cube to acceptable values. In the final design, 0.357-in. (0.95 cm) thick, mild steel plates were employed to form all six sides of the cube. These steel plates were reinforced with longitudinal I-beams and lateral angle and plate bracing so that

the cube could withstand a working pressure of 50 psi (345 kPa) over any side. The gross weight of the steel structure is estimated to be about 5 tons (4500 kg).

### 3.2.2 Cube Construction

The cube was designed to be built in three separate sections: 1. the bottom with four base legs, 2. the four sides, and 3. the top. These three sections were then bolted together to form the completed structure. In typical use, the four sides remain bolted to the bottom section and only the top is removed as the cube is filled or emptied of sand. The construction procedure for these sections was: 1. complete the bottom section with base legs, 2. tack weld the four sides together and bolt them to the bottom, 3. complete the top of the cube and examine the fit with the four sides, and 4. with the top removed, finish welding the four sides of the cube together.

The top and bottom sections are similar in design except for the addition of four legs on the bottom section. Each section begins with a 7-ft (2.1 m) square steel plate. Steel reinforcement is then welded to the plate as shown in Figs. 3.2 and 3.3. Along the edges of the plate, angle sections are welded which have bolt holes fabricated in them to allow the top and bottom sections to be secured to the four sides. The angle sections on the east and west edges are L2x2 each with a row of seven equally spaced 0.625 in. (1.58 cm) diameter bolt holes, and the sections on the north and

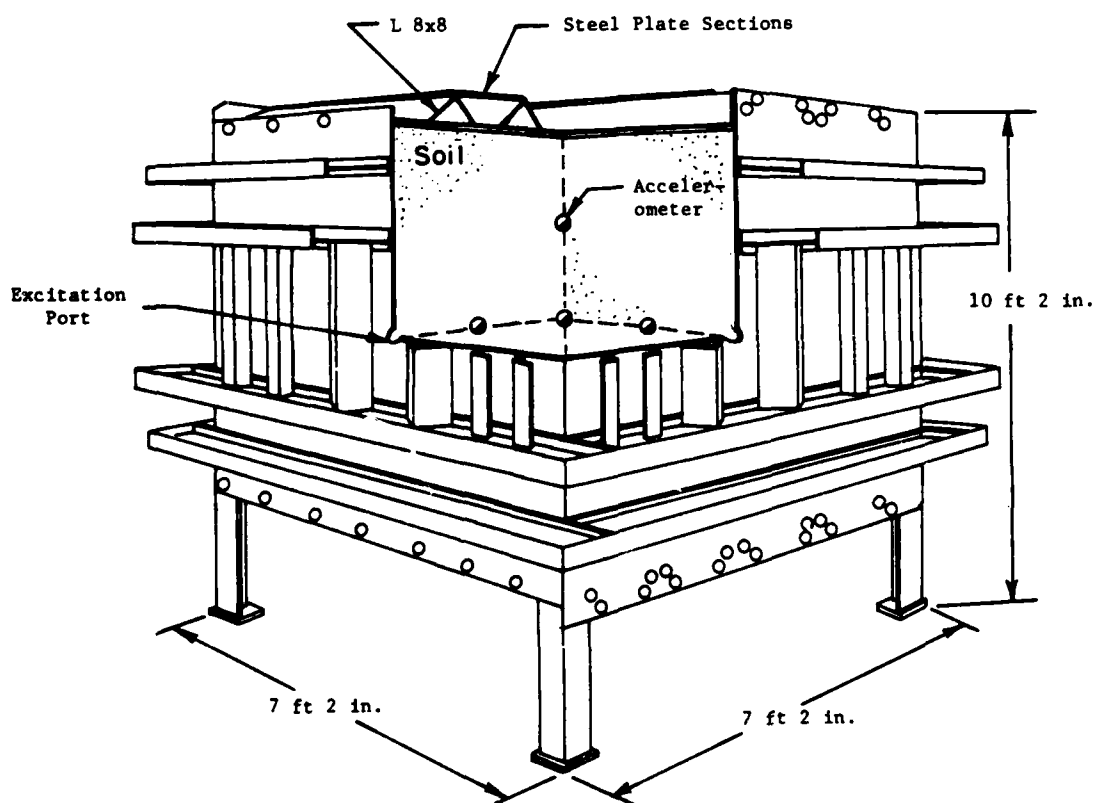


Fig. 3.2 - Cut-Away, Isometric View of Triaxial Cube  
Showing Top Reinforcement Details



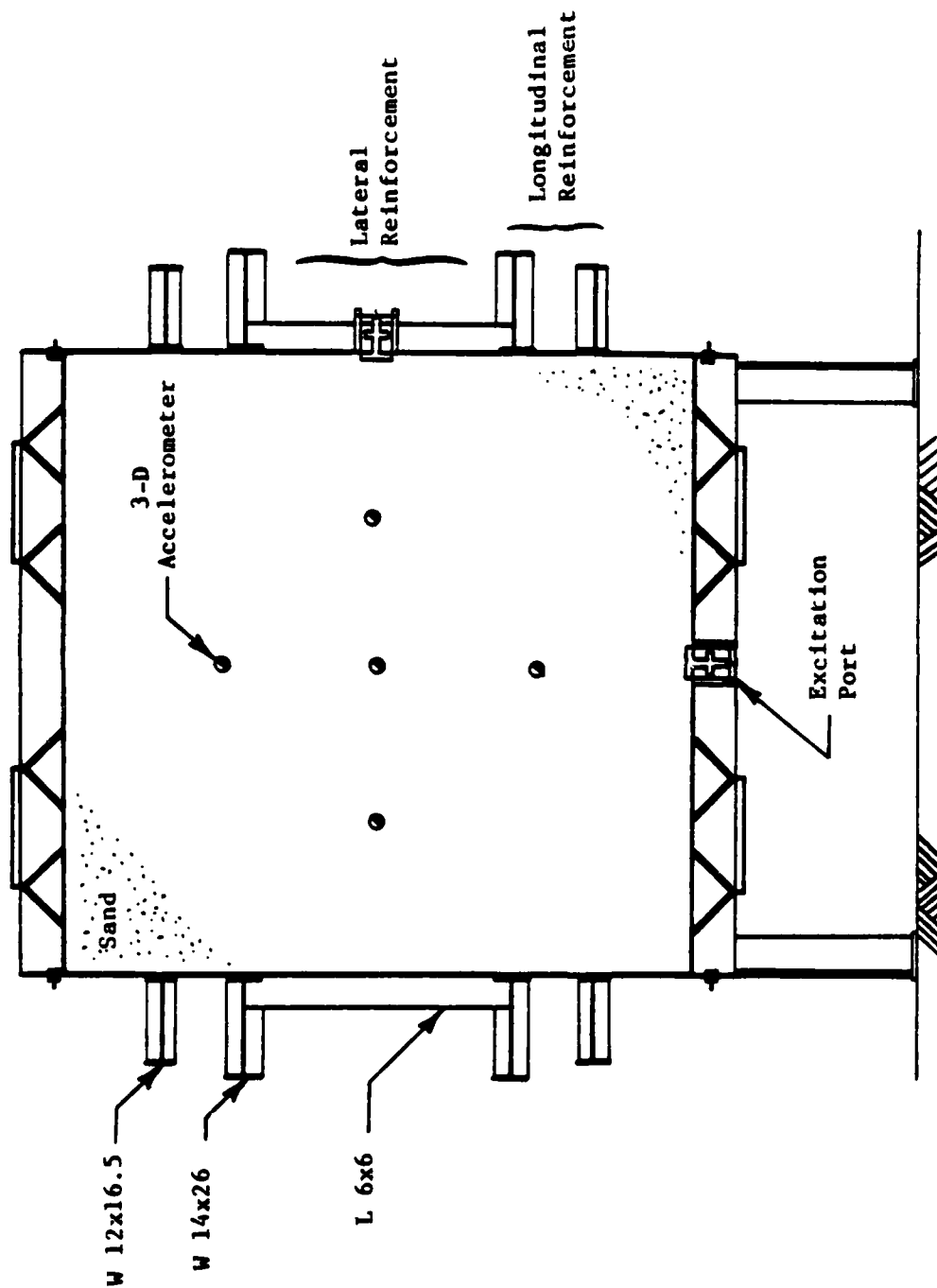


Fig. 3.3 - Cross-Sectional View Along Central Vertical Plane in Triaxial Cube

south edges are  $L6 \times 3\frac{1}{2}$  each with a pattern of seventeen 1.0-in. (2.54 cm) diameter bolt holes. Four  $L8 \times 8$  angles are welded across the steel plate in two pairs, each pair centered on half of the steel plate. Additional reinforcement of 0.5-in. (1.27 cm) thick steel plate is welded between the adjacent  $L8 \times 8$  angles for their entire length of 7 ft (2.1 m).

The legs on the bottom section are included in the design to allow access to the bottom of the cube with its excitation port (see Section 3.3). The legs are fabricated from  $L5 \times 5$  angles and elevate the bottom of the cube 2.5 ft (.76 m) above the floor surface. Reinforcement of 0.5-in. (1.27 cm) thick steel plate is included above each leg to prevent punching through the bottom face of the cube by the legs when the cube is filled with sand. Small sections of 0.5-in. (1.27 cm) thick steel plate are welded onto the leg angles to withstand any buckling or bending moment in the legs due to the weight of the sand and cube.

For the top and bottom sections, the reinforcement was first tack welded to the steel plates and then completely welded together as a unit. Unfortunately, these sections had to be welded without being secured in place with the cube framework. This permitted some slight bowing of the steel plates due to the welding heat which was corrected in the final stage of welding.

The four sides of the cube are constructed of 0.375-in. (0.95 cm) thick, steel plates with angle and I-beam reinforcement. The steel plates are 7-ft wide (2.1 m) with two plates 7.5-ft (2.3 m)

high and the other two plates 8.2-ft (2.5 m) high. The additional height contains fabricated bolt holes corresponding to those of the angles along the top and bottom sections. Steel angles are vertically welded as lateral reinforcement around the mid-section of the sides as shown in Figs. 3.3 and 3.4. Each side has four,  $L3\frac{1}{2} \times 3\frac{1}{2}$  and two,  $L6 \times 6$  angles. The angles transfer the load to two, longitudinal, 14-in. (35.6 cm),  $W14 \times 26$  I-beams. The I-beams are horizontally welded to form two continuous rings around the cube with the lateral reinforcement between them. Two more longitudinal rings of 12-in. (30.5 cm),  $W12 \times 16\frac{1}{2}$  I-beams restrict the bending of the upper and lower regions of the steel plates. The longitudinal reinforcement is shown in Figs. 3.3 and 3.5. The extreme edges of the steel plates are rigid due to the plate-to-plate welding on the sides and the bolt connections along the top and bottom sections.

The procedure used in constructing the sides of the cube consisted of: 1. tack welding the reinforcement to the side plates, 2. bolting each side to the already completed bottom, 3. tack welding the four sides together while bolted to the bottom, and 4. final welding of the reinforcement to the side plates. The procedure was followed in order to reduce the possible deformation of the thin, flat steel plates due to the welding heat. Initial tack welding secured the reinforcement to the side plates with a minimum of heat created in the plates, thereby reducing the curvature produced in the side plates. With the four sides bolted to the bottom, tack welding of the plates together ensured that the

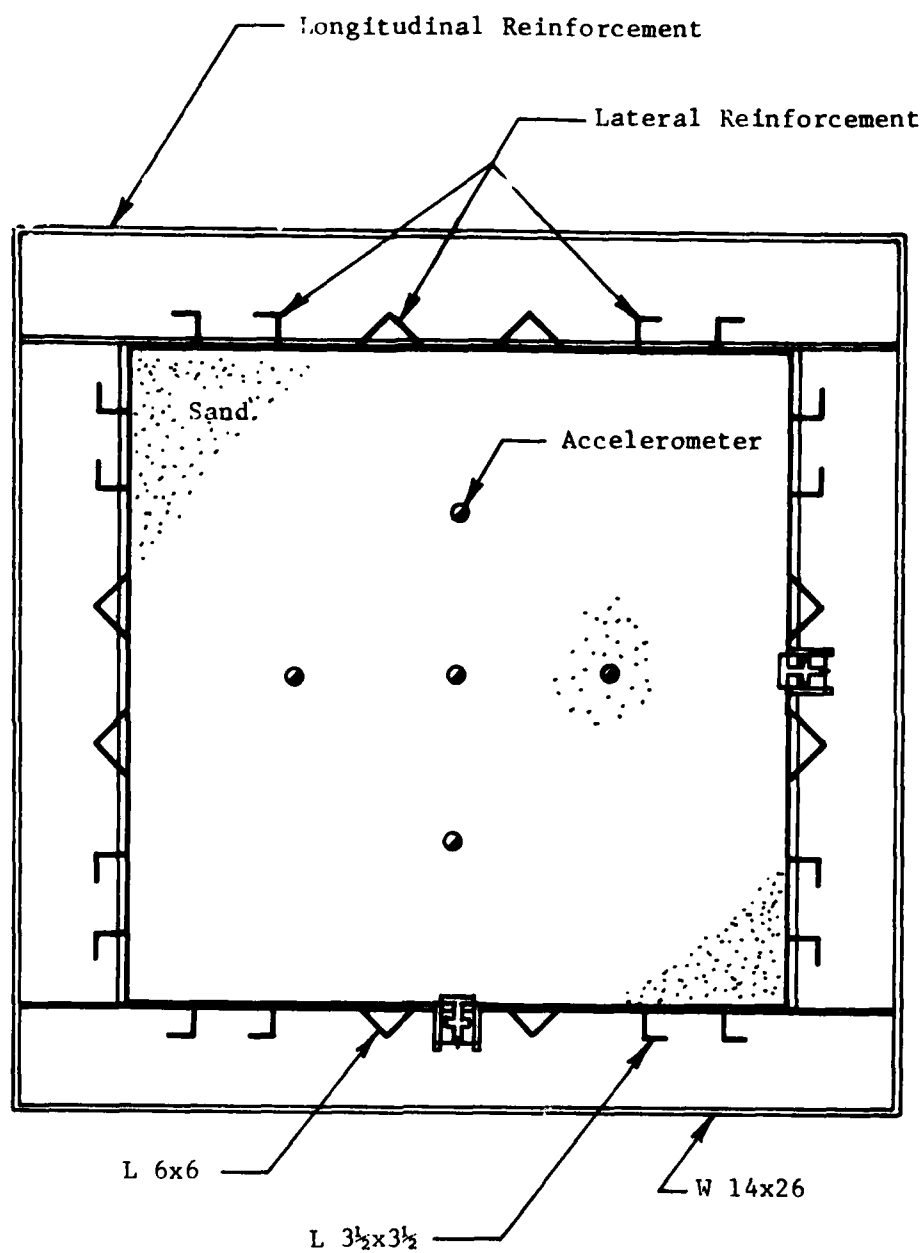
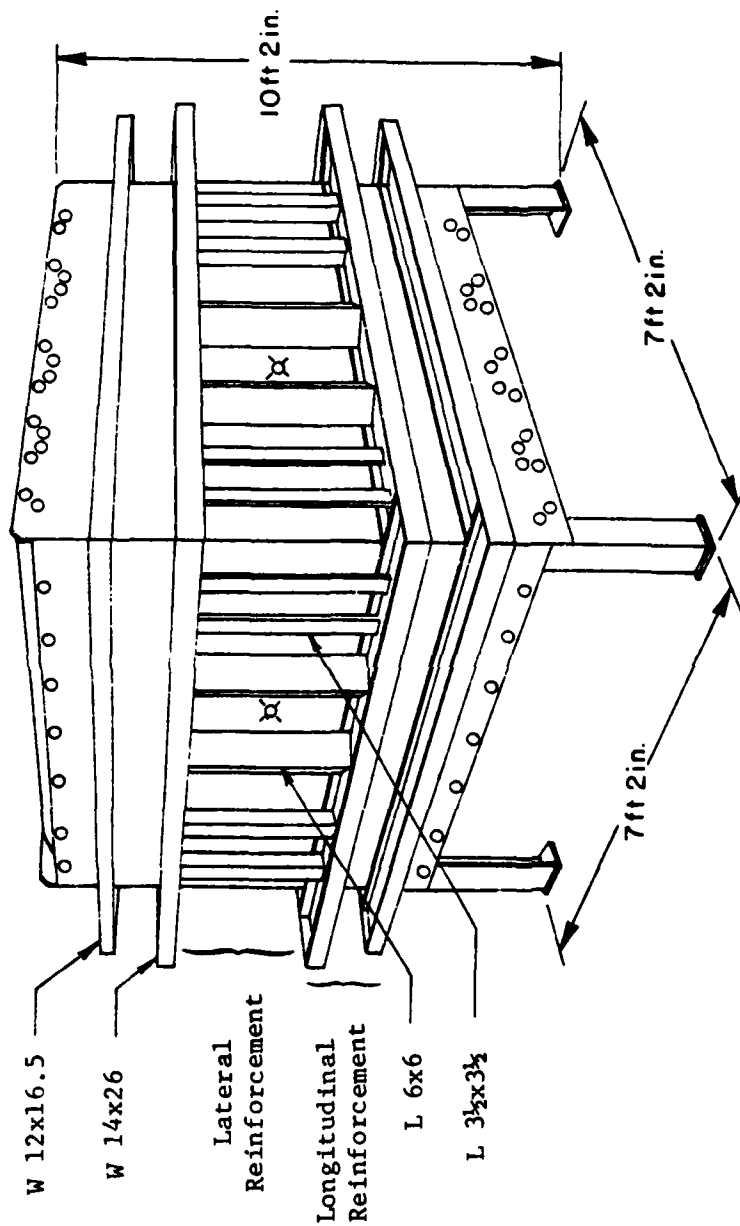


Fig. 3.4 - Cross-Sectional View Along Central Horizontal Plane in Triaxial Cube



Note: See Figs. 3.3 and 3.4 for  
Cross-Sectional Detail Views

Fig. 3.5 - Isometric View of Triaxial Cube Showing Side Reinforcement Details

final shape would not deform considerably from the design shape. Measurements of the finished cube verified that there was no significant deviation of the cube from the desired shape. The final interior dimensions measured along the edges and across the center of all plates varied by less than  $\pm 0.785$  in. (2.0 cm) from the designed length of 7 ft (84 in. or 213.4 cm), or 0.9 percent.

### 3.2.3 Special Features of the Cube Structure

The final design of the structure incorporates several desirable features. The cube has been designed as a free-standing structure without the need of any external support. This permits the cube structure to be located at any site where the associated equipment has adequate support. In addition, lifting lugs are provided on the top section of the cube to permit movement of the cube, whether full or empty of soil, with the 25-ton (22,700 kg) overhead crane available at the Ferguson Laboratory. Further, excitation ports were fabricated in each face of the cube to provide complete versatility in the location of wave generation. A source hammer can, therefore, be placed in any of the six faces.

To make access to the cube easier and safer during operation, a steel ladder and wood scaffolding were constructed. The steel ladder was built at the same height as the uppermost I-beam, approximately 9 ft (2.7 m) above the floor surface. This allows easy access to the top of the cube and provides a safe elevated working platform. Rollers were included on the ladder to

facilitate movement around the cube as space restrictions dictate. Wood scaffolding was constructed to provide large working platforms at the same height as the uppermost I-beam and to run along two sides of the cube. The scaffolds provide a safe walkway during cube filling operations. After the cube is filled with sand the scaffolds can be easily dismantled and stored near the cube. Figure 3.6 shows the assembled scaffolding next to the cube.

The cube was painted two shades of blue on the outside, light blue on the steel plates and dark blue on the reinforcement. All of the inside of the cube was painted light blue. The steel ladder was also painted light blue. Figure 3.7 shows the completed cube structure.

### 3.3 LOADING SYSTEM

To study wave propagation in soil, it is necessary to apply confining stresses on the soil mass which attempt to model those three-dimensional stresses the soil is subject to in the field. By designing a loading system which simulates field conditions, the resulting wave propagation data can be examined more realistically. Non-rigid membranes were desired for the loading system in order to model stress-controlled conditions. A non-rigid, stress controlled boundary allows non-uniform strains in the sand mass but better simulates desired conditions of uniform stresses within the sand (Arthur and Menzies, 1972). Rigid, strain-controlled boundaries can cause mechanical problems due to sample deformation

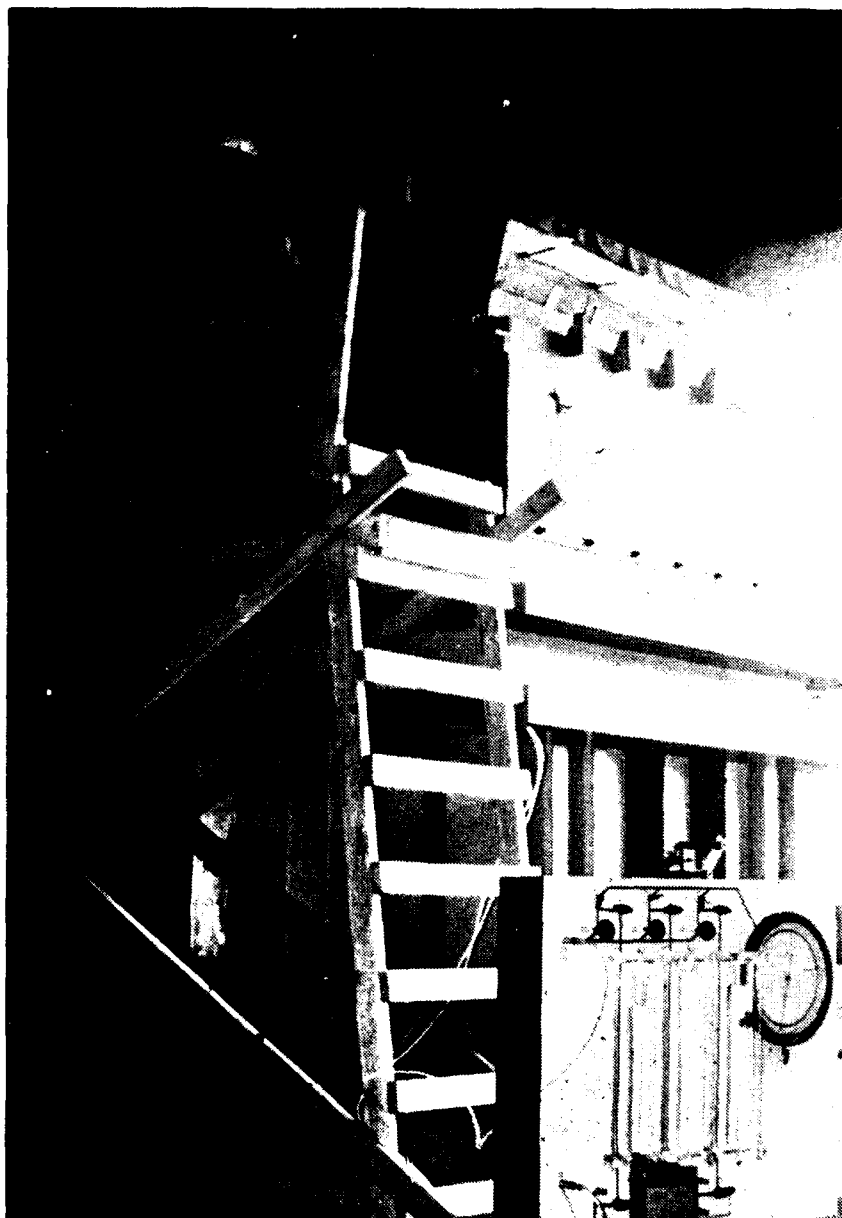


Fig. 3.6 - Sand Filling Operation in Progress  
with Wood Scaffolding in Place



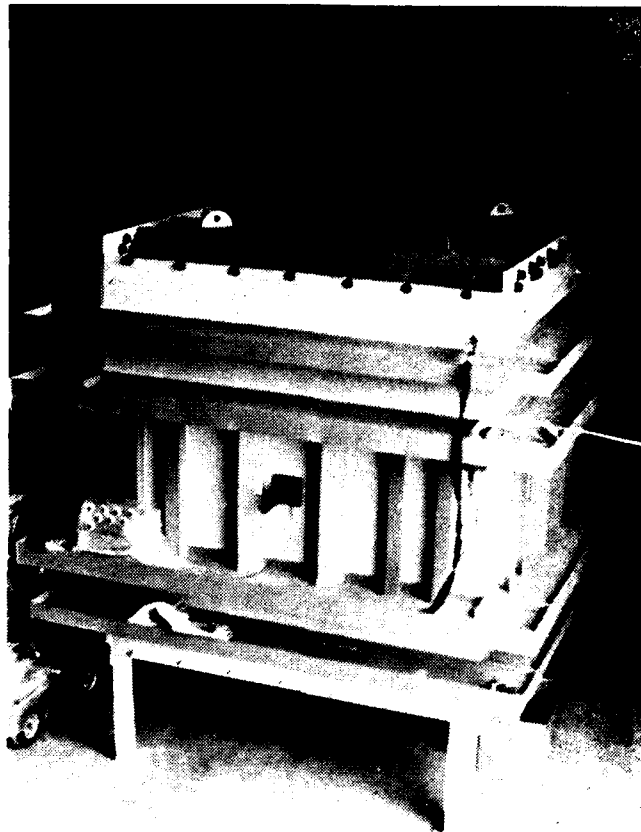


Fig. 3.7 - Completed Cube Structure

in the corners of the cube. Further, rigid boundaries, although causing uniform displacements, do not guarantee uniform stresses in the sand mass.

### 3.3.1 Membrane Operation

Confining stresses are applied to the sand mass by three membranes placed on the inside of the cube: one along the top and one on each of two adjacent sides. An exploded view of the membranes within the cube is shown in Fig. 3.8. In this configuration, one membrane is used to apply pressure along each of the three principal axes of the cube. The membranes are confined along their perimeter by steel ribs of 3/4x3/16 in. (1.9 cm x 0.48 cm) bar section welded along the edges of the inside faces of the cube at 45-degree angles away from the plane of the cube face. These ribs are assumed to confine the membrane edges from expanding toward an adjacent membrane, thereby preventing the tendency of the membranes to stretch and burst along the edges (Sutherland and Mesdary, 1969; Arthur and Menzies, 1972). With this confinement, each membrane is isolated from the others, and so each membrane exerts a pressure only along its respective axis. This arrangement permits independent control of the pressure in each of the three principal directions. Loading conditions on the sand can then be isotropic ( $\sigma_1 = \sigma_2 = \sigma_3$ ), biaxial ( $\sigma_1 > \sigma_2 = \sigma_3$ ), or true triaxial ( $\sigma_1 > \sigma_2 > \sigma_3$ ).

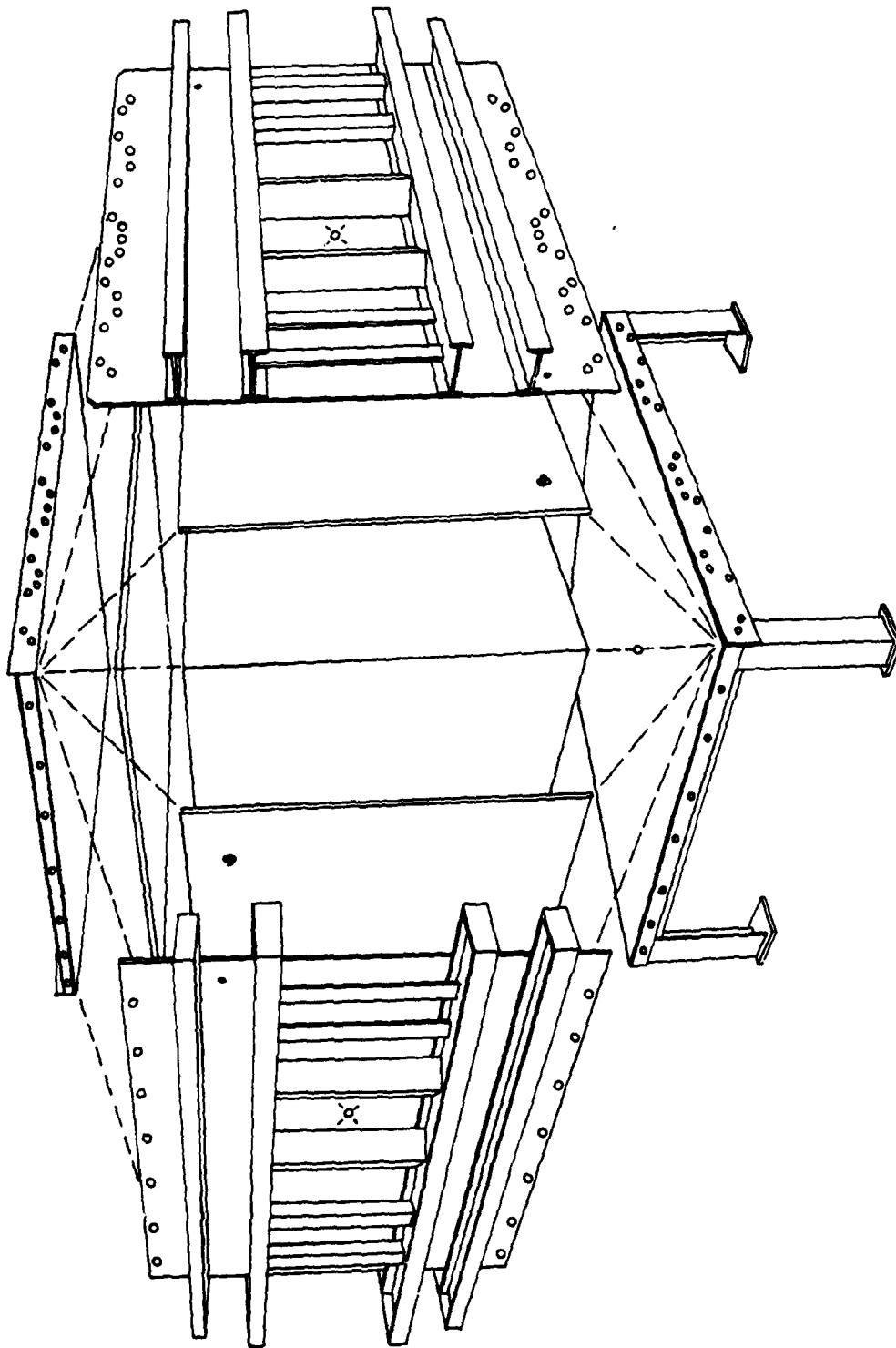


Fig. 3.8 - Exploded View of Triaxial Cube

### 3.2.2 Membrane Characteristics

Initial discussion of the loading system lead to an ideal membrane design which would: 1. be capable of attaining and indefinitely maintaining the maximum desired pressure of 50 psi over the entire cube face, 2. have rugged and durable construction with puncture and tear resistant materials, 3. present no operational hazards, 4. be simple and quick to pressurize, 5. be manageable, and 6. have a reasonable cost. It was felt that the final membrane design should incorporate an optimum mixture of these characteristics. Triaxial cells of much more limited size possess membranes with similar characteristics (Ko and Sture, 1974; Ko and Scott, 1967; Laier, Schmertmann, and Schaub, 1975).

An important design consideration of the membranes was the decision to use water and not air to pressurize the membranes. Fluid under these pressures is safer than air because of the incompressibility of the fluid. Leakage detection in the membranes would be easier with water filled membranes since water can be visually monitored while air cannot. Water entering the membranes would be indicative of leakage and water elevations in the panel board accumulators (see Section 3.3.5) could be easily monitored. Finally, water provides a more desirable vertical pressure distribution on the sand mass, as compared to air. This stems from the fact that, for any elevation in the cube, the water or air and the sand exhibit side forces due to the weight of material above it. This side force is in addition to any pressure in the water or air.

For the water the lateral force would be equal to the weight of water above it ( $K = 1.0$ ), or 62.4 psf per ft (9.8 kPa per m) of elevation head. While for sand, the force is estimated to average about 0.4 of the weight above a given load ( $K = 0.4$ ), or about 40 psf per ft (6.3 kPa per m) of elevation. The density of air is so small that its side forces are negligible. There are organic fluids available which possess densities lighter than water and are therefore more mathematically attractive but their high cost and hazardous properties reduce their value. Therefore, it was decided to use water. Also, it was decided to commence testing at 10 psi to reduce the significance of the non-uniform vertical and horizontal pressure distribution.

### 3.3.3 First-Design Membranes

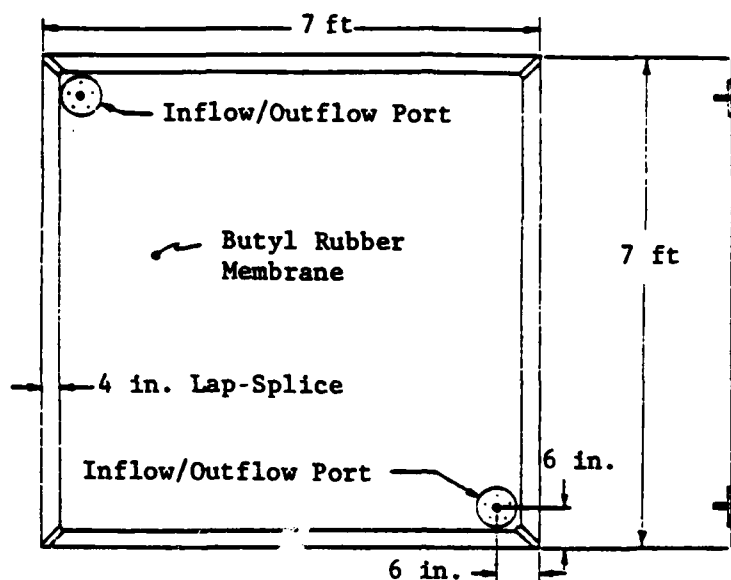
A number of possible membrane solutions were considered, which fell into three general categories: 1. use of a currently manufactured product, either directly as produced or modified as required, 2. use of membranes professionally constructed as per specifications, or 3. construction of membranes ourselves. Those products currently manufactured include dunnage bags, water pressure bags, and utility bags. Each of the solutions contained most of the desired membrane features, with the solutions having a wide range of cost and each solution possessing its own drawbacks.

After examining each of the potential solutions it was decided to construct the membranes ourselves. This choice seemed

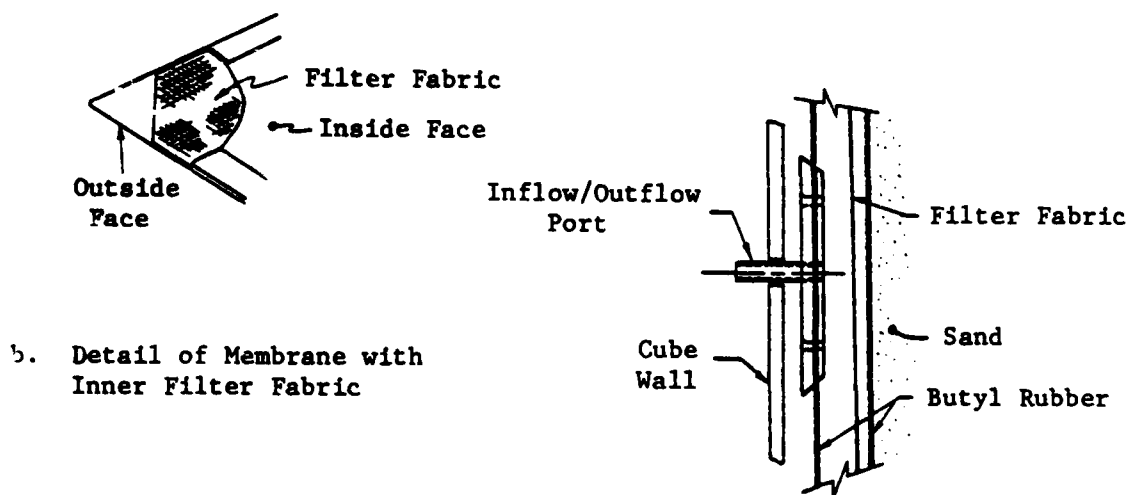
to offer fabricated membranes at the lowest cost and of the precise configuration needed. This version of the loading system consisted of membranes made of 0.063-in. (0.16 cm) thick, Butyl rubber sheets. Each membrane was formed by bonding together the edges of two sheets of Butyl rubber; a smaller sheet cut to the size of the cube face against which it was to be placed, and a larger sheet cut to allow a 4-in. overlap splice along the perimeter edges of the smaller sheet. The edges of these two sheets were bonded together with cement to form a continuous lap seal around the perimeter of the smaller sheet. A sealant was placed inside the membrane along all lap-splice seams to form a water tight seal between the two sheets. In addition, a sheet of filter fabric material was placed between the rubber sheets in each membrane, permitting water to permeate freely throughout the membrane. Water under pressure throughout the membrane would ensure that the pressure would be distributed equally and completely across the cube face in contact with the membrane. Figure 3.9 shows the details of construction of these membranes.

The procedure for membrane construction consisted of:

1. cutting and aligning the rubber sheets and filter fabric,
2. cleaning the sheets along the overlap splice with a wire brush and heptane, a rubber solvent,
3. applying the sealant with a caulking gun in a continuous bead along the inside fold of the intended overlap splice,
4. placing the bonding cement on the corner sections of the rubber sheets to be sealed and folding over



a. Typical Membrane with Inflow/Outflow Ports



b. Detail of Membrane with Inner Filter Fabric

c. Expanded View of Inflow/Outflow Port

Fig. 3.9 - Construction of First-Design Membranes

and pressing together the corners, and 5. repeating step 4 along the perimeters of the rubber sheets.

Pressurizing the membranes was to be accomplished through two inflow/outflow ports incorporated in opposite corners of each membrane. These ports provided a channel from the exterior pressure lines through the steel cube walls and into the membranes. These ports consisted of a 4-in. (10.2 cm) long by 0.38-in. (1.0 cm) diameter pipe nipple passing through one of the Butyl sheets. This short pipe was screwed into two, 6-in. (15.2 cm) diameter steel plates between which was fastened the rubber sheet. The plates had a combined thickness of 0.5 in. (1.3 cm). Sealant was placed around the 6-in. (15.2 cm) diameter steel plates of the port and along the screwholes and connections to prevent any water leakage. Once the sand was in place, the membranes would be filled with water through the bottom port while air would be expelled from the top port until the water level in the membrane reached the top port.

The membranes were pretested to determine how well they were sealed. This was performed by pressurizing the membranes while confined in a "test chamber." A load bearing floor which was available at the Ferguson Laboratory was used as the bottom, bearing plate. A wood frame was constructed around the membrane. The wood frame was bolted to the floor and was used to resist lateral expansion of the membranes. The membrane was then placed on the floor with the ports pointing upward. The top of the cube



was set on the wood frame and bolted down to the floor to restrict the expansion room of the membranes as they were filled and pressurized.

Leakage was found in all membranes around the ports and along the seams near the corners. There were two primary reasons for these leaks; the complexity of constructing a large waterproof membrane from Butyl sheets and our own inexperience in working with Butyl rubber and bonding cement. Several solutions were considered: 1. cover the steel plates of the ports and nearby rubber membrane area with extra sealant and patch with an additional sheet of rubber, 2. replace the present ports with ones molded in rubber, 3. mold the membrane corners in a rubber covering, and 4. seal and patch the leaks as found by pressure testing. These solutions were judged too costly, either directly with dollars or indirectly with time, and too uncertain as to their effectiveness in preventing leaks.

The possibility of using air in the leaking membranes instead of water was re-examined. Water had the advantages previously discussed, but air had the advantage that the pressure could be maintained in the membranes, despite leakage, by continually injecting air and continuing to test. The use of air in the leaky membranes was rejected, however, because air leakage would cause vibrations disruptive to the sensitive accelerometer records and could build up a pressure in the sand in the cube so that the effective stress would not be known.

### 3.3.4 Final Membrane Design

It was evident that a new membrane design was needed and so the various solutions were reviewed. Because of the prohibitive cost, having the membranes professionally constructed was eliminated from further consideration. Of those products currently manufactured, dunnage bags and water pressure bags were most applicable. However, both bags would have to be modified in some manner before they could be used in the cube. Essentially both products are similar in design and material. The dunnage bags are intended for air inflation to protect shipped cargo and are only available in certain sizes. The water pressure bags are for water storage and can be manufactured to a variety of dimensions. Each type of bag would need a second fitting installed in the membrane to form the inflow/outflow ports. Both fittings could be placed as per specification. Filter fabric could not be used with either bag because of problems with heat generated during manufacturing and the inability to secure the filter fabric inside the membranes once constructed. In terms of materials, nylon reinforced rubber is used in the construction of both bags and each type of bag could withstand a maximum pressure of 40 psi (276 kPa) under the limited expansion which would occur in the triaxial cube. In terms of cost, water pressure bags are slightly less expensive than dunnage bags.

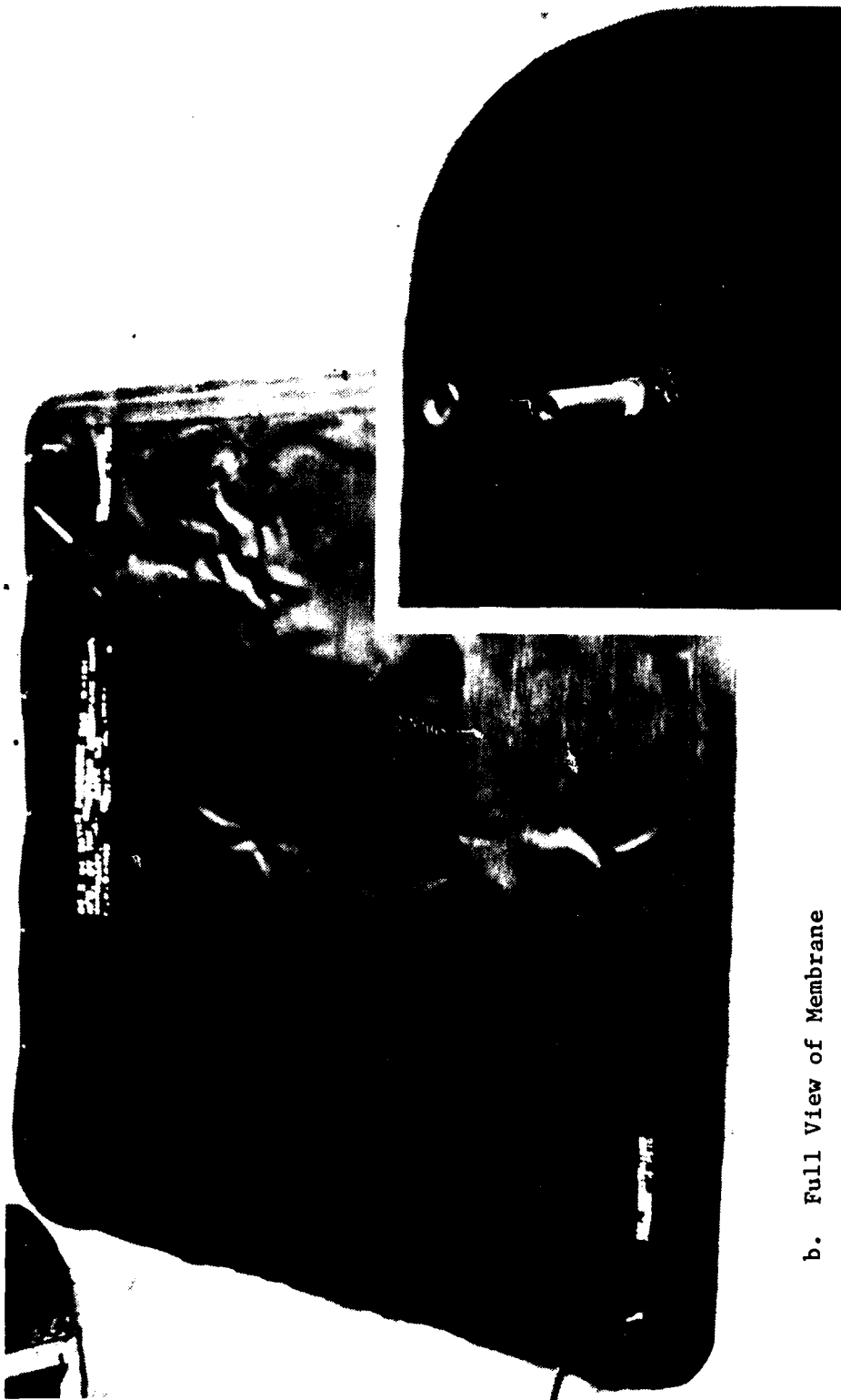
Water pressure bags, manufactured by the Goodyear Aerospace Corporation, were chosen because of the variety of sizes offered and the slightly lower cost. The loading system consists

of membranes made of 1/16-in. (0.16 cm) thick, abrasion-resistant, nylon-reinforced rubber sheeting. Each of the membranes is formed as a one-piece, vulcanized, water retaining unit, manufactured with the same dimensions as the respective cube face. Two fittings are located in opposite corners of the bags as specified. These fittings are 1/4-in. (0.64 cm) diam pipe nipples of 3/4 in. (1.91 cm) length to which pressure lines at the Ferguson Laboratory can be attached. Grommets are installed along what will become the upper edge of the two side membranes to facilitate hanging the bags on the cube during filling. Figure 3.10 is a photograph of one of these membranes with a close-up view of one of the fittings.

Both heat and pressure are used to vulcanize these membranes, in a process whereby a bonding compound reacts with the rubber sheets. Paper is placed between the rubber sheets where it is desired to keep the sheets separated. When completed, the membranes are inflated to tear apart the paper which becomes stuck to the rubber sheets during the heat and pressure stages. Personnel at Goodyear felt that the paper on the inside of the membranes would act much like filter paper and allow the water pressure to be evenly distributed over the entire membrane.

### 3.3.5 Hydraulic Loading of Membranes

The membranes are loaded throughout the working pressure range of 10 to 40 psi (69 to 276 kPa). With the membranes full of water, air pressure is used to pressurize the water. This is



b. Full View of Membrane

a. Close-up View of Port

Fig. 3.10 - Membrane Used to Apply Load to Sand Sample in Cube

accomplished through a specially constructed panel board shown schematically in Fig. 3.11 and by a photograph in Fig. 3.12. Air pressure from the Ferguson Laboratory air supply enters a manifold in the panel board at 125 psi and is then independently controlled by three air regulators, one regulator for each membrane.

The air pressure is set using the air regulators in conjunction with a 12-in. Heise type CM pressure gauge (accurate to within  $\pm 0.1$  percent of full scale reading) which is mounted in the panel board. The gauge is also used to monitor the pressure in each membrane during testing. The regulated air pressure for each membrane passes to an air-water accumulator where the air pressure is transformed into water pressure. The water pressure is then directed toward a membrane outlet in the panel board to which a pressure line from the membrane is connected.

The panel board can also be used to fill the membranes as the sand is placed. A water source from the Ferguson Laboratory is connected to the panel board. Water can be pumped directly through the accumulator to the membranes. As a membrane nears full capacity, up to 0.5 gallons (1.9 L) of water can be stored in the accumulator from where it can be forced into the membrane with the aid of air pressure.

### 3.4 EXCITATION PORTS

Since the objective of this research is to study the propagation characteristics of P- and S-waves through a soil mass, a mechanism for generating these waves at the soil boundaries is

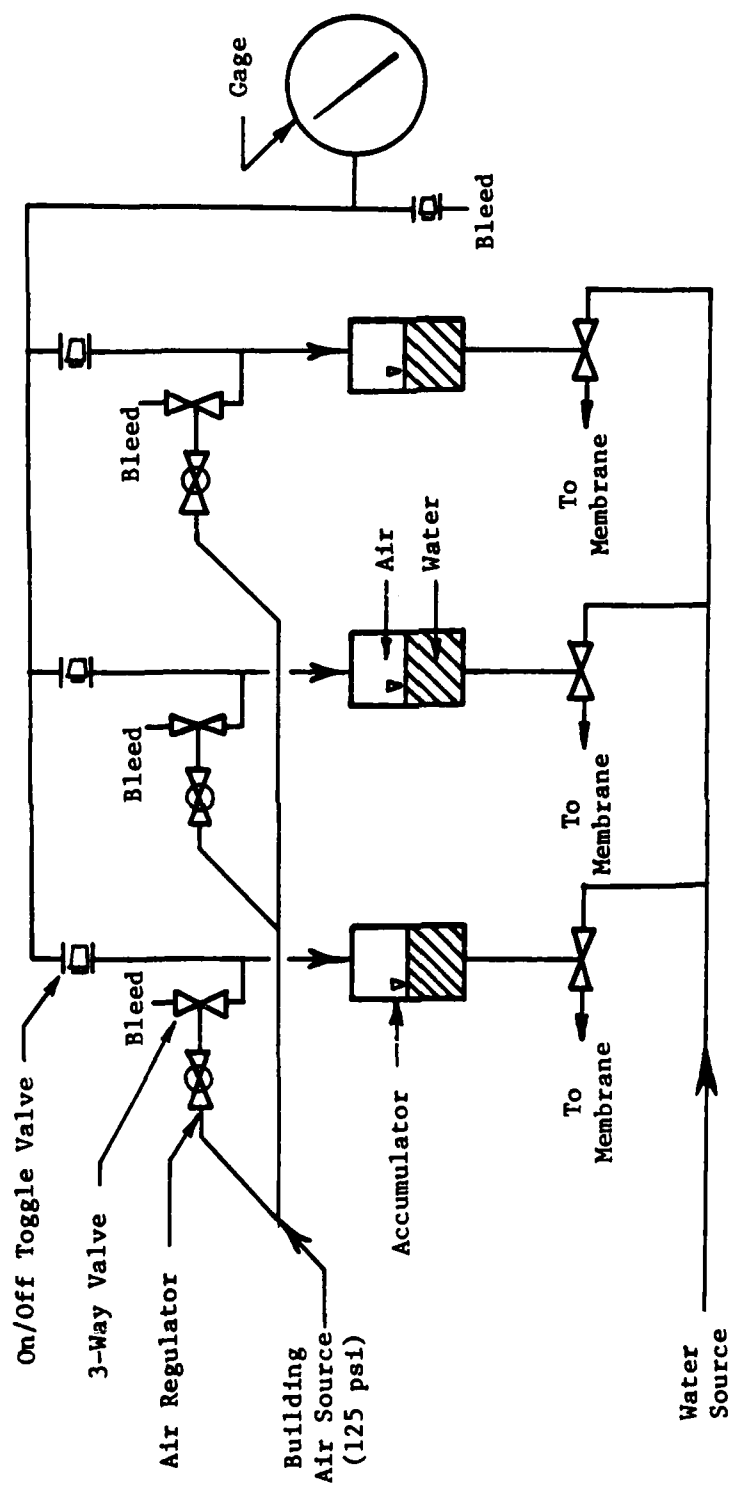


Fig. 3.11 - Schematic of Air/Water System Used to Pressurize the Membranes

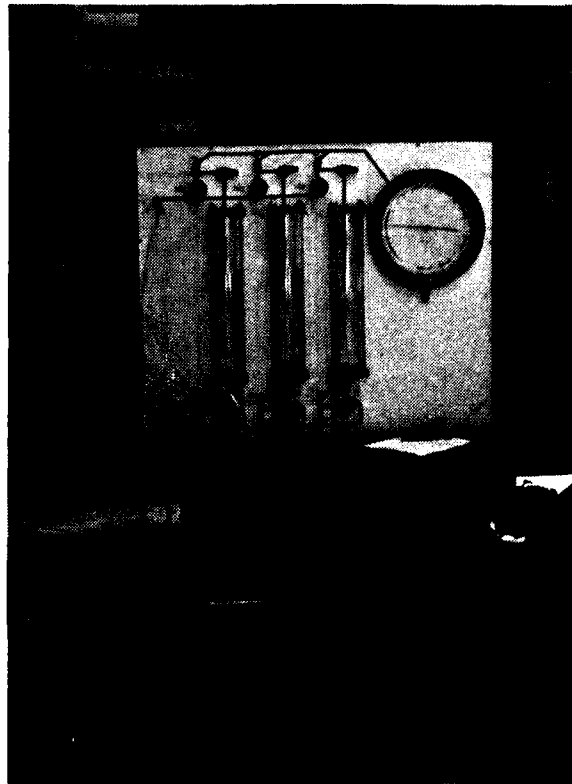


Fig. 3.12 - Panel Board Used to Pressurize  
Membranes in Cube

necessary. The ideal situation is a wave source in contact with the boundary of the soil mass inside the cube which is excitable from outside the cube. To achieve this goal, ports (i.e., holes in the cube walls) have been placed in the center of three mutually perpendicular sides of the cube: the bottom and two adjacent sides. At each port, an excitation system is attached which is composed of: 1. an excitation anvil, 2. a hand-held hammer, 3. an external frame, 4. an external adjustment screw, and 5. an internal frame. This system (without the hand-held hammer) is shown in Figs. 3.13 and 3.14.

#### 3.4.1 Wave Generation

The excitation port permits generation of P-waves or S-waves at the boundary of the soil mass by striking the anvil with the hand-held hammer. A 3-in. (76.2 mm) square plate at about the midlength of the shaft of the anvil is provided for the striking surface. Shear waves are generated in the soil by striking this plate either horizontally or vertically (parallel to the side of the cube). Compression waves are generated by striking the plate on the anvil in the direction of the axis of anvil (perpendicular to the side of the cube).

#### 3.4.2 Soil-Anvil Contact

To generate distinct waves, intimate contact between the soil and base of the anvil is essential. The base of the anvil in contact with the soil is knurled to maximize this contact.



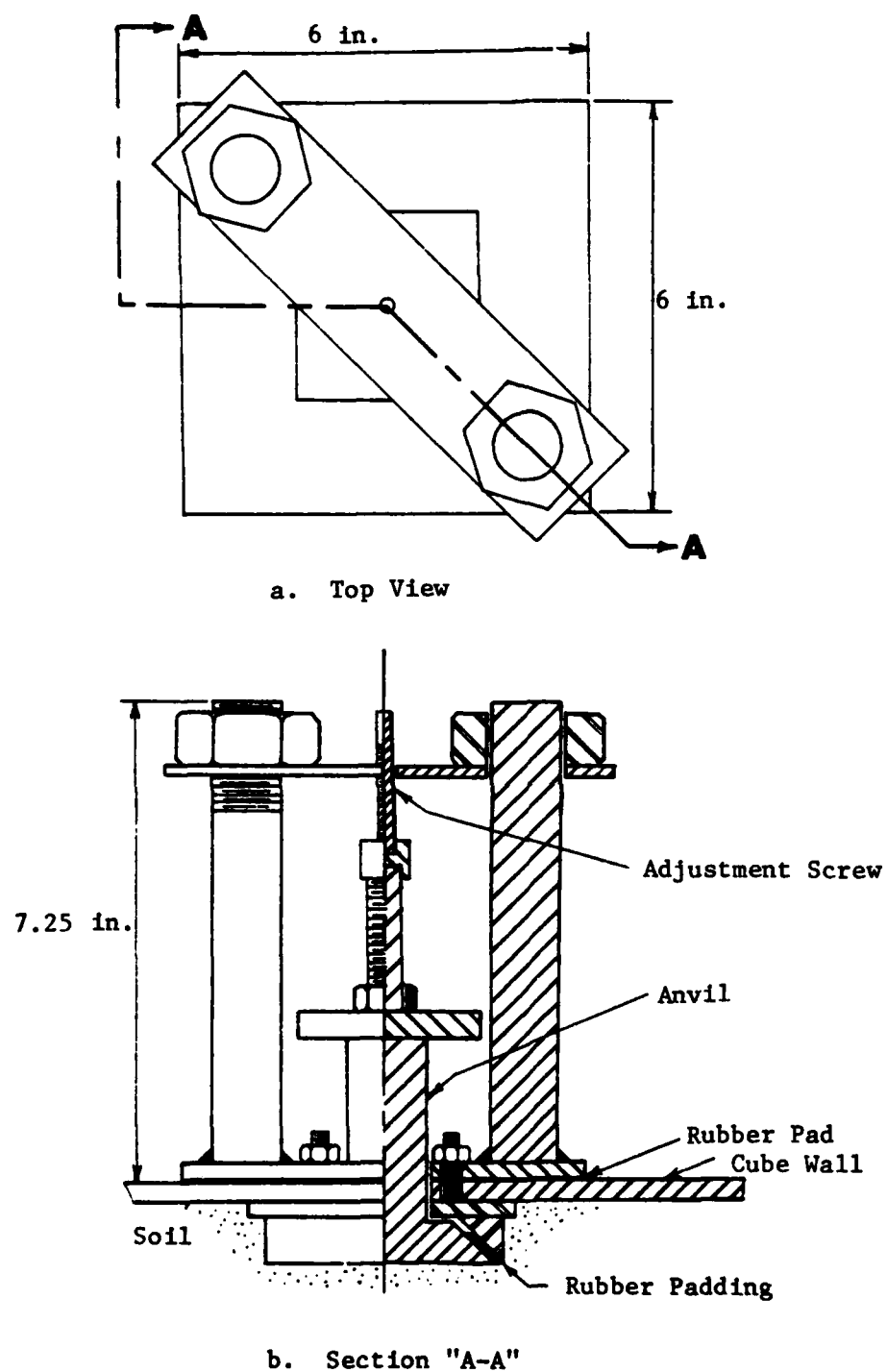


Fig. 3.13 - Excitation Hammer in Each Port of Triaxial Cube

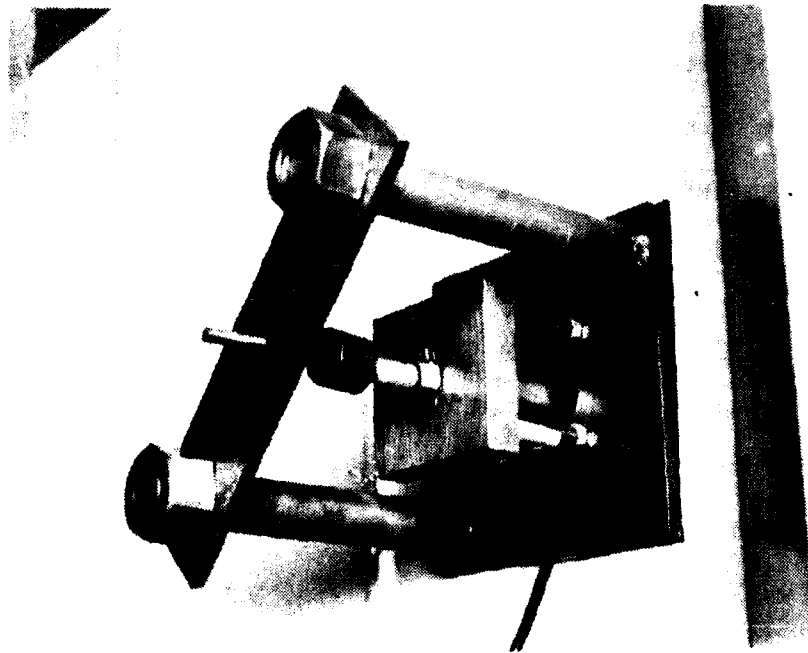


Fig. 3.14 - Close-up View of Excitation Port  
Without Impulse Hammer

Additionally, the base of the anvil which is in contact with the soil must maintain the same pressure against the soil as the surrounding face of the cube. This is accomplished by using the adjustment screw shown in Fig. 3.13 to push the anvil against the soil. The screw is threaded through a plate and bears against the anvil itself. The plate is part of an external frame which is bolted to the outside of the cube. The bolts holding the external frame on the outside of the triaxial cube are actually part of an internal frame which prevents soil displacement around the base of the anvil inside the cube when the anvil is excited.

#### 3.4.3 Additional Design Considerations

Vibrations in the wall of the cube become background noise on the waveform records and must be minimized wherever possible. For this reason, rubber padding has been placed between the external frame and wall of the cube as shown in Fig. 3.13.

The excitation port assembly protrudes about 6 in. (15.2 cm) outside of the cube (see Fig. 3.14) and about 0.9 in. (2.29 cm) inside of the cube. These sizes were chosen for ease of handling and use. The base of the anvil which contacts the soil is also 3 in. (7.6 cm) square and was selected after investigation of the effect of base size on wave generation characteristics.

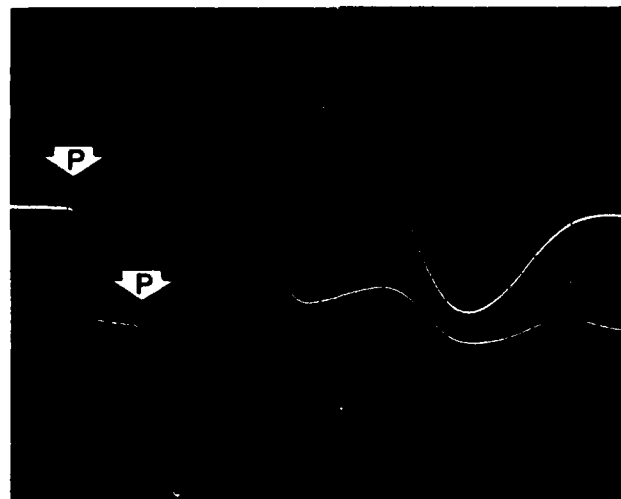
#### 3.4.4 Preliminary Testing for Anvil-Base Design

Wave propagation tests were performed in the Dynamic Response Test Facility at the Balcones Research Center of The

University of Texas. This facility is composed of sand that is very similar to that which was used in the initial tests in the cube. Three different sizes of base plates were tested: 2-3/16 in., 3-1/2 in., and 4 in. (5.6 cm, 8.9 cm, and 10.2 cm) in diameter.

The test set-up mirrored the conditions in the cube. Horizontal and vertical geophones were buried at depths of 12 and 24 in. (30.5 and 61.0 cm) below the ground surface for monitoring the waveforms in a similar fashion to the accelerometers in the cube. The base plates were placed on the ground surface (representing the soil boundary in the cube) directly over the buried geophones. The base plates were then struck vertically and horizontally to generate P-waves and S-waves in the soil. Polaroid pictures of the traces on an analog oscilloscope were used to record the waveforms monitored by the geophones. Typical records are shown in Fig. 3.15.

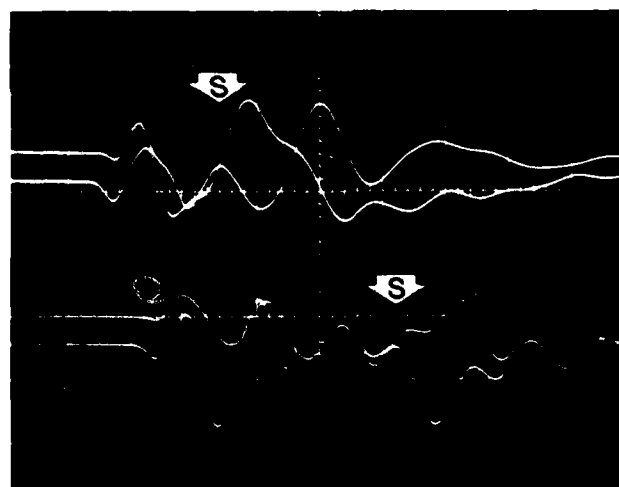
After analysis of over 75 records, it was concluded that the distinctness of the P-wave arrival was the same for all bases, but there was a slight improvement in the distinctness of the S-wave arrival with increasing base size. Since a small port is desirable in the cube to simulate a point source and since the improvement in the S-wave was greater between the 2-3/16-in. (5.6 cm) and 3-1/2-in. (8.9 cm) diameter plates than between the 3-1/2-in. (8.9 cm) and 4-in. (10.2 cm) diameter plates, a 3-in. (7.6 cm) square base plate for the anvil was chosen which has about the same contact area as the 3-1/2-in. (8.9 cm) diameter circular plate.



0.001 sec

$$v_p = \frac{1 \text{ ft}}{0.001 \text{ sec}} = 1000 \text{ fps}$$

- a. Travel Time Record of Compression Wave Using Vertical Geophones



0.0028 sec

$$v_p = \frac{1 \text{ ft}}{0.0028 \text{ sec}} = 360 \text{ fps}$$

- b. Travel Time Record of Shear Wave Using Horizontal Geophones

**Fig. 3.15 - Typical Travel Time Records for Surface Source and Embedded Receivers**

### 3.5 MONITORING AND RECORDING SYSTEM

Compression and shear waves propagating through the sand in the cube are monitored and recorded with the electronics shown schematically in Fig. 3.16. The core of this measurement system is a spatial array of three-dimensional (3-D) accelerometers buried in the soil. Three, 3-D accelerometers are placed along each of the three principal axes of the sand mass as shown in Figs. 3.3 and 3.4. A spacing of about 1.5 ft (0.46 m) is used between adjacent 3-D accelerometers. Spacing between the accelerometers closest to the cube wall and the wall is about 2 ft (0.61 m) so that minimum interference is caused by reflections of the waves off of the walls (as discussed in Section 6.2.1). A pair of digital oscilloscopes are used to record the accelerometer signal output.

#### 3.5.1 Accelerometers

Each 3-D accelerometer package is composed of three accelerometers rigidly attached in a 1.57-in. (44 mm) square wooden block as shown in Figs. 3.17 and 3.18. One accelerometer is aligned along each of the three principal axes of the cube. Wood (birch) was chosen as the 3-D accelerometer housing material so that the weight of the 3-D package would equal that of the sand displaced by the package and so that the stiffness difference between the block and surrounding sand would be minimized. The average weight of the 3-D packages including accelerometers is 0.31 lb (0.16 kg) resulting in an average density of 100.3 pcf

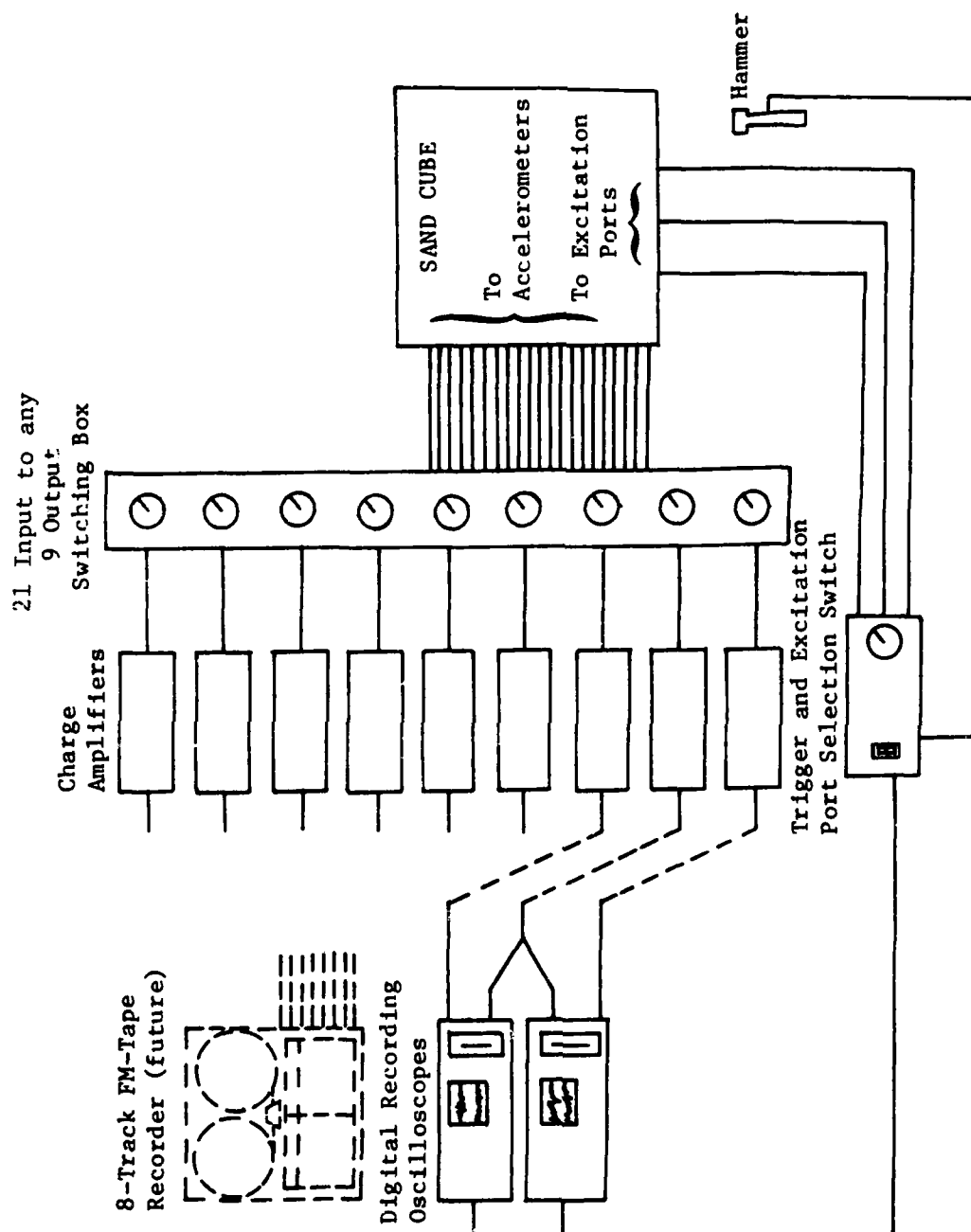


Fig. 3.16 - Schematic of Monitoring and Recording Systems

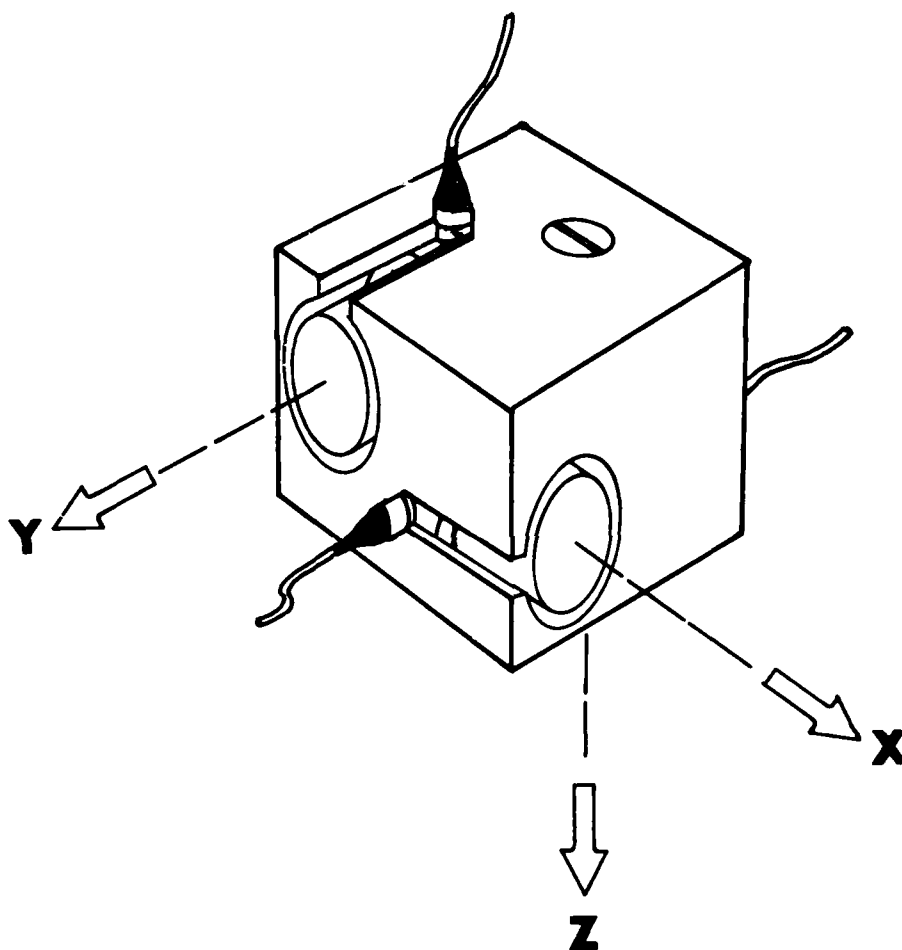


Fig. 3.17 - Isometric View of 3-D Accelerometer Package



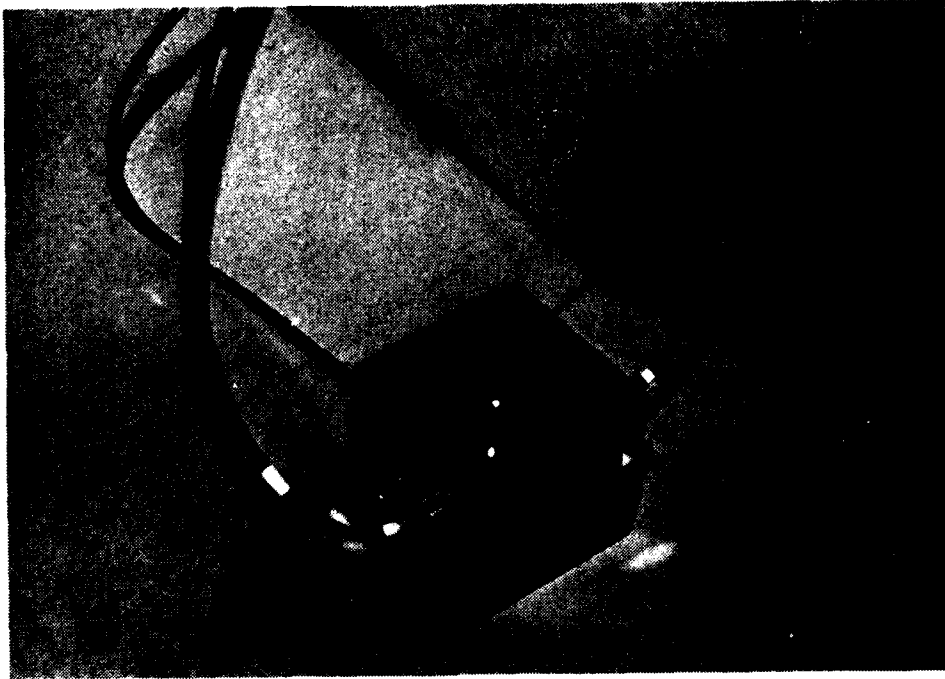


Fig. 3.18 - Three-Dimensional Accelerometer  
Block with Accelerometers Installed

( $1623 \text{ kg/m}^3$ ) compared to an average density of about 96.6 pcf ( $1563 \text{ kg/m}^3$ ) for the sand (see Section 5.2.1).

Monitoring of low-amplitude wave propagation through the sand requires highly sensitive accelerometers. Endevco Isoshear accelerometers, model 7701, were used. Each accelerometer has a sensitivity of 0.001 g and a cross sensitivity (sensitivity to movement not along the major axis) of less than one percent. They are small in size (0.625 in. dia. x 0.78 in. long (1.6 x 2.0 cm)) and weight (1.0 oz. (28 g)) so as to create minimum interference as a wave passes and to track closely the particle motion of the wave. Figure 3.19 shows the placement of one accelerometer into the wooden block.

The electronic signal from each accelerometer is carried by a coaxial cable of silver plated copperweld conductor with a fused teflon jacket designed for signal reliability. To ensure integrity of the wire in the cube during testing, a soil specimen of the same sand used in the cube was prepared for static triaxial soil testing with a piece of wire embedded in it. After a number of isotropic, drained loading cycles, the sample was sheared under drained conditions. No degradation of the wire or wire covering was evident. Therefore, it was assumed that no additional protection was required for the cables in the triaxial cube.

The electrical cables from the accelerometers pass through two small ports in the east side of the cube. After all the wires are inserted, the ports are sealed against sand loss by a

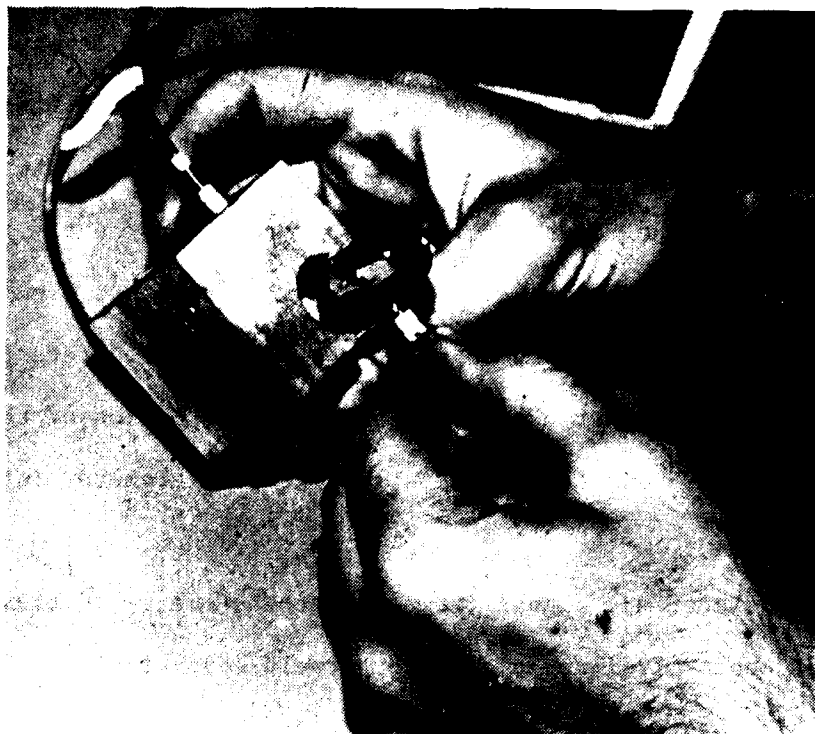


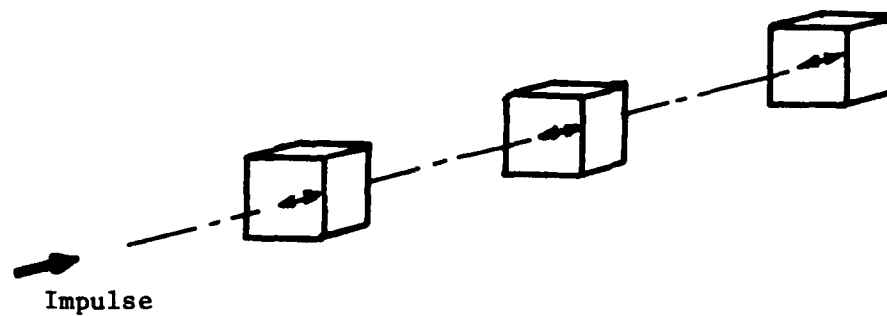
Fig. 3.19 - Accelerometer Being Placed into a  
3-D Accelerometer Block

waterproofing rubber sealant applied from the inside of the cube. The 21 wires are connected to a switching box outside the cube so that any nine accelerometers can be connected with charge amplifiers. Any of these nine signals may then be recorded on the digital oscilloscopes, FM digital tape recorder (future), or spectrum analyzer (future).

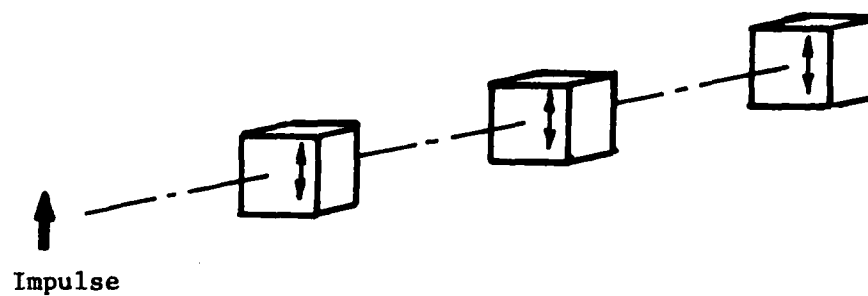
### 3.5.2 Recording Devices

Normally three accelerometers are monitored simultaneously each time an impulse is applied to the source. The three accelerometers of interest lie along the axis of the source being excited and are sensitive along the same direction as the motion of the anvil as illustrated in Fig. 3.20. Because each digital oscilloscope is only a two-channel device, two oscilloscopes are required to record the output from the three accelerometers with one accelerometer output being duplicated between the two oscilloscopes for reference. The oscilloscopes are triggered electronically when the hand-held hammer strikes the anvil of the excitation port. At this instant, a voltage drop is sent from the trigger to the oscilloscope by means of a resistance-capacitance circuit initiating the recording cycle. The trigger has a switch to select any of the three excitation ports in use.

With the digital oscilloscope, each waveform is recorded on a floppy diskette for later recall and study. By saving a waveform digitally, the arrival times and amplitudes may be directly



a. P-Wave Accelerometer Orientation



b. Typical S-Wave Accelerometer Orientation

Fig. 3.20 - Accelerometer Orientation in 3-D Packages  
Relative to Impulse of Source

read from the oscilloscope upon replaying the digital record. The possibility of future direct oscilloscope-computer hook-up is also possible. In the future, rather than the oscilloscope, an FM digital tape recorder or spectrum analyzer can be used permitting recording for analysis in the laboratory at a later date or direct Fourier analysis.

### 3.6 STRESS MEASUREMENT

Stresses in the sand within the cube were monitored by total stress cells within the sand and by pressure gages measuring the water pressure in the membranes. This was done in an attempt to insure that the pressure in the sand is the same as that applied through the loading system. Three total pressure cells, manufactured by Terra Technology, were used to monitor soil pressure in each of the three principal stress directions. Each cell is a 0.375-in. (0.95 cm) thick by 6-in. (15.2 cm) square unit filled with oil (see Fig. 3.21). A change in stress on the square face of the cell changes the pressure that the oil exerts on an electric sensor. The sensor is housed in a 1-in. dia. by 8-in. long (2.5 x 20.3 cm) sensing unit, rigidly attached to the cell by a thin tube approximately 0.38-in. dia. by 6-in. long (.95 x 15.2 cm) which therefore must also be placed in the soil. A pressure change causes a deformation of a small strain gage in the sensor, resulting in a piezoresistive change in the gage full inductance bridge. The signal generated is carried by four-wire cables through

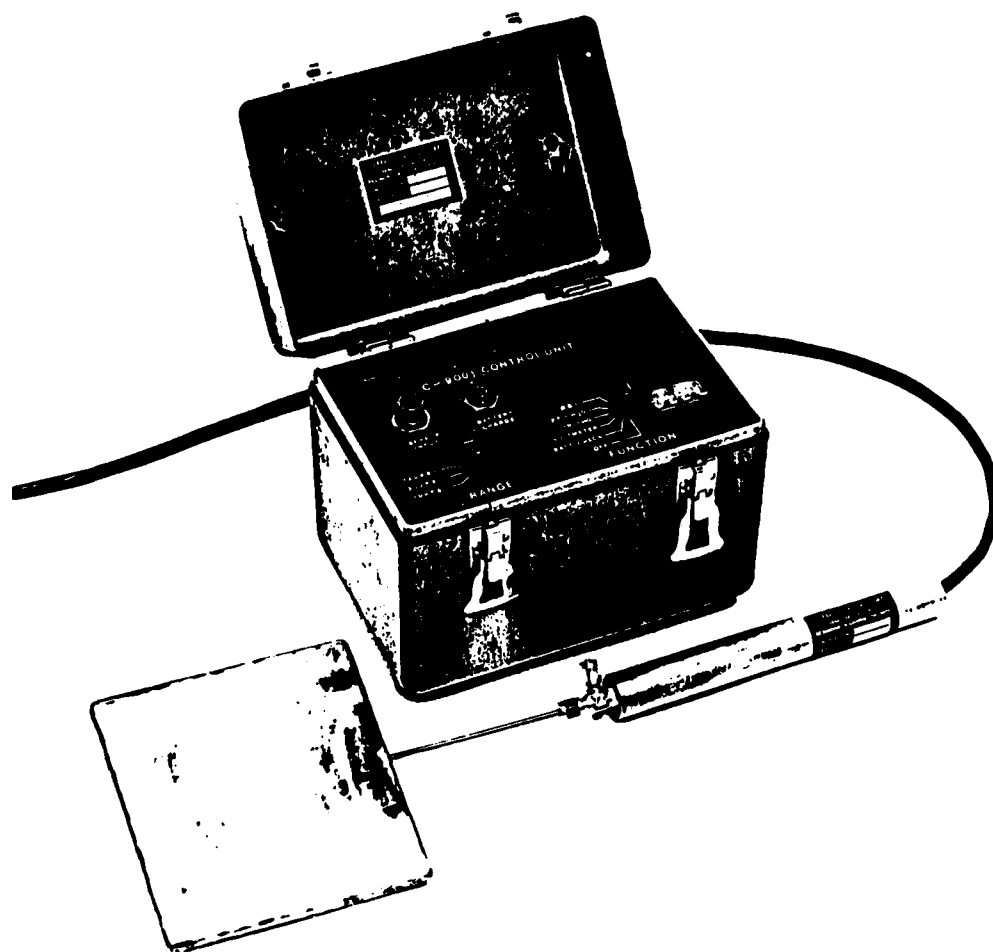


Fig. 3.21 - Soil Stress Cell and Control Unit  
(from Terra Technology literature)

sealed holes in the east and south faces of the cube to an external control unit.

The control unit automatically converts the signal from the sensing unit into a digital output for direct pressure reading in units selectable of psi, feet of water, or inches of mercury. Three pressure ranges are available: 0-100 psi, 0-300 psi, 0-750 psi (0-698, 0-2067, 0-5168 kPa). Since the maximum design pressure of the cube is 50 psi (345 kPa), the smallest range, 0-100 psi (0-698 kPa), was used.

The cells were positioned in the cube so that they did not interfere with generation or monitoring of P- and S-waves. Details on the placement and results of the stress cells are discussed in Section 5.3.2.

### 3.7 STRAIN MEASUREMENT

To monitor strains in the soil sample during confinement, six pairs of soil strain gages were embedded in the sand when the sample was constructed. Bison soil strain gages, model 4000 series, were used. Each pair of gages consists of two, free-floating, disk-shaped sensors embedded in the sand and separated by a known distance. Two sizes were used in these tests as shown in Fig. 3.22: 0.25-in. thick by 2-in. diam (0.64 x 5.1 cm) and 0.38-in. thick by 4-in. diam (0.96 x 10.2 cm). One sensor acts as a driving coil and the other as the receiving coil. The roles are interchangeable and determined by the control unit outside the triaxial cube. The separation of the sensors is related to the electro-magnetic



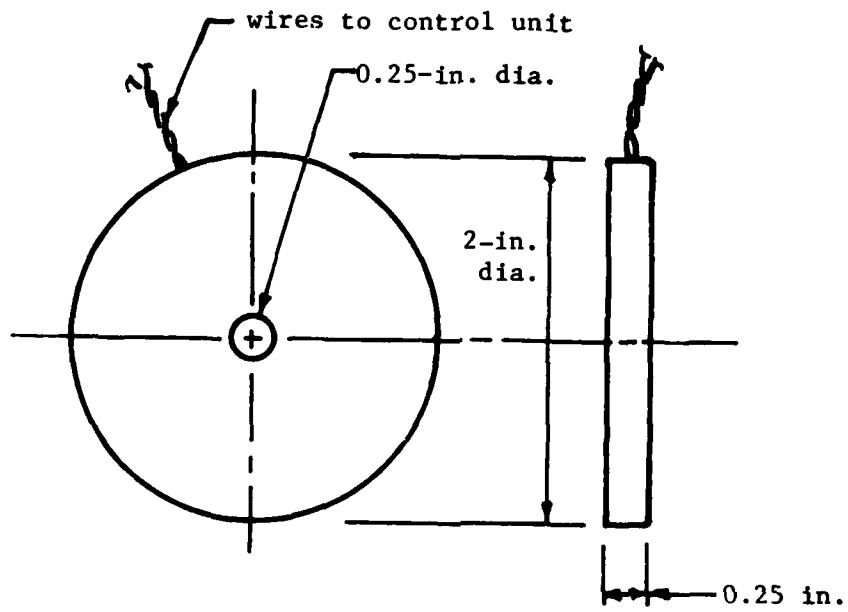


Fig. 3.22 - Typical 2-in. Diameter Soil Strain Gage

coupling between the sensors, acting in the same manner as the primary and secondary windings of a transformer (Wetzel and Vey, 1970; Truesdale and Schwab, 1967). The amplitude dial reading resulting from balancing an inductance bridge is calibrated to the absolute spacing of the sensors. Strain may be calculated from the difference between initial and final spacings. The output meter used for balancing may be calibrated to read strain for a single set of coils directly from the offset from null position if the strain is less than four percent. However, in these tests, several sets of coils were used, so strain had to be calculated from the difference between individual readings.

Each pair of gages is used to measure strain only along the axis running from the center of one sensor to the center of the other in the pair with both sensors facing each other. Therefore, six pairs are used in the cube: a 2-in. (5.1 cm) diam pair separated 4 in. (10.2 cm) and a 4-in. (10.2 cm) diam pair separated 8 in. (20.4 cm), each oriented parallel to an axis of the cube. The gages were positioned such that they would not interfere with wave propagation and conversely, any steel components would not interfere with the electro-magnetic field generated by the sensors.

Each sensor size (2-in. and 4-in. (5.1 and 10.2 cm) diameter) has a separate set of calibration curves. Although cable length will affect the calibration within a sensor size, the cables of the sensors used are similar enough so that the same

calibration curves for a given size can be used without any loss of accuracy.

The wires from each sensor were passed through holes that were later sealed in the east face of the cube. The wires were attached to a switching box outside the cube. The sensors may be read one pair at a time on the external control unit which contains all the driving, balancing and output components required to operate the sensors. The control unit has an optional output port which can be attached to a recorder to monitor strain with time. This option is not necessary for the current research.

Details on placement in the sand, problems with the unit, and final results are presented in Section 5.3.3.

### 3.8 TEST SAMPLE

#### 3.8.1 Soil-Cube Boundary

Uniform stress throughout the soil sample can be achieved only if there is no restraint at the soil-cube boundaries; that is, the soil must be free to move parallel to the face (free-free condition) (Rowe and Barden, 1964; Roscoe, 1953; Bishop and Green, 1965). To allow this movement, greased plastic sheets were placed between all six faces of the cube and the sand sample.

The greased sheets were composed of two layers of 4-mil (0.1 mm) polyethylene separated by a thin coat of WD-40 oil. The method of attachment of the sheets to the cube is presented in Section 5.3.1.

### 3.8.2 Sand Placement

The object of the sand placement system was to fill the cube with sand of a uniform density over the entire height of the cube. The method of raining sand through air (pluviation) was chosen over other methods because of the efficiency and uniformity of placement attainable with this method. Raining sand through air has been shown to yield uniform, medium-dense samples when the height of fall is 2.5 ft (.76 m) or greater (Kilbuszewski, 1948; Beiganousky and Marcusson, 1976). Marcusson and Beiganousky (1977) also found that when they rained sand through several layers of screens with openings of about 0.25 in. (0.64 cm), the variation in density was only  $\pm 0.5$  pcf ( $8 \text{ kg/m}^3$ ) for a given drop height.

The original raining system is shown in Fig. 3.23 and is composed of a "V" shaped hopper which can be moved across the top of the cube. The outlet at the bottom of the hopper is 8 in. (20.3 cm) wide by 7 ft (1.73 m) long. The hopper has a gate for flow control and two screens (with mesh openings of 0.25 in. (0.64 cm)) spaced approximately 3 in. (7.6 cm) apart just above the bottom of the hopper. The gate is comprised of a series of twelve, 3-in. by 12-in. (7.6 cm by 30.5 cm) doors that are regulated in tandem by a lever system allowing adjustment of the opening size. The hopper sits on a 30-in. (76.2 cm) high wooden collar which bolts to the top of the cube so that the drop height of the sand into the cube ranges from 9.5 ft (2.9 m) at the start of the filling operation to 2.5 ft (0.8 m) at the conclusion. The volume

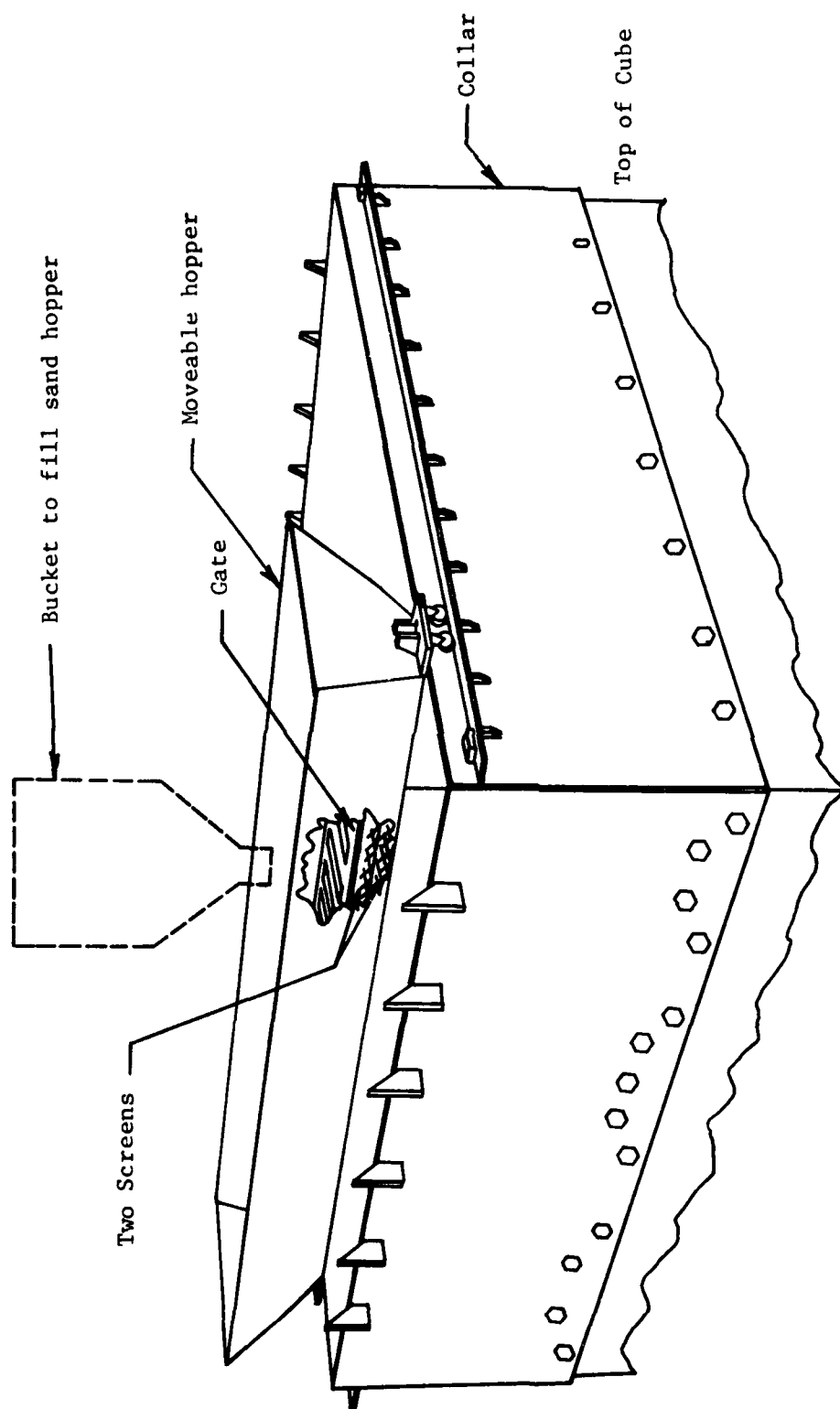


Fig. 3.23 - Original Sand Placement System

held by the rainer is approximately 7 cu ft ( $0.2 \text{ m}^3$ ) which results in depositing a layer slightly more than 1-in. (2.5 cm) thick for each filling. For convenience, the bolt holes in the collar match those around the perimeter of the top of the cube so that the collar can easily be attached. The entire system is disassembled and stored when not in use. The method for placing sand using the original raining system and a modified version is discussed in Section 5.3.1.

### 3.8.3 Density Measurement of Sample

A special density device was constructed to measure density of the sand sample during construction to evaluate its uniformity while the cube was being filled. Three identical containers were made of 0.25-in. (.64 cm) thick plexiglass. The containers had an ID of 6 in. (15.2 cm) and a height of 3 in. (7.6 cm), which resulted in a volume of 8.64 cu in. (0.05 cu ft or 142 cu cm). The top edge of the cylinder was machined to an angle of 45 degrees sloping out to minimize additional sand bouncing into the container upon striking the container during the raining process. Details on placement and results are in Section 5.3.1.

## 3.9 SUMMARY

The triaxial testing device was designed and built to hold a soil cube measuring 7 ft (2.1 m) on a side. Membranes were purchased to place between the cube face and the soil to apply pressure from the panel board to the soil. Apparatus for generating, monitoring, and recording P- and S-waves were acquired as

were stress and strain monitoring devices. Methods for raining the sand into the cube and monitoring its density were devised. With the cube and associated equipment complete, the sand was then chosen, and the filling of the cube was begun.

Intermediate-amplitude (single-amplitude shearing strain in the range of 0.001 to 0.01 percent), resonant column tests were also performed over the pressure range of 2.5 to 80 psi (16.2 to 551.2 kPa). These tests show that shear modulus begins to decrease with increasing shear strains above approximately 0.003 percent. Since shearing strains were kept below this value during testing in the cube, there should be no effect of the shearing strain, and velocities should be constant at a given pressure.

The results of the low- and intermediate-amplitude resonant column tests for shear modulus have been assumed to hold for the constrained modulus and may, therefore, be applied to the results of P-wave velocity determination. Complete details of the determination of the engineering properties of the sand can be found in Appendix. A which was taken directly from Knox, 1982 and is contained herein for completeness.



## CHAPTER FOUR

### ENGINEERING PROPERTIES OF SAND

The soil used in this research was a uniform, medium to fine, washed mortar sand, which classifies as SP in the Unified Soil Classification System. Results of a grain size analysis show an effective grain size,  $D_{10}$ , of 0.28 mm and a uniformity coefficient,  $C_u$ , of 1.71. When placed, the sand had been air-dried to a water content less than 0.5 percent.

Consolidated drained triaxial tests (S-tests) were run to determine shear properties of the sand. The results show that  $\bar{c}$  is essentially zero and  $\bar{\phi}$  varies with density from 35 degrees for a loose sample with a density of 86 pcf ( $1343 \text{ kg/m}^3$ ) to 42 degrees for a dense sample with a density of 99 pcf ( $1602 \text{ kg/m}^3$ ).

Dynamic properties of the sand were measured in the laboratory by low-amplitude (single-amplitude shearing strain less than 0.001 percent), resonant column tests over a pressure range of 2.5 psi (15 kPa) to 40 psi (276 kPa). Results from low-amplitude tests at three different void ratios show a linearly increasing relationship between  $\log G$  and  $\log \bar{\sigma}_0$  with a slope of 0.48. No significant effect of stress history on the value of shear modulus was seen for these tests. Material damping ratio was found to decrease with increasing effective confining pressure, ranging from 1.3 percent at low pressures to 0.3 percent at high confining pressures.

## CHAPTER FIVE

### TESTING PROGRAM AND PROCEDURES

#### 5.1 INTRODUCTION

The initial testing program for the model cube consisted of measurement of velocity and attenuation of compression and shear waves through a dry sample of sand of medium density. The sample was constructed in May and June, 1981, over a period of six weeks. It was subsequently loaded with the following three pressure sequences: first, a sequence using isotropic confinement; second, a sequence using confinement with a constant mean effective principal stress; and finally, a sequence using confinement with a varying mean effective principal stress. The sequences of loading are listed in Table 5.1 and shown graphically with time in Fig. 5.1.

##### 5.1.1 Isotropic Confinement

Loading with a series of isotropic steps was initially performed to determine the relationship between velocity and mean effective principal stress,  $\bar{\sigma}_0$ , as determined in the cube. These results were also used to: 1. compare with standard laboratory resonant column tests run on the same sand, and 2. evaluate the structural anisotropy of the sample.

TABLE 5.1  
Pressure Loading Sequences

Test No.	Date of Test (1981) Month and Day	Effective Vertical Stress	Effective Horizontal Stresses		Mean Effective Principal Stress	Earth Pressure Coefficients	
		$\bar{\sigma}_v$ (psi)	$\bar{\sigma}_{NS}$ (psi)	$\bar{\sigma}_{EW}$ (psi)	$\bar{\sigma}_o$ (psi)	$K_{13} = \frac{\bar{\sigma}_1}{\bar{\sigma}_3}$	$K_{23} = \frac{\bar{\sigma}_2}{\bar{\sigma}_3}$
(1)	(2)	(3)	(4)	(5)	(6)	(7)	(8)
1. ISOTROPIC CONFINEMENT							
1	7/8	10	10	10	10	1.00	1.00
2	7/9	20	20	20	20	1.00	1.00
3	7/14	40	40	40	40	1.00	1.00
4	7/14	20	20	20	20	1.00	1.00
5	7/14a	20	20	20	20	1.00	1.00
2. CONSTANT MEAN EFFECTIVE PRINCIPAL STRESS							
5	7/21	22	19	19	20	1.16	1.00
6	7/21	24	18	18	20	1.33	1.00
7	7/21	26	17	17	20	1.53	1.00
8	7/22	28	16	16	20	1.75	1.00
9	7/22	30	15	15	20	2.00	1.00
10	7/22	32	14	14	20	2.29	1.00
11	7/23	28	16	16	20	1.75	1.00
12	7/23	24	18	18	20	1.33	1.00
13	7/23	20	20	20	20	1.00	1.00
14	7/23	22	20	18	20	1.22	1.10
15	7/23	24	18	18	20	1.33	1.00
16	7/24	26	18	16	20	1.63	1.12
17	7/24	26	20	14	20	1.86	1.43
18	7/24	28	18	14	20	2.00	1.28
19	7/24	30	16	14	20	2.14	1.14

TABLE 5.1  
Pressure Loading Sequences  
(Continued)

Test No.	Date of Test (1981) Month and Day	Effective Vertical Stress	Effective Horizontal Stresses		Mean Effective Principal Stress $\bar{\sigma}_o$	Earth Pressure Coefficients	
		$\bar{\sigma}_v$ (psi)	$\bar{\sigma}_{NS}$ (psi)	$\bar{\sigma}_{EW}$ (psi)		$K_{13} = \frac{\bar{\sigma}_1}{\bar{\sigma}_3}$	$K_{23} = \frac{\bar{\sigma}_2}{\bar{\sigma}_3}$
(1)	(2)	(3)	(4)	(5)	(6)	(7)	(8)
20	8/5	36	12	12	20	3.00	1.00
21	8/5	34	14	12	20	2.83	1.16
22	8/5	30	18	12	20	2.50	1.50
23	8/5	25	23	12	20	2.08	1.92
3. VARYING MEAN EFFECTIVE PRINCIPAL STRESS							
24	8/6	15	15	15	15.0	1.00	1.00
25	8/6	20	15	15	16.7	1.33	1.00
26	8/6	25	15	15	18.3	1.67	1.00
27	8/6	30	15	15	20.0	2.00	1.00
28	8/6	35	15	15	21.7	2.33	1.00
29	8/6	40	15	15	23.3	2.67	1.00
30	8/6	40	20	20	26.7	2.00	1.00
31	8/7	40	25	25	30.0	1.60	1.00
32	8/7	40	30	30	33.3	1.33	1.00
33	8/7	40	35	35	36.7	1.14	1.00
34	8/7	40	40	40	40.0	1.00	1.00
35	8/7	40	35	35	36.7	1.14	1.00
36	8/7	40	30	30	33.3	1.33	1.00
37	8/10	40	25	25	30.0	1.60	1.00
38	8/10	40	20	20	26.7	2.00	1.00
39	8/10	40	15	15	23.3	2.67	1.00
40	8/10	35	15	15	21.7	2.33	1.00

TABLE 5.1  
Pressure Loading Sequences  
(Continued)

Test No.	Date of Test (1981) Month and Day	Effective Vertical Stress	Effective Horizontal Stresses		Mean Effective Principal Stress	Earth Pressure Coefficients	
		$\bar{\sigma}_v$	$\bar{\sigma}_{NS}$	$\bar{\sigma}_{EW}$	$\bar{\sigma}_o$	$K_{13} = \frac{\bar{\sigma}_1}{\bar{\sigma}_3}$	$K_{23} = \frac{\bar{\sigma}_2}{\bar{\sigma}_3}$
(1)	(2)	(psi) (3)	(psi) (4)	(psi) (5)	(psi) (6)	(7)	(8)
41	8/10	30	15	15	20.0	2.00	1.00
42	8/10	25	15	15	18.3	1.67	1.00
43	8/11	20	15	15	16.7	1.33	1.00
44	8/11	15	15	15	15.0	1.00	1.00
45	8/11	40	15	15	23.3	2.67	1.00
46	8/11	40	20	15	25.0	2.67	1.33
47	8/11	40	25	15	26.7	2.67	1.67
48	8/11	40	30	15	28.3	2.67	2.00
49	8/14	40	35	15	30.0	2.67	2.33
50	8/14	40	40	15	31.7	2.67	2.69
51	8/14	40	35	15	30.0	2.67	2.33
52	8/17	40	30	15	28.3	2.67	2.00
53	8/17	40	25	15	26.7	2.67	1.67
54	8/17	40	20	15	25.0	2.67	1.33
55	8/17	40	15	15	23.3	2.67	1.00
56	8/17	15	15	15	15.0	1.00	1.00
57	8/17	15	20	15	16.7	1.33	1.00
58	8/17	15	25	15	18.3	1.67	1.00
59	8/17	15	30	15	20.0	2.00	1.00
60	8/18	15	35	15	31.7	2.33	1.00
61	8/18	15	40	15	23.3	2.67	1.00
62	8/18	20	40	15	25.0	2.67	1.33
63	8/18	25	40	15	26.7	2.67	1.67

TABLE 5.1  
Pressure Loading Sequences  
(Continued)

Test No.	Date of Test (1981) Month and Day	Effective Vertical Stress	Effective Horizontal Stresses		Mean Effective Principal Stress	Earth Pressure Coefficients	
		$\bar{\sigma}_v$	$\bar{\sigma}_{NS}^*$	$\bar{\sigma}_{EW}^{**}$	$\bar{\sigma}_o$	$K_{13} = \frac{\bar{\sigma}_1}{\bar{\sigma}_3}$	$K_{23} = \frac{\bar{\sigma}_2}{\bar{\sigma}_3}$
(1)	(2)	(3) (psi)	(4) (psi)	(5) (psi)	(6) (psi)	(7)	(8)
64	8/18	30	40	15	28.3	2.67	2.00
65	8/19	35	40	15	20.0	2.67	2.33
66	8/19	40	40	15	31.7	2.67	2.67
67	8/19	20	20	20	20.0	1.00	1.00
68	8/19	10	10	10	10.0	1.00	1.00

\*  $\bar{\sigma}_{NS}$  = effective principal stress along the north-south (horizontal) axis of the cube

\*\*  $\bar{\sigma}_{EW}$  = effective principal stress along the east-west (horizontal) axis of the cube

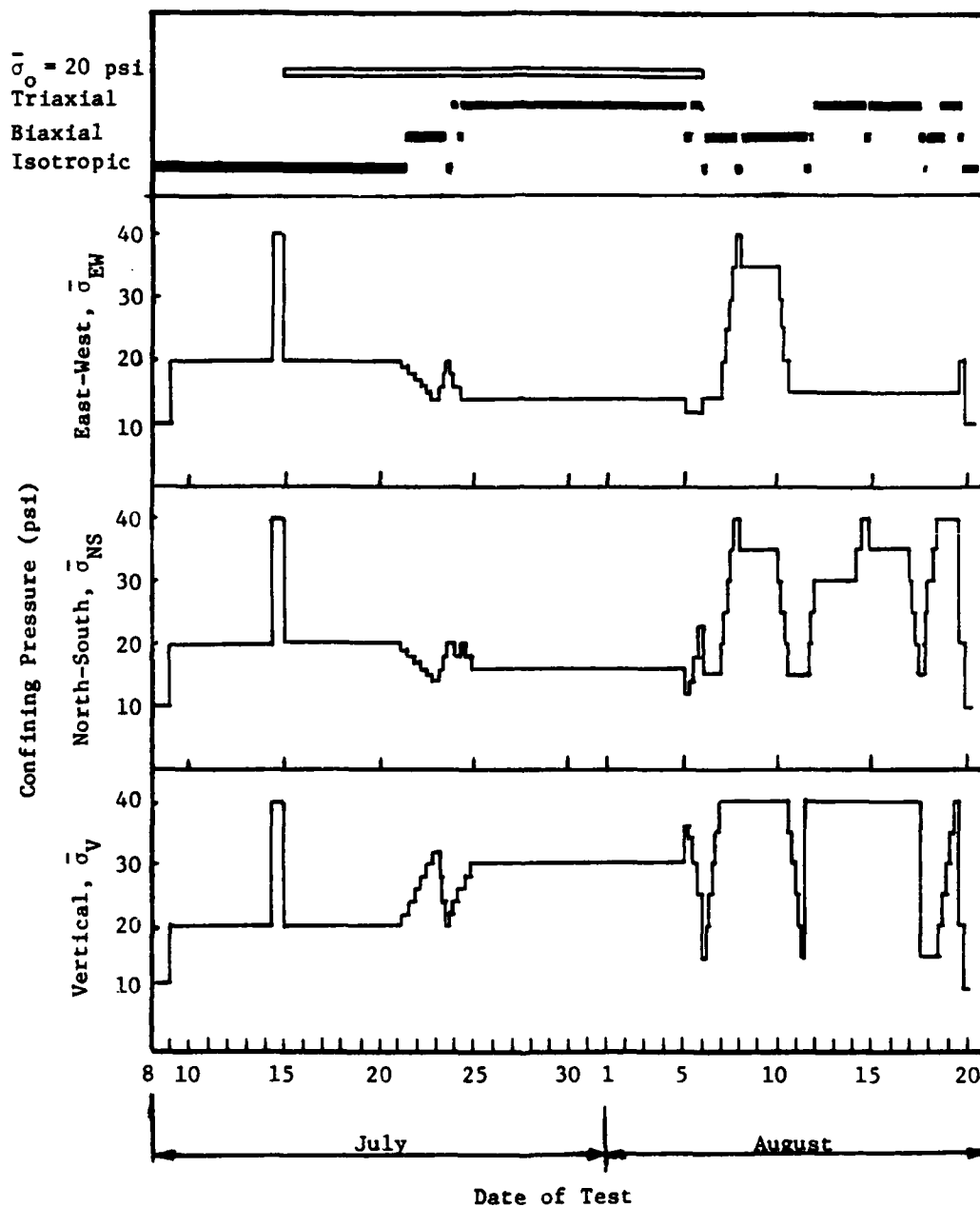


Fig. 5.1 - Variation in Confining Pressure Along each Axis of the Cube with Time

### 5.1.2 Confinement with Constant Mean Effective Principal Stress

The isotropic series was followed by a series of tests with a constant  $\bar{\sigma}_0$ . These tests included both biaxial and triaxial loadings. In the biaxial series, a lateral pressure coefficient,  $K_{13}$ , was used to describe the tests as:

$$K_{13} = \frac{\bar{\sigma}_1}{\bar{\sigma}_3} \quad (5.1)$$

where:  $\bar{\sigma}_1$  = major effective principal stress, and  
 $\bar{\sigma}_3$  = minor effective principal stress.

In these tests,  $K_{13}$  was varied while  $\bar{\sigma}_0$  was kept constant at 20 psi (138 kPa). In the triaxial series, a second earth pressure coefficient,  $K_{23}$ , was defined as:

$$K_{23} = \frac{\bar{\sigma}_2}{\bar{\sigma}_3} \quad (5.2)$$

where:  $\bar{\sigma}_2$  = intermediate effective principal stress.

The value of  $K_{23}$  varied in addition to variation of  $K_{13}$ . The value of  $\bar{\sigma}_0$  was kept constant at 20 psi (138 kPa) through the triaxial series. The mean effective principal stress was kept constant to investigate the assumption by Hardin and Black (1966) that the shear wave velocity and attenuation are a function only of  $\bar{\sigma}_0$  and, therefore, should not vary if  $\bar{\sigma}_0$  does not vary.

The biaxial series involved slowly increasing the vertical stress while decreasing the lateral stress. The value of  $K_{13}$  increased from 1.00 (isotropic) to 2.29, but the stress remained safely below the shear failure envelope as shown in Fig. 5.2.



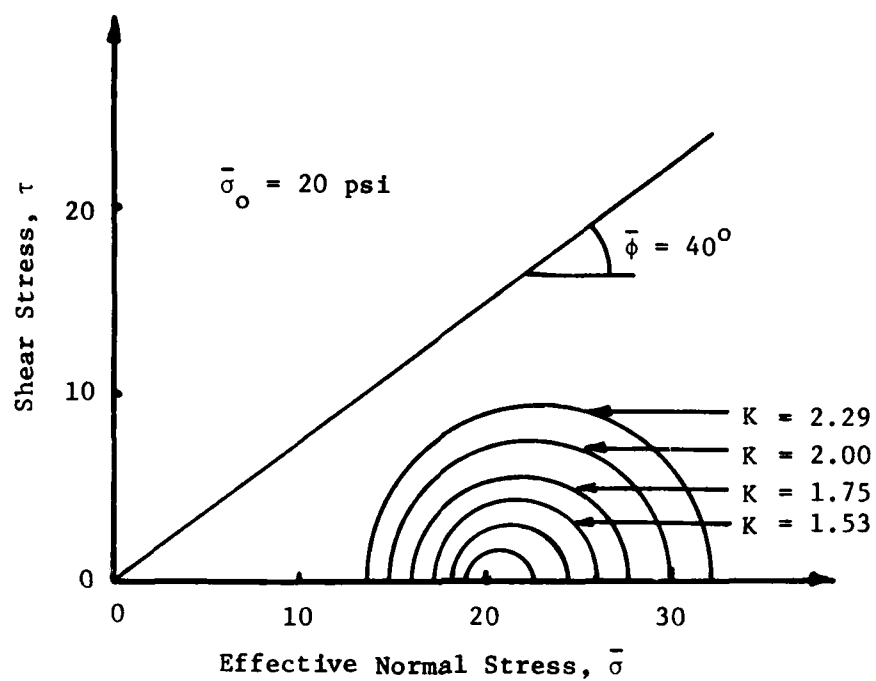


Fig. 5.2 - Mohr-Coulomb Envelope for Biaxial Confinement with Constant Mean Effective Principal Stress

The biaxial loading sequence was reversed, and readings were repeated at several previous states of stress to determine if a hysteretic effect existed.

Once the isotropic state of 20 psi (138 kPa) was again achieved upon completion of the biaxial series, the triaxial series of confinement with constant  $\bar{\sigma}_0$  was begun. The vertical stress was increased, and the lateral stress was decreased to maintain a constant  $\bar{\sigma}_0$  and also remain below the failure envelope as shown in Fig. 5.3. However, in the triaxial series, the intermediate principal stress was not kept equal to the minor principal stress, thereby permitting  $K_{23}$  to range from 1.00 to 1.90. The limits of  $K_{23}$  are a minimum of 1.00 for isotropic loading and biaxial loading where  $\bar{\sigma}_2$  equals  $\bar{\sigma}_3$ , and a maximum equal to  $K_{13}$  for biaxial loading where  $\bar{\sigma}_2$  equals  $\bar{\sigma}_1$ . The constant  $\bar{\sigma}_0$  sequence was chosen to minimize pressure differences between steps with the usual change being only 2 psi (14 kPa) in any direction.

### 5.1.3 Confinement with Varying Mean Effective Principal Stress

Originally, the first two series were going to complete the initial testing of the sand sample. However, upon examination of the initial results, it was decided to add a third pressure series in which the mean effective principal stress was varied. As a result, additional biaxial and triaxial testing was performed.

To start the series, the sample was lowered to an isotropic pressure of 15 psi (103 kPa). A biaxial sequence was performed by

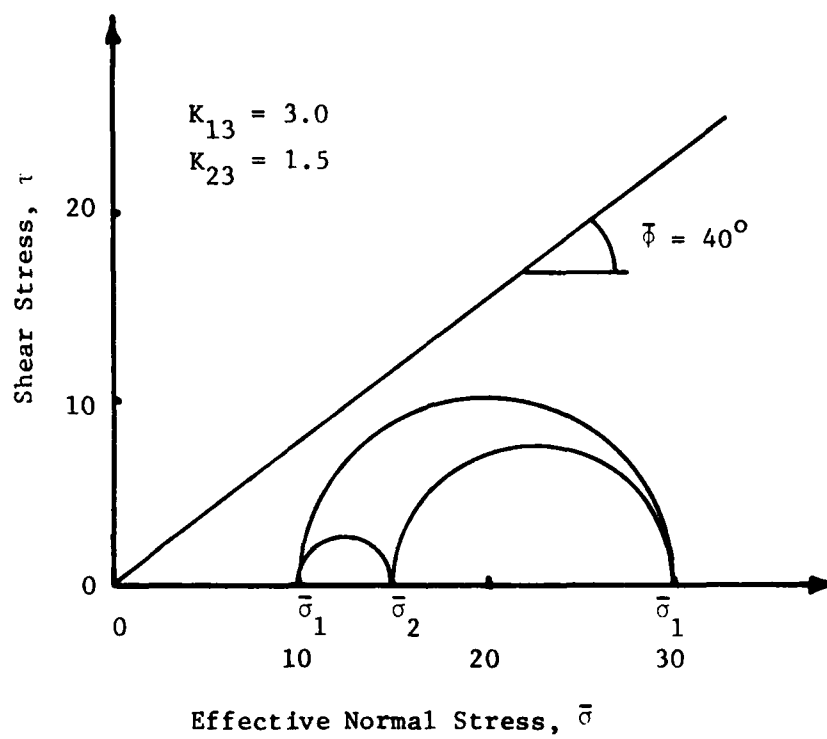


Fig. 5.3 - Mohr-Coulomb Envelope for a Typical Test Under Triaxial Confinement

increasing the vertical stress to 40 psi (276 kPa) in 5-psi (34 kPa) increments while maintaining constant horizontal stresses. In this way, the effect on the compression and shear wave velocities of varying only the major principal stress,  $\bar{\sigma}_1$ , could be studied. The horizontal stresses were then increased to 40 psi (276 kPa) in 5-psi (34 kPa) increments while keeping the vertical stress constant at 40 psi (276 kPa). This sequence was performed to study the effect of varying only the minor principal stress,  $\bar{\sigma}_3$ , on  $V_p$  and  $V_s$ .

At this point in testing, the cube was at an isotropic confinement of 40 psi (276 kPa) which was also the maximum pressure achieved at the end of the first isotropic confinement series. The data gathered at this pressure was used together with other such points when an isotropic confinement existed, to study the effect of stress history on the wave velocity. To observe if there was any hysteresis in the data from the biaxial tests, the entire sequence was run again in reverse order: first,  $\bar{\sigma}_3$  was lowered in 5-psi (34 kPa) increments to 15 psi (103 kPa) and then  $\bar{\sigma}_1$  was lowered in 5-psi (34 kPa) increments to 15 psi (103 kPa). The final test in this sequence was again at an isotropic confinement of 15 psi (103 kPa).

To study the effect of the intermediate principal stress,  $\bar{\sigma}_2$ , on compression and shear wave velocities, a triaxial sequence was run. The pressure was set to a maximum biaxial load with the vertical stress equal to 40 psi (276 kPa) and horizontal stresses

equal to 15 psi (103 kPa). One of the horizontal stresses was increased in 5-psi (34 kPa) increments to 40 psi (276 kPa) and then was decreased back to 15 psi (103 kPa) in 5-psi (34 kPa) increments to note any effect of hysteresis.

Structural anisotropy and its possible effect on the biaxial and triaxial series was investigated by running a shortened series of biaxial and triaxial tests. In this series the axes for stresses were rotated with the major principal axis as north-south rather than vertical and the intermediate principal axis as vertical rather than north-south.

## 5.2 TESTING PROCEDURES

Once the triaxial cube was constructed and all the associated equipment was thoroughly checked, construction of the sand sample was begun. First, the walls of the cube were cleaned, and the membranes and greased sheets were attached. The sand was then dried in the sun to a moisture content of less than one percent and rained into the cube to form a sample of medium density. At predetermined elevations, raining of the sand was stopped and electronic equipment was placed in the sand. When the soil specimen was completed, the top of the cube was securely fastened. The sample was then loaded, compression and shear waves were generated, and the accelerometer responses were recorded along all three axes at each pressure. The following sections describe, in detail, the work from sample construction through dynamic testing.

### 5.2.1 Sample Construction

The first step in constructing the sample was to clean the accumulated dust, oil and dirt from the inside of the cube and to bolt the collar of the raining system (see Section 3.8.2) to the top. Next, the greased sheets and membranes were installed inside the cube on the sides and bottom. The two rubber membranes which were used to apply lateral loading were hung on the north and west faces of the cube as shown in Fig. 5.4. Rope was passed through the grommets in the top of the membranes and then through the extra bolt holes in the top of the cube which were not used to attach the collar. The ropes were tied off to convenient anchors along the outside of the cube and collar.

On the inside of the cube, two sheets of plastic were placed on the bottom and on each of the four sides, including placement over the membranes previously hung on two sides. The sheets on the sides were held in place by pieces of duct tape. (The tape, in addition to the ropes holding the membranes, was removed before attaching the top of the cube.) Small openings were cut in the plastic sheets as required for the three sources and five holes through which electrical wires passed. The outer sheet of each pair of sheets (which eventually touched the sand) was lifted by one person while another placed a thin layer of WD-40 oil on the inner sheet with a paint roller as shown in Fig. 5.5. The outer sheet was allowed to drop back in place and then was pressed smooth with a clean, dry roller. This resulted in a system of a



Fig. 5.4 - Rubber Membranes Being Attached to the  
North and West Faces of the Cube



Fig. 5.5 - Layer of Oil Being Applied to Plastic Sheet on West Face of Cube



thin layer of oil sandwiched between two plastic sheets having a clean contact with the sand on one side and cube or membrane on the other side. The purpose of the oil was to minimize friction between the layers of plastic and, therefore, between the sand and the walls of the cube so that little shearing stress could develop at the sand-cube boundary. Uniform stresses across each side of the sample could not have been achieved if shearing stresses developed between the sand and cube walls (Section 3.8.1).

The string-spring assembly (Section 5.2.2) used to determine elevation and levelness of the sand was placed at the 24-in. (61 cm) level, the first level at which raining of the sand was halted for placement of electronics.

The sand for these tests was supposed to be dry which for this work was taken to be a moisture content of less than one percent. However, the sand had to be stored outdoors, exposed to the weather, and was damp. The early summer in Austin is usually sunny and dry with temperatures reaching above 90 degrees F. Unfortunately, May and June of 1981 were unusually damp. Intermittent strong rains, averaging three nights per week, precluded storage of dry sand for more than one day. Several methods of covering the sand were tried in an attempt to keep rain water out of the sand, but all were unsuccessful. Therefore, before placement in the cube, the sand was spread in approximately one cubic yard ( $0.9 \text{ m}^3$ ) lots to a thickness of one to two inches (2.5 to 5.0 cm) and dried in the sun. An acceptable water content could be achieved in one-half

to three hours, depending upon the initial water content (directly related to how recently the last rain was) and the daily humidity. Figure 5.6 shows the sand being dried. When dry, this sand was placed in the cube while another layer was spread to dry.

After the sand dried in the sun, it was shoveled into a  $3/4$ -cu yd ( $0.6 \text{ m}^3$ ) concrete bucket which had been moved by forklift to the outdoor drying area. A screen with 0.25-in. (0.64 cm) openings was placed over the top of the bucket before it was filled so that foreign matter that may have found its way into the outdoor storage pile would be removed. (Little foreign matter was found in the sand.) Once the bucket was filled, it was moved by forklift into the building where it was attached to the overhead crane. The crane was used to lift the bucket over the cube so that sand could be rained into the cube.

The initial method for raining sand into the cube was as follows. About one third of the sand in the bucket was emptied into the hopper to fill it. The hopper gate was then opened to give the desired flow rate while the hopper was moved at a constant rate along the rails of the collar attached to the top of the cube. When the hopper was empty, the gate was closed and the process was repeated. Unfortunately, the force of the sand on the gates always forced them to open fully. Because of this problem, after one or two uses, the raining system was modified as described below.

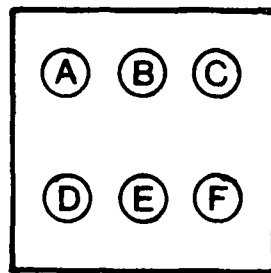
After one bucket load of sand, it was decided to modify the raining system since the force of the sand caused the hopper



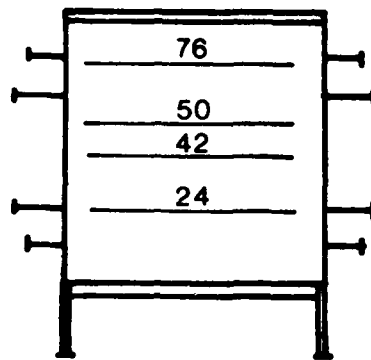
Fig. 5.6 - Sand Being Air-Dried in Outdoor Storage Bin

to stay in its fully open position. Experimentation revealed that the sand could be placed directly from the concrete bucket at the same rate as through the open rainer, but without the set-up time required to fill the hopper. Therefore, the approach was simply to swing the bucket manually in the north-south direction while the crane moved the bucket in the east-west direction. A 0.25-in. (0.64 cm) wide (north-south) by 10 in. (25.4 cm) long (east-west) rectangular curtain of sand dropped out of the bucket at an initial angle of about 45 degrees causing it to disperse and rain quite evenly over the top surface of the sand in the cube. Since considerable time could be saved using the bucket directly while maintaining a seemingly uniform sample, the cube was filled directly with the bucket.

The sand density was measured at four elevations in the cube. At each measurement elevation, raining of sand into cube was halted, and the special density device described in Section 3.7.3. was placed on the current surface of the sand. Several different horizontal locations were chosen as shown in Fig. 5.7 so that the density of samples from all sections of the cube could be compared. Raining of the sand continued with the device in place until the sand surface was just above the top of the device, and it was full. The full container was then removed, and the sand in the container carefully transferred to a self-sealing (Ziplock) bag. The bags were transported back to the main campus where they were weighed on



a. Top View of Cube



b. Elevations Where Raining of Sand was Halted for Density Measurements

Fig. 5.7 - Location of Density Measurements Taken During Filling of Cube

a Metler balance. The density was computed by dividing this weight by the known volume of the density device.

The resulting densities and their locations within the cube together with the resulting void ratios are tabulated in Table 5.2. The average density is 96.6 pcf ( $1547 \text{ kg/m}^3$ ), and the standard deviation is only about two percent of this value, or 1.9 pcf ( $30 \text{ kg/m}^3$ ). Therefore, the sample can be considered quite uniform as deposited by the modified sand raining system.

#### 5.2.2 Placement of Electronics

It is crucial that the exact distances between accelerometers in the cube be known for computation of wave travel times. It is also important that the stress and strain cells be oriented in the correct direction to eliminate cross interference. To satisfy both requirements, a surveying system was developed. The system consisted of small eyebolts attached at predetermined elevations along the fins of the cube which surround each membrane to prevent lateral expansion under load. Two string-spring assemblies were hooked into sets of eyebolts in opposite corners to form an "x" across the middle of the cube. The springs maintained tension in the string to minimize sagging at the center so that the "x" was at a known elevation.

This "x" provided many useful functions. The center of it was the center of the horizontal plane in the cube which was directly over the source in the bottom. This center was used in

TABLE 5.2

Densities and Void Ratios of Sand at  
Various Elevations in the Cube

Height Above the Bottom in.	Location*	Density pcf	Void Ratio** e
(1)	(2)	(3)	(4)
24	D	94.7	0.77
42	C	97.7	0.71
42	D	97.9	0.70
42	F	100.0	0.67
50	B	95.4	0.75
50	F	97.8	0.71
50	D	97.5	0.71
70	E	95.5	0.75
70	A	95.7	0.75
70	C	93.7	0.78
Average		96.6	0.73
Std. Deviation		1.9	0.03

\* See Fig. 5.7.

$$** \quad e = \frac{\gamma_w G_s}{\gamma_d} - 1 \quad \text{where } G_s = 2.68$$

horizontally locating the accelerometers. Also, the strings formed a nearly level plane which was used to monitor filling of the cube and to level the placement of accelerometers, stress devices, and strain devices. Finally, since the "x" was at a known elevation, the vertical distance from the level plane to any item could be measured by use of a plumb-bob. In this manner, the location of the accelerometers was determined. Each time an accelerometer package was placed in the center of the cube, a plumb-bob was hung from wooden rod inserted through the open, center bolt hole in the top of the north and south walls to verify the horizontal distances.

Raining of the sand in the cube was halted five times to allow placement of electronic devices at the following elevations above the bottom: 24 in., 42 in., 50 in., 56 in., and 60 in. (60.9, 106.7, 127.0, 142.2, and 152.4 cm). At the 24-in. (60.9 cm) level, two pairs of horizontal strain sensors were placed along with the first 3-D accelerometer package as seen in Fig. 5.8. The second level, 42 in. (106.7 cm), represented the mid-height of the sample. All three stress cells were placed at this level along with five, 3-D accelerometer packages and the lower strain sensor of the vertical 4-in. (10.3 cm) diameter pair as shown in Fig. 5.9. The second strain sensor of the 4-in. (10.3 cm) diameter pair was the only item placed at the 50-in. (127.0 cm) level. The lower 2-in. (5.1 cm) diameter vertical strain sensor was placed along with the two, 2-in. (5.1 cm) diameter horizontal



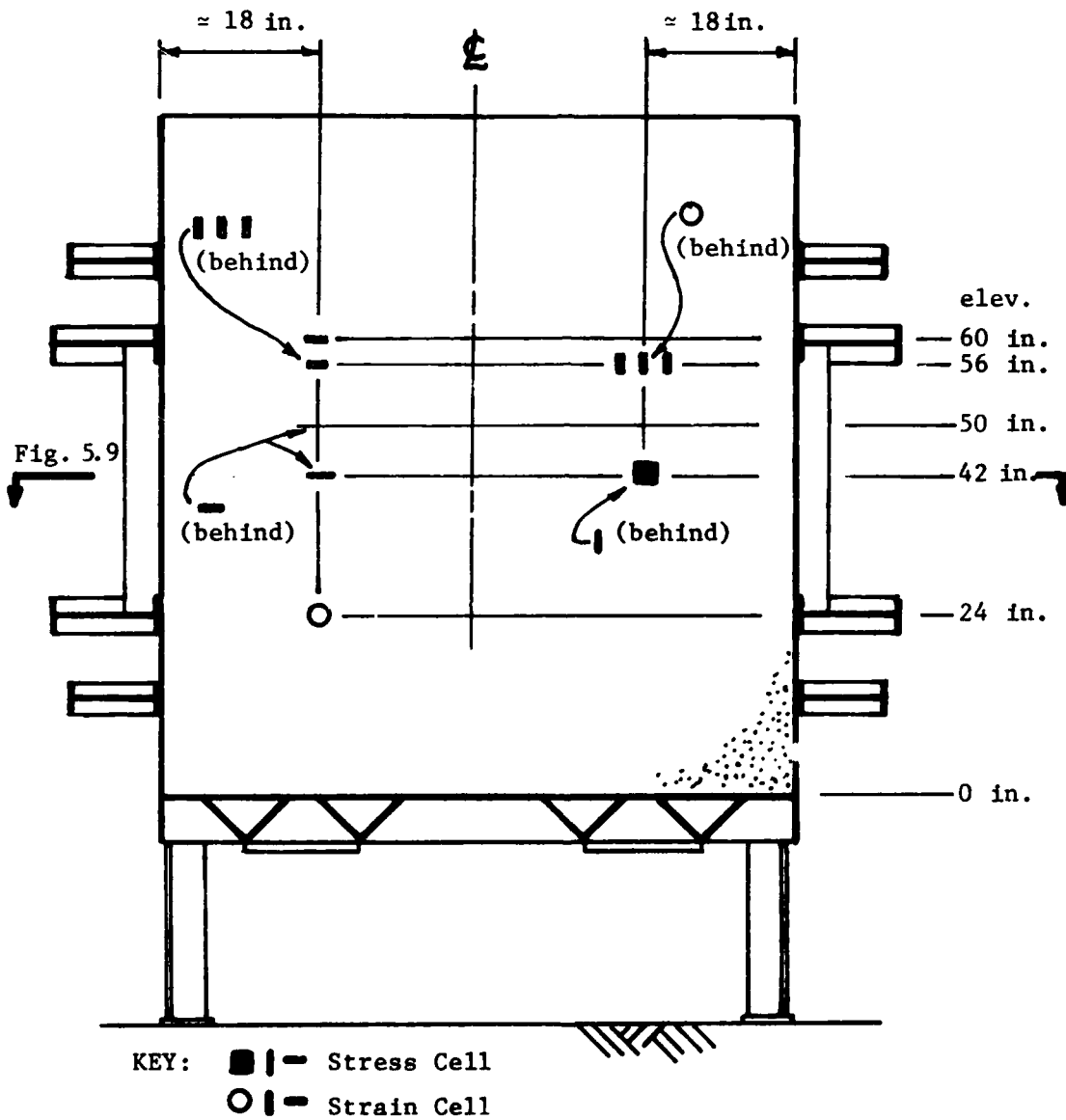


Fig. 5.8 - Location of Stress and Strain Measuring Devices in Cube When Looking West Through The Cube

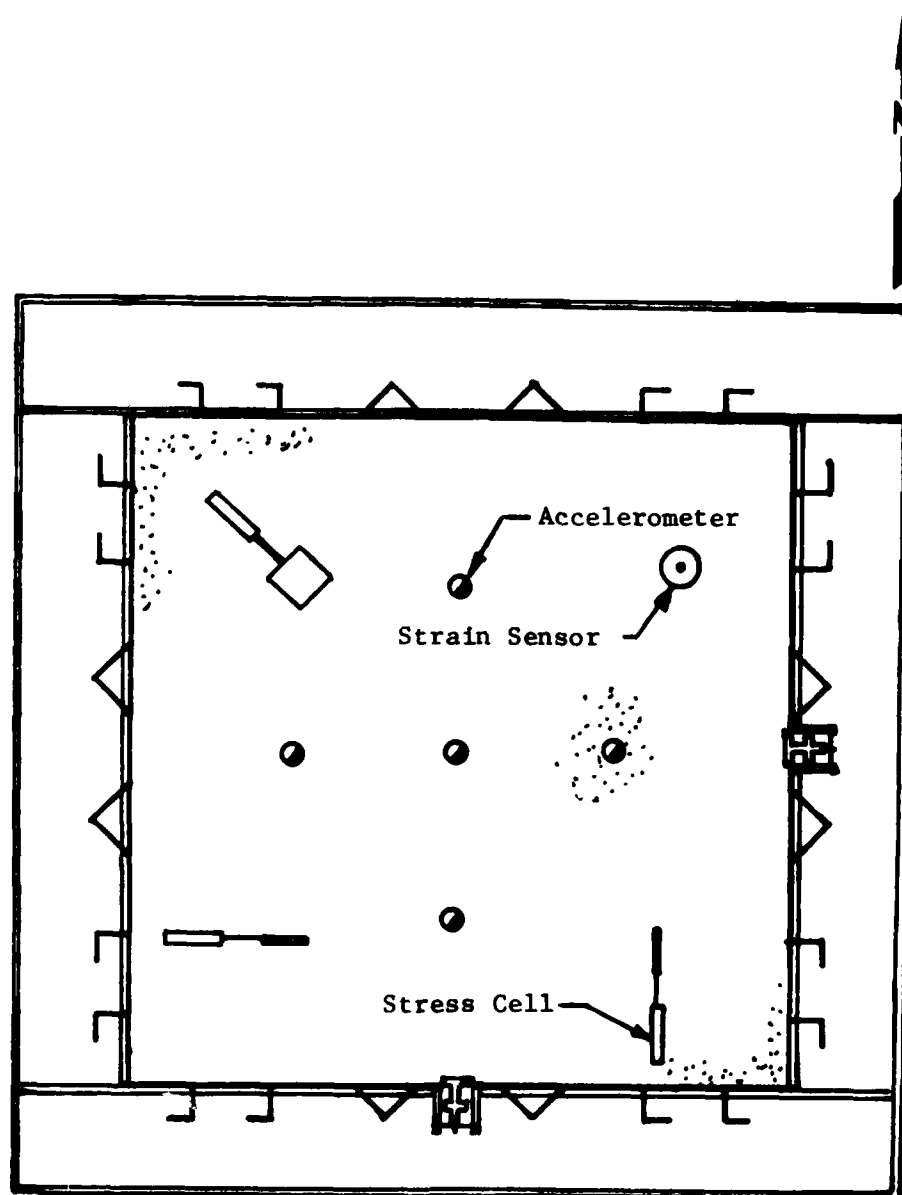


Fig. 5.9 - Horizontal Location of Stress and Strain Measuring Devices at Mid-Height of Cube

strain sensor and the final 3-D accelerometer package. The final accelerometer-to-source distances are listed in Table 5.3.

To place the electronic devices in the sample, the raining of sand was stopped, and a person in a personnel cage was lowered by crane into the cube. As shown in Fig. 5.10, the cage has an open side to permit hand placement of devices and measurement of distances. There are rubber bumpers on the sides to prevent damage to the interior of the cube, and the cage was never permitted to touch the sand surface so that no disturbance of the sand occurred. After completing placement of devices at a given level, the string-spring assembly was moved to a higher level, the wires were passed through holes in the wall of the cube, and raining was resumed.

The stress cells were positioned at mid-height of the cube so that they did not interfere with generation or monitoring of P- and S-waves. The cell used to monitor pressure in the vertical direction was simply placed directly on the level sand surface as shown in Figs. 5.11a and 5.12. The two cells used to monitor horizontal stresses in the sand were oriented parallel to the vertical walls of the cube and were slightly embedded on their side as shown in Figs. 5.11b and 5.13. The wires from the cells were passed through three holes in the south and east walls as can be seen in Fig. 5.14. Raining of the sand was continued until sand covered the cells. This placement method is essentially the same as that described by Hadala (1967).

TABLE 5.3  
Source-Accelerometer Distances Determined  
After Placement

Source*	Receiver	Axis of Sensitivity	Distance (ft)
(1)	(2)	(3)	(4)
1	1	Vertical	1.99
2	1		1.94
3	1		1.97
1	2		3.34
2	2		3.50
3	2		3.44
1	3		4.91
2	3		5.00
3	3		4.94
1	1	North-South	1.99
2	1		1.94
3	1		1.94
1	2		3.40
2	2		3.44
3	2		3.44
1	3		4.96
2	3		4.94
3	3		4.94
1	1	East-West	1.93
2	1		2.00
3	1		2.00
1	2		3.35
2	2		3.50
3	2		3.50
1	3		4.79
2	3		5.00
3	3		5.00

\* 1 = Vertical, 2 = South, 3 = East.

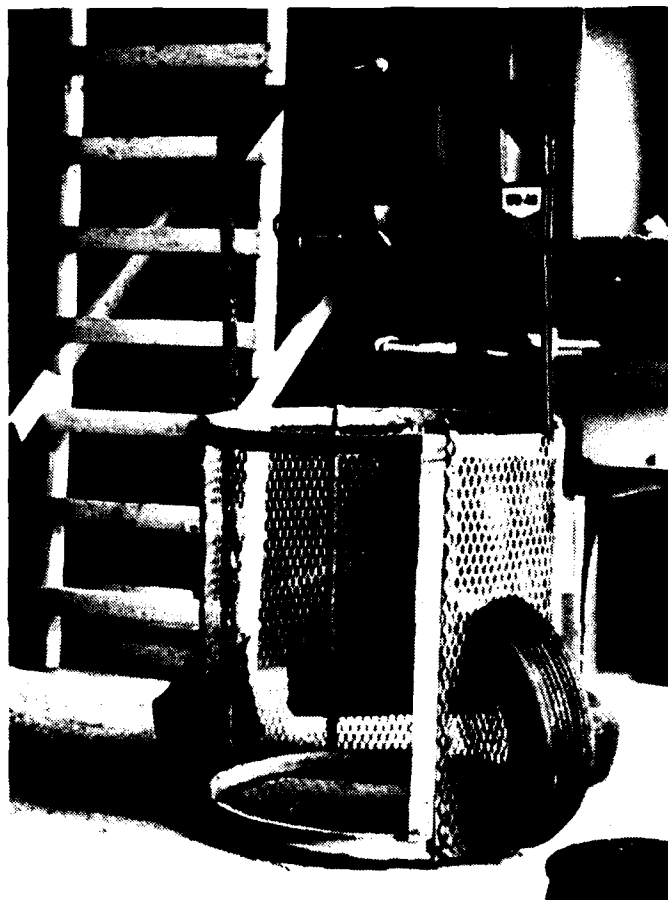
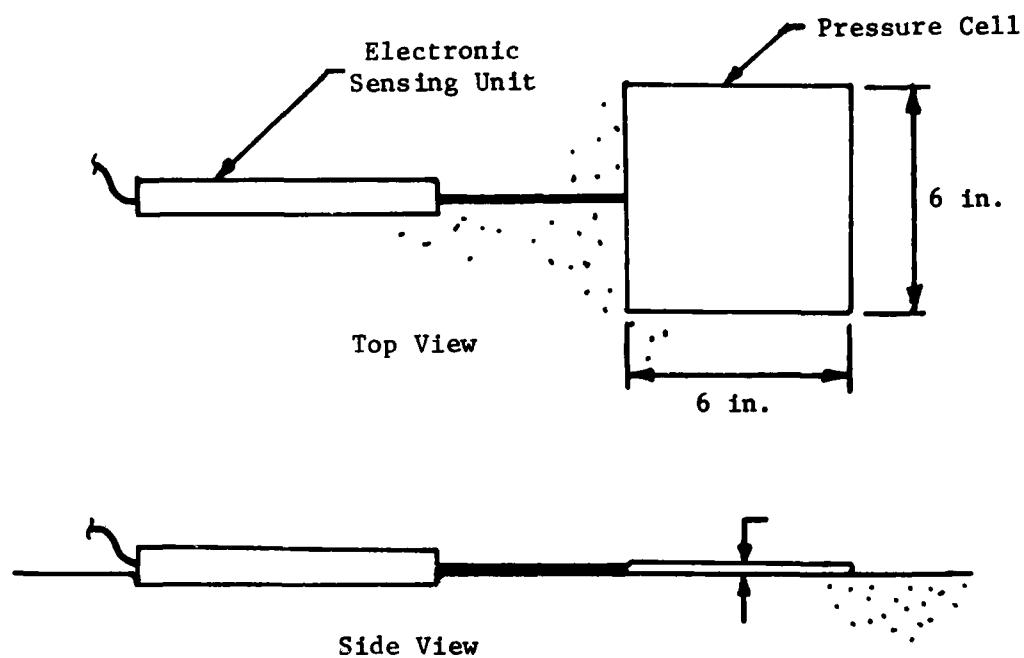
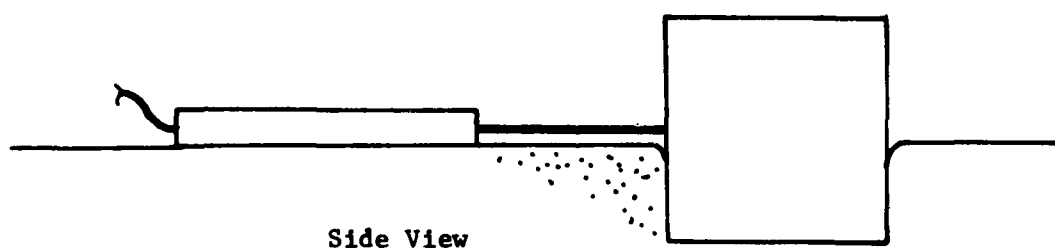


Fig. 5.10 - Personnel Cage Used in Placement of Electronic into Sand During Filling Operation



a) Horizontal Orientation of Cell Monitoring Vertical Stress



b) Vertical Orientation of Cells Monitoring Horizontal Stress

Fig. 5.11 - Placement of Total Stress Cells When the Cube Was Half Filled

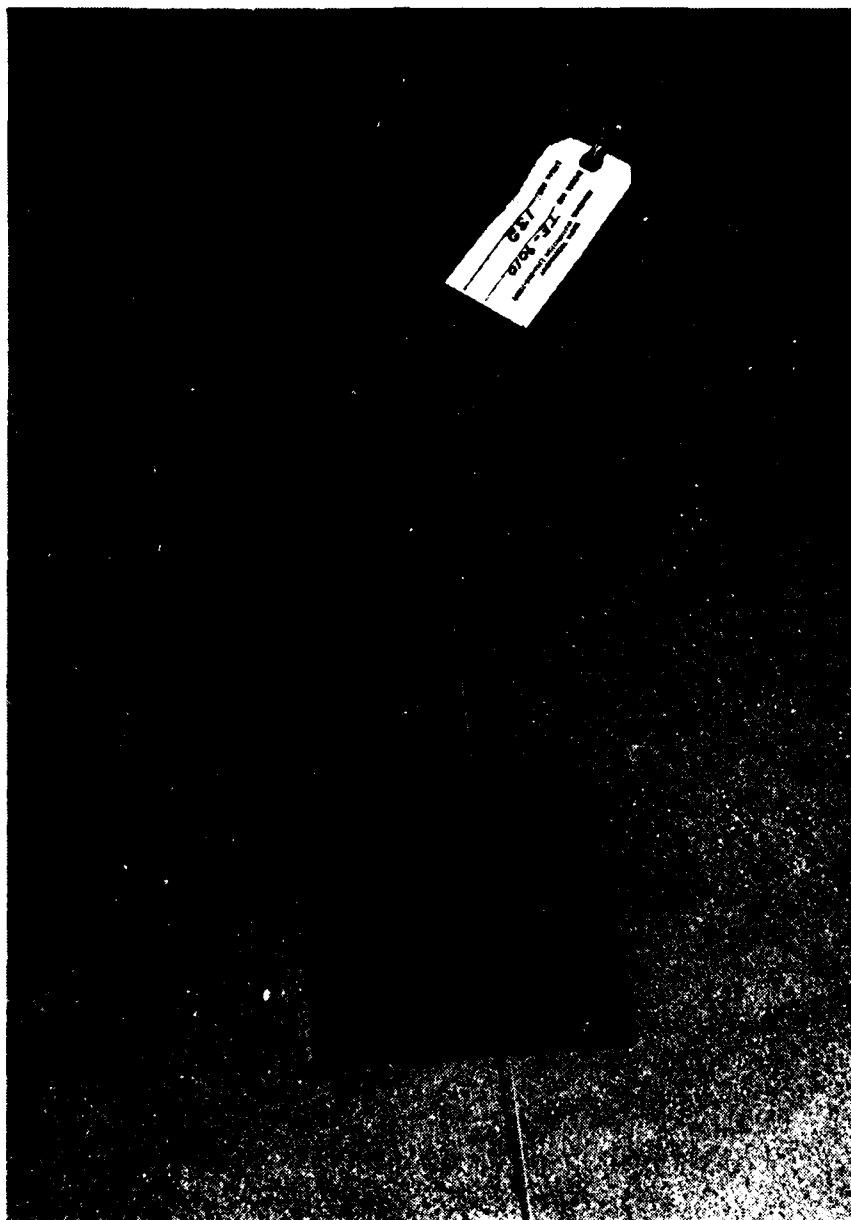


Fig. 5.12 - Total Stress Cell for Vertical Stress  
Measurement Placed on Sand Surface During  
Building of Sample

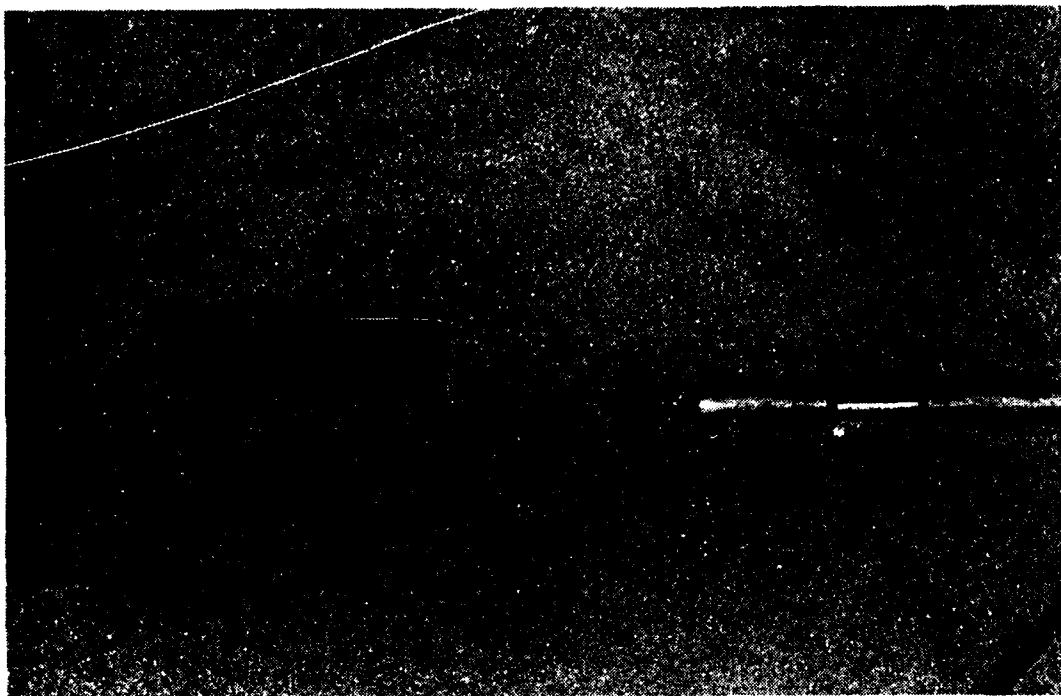


Fig. 5.13 - Total Stress Cell for Horizontal Stress  
Measurement Placed on Sand Surface During  
Building of Sample





Fig. 5.14 - Wires from Stress Cells Fed Through  
East Wall of the Cube

Hadala experimented with three methods of placing stress cells in dry sand which was rained into a container. Although the stress cells used by Hadala were of a slightly different construction, i.e. different manufacturer and smaller size, the results of his tests can be applied to the stress cells used in the cube. Hadala found the best method for placement in dry sand to be setting of the gage directly on the sand surface and continuation of the filling around it. This method resulted in smaller scatter in measured pressures and a lower, mean over-registration ratio,  $R$ , where  $R$  is defined as:

$$R = \frac{1}{n} \sum_{i=1}^n \frac{\sigma_i}{\bar{\sigma}} \quad (5.3)$$

where  $n$  = number of gages,

$\sigma_i$  = stress reading of gage  $n$ , and

$\bar{\sigma}$  = actual stress on gage  $n$ .

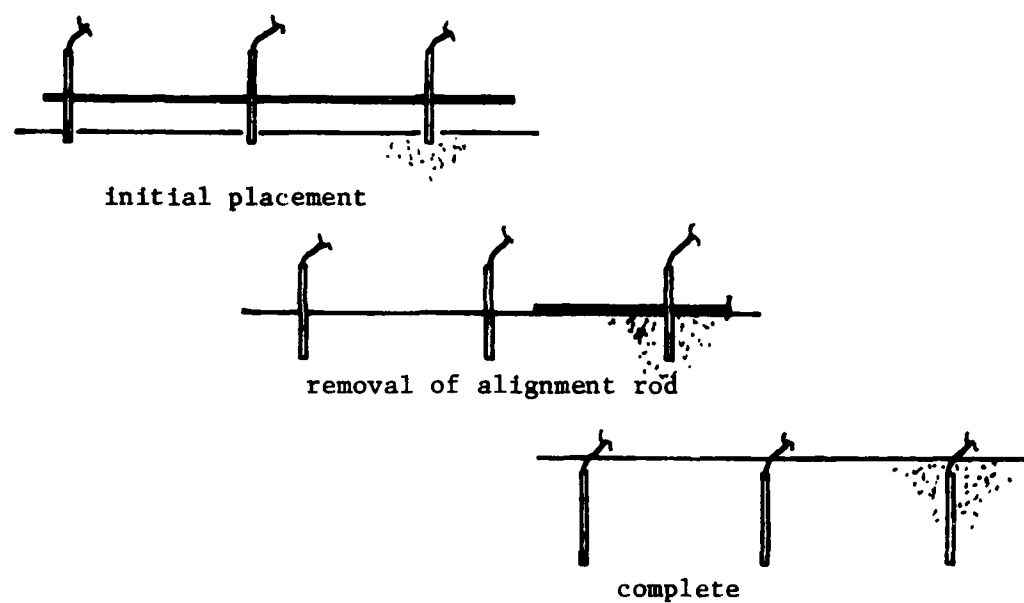
The typical value of  $R$  in his experiments was about 22 percent for the placement method described above. Larger values, up to 40 percent, were found for tamping the stress cell into the sand and the raised-mound method. The raised-mound method involves excavating sand, placing the stress cell and replacing and tamping the excavated sand over the cell.

Each pair of strain sensors had to be oriented with respect to each other so that certain surfaces of the disks faced each other. Unfortunately, this orientation could only be determined by connecting the cells to the control unit. The control unit was

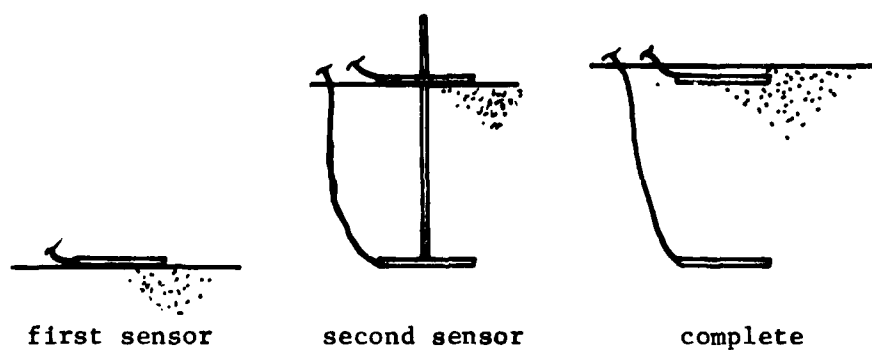
not available until the middle of testing because of a problem with the needle of the meter on the unit which stuck whenever it was deflected full-scale to the left. The manufacturer, Bison, Inc., took approximately six months to correct this minor problem. Rather than delay the tests, it was decided to place three sensors, rather than two, at each horizontal location in the cube. This method doubled the chances of having one operational pair at each location. When the control unit finally arrived back in working order (it was first returned, unfixed, in four months), it was found that four pairs of the six sets were operational.

Each sensor has a small hole in the center to aid in placement in the sand. For horizontal strain measurement, three sensors were placed on an alignment rod at a spacing of twice the sensor diameter as shown in Fig. 5.15a. The assembly was then set on the sand with the rod parallel to the level surface and pointing along the axis to be measured. Sand raining was then continued until the bottom of the rod was just at the sand surface. The rod was removed at this point because the sand could support the sensors for the remainder of the filling operation as shown in Fig. 5.16.

For vertical strain measurement, a sensor was placed on its face on the level sand surface as shown in Fig. 5.15b after the raining was stopped. An alignment rod was placed in the hole of the sensor perpendicular to the sand surface. Raining of the sand was continued until the sand level reached the mark on the rod indicating a distance of two diameters. The second sensor was



a) Horizontal Placement



b) Vertical Placement

Fig. 5.15 - Placement of Strain Sensors When the Cube was Partially Filled



Fig. 5.16 - Horizontal Strain Sensors Placed in the Sand During the Building of the Sample

inserted onto the alignment rod so that it was over the first sensor at a predetermined separation. The rod was then carefully removed, and sand was poured into the resulting hole. Raining was then continued. This method was similar to that described by Wetzel and Vey (1970).

The wires from all the sensors were fed through either of two holes in the east face of the cube. The holes were sealed with rubber, watertight sealant before the sand covered them.

In both horizontal and vertical strain gage placement, lateral and rotational misalignment must be avoided. Truesdale and Schwab (1967) found that errors in strain measurements will occur if the sensors are displaced laterally more than ten percent of the spacing between sensors or if the sensors are rotated greater than ten degrees off of the axis between the pair. The use of the alignment rod minimizes these problems.

While sand was being placed in the cube, the side membranes were being filled with water. The object was to keep the water elevation approximately one in. (2.5 cm) above the sand elevation to ensure that the membrane did not pinch together, closing off a portion of the membrane. If this pinching occurred, pressure might not be uniform over the face of the sand cube which would cause an unknown stress distribution within the sample.

The height of water in the membranes was kept at a maximum of 3 in. (7.5 cm) above the sand surface to prevent any localized passive failure of the top edge of the sand. Water was added

through the air-water panel board to the lower ports of the membranes while the upper ports were open to allow air to escape. When the water elevation reached the top port, a quick-connect was attached to the port and a simple piezometer tube was attached to monitor the final few inches of filling.

Filling of the cube was stopped one in. (2.5 cm) below the top to allow room for the top membrane. The rope supporting the side membranes was removed as was the duct tape supporting the greased sheets. The wooden collar was removed, and the sand surface leveled as shown in Fig. 5.17. A precut sheet of plastic was laid over the top surface and WD-40 oil applied in a thin coat. A second plastic sheet was then placed on top of the oiled sheet after which the top (final) membrane was placed. The steel top was attached and securely bolted. The top membrane was filled with water to fill the void between the top of the sand and the top of the cube. Pressure within the membrane was monitored to ensure that the sand was not subjected to any loading.

The cube and surrounding area was thoroughly cleaned and testing was commenced.

### 5.2.3 Loading the Soil

Each membrane was connected to a separate pressure outlet in the panel board (Fig. 3.12) so that the stress along each axis could be individually controlled and monitored. The sample was loaded and tested along each step of the series listed in Table 5.1.

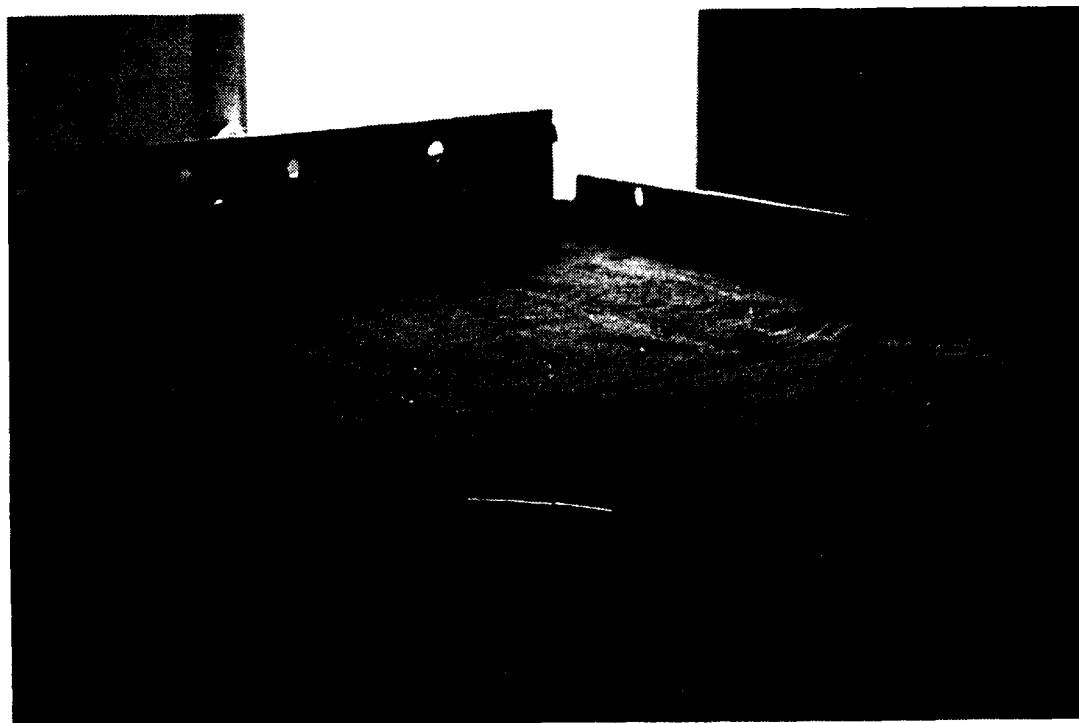


Fig. 5.17 - Sand Surface upon Completion of Building  
of the Sample



To ensure that the stress path initially followed isotropic loading and later maintained a constant mean effective principal stress, the pressure was varied by less than 0.5-psi (3 kPa) increments in a linear progression between pressure steps. This was accomplished by pressurizing all three axes at once and monitoring the rate of change in pressure and adjusting the settings as required.

The stresses and strains at each sub-step were measured on the stress cells and strain sensors to monitor the stress level in the cube and verify the magnitude of the strains as discussed in Section 5.3.4. The change in volume of the membranes (amount of water flowing into or out of the membranes) was also monitored.

The cube was loaded so that the planned state of stress occurred at the center of the cube. Therefore, the effects of overburden pressure, hydraulic gradient, and differing piezometric elevations between the membranes and the pressure panel board had to be taken into account when reading the gage at the panel board. The necessary corrections can be expressed in terms of the following equations:

$$\text{Vertical Correction: } P_G = P_C - 2.4 + -0.036h \quad (5.4)$$

$$\text{Horizontal Correction: } P_G = P_C - 1.5 + 0.036h \quad (5.5)$$

where:  $P_G$  = reading on pressure gage at panel board, in psi,  
 $P_C$  = pressure at center of cube, in psi, and  
 $h$  = difference in elevation between top of cube and  
 air/water interface at panel board, in inches.

The difference in elevation between the top of the cube and the air-water interface at the panel board,  $h$ , is not constant. As the soil compacts or dilates, the column of water falls or rises, respectively. However, the change in elevation of one in. (2.5 cm) results in less than a 0.04 psi (0.25 kPa) change in pressure, or a change of the entire 18-in. (45.7 cm) high accumulator on the panel board results in only a 0.6 psi (4.4 kPa) change in pressure. Therefore, the pressure can be considered constant using a constant value for  $h$  and maintaining the water level at an approximately constant level.

#### 5.2.4 Problems in Use of Stress and Strain Measuring Devices

Problems arose in attempting to use the stress and strain devices which significantly reduced their usefulness. The problem with the strain sensors was not in the device itself, but rather with the manufacturer. As mentioned in Section 5.2.2, the control unit for the sensors originally arrived from Bison, Inc. in disrepair. The unit was returned for repair with the understanding that the delay would be short. The unit was returned four months later when the cube was about to be filled, and no repairs had been made. It was again sent to the manufacturer, and two months later the unit was returned in time to record data for the second half of the testing only.

The available data from the strain gages are plotted against pressure in Fig. 5.18 for the three axes. A strain of 0.1 percent was arbitrarily chosen for the strain up to the loading

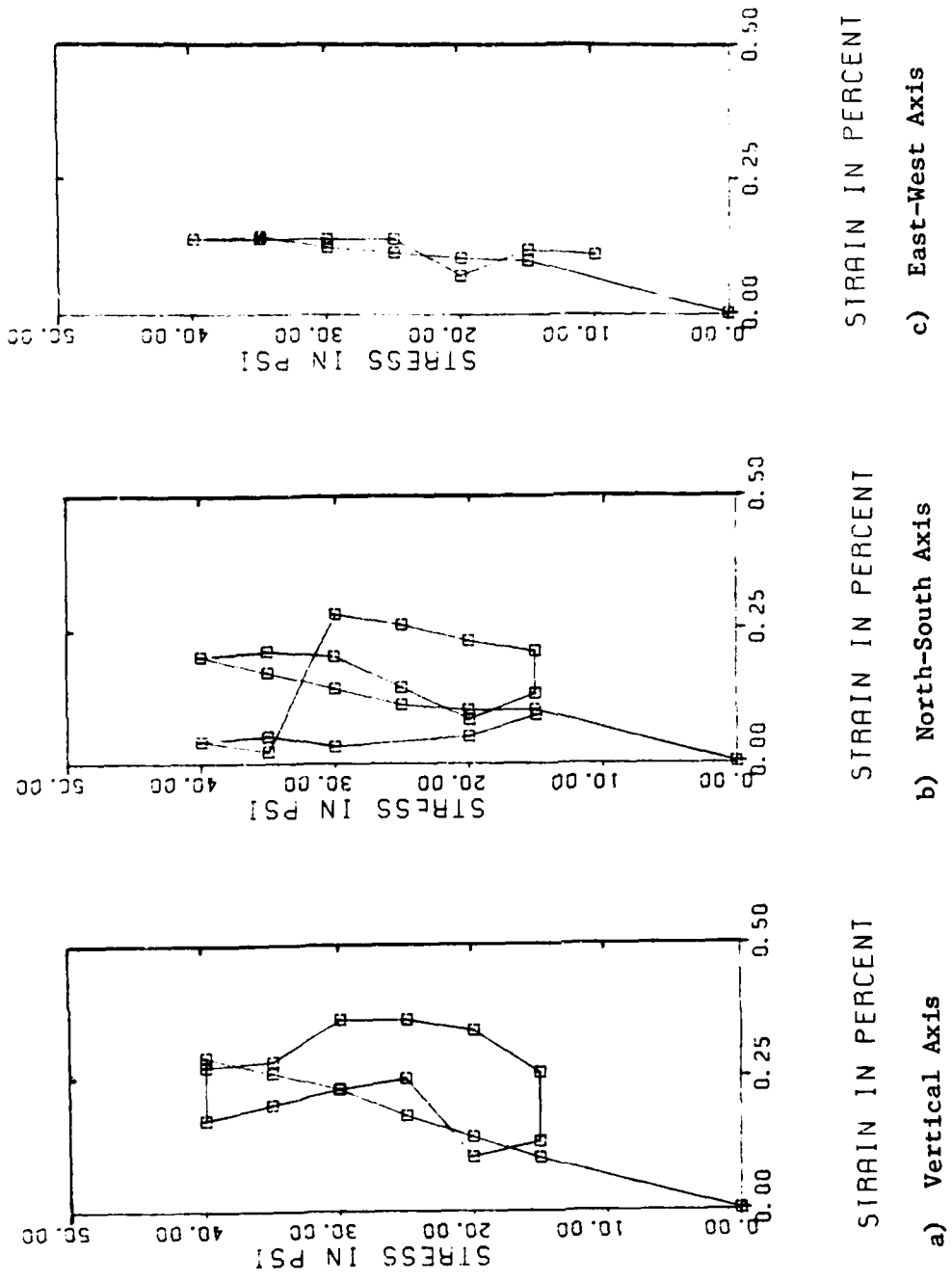
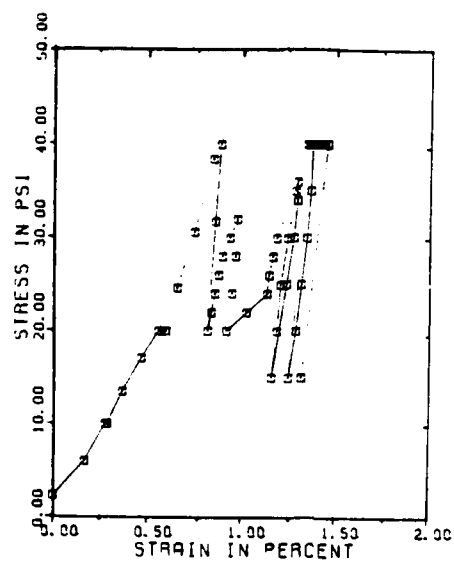


Fig. 5.18 - Stress-Strain Curves for Each Axis of the Cube Based on Strain Gages

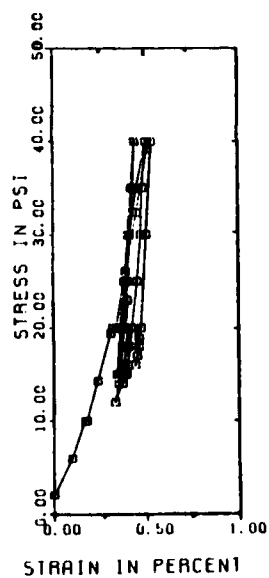
of 15 psi (103 kPa) when the strain gages began to operate. From this limited data, the stress-strain properties cannot be predicted because of the scatter and lack of data points. The loading, however, may be considered small-strain loading because the maximum strain is about 0.3 percent over the range in pressures measured.

A rough estimate of strain with respect to change in stress was made by monitoring the number of times the accumulator had to be filled or drained because of water flowing into or out of the membranes during loading. This volumetric strain along each axis is shown in Fig. 5.19. The large initial strain is believed to have been caused by seating of the membranes in the cube. Any voids between the membranes and face of the cube and in the corners of the cube had to be filled before the membrane could exert pressure on the sand. After the initial seating, the stress-strain relationship is fairly linear with no evidence of stress history. The actual strains are probably less than the volumetric strain because of the unmeasurable compliance in the loading system. The values of the elastic modulus,  $E$ , derived from the slopes of the curves are 18,000 psi (124,000 kPa), vertical, and 16,000 psi (110,000 kPa), north-south and east-west.

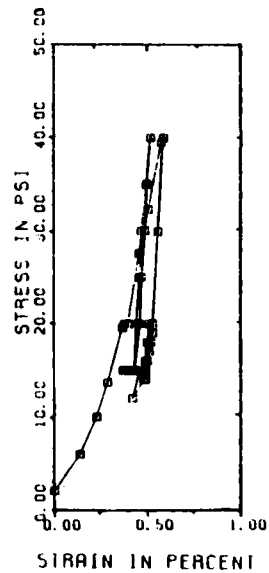
The stress cells were supposed to be calibrated so that a digital pressure readout was possible. Hadala (1967) discussed the inherent errors associated with stress cells in cohesionless soil. The major problem occurs from sand arching around the cell. Proper placement of the cell can minimize this problem (Section 5.2.2),



a) Vertical Axis



b) North-South Axis



c) East-West Axis

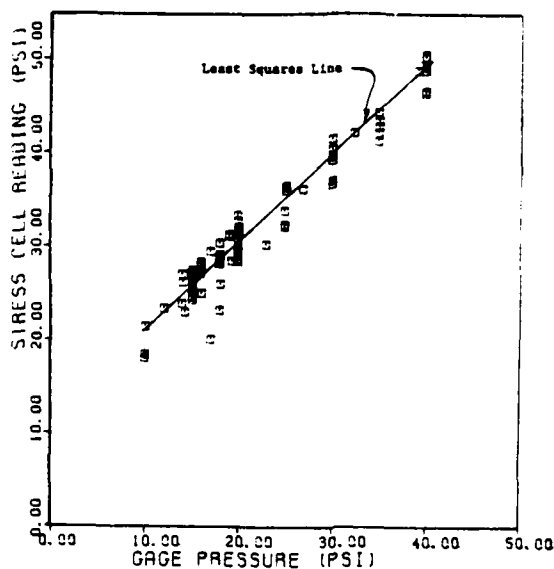
Fig. 5.19 - Stress-Strain Curves for Each Axis of the Cube Based on Water Flowing Into and Out of Membranes

but even the best placement method results in an average range of 22 percent over- or under-reading. A minor error inherent to the type of stress cell used in these tests was that the soil pressure caused a comparable oil pressure which deflects a strain gage in the unit. Problems may arise from the slight compressibility of the soil and possible small non-linearity of the strain gage.

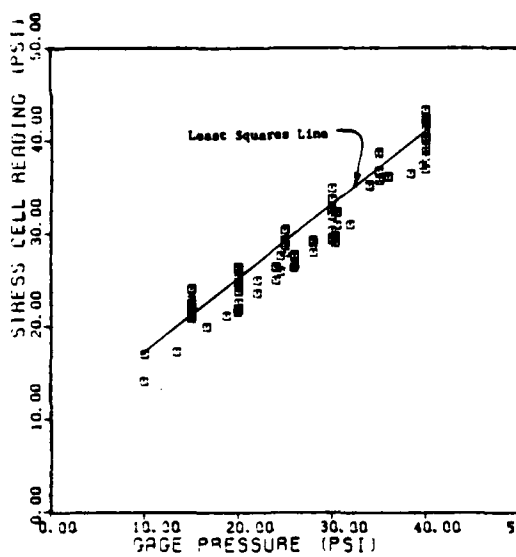
Figure 5.20 shows the stress applied by the loading system versus the stress read by the stress cell along each axis. Within some scatter, the variation is linear, but not a direct correspondence. Therefore, if the cells are to be used in the future, calibration curves can and must be made for each cell in the laboratory before placement in the soil.

#### 5.2.5 Dynamic Testing

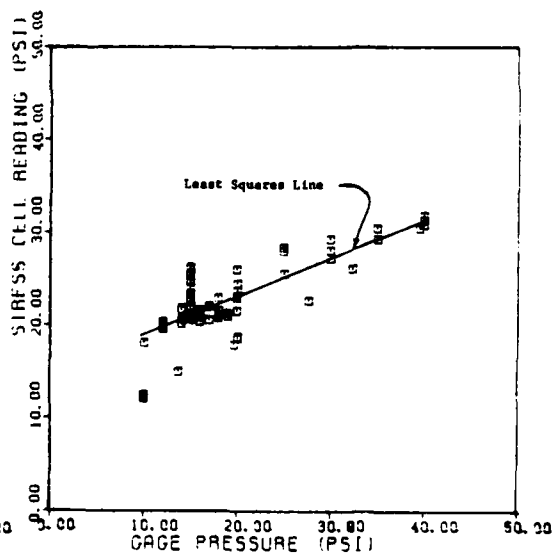
Nine sets of waveforms were recorded at each state of stress since a compression wave and two, mutually perpendicular shear waves were generated along each axis. Each set of three waveforms results from the output simultaneously recorded from the three accelerometers positioned along the direction of wave propagation and oriented in the direction of particle motion. For example, a compression wave generated at the east source would be recorded on the horizontal accelerometers sensitive in the east-west direction in the three, 3-D accelerometer packages lying along the east-west axis of the cube. (Operation of the accelerometers is discussed in Section 3.5.1.)



a) North-South Axis



b) Vertical Axis



c) East-West Axis

Fig. 5.20 - Stress Cell Reading versus Pressure  
Determined by Panel Board Gage for Each  
Axis of the Cube

Each set of waveforms was generated by striking the anvil of a source on the cube with a hammer. The mechanical action generated a wave through the sand. The direction of the impulse of the hammer determined the direction of the particle motion, and therefore the type of wave. As the hammer struck the source, the two digital oscilloscopes were electrically triggered, starting the recording of the waveforms. Full details of the operation of the trigger and source can be found in Section 3.3.

The waves were recorded on the magnetic storage diskettes of a pair of two-channel oscilloscopes with the output from the middle accelerometer recorded on both oscilloscopes as a reference. Appendices C to E show typical sets of P-wave traces along with their data reduction. Data reduction is discussed in Chapter 6.

### 5.3 SUMMARY AND CONCLUSIONS

A testing program was selected which permitted testing with: 1. isotropic confinement, 2. confinement with a constant mean effective principal stress, and 3. confinement with a varying mean effective principal stress. The sand was tested in a dry state and therefore could be placed in the cube by a raining technique discussed in the chapter. Raining was halted at predetermined elevations to allow for placement of accelerometers, stress cells, and strain sensors, and to permit determination of density. The density tests showed the sample to be quite uniform with an average density of 96.6 pcf ( $1547 \text{ kg/m}^3$ ). Because of



problems discussed in the chapter, the stress and strain cells were not used to their full potential. Rather, they could only give an estimation of what was occurring in the cube when subjected to load.

Dynamic testing began on July 8, 1981, and was completed on August 19, 1981. The method of analyzing the data is discussed in Chapter 6, and the results of the testing are discussed in Chapters 6 through 8.

## CHAPTER SIX

### ISOTROPIC CONFINEMENT

#### 6.1 INTRODUCTION

The first step in the study of the effect of the triaxial state of stress on P-wave velocity is the analysis of the effect of an isotropic state of stress on  $V_p$ . To obtain isotropic loading, confining pressures were applied so that principal stresses were the same along all three axes of the cube ( $\bar{\sigma}_1 = \bar{\sigma}_2 = \bar{\sigma}_3$ ). Compression wave velocities were then measured along each axis at various isotropic states of stress.

In reality, true isotropic confinement could not be achieved at all points within the 7-ft (2.1 m) cube because of small inherent pressure gradients. In the vertical direction, even though a constant pressure was applied to the boundary, there was a slight increase in stress with depth caused by the weight of the soil. The change in vertical stress from top to bottom of the cube was less than 5 psi (34 kPa), or less than  $\pm 2.5$  psi (17 kPa) from the value applied at the center of the cube. For stresses applied in the horizontal direction, there was the effect of the increasing hydraulic head with water depth in the membranes. The hydraulic head caused a change in horizontal stress from top to bottom of the cube of about 2.5 psi (17 kPa) or  $\pm 1.2$  psi (8 kPa) from the value applied at the mid-height of the cube. Therefore,

the state of stress varied slightly along the vertical axis of the cube, with stress increasing with depth. There was, however, no variation in the state of stress along horizontal planes in the cube.

The values of all pressures reported in this study represent the values of pressures applied at the center of the cube. As discussed in Section 6.3, only interval velocities were used in the final analysis. The largest interval was a distance of 3 ft (0.9 m) between receivers 1 and 3 (see Fig. 3.20). Therefore, variations in pressures in the area over which data was collected was about half of those over the entire sand sample. Within the range of isotropic pressures used (10 psi (69 kPa) to 40 psi (276 kPa)), the variation in pressure over the area of interest was: 3 to 12 percent ( $\pm 1.2$  psi (8 kPa)) in the vertical direction and 1.5 to 6 percent ( $\pm 0.6$  psi (4 kPa)) in the horizontal direction. As a result, these pressure gradients were small and were neglected.

The method of data analysis is briefly presented in this chapter. The effect of structural anisotropy is then presented after which the variation of P-wave velocity with isotropic loading is shown. The effects of biaxial and triaxial confinement on  $V_p$  are discussed in Chapters 7 and 8, respectively.

## 6.2 DATA ANALYSIS

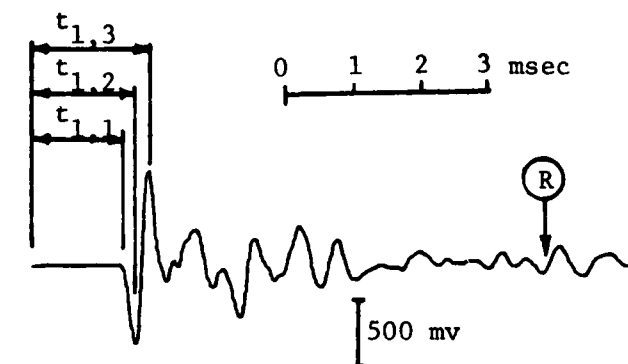
Data were collected at the Ferguson Laboratories over a six week period. At each confining pressure, travel time records for each wave propagating along each of the three axes of the cube

were recorded on magnetic disks as described in Chapter 5. These records were returned to the main campus for analysis. Values for travel times and amplitudes were determined, from which velocities, frequencies, strain amplitudes, and data for damping were computed as detailed in the sections that follow.

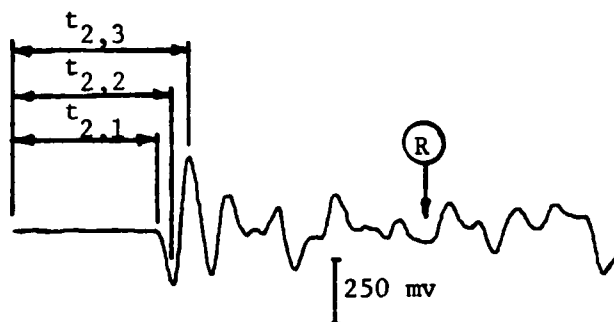
#### 6.2.1 Determination of Velocity

At each pressure, travel times for the first arrival, first trough and first peak were determined from each set of three accelerometer records along each axis of the cube. A typical set of records showing these direct-arrival measurements along one axis is shown in Fig. 6.1. In addition to the direct arrivals, reflections of P-waves off the opposite wall in the cube are noted by R in Fig. 6.1. The reflections occur at a large enough time after the direct arrivals so that they do not interfere with the data collection. This point is discussed further in Section 6.2.5.

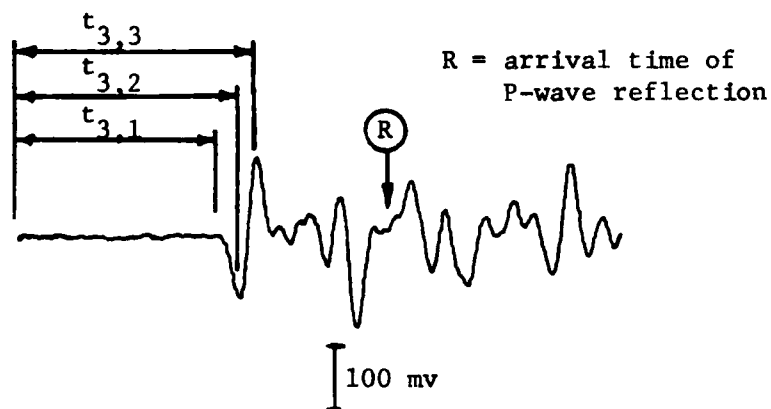
A specially developed FORTRAN IV program, CUBE (see Appendix B), was used to compute velocities from travel times. The distances between sources and receivers used in the computation of velocities in program CUBE were measured to an accuracy of 0.063 in. (1.5 mm) when the accelerometers were placed in the cube. Distances were measured from the face of the source in contact with the sand to the center of the accelerometer. Interval distances were simply determined as the differences between direct distances. Separate distances were input for each accelerometer. All distances



a. Receiver Nearest Source (Record 1)



b. Middle Receiver (Record 2)



c. Receiver Farthest from Source (Record 3)

Fig. 6.1 - Compression Wave Travel Time Determined from a Set of Three Accelerometer Records Along One Axis of the Cube

will be checked when the cube is emptied to ensure that the accelerometer positions were not significantly changed during testing. However, since the maximum strain as measured by the strain sensors was less than 0.01 percent (refer to Section 5.2.4), it is doubtful that any significant movement of the accelerometers occurred.

As shown in Fig. 6.1, a total of nine travel times determined from each set of three accelerometer records:

1. Source to initial arrival:

Record 1,  $t_{1,1}$ ; Record 2,  $t_{2,1}$ ; Record 3,  $t_{3,1}$

2. Source to first trough:

Record 1,  $t_{1,2}$ ; Record 2,  $t_{2,2}$ ; Record 3,  $t_{3,2}$

3. Source to first peak:

Record 1,  $t_{1,3}$ ; Record 2,  $t_{2,3}$ ; Record 3,  $t_{3,3}$

From these nine travel times, three direct velocities and nine interval velocities were computed as follows:

1. Direct velocities (source to initial arrival):

Record 1, Record 2, Record 3

2. Interval velocities:

- a. First arrival to first arrival:

Record 1 to Record 2

Record 2 to Record 3

Record 1 to Record 3

b. First trough to first trough:

Record 1 to Record 2

Record 2 to Record 3

Record 1 to Record 3

c. First peak to first peak:

Record 1 to Record 2

Record 2 to Record 3

Record 1 to Record 3

These velocities were then plotted against confining pressure on logarithmic plots to determine the variation in P-wave velocity with isotropic loading.

#### 6.2.2 Determination of Predominant Frequency

The predominant frequency of the direct P-wave can be determined from the three fractional values of the period, 0.25 T, 0.50 T, and 0.75 T, measured from each accelerometer record as shown in Fig. 6.2. These fractional periods are easily determined from the intervals between the travel times for each record shown in Fig. 6.1. The range in values of predominant frequencies, as determined by program CUBE, was large: 600 Hz to 2700 Hz, with an average of about 1000 Hz. There appears to be no influence on the frequency from changes in confining pressure. In the later biaxial and triaxial tests (tests 24 to 44 in Table 5.1), the vertical pressure was increased from 15 psi (103 kPa) to 40 psi (276 kPa), and the frequency varied from about 700 Hz to about

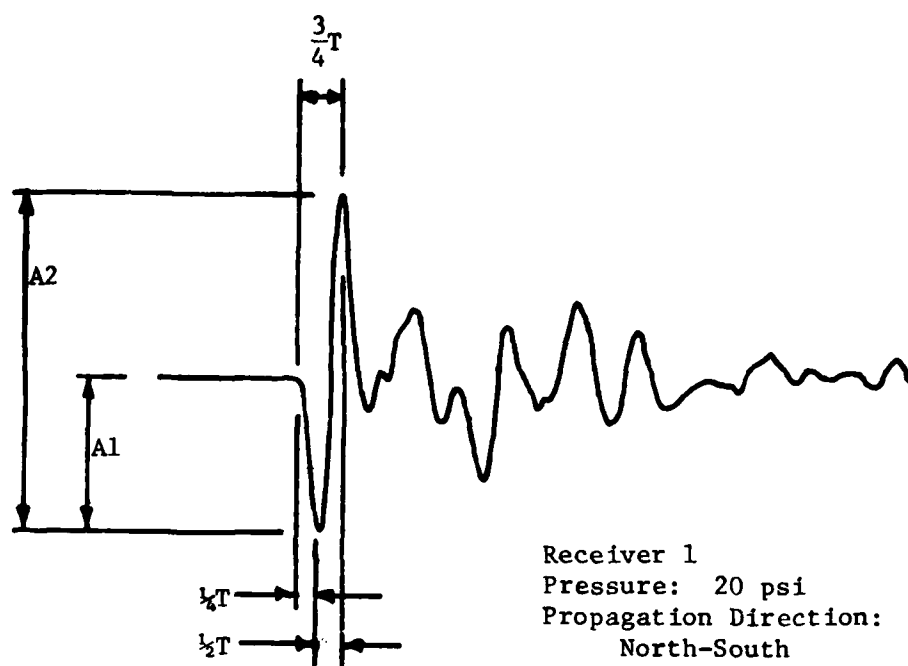


Fig. 6.2 - Determination of Particle Amplitudes and Predominant Period from a Typical Accelerometer Record



1000 Hz without any definite pattern. There were trends in frequency depending upon the fractional period used to determine the frequency. The value of time measured for 0.25 T was only slightly less than that measured for 0.50 T causing a larger frequency value computed for 0.50 T than for 0.25 T. The value from 0.75 T was an average of these two values because of the way the data was measured.

The predominant frequency has two uses in this study. First it is used to estimate the strain amplitude in Section 6.2.4 and then it is used to estimate the wavelength in Section 6.2.5. In either case the scatter in the values is of little concern since only approximations are being made.

### 6.2.3 Determination of Particle Amplitude

Two amplitudes of wave particle motion were determined from each accelerometer record as shown in Fig. 6.2: the amplitude of the first trough, A1, and the double amplitude of the first trough-to-peak amplitude, A2. This data is being held for future analysis to determine the effect of confining pressure on the attenuation of compression waves.

The charge amplifier used with the accelerometers was calibrated so that the output voltage (y-axis on an output record) corresponded to 20 V peak-to-peak for an acceleration of one g ( $32.2 \text{ ft/s}^2$  or  $9.8 \text{ m/s}^2$ ) peak-to-peak. With this relationship between amplitude and acceleration, the peak acceleration of each

trace can be determined. Values of peak acceleration ranged from 0.002 g to 0.6 g (0.02 to 5.8 m/s<sup>2</sup>) with an average of about 0.02 g (0.2 m/s<sup>2</sup>). In general, the amplitude of the first trough, A<sub>1</sub>, was about equal to half of the trough-to-peak amplitude, A<sub>2</sub>.

#### 6.2.4 Determination of Strain Amplitude

For a plane wave, linear strain amplitude,  $\epsilon$ , can be determined from the particle velocity,  $\dot{u}_p$ , and propagation velocity,  $V_p$ , as follows (Richart, et al, 1970):

$$\epsilon = \frac{\dot{u}_p}{V_p} \quad (6.1)$$

and

$$\dot{u}_p = (2\pi f) A \quad (6.2)$$

where:  $f$  = wave frequency, and

$A$  = peak particle amplitude.

For our measurements, the acceleration,  $\ddot{z}$ , can be related to the peak particle amplitude using a harmonic approximation:

$$\ddot{z} = (2\pi f)^2 A \quad (6.3)$$

which means:

$$\dot{u}_p = \frac{\ddot{z}}{2\pi f} \quad (6.4)$$

By combining Eq. 6.4 with Eq. 6.1, the relationship between strain amplitude, acceleration, frequency, and P-wave velocity for a plane wave is:

$$\epsilon = \frac{\ddot{z}}{(2\pi f) V_p} \quad (6.5)$$

The sources in the cube tend to generate spherical waves and Eq. 6.5 is applicable only to plane waves. Therefore, values of strain amplitude computed by the equation will be slightly in error. However, it has been used as an approximation to reflect the order of magnitude of the strains in the sand in the cube. With this approximation, at the receiver closest to the source, the maximum strain amplitude for the P-waves in the sand was about  $5 \times 10^{-5}$  percent. Because this is less than  $1 \times 10^{-3}$  percent, the testing in this sand may be considered to be low amplitude and the effect of strain amplitude can be ignored. The low-amplitude dynamic properties of this sand are discussed in Appendix A.

#### 6.2.5 Determination of Wavelengths

Having previously determined the P-wave velocity,  $V_p$ , and frequency,  $f$ , the wavelength,  $\lambda$ , can be computed from the equation

$$\lambda = \frac{V_p}{f} \quad (6.6)$$

As the confining pressure was increased, the frequency stayed fairly constant while the P-wave velocity increased (see Sections 6.2.2 and 6.3). Therefore, the wavelength increased with confining pressure. Using the average minimum velocity of 1120 fps (341 ms) (at 10 psi (69 kPa) in the vertical direction) and the

average maximum velocity of 1820 (555 m/s) (at 40 psi (276 kPa) in the north-south direction) together with an average frequency of 1000 Hz, the range in wavelengths was 1.1 ft to 1.8 ft (0.34 m to 0.56 m) in the sand in the cube.

For the results to be easily interpreted, the wavelength must be short enough that the full wave passes by any receiver before the start of a wave reflected off a face of the cube reaches the same receiver. This critical distance is twice the distance between the receiver furthest from the source and the face of the cube opposite the face with that source. The accelerometers were positioned so that this distance is about 4 ft (1.2 m) which is more than twice the longest wavelength. Therefore the wavelengths are short enough to be read without interference from reflections.

Conversely, the wavelength must be long enough that the accelerometer block properly tracks the particle motion of the soil. If the wavelength is too small, the block acts as a boundary rather than as a part of the sample. If the block is about one eighth the size of the wavelength, it behaves as the soil. Since the block is 1.75 in. (44 mm) square, the minimum wavelength is 1.17 ft (.35 m) which is approximately the same as the minimum wavelength. Therefore, testing seems to have been conducted within an acceptable range of wavelengths.

### 6.3 DIRECT AND INTERVAL VELOCITIES

Compression wave velocities (direct and interval) were first analyzed separately for propagation along each axis to evaluate the effect of structural anisotropy in the sand sample as discussed in Section 6.5. Figure 6.3 is a logarithmic plot of P-wave velocity versus confining pressure for all wave velocities determined along the vertical axis. The graph is difficult to interpret because of the amount and scatter of the data. This same result occurred for measurements along the other two axes. However, if the data is divided into direct and interval velocities, as shown in Figs. 6.4 to 6.6, it is evident that the interval velocities follow a linear  $\log V_p - \log \bar{\sigma}_0$  relationship, but the direct velocities are nonlinear, generally falling below the interval values. The scatter in the interval velocity is reduced without the direct velocity values.

Two factors contribute to the nonlinearity of the  $\log V_p - \log \bar{\sigma}_0$  plot for the direct velocity data. Any triggering problems are reflected in direct velocities but not in interval velocities (Hoar and Stokoe, 1978). A delay in triggering causes an increase in the direct travel time determined at all three measurement points along each axis. However, the amount of the time increase relative to the total travel time varies inversely with the distance from the source. On the other hand, interval velocities are unaffected by triggering delays. It was noted during testing that as the voltage of the 9-volt battery in the trigger box

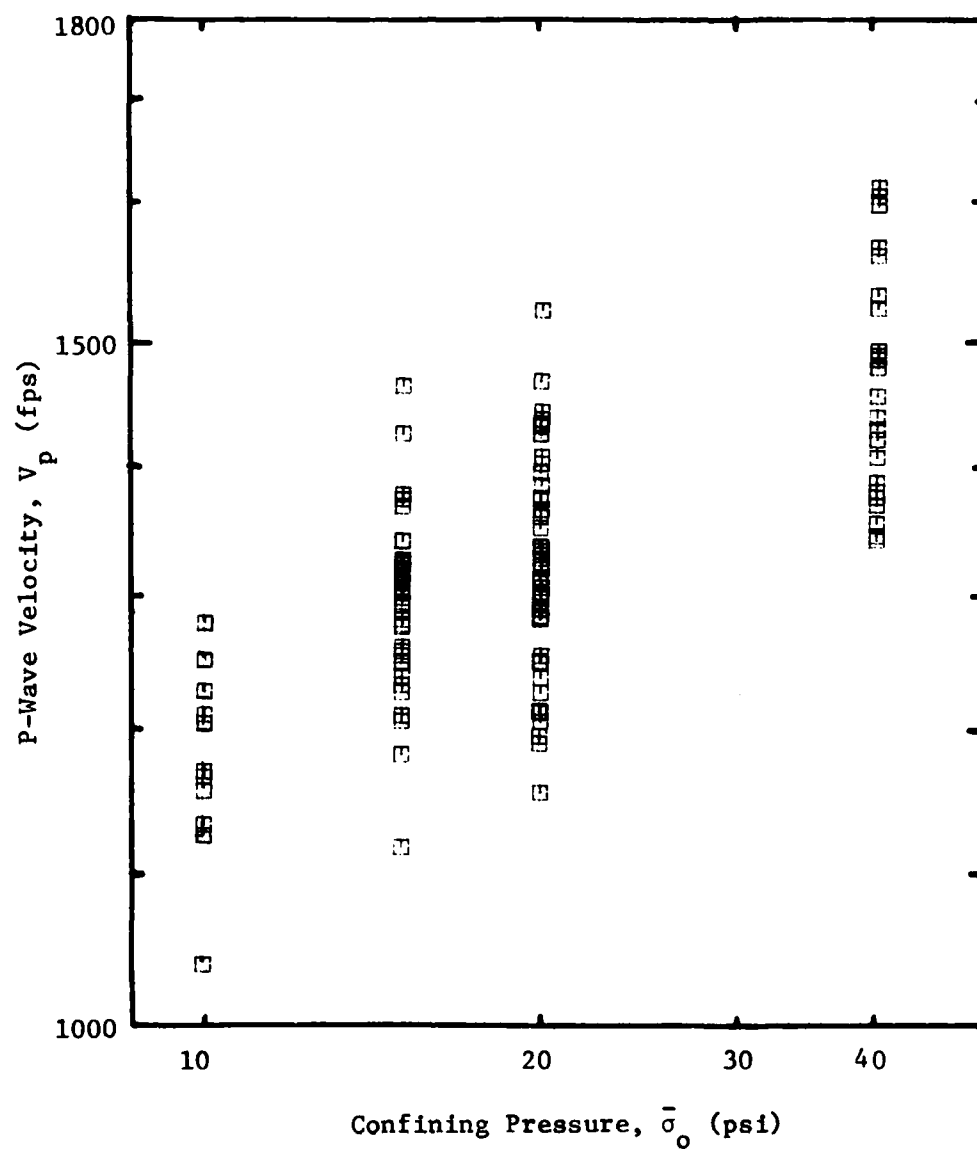
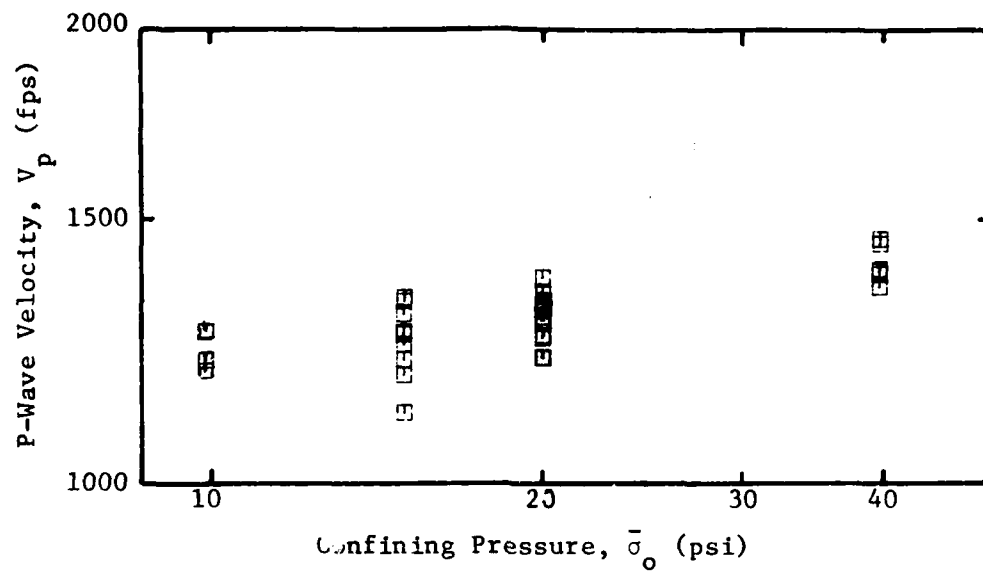
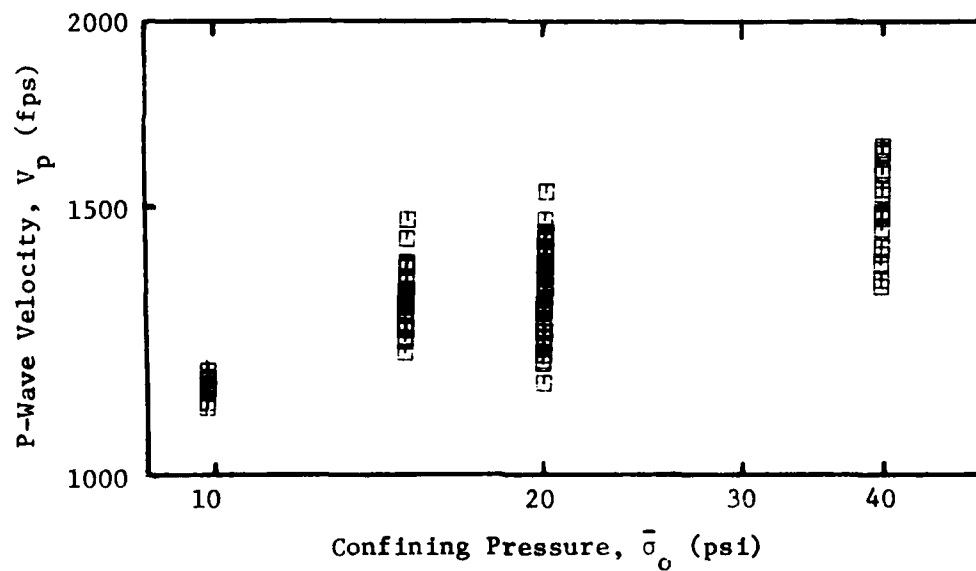


Fig. 6.3 - Variation in Compression Wave Velocity in the Vertical Direction with Isotropic Confining Pressure

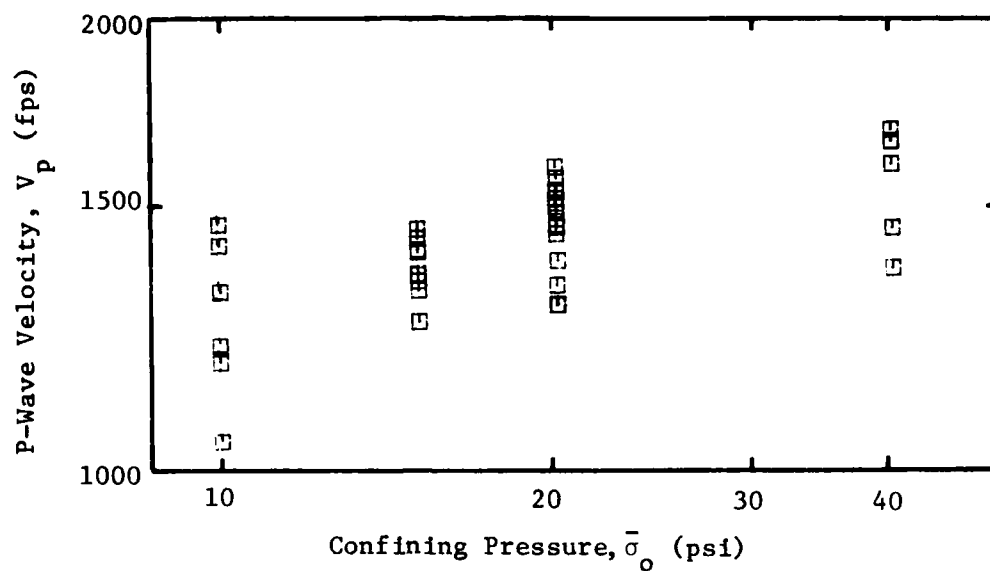


a) Direct Velocity

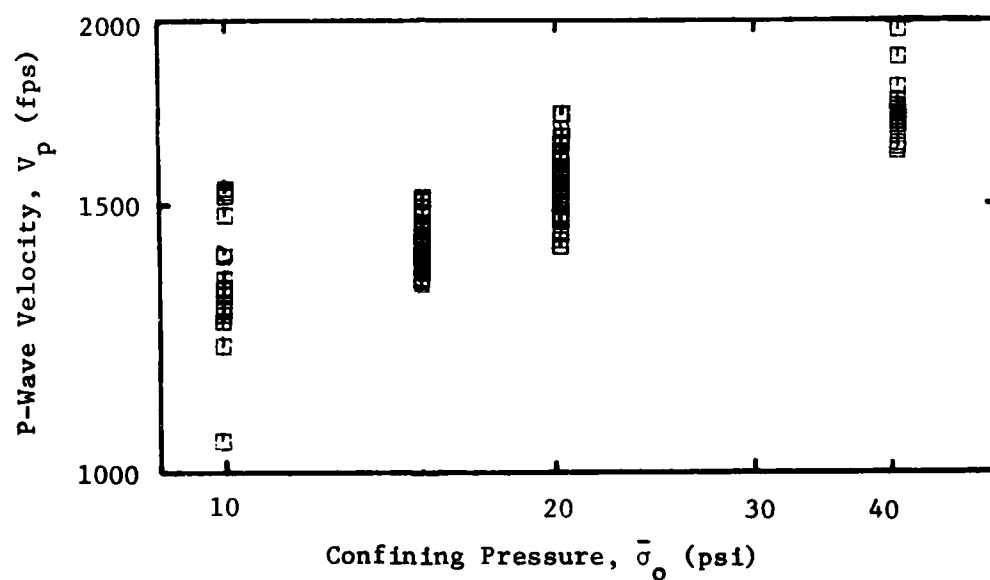


b) Interval Velocity

Fig. 6.4 - Variation in Direct and Interval Compression Wave Velocity along the Vertical Axis of the Cube with Isotropic Confining Pressure



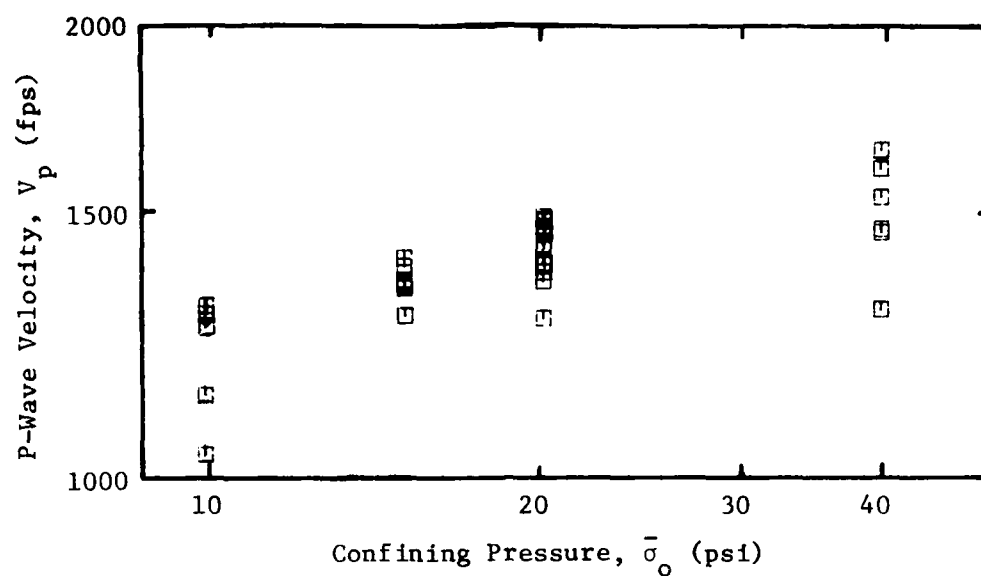
a) Direct Velocity



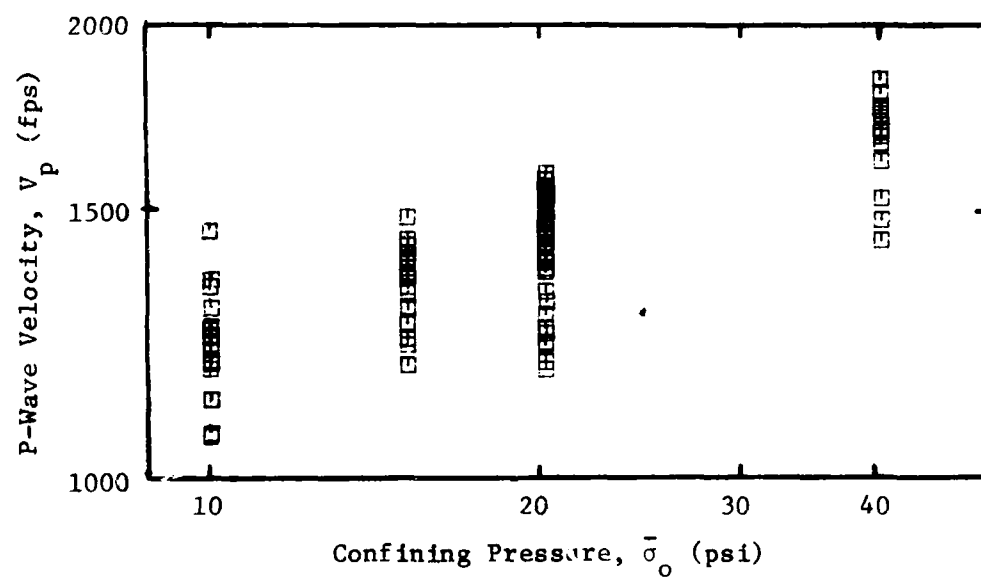
b) Interval Velocity

Fig. 6.5 - Variation in Direct and Interval Compression Wave Velocity along the North-South Axis of the Cube with Isotropic Confining Pressure





a) Direct Velocity



b) Interval Velocity

Fig. 6.6 - Variation in Direct and Interval Compression Wave Velocity along the East-West Axis of the Cube with Isotropic Confining Pressure

decreased to 5 volts, the trigger became erratic - sometimes slow, sometimes fast. Therefore, the measurement of direct velocities was adversely affected.

The other major factor contributing to problems with the measured direct velocities is variable soil properties. While soil density varies somewhat throughout the cube, which causes minor scatter in the data, there are several problems inherent in measurement between the source and any receivers. Any problems near the source or between the source and first receiver are only seen in the direct velocities since interval velocities are determined between receivers. Uniform soil placement along the boundary is difficult. This soil placement problem is compounded by the protrusion of the source into the cube. It is, therefore, very easy for a soft spot to develop at the source. The soft spot, being a zone of low density, would have a lower modulus which would be reflected by lowered direct velocities.

A soft spot also may have developed at the two horizontal ports during testing. About half-way through the tests, the east port began to leak sand. The north port also began to leak sand when only about ten tests remained to be performed. The maximum total loss of sand from either port did not exceed 0.5 cu. in. (8.2 cu. cm) but that was enough to cause the reseating of the source at a very slightly skewed angle and the probable development of a soft spot in front of the source. The net probable result of this occurrence would be a decrease in direct velocities. However,

a soft spot would not affect interval velocities. The major effect of the soft spot was caused by reseating of the source, resulting in poor quality wave forms containing small echos and reverberations. A typical record before sand loss is shown in Fig. 6.7 and can be compared to a record after sand loss in Fig. 6.8.

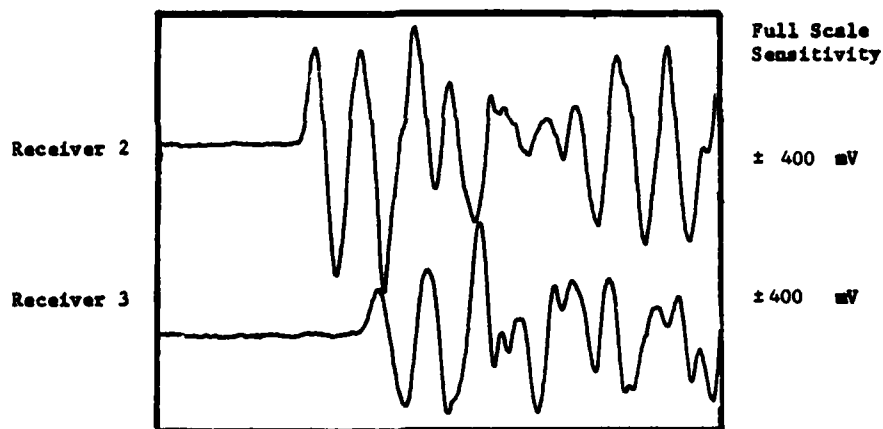
Because of the problems discussed above which resulted in direct velocities not properly reflecting the stiffness of the confined sand, it was decided that only interval velocities would be used in the final analysis.

#### 6.3.1 Short-versus Long-Interval Measurements

Since travel time measurements were made using three receivers, interval velocities were computed over three intervals with the following nominal spacings: receiver 1 to receiver 2, 1.5 ft (0.45 m); receiver 2 to receiver 3, 1.5 ft (0.45 m); and receiver 1 to receiver 3, 3.0 ft (0.91 m). Relatively speaking, the first two intervals can be considered short intervals and the third one can be considered a long interval. There are certain advantages in using times and velocities determined from the long interval. First, since the longer interval involves measurements over a longer distance, there is less chance of error from highly localized variations in soil properties. Second, since the values of time and distance are longer, the precision of these values and resulting velocities is higher. Finally, the short intervals are



Disk/Track Number: 6-3/5  
Record Length: 10.2 msec



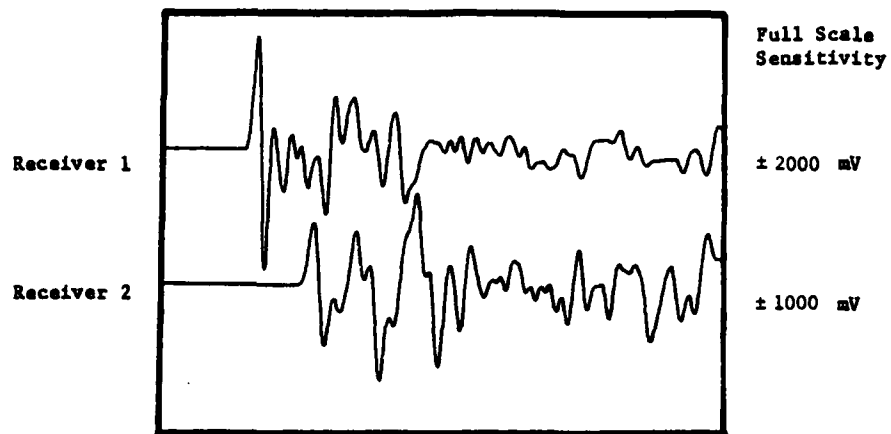
Disk/Track Number: 6-4/5  
Record Length: 10.2 msec

TEST NUMBER: 24

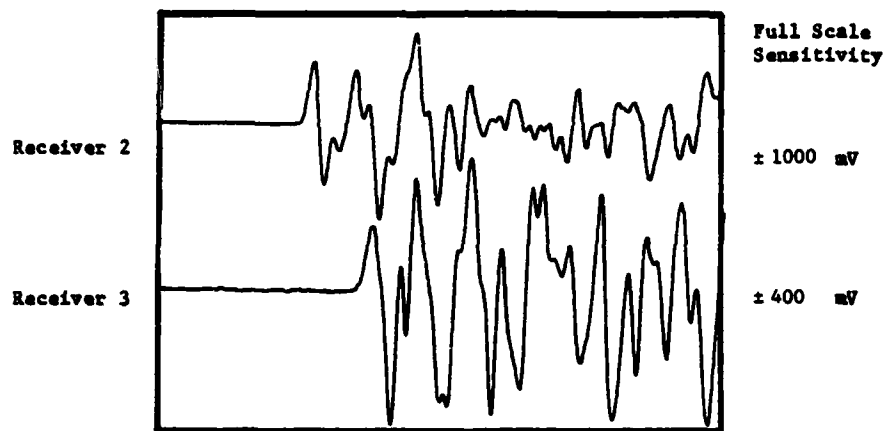
PROPAGATION DIRECTION: East-West

PRESSURE ALONG AXIS: 15 psi

Fig. 6.7 - Typical Set of Accelerometer Traces for the East-West Axis Before Sand Leakage from the East Port



Disk/Track Number: 13-1/7  
Record Length: 10.2 msec



Disk/Track Number: 13-2/7  
Record Length: 10.2 msec

TEST NUMBER: 50

PROPAGATION DIRECTION: East-West

PRESSURE ALONG AXIS: 15 psi

Fig. 6.8 - Typical Set of Accelerometer Traces for the East-West Axis After Sand Leakage from the East Port

each one half the length of the long interval, and therefore, the long interval represents the average of the two short intervals.

Figure 6.9 shows the variation in P-wave velocity measured in the vertical direction over the three intervals. The interval velocity for receiver 1 to 2 consistently falls above the long-interval (receiver 1 to 3) velocity and conversely, the receiver 2 to 3 interval velocity consistently falls below the long-interval velocity. Rather than oversimplify the data by eliminating the short-interval velocities, it was decided to keep all interval data because the short-interval velocities are useful as a measure of inherent scatter in the system. Figure 6.10 shows how the short intervals reflect scatter in the velocities. The results in Fig. 6.10 are for measurements along the vertical axis and show a scatter of about  $\pm 10$  percent. The plot is similar for the two horizontal axes.

### 6.3.2 Statistical Presentation

To present the data in an easily interpretable manner, a simple statistical approach was used. The data was plotted on the standard logarithmic graph of P-wave velocity versus isotropic confining pressure. However, not all data points were shown. Instead, all interval velocities at a given pressure were analyzed to find the mean, standard deviation, and minimum and maximum values. The mean value was then plotted as a circle and a vertical line was drawn from the maximum to minimum values to reflect the total range

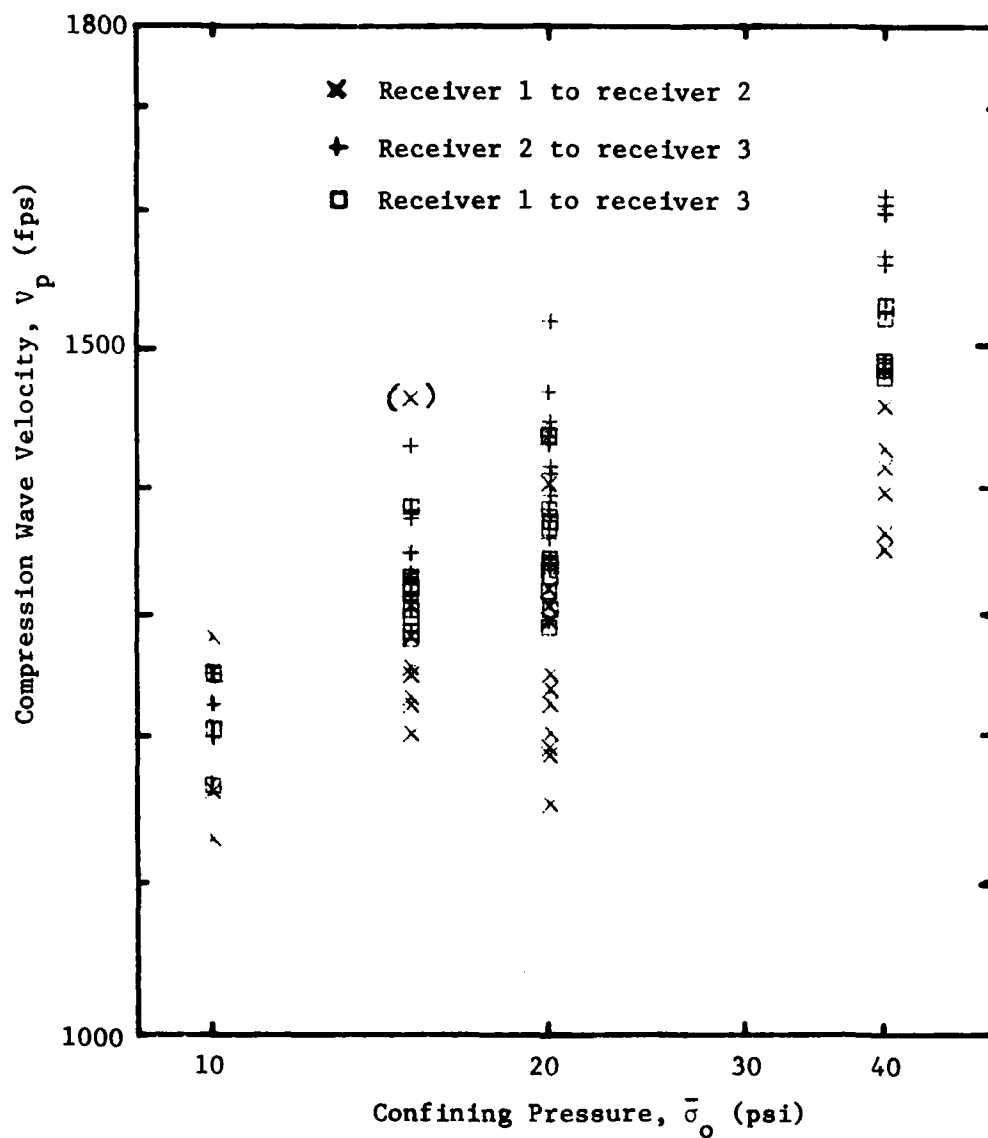


Fig. 6.9 - Comparison of the Variation of Interval Compression Wave Velocity for Long and Short Intervals with Isotropic Confining Pressure

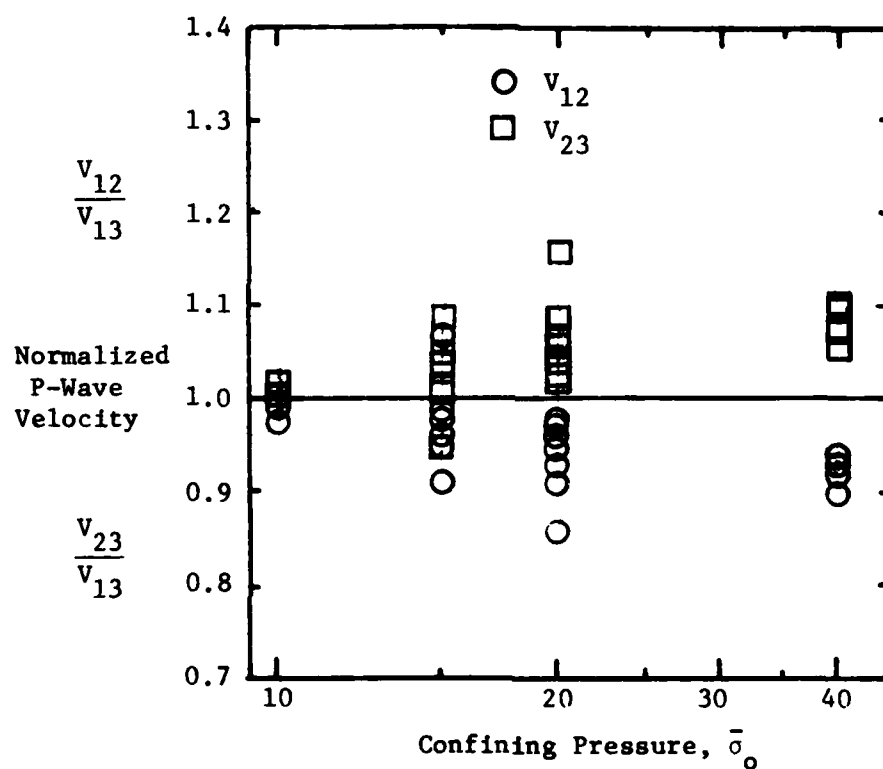


Fig. 6.10 - Compression Wave Velocity for the Short Interval Normalized to the Long-Interval Value along the Vertical Axis versus Isotropic Confining Pressure

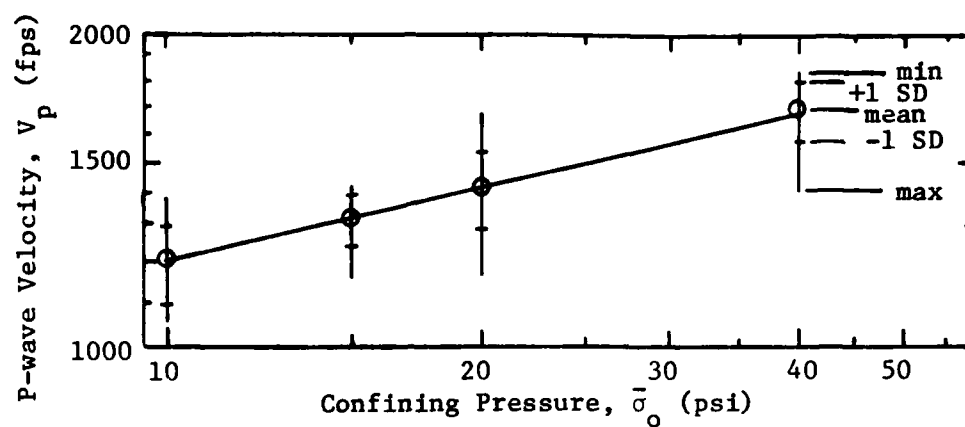


in the data. Horizontal tick marks were made along this vertical line at a distance of one standard deviation above and below the mean to reflect the scatter in the data. To show the trend in the data, a least-squares, best-fit line was fit through the data.

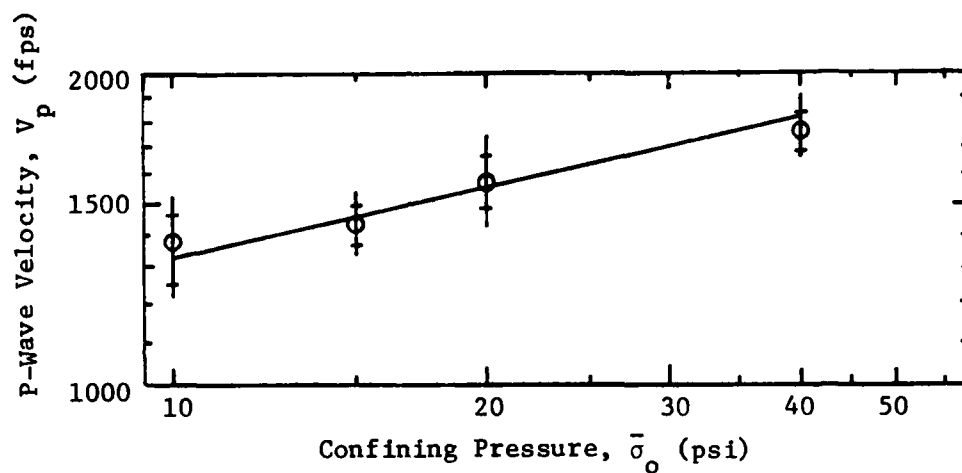
Figure 6.11 shows this final plot for each of the three axes of the cube. The least-squares line is within one standard deviation of the average velocity in all cases but one.

#### 6.4 EFFECT OF STRESS HISTORY

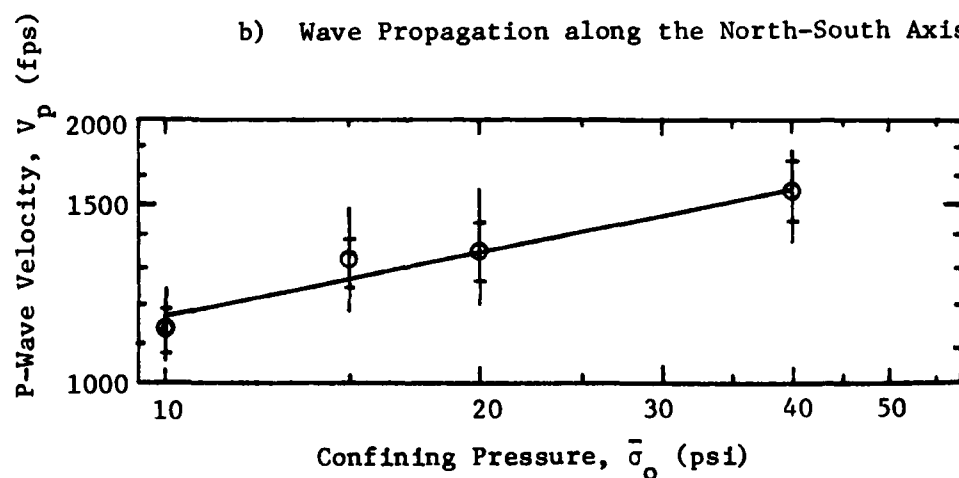
Testing at an isotropic state of stress occurred at various times throughout the complete test series with this sand specimen as shown in Fig. 5.1. Preliminary resonant column tests showed no effect of stress history on the velocity of the shear wave (Appendix A, Section A.4.1). It was believed, therefore, that there would be no effect of stress history on the P-wave velocity either. This belief was confirmed when velocities from repeated isotropic states of stress were compared. Table 6.1 lists the repeated tests and resulting average interval velocities and standard deviations for measurements made with waves propagating in each direction. In all cases, average velocities at each confining pressure are close, well within a standard deviation. It should also be noted that the standard deviations are always less than ten percent of the average velocity and usually are about five percent which can be considered to be small scatter.



a) Wave Propagation along the East-West Axis



b) Wave Propagation along the North-South Axis



c) Wave Propagation along the Vertical Axis

Fig. 6.11 - Variation in Compression Wave Velocity with Isotropic Confining Pressure for Propagation along Each Axis of the Cube

TABLE 6.1

Average Interval Velocities and Standard Deviations  
For Repeated Isotropic States of Stress

Wave Propagation Direction	Isotropic Confining Pressure (psi)	Test Number*	Average Interval Velocity (fps)	Standard Deviation (fps)
(1)	(2)	(3)	(4)	(5)
Vertical	15	24	1348	82
		44	1298	54
		56	1298	49
	20	2	1399	37
		4	1312	82
		4A	1321	79
		13	1355	123
		67	1306	53
	40	3	1510	122
		34	1548	93
North-South	10	1	1288	57
		68	1419	106
	15	24	1427	69
		44	1423	71
		56	1408	47
	20	2	1549	87
		4	1562	99
		4A	1570	89
		13	1551	97
		67	1597	73
	40	3	1795	100
		34	1718	42

\* See Table 5.1.

TABLE 6.1

Average Interval Velocities and Standard Deviations  
For Repeated Isotropic States of Stress

(Continued)

Wave Propagation Direction	Isotropic Confining Pressure (psi)	Test Number*	Average Interval Velocity (fps)	Standard Deviation (fps)
(1)	(2)	(3)	(4)	(5)
East-West	10	1	1231	117
		68	1218	87
	15	24	1349	68
		44	1341	85
		56	1335	97
	20	2	1528	49
		4	1467	61
		4A	1498	52
		13	1435	118
		67	1413	69
	40	3	1670	148
		34	1714	49

\* See Table 5.1.

There is no particular trend in the average velocities. That is, the velocities do not increase or decrease with stages. The randomness of the small variation between tests can best be seen in Fig. 6.12. In this figure, all vertical velocities at 20 psi (137 kPa) have been normalized to the overall, average, interval velocity and plotted against time. The most apparent line through the data is the horizontal line equal to unity. Therefore, there is no effect of stress history on the sample.

#### 6.5 EFFECT OF STRUCTURAL ANISOTROPY

Structural anisotropy is the inherent anisotropy in the stiffness of the soil skeleton which causes a difference in P-wave velocities in different directions under identical loading conditions. Before the effect of isotropic confining pressure on P-wave velocity can be determined, the effect of structural anisotropy must be determined. In the cube, structural anisotropy is induced in the sand while building the sample. Arthur and Menzies (1972) found that sand cannot be rained into a container without causing some anisotropy in the stress-strain behavior between the horizontal and vertical directions. The sand in the cube was rained in layers with the bucket being moved by the crane in the east-west direction while being swung by hand in the north-south direction. The sand fell in a rectangular curtain about 10 in. (254 mm) by 0.25 in. (6.4 mm) as discussed in Section 5.2.1.

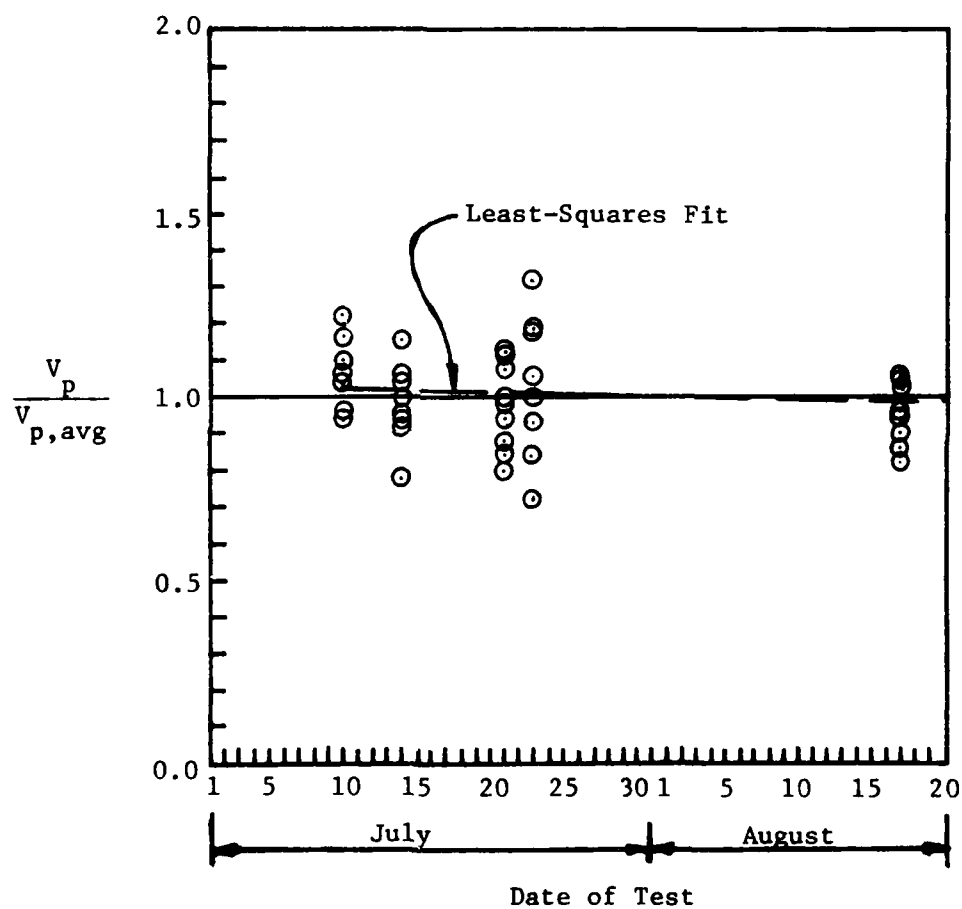


Fig. 6.12 - Variation with Time of Interval Compression  
Wave Velocity along the Vertical Axis at 20 psi  
Normalized to the Average Interval Compression  
Wave Velocity

Therefore, each of the three principal axes of the soil sample may be expected to exhibit slightly different characteristics, or structural anisotropy.

Under each isotropic load, P-wave velocities were measured along all three axes of the cube to observe any variation between the velocities which would then be attributed to structural anisotropy. The resulting logarithmic graphs of P-wave velocity versus confining pressure for each axis are presented in Fig. 6.11 and the method of presentation is discussed in Section 6.3.2. The three curves (lines) are shown together in Fig. 6.13. The three axes of the cube yield  $\log V_p - \log \bar{\sigma}_o$  relationships with similar slopes ( $0.25 \pm 0.03$ ) and differing intercepts.

From Fig. 6.13, it might be said that P-wave velocity in any direction is equal to the overall average plus or minus 8 percent scatter. But, as mentioned in Section 6.4, the scatter along any axis was usually less than 5 percent. Also, the scatter along each axis decreased with increasing pressure, being about 10 percent at 10 psi (69 kPa) and less than 3 percent at 40 psi (276 kPa). The resolution between the horizontal axes is the precision of the pressure gage which was read to an accuracy of 0.1 psi (0.7 kPa). Therefore, the variation in P-wave velocity with axis cannot be explained as simply scatter.

Since a pressure gradient exists in the cube, velocities will increase slightly with depth causing some wave refraction. This

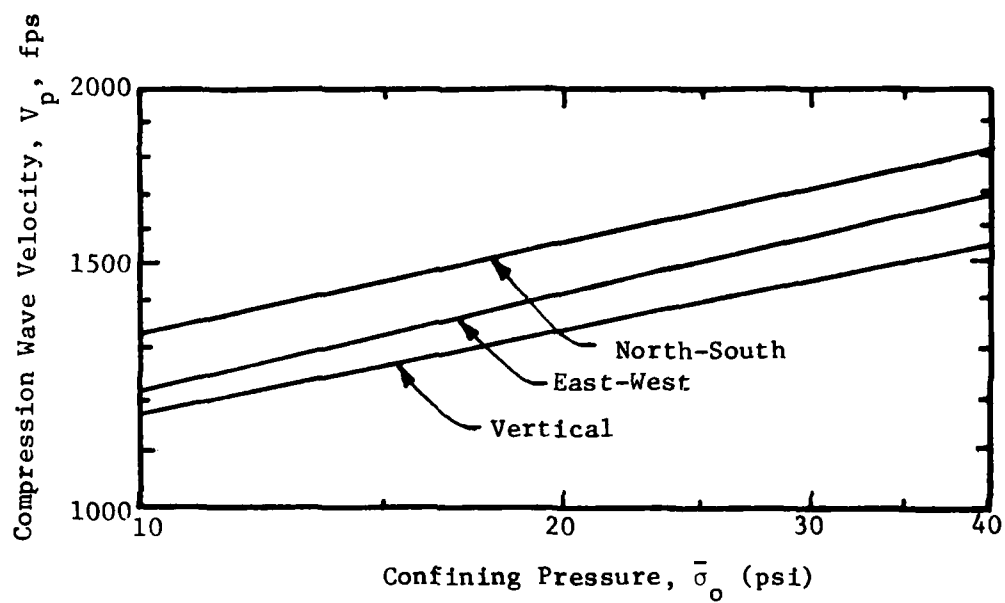


Fig. 6.13 - Variation in Compression Wave Velocity with Isotropic Confining Pressure for the Three Cube Axes



effect would make the horizontal velocities appear higher than the vertical velocity. Although refraction may occur, its effect would be so small that it would not explain the large differences in velocities. Therefore, the cause of the different P-wave velocity along the different axes must be due to structural anisotropy. If the slopes had also varied, then loading stress anisotropy would be a factor because data points would have shifted horizontally along the x-axis (stress) rather than the y-axis (velocity).

Since the evidence only points to structural anisotropy, the velocities in the three directions can be correlated at any pressure. Arbitrarily choosing the vertical axis as the base, the following relationships exist for this sample:

$$V_{P(NS)} = 0.40 V_{P(V)}^{1.15} \quad (6.7)$$

$$V_{P(EW)} = 0.33 V_{P(V)}^{1.20} \quad (6.8)$$

where:  $V_{P(V)}$  is the P-wave velocity in the vertical direction,  
 $V_{P(NS)}$  is the P-wave velocity in the north-south direction,  
 and  
 $V_{P(EW)}$  is the P-wave velocity in the east-west direction.

It must be noted that structural anisotropy is completely sample dependent. The above equations are only valid for the sample of sand used in this test series. A series of isotropic tests with data collected along the three axes should be made on all samples to determine the effect of structural anisotropy on that

sample. Since the effect on the P-wave velocity caused by structural anisotropy is important, it should be determined in all future tests.

#### 6.6 EFFECT OF ISOTROPIC CONFINEMENT

The variation of P-wave velocity with isotropic confining pressure along each axis of the cube is shown in Fig. 6.11. In all three directions, the variation can be represented by a linear relationship on the log-log plot and can, therefore, be expressed in the form used by Hardin and Richart (1963):

$$V_p = C_1 \bar{\sigma}_o^m \quad (6.9)$$

where:  $V_p$  = P-wave velocity, in fps,  
 $\bar{\sigma}_o$  = isotropic confining pressure, in psf,  
 $C_1$  = constant ( $C_1 = V_p$  when  $\bar{\sigma}_o = 1$  psf), and  
 $m$  = slope of the curve.

The slopes of the three curves are between 0.20 and 0.24, which is slightly less than the laboratory results presented by Hardin and Richart (1963). After many tests, they concluded that within the range of 2000 psf to 8000 psf (96 to 383 kPa) the compression wave velocity in sands varied as in Eq. 6.9 with a slope of  $0.25 \pm 10$  percent. For lower pressures, the range was found to be 0.33 to 0.25. The slopes from velocities along the north-south and east-west axes fall within this range, but the

velocities along the vertical axis fall just below the range.

The values should be considered close enough for agreement.

The values of  $m$  and  $C_1$  in Eq. 6.9 vary according to the axis of propagation and must reflect, therefore, the different properties of a soil and can be expressed as:

$$m = F(P_1, P_2, P_3, \dots) \quad (6.10)$$

$$C_1 = F(P_1, P_2, P_3, \dots) \quad (6.11)$$

where  $P_1, P_2, P_3, \dots$  are various soil properties. Since only one soil sample was tested in this research, the only factor that is evident is the effect of structural anisotropy as discussed in Section 6.5. The values of  $m$  and  $C_1$  in each direction are listed in Table 6.2.

Hardin (1978) also developed a dimensionless equation relating pressure to the shear modulus,  $G_{\max}$ :

$$G_{\max} = \frac{A \text{ OCR}^k}{F(e)} P_a^{1-n} \bar{\sigma}_o^n \quad (6.12)$$

where  $A = \text{constant},$

$\text{OCR} = \text{over-consolidation ratio},$

$k = \text{factor related to plasticity},$

$F(e) = \text{function of the void ratio, } e, (F(e) = 0.3 + 0.7e^2),$

$P_a = \text{atmospheric pressure in desired units of } G_{\max},$

$\bar{\sigma}_o = \text{pressure in desired units of } G_{\max}, \text{ and}$

$n = \text{slope of the curve}.$

TABLE 6.2

Constants for Equations 6.9 and 6.14\*

Direction	$C_1$	m	C	n
(1)	(2)	(3)	(4)	(5)
Vertical	271	.20	1136	.40
North-South	250	.23	1529	.46
East-West	210	.24	1255	.48

$$* \quad v_p = C_1 \bar{\sigma}_o^m$$

$$M = 2.00 \, C \, \text{Pa}^{1-n} \bar{\sigma}_o^n$$

Using known relationships between the shear modulus and the constrained modulus,  $M$ , he rewrote the equation for compression data consolidating all new constants into two constants, the Poisson's ratio,  $\nu$ , and  $C$ :

$$M = \frac{(1-\nu)C \text{ OCR}^k}{(1+\nu)(1-2\nu)F(e)} p_a^{1-n} \frac{\sigma}{\sigma_o}^n \quad (6.13)$$

In this testing, sand was used, so the factor  $k$  equals zero and  $\nu$  is about 0.3. The maximum strain was less than 0.01 percent; therefore, the void ratio can be considered constant with a value of 0.73 (Section 5.2.1). The equation then simplifies to:

$$M = 2.00 C p_a^{1-n} \frac{\sigma}{\sigma_o}^n \quad (6.14)$$

Table 6.2 also lists the values of the constant  $C$  and slope  $n$  for the three axes.

## 6.7 SUMMARY AND CONCLUSIONS

The method used to determine the variation in P-wave velocity with isotropic confining pressure has been explained. Direct velocities were not used because of the poorer quality of the data compared to the interval velocities due to the inherent problems associated with direct velocity measurement discussed in Section 6.3.1. The difference in the curves of velocity versus confining pressure can be explained as the result of structural anisotropy induced in the raining process. The effects are not extremely large, but none-the-less important.

It has been shown that the P-wave velocity varies linearly with the isotropic confining pressure on a log-log plot with a slope close to 0.25. Therefore Eq. 6.9 can be written relating the two with the slope,  $n$ , and one constant,  $C_1$ , related to soil properties. The dimensionless equation by Hardin (1978), Eq. 6.13, may also be used to relate the pressure to the constrained modulus. For this sample, the equation again reduces to only two constants relating the pressure to the modulus. These equations and the resulting constants are presented in Table 6.2. With the relationship between P-wave velocity and isotropic confinement known, the effect of biaxial confinement may now be studied.

## CHAPTER SEVEN

### BIAXIAL CONFINEMENT

#### 7.1 INTRODUCTION

After studying the effect of the isotropic state of stress on P-wave velocity, the next step was to study the effect of the biaxial state of stress on  $V_p$ . To obtain biaxial loading, confining pressures were applied such that the major principal stress,  $\bar{\sigma}_1$ , was acting along one axis of the cube while the minor principal stress,  $\bar{\sigma}_3$ , was acting along the other two axes. For the majority of these tests, the major principal stress was oriented along the vertical axis of the cube. However, a final series of tests was performed with  $\bar{\sigma}_1$  oriented along the north-south axis of the cube to study any effect of structural anisotropy.

Two series of biaxial tests were performed. In the first series, either the major or minor principal stress was varied while the other principal stress was kept constant. Testing in this manner was performed to observe the effect of each stress component on P-wave velocity. This test series is referred to as biaxial confinement with a variable mean effective principal stress. The mean effective principal stress,  $\bar{\sigma}_o$ , is defined as:

$$\bar{\sigma}_o = 1/3 (\bar{\sigma}_1 + 2\bar{\sigma}_3) \quad (7.1)$$

In the second test series, both principal stresses were varied simultaneously in such a manner that  $\bar{\sigma}_0$  was kept constant. This test series is referred to as biaxial confinement with a constant mean effective principal stress.

Throughout both test series, compression wave velocities were measured along each axis of the cube at the various biaxial states of stress. The lateral pressure coefficient,  $K_{13}$ , defined as:

$$K_{13} = \frac{\bar{\sigma}_1}{\bar{\sigma}_3} \quad (7.2)$$

varied from 1.0 to 3.00 as listed in Table 5.1.

The method of data analysis and presentation of the biaxial tests is the same as that presented in Chapter 6 for the isotropic tests. A typical set of biaxial records is presented in Appendix D. The variation in  $V_p$  for biaxial confinement with a variable mean effective principal stress is presented first because it more easily shows the effect of biaxial loading. The effects of structural anisotropy and stress history are also incorporated into this section. The effect on  $V_p$  of biaxial confinement with a constant mean effective principal stress is then presented in the Section 7.3. The effect of triaxial confinement on  $V_p$  is discussed in Chapter 8.

## 7.2 TESTING WITH A VARIABLE MEAN EFFECTIVE PRINCIPAL STRESS

The biaxial testing series with a variable mean effective principal stress began with the soil sample under an isotropic



loading of 15 psi (103 kPa). The vertical stress,  $\bar{\sigma}_1$ , was then increased in 5-psi (34 kPa) increments to 40 psi (276 kPa) while  $\bar{\sigma}_3$  was held constant. The two horizontal stresses ( $\bar{\sigma}_3$ ) were then increased in 5-psi (34 kPa) increments until an isotropic loading of 40 psi (276 kPa) was reached. Table 5.1 shows these tests as numbers 24 through 29 and 39 through 44, and the load history can be seen in Fig. 5.1 during the time of August 6 through August 11, 1981.

The entire biaxial series was then reversed to evaluate any effect of stress history as discussed in Section 7.2.4. These tests are listed in Table 5.1 as numbers 29 through 39, and the load history can be seen in Fig. 5.1 during the time of August 6 through August 10, 1981.

Tests to evaluate the effect of structural anisotropy on P-wave velocity under biaxial confinement were performed by using the north-south axis to replace the vertical axis of the cube as the major stress axis. Table 5.1 lists these tests as numbers 56 through 61, and the load history can be seen in Fig. 5.1 during the time of August 17 and August 18, 1981. This testing is discussed in Section 7.2.5.

#### 7.2.1 Notation for Stresses

For consistency in the complete research project, the notation used to define the orientation of principal stresses relative to wave motion in the presentation is the same as that

adopted by Knox (1981) in the investigation involving shear waves. Principal stresses are defined in terms of wave propagation and particle motion as follows:

- $\bar{\sigma}_a$  = effective principal stress in the direction of wave propagation,
- $\bar{\sigma}_b$  = effective principal stress in the direction of particle motion, and
- $\bar{\sigma}_c$  = effective principal stress (or stresses) in the direction perpendicular to the  $\bar{\sigma}_a$  and  $\bar{\sigma}_b$  direction (or directions).

These symbols are based on S-waves for which each of the three symbols represent different axes. However, for P-waves, the direction of wave propagation is also the direction of particle motion. Hence,  $\bar{\sigma}_a$  equals  $\bar{\sigma}_b$ , and  $\bar{\sigma}_c$  represents the principal stress in two directions. Therefore a second subscript was added to  $\bar{\sigma}_c$  to denote the principal stress component along each  $\bar{\sigma}_c$  axis, i.e.  $\bar{\sigma}_{c1}$  or  $\bar{\sigma}_{c3}$ . For example, with  $\bar{\sigma}_1 = 40$  psi (276 kPa) and  $\bar{\sigma}_3 = 15$  psi (103 kPa), P-wave testing was performed along all three axes of the cube and was denoted as follows:

1. for testing along the major principal axis (vertical orientation)
 
$$\bar{\sigma}_{a1} = \bar{\sigma}_{b1} = 40 \text{ psi}, \bar{\sigma}_{c3} = 15 \text{ psi}, \text{ and } \bar{\sigma}_{c3} = 15 \text{ psi},$$
2. for testing along one of the minor principal axes (north-south orientation)

$$\bar{\sigma}_{a3} = \bar{\sigma}_{b3} = 15 \text{ psi}, \bar{\sigma}_{c1} = 40 \text{ psi}, \text{ and } \bar{\sigma}_{c3} = 15 \text{ psi}, \text{ and}$$

3. for testing along the other minor principal axis (east-west orientation)

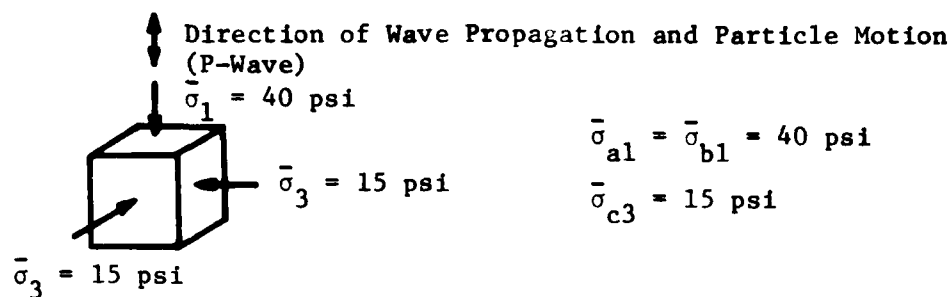
$$\bar{\sigma}_{a3} = \bar{\sigma}_{b3} = 15 \text{ psi}, \bar{\sigma}_{c1} = 40 \text{ psi}, \bar{\sigma}_{c3} = 15 \text{ psi}.$$

This notation is illustrated in Fig. 7.1.

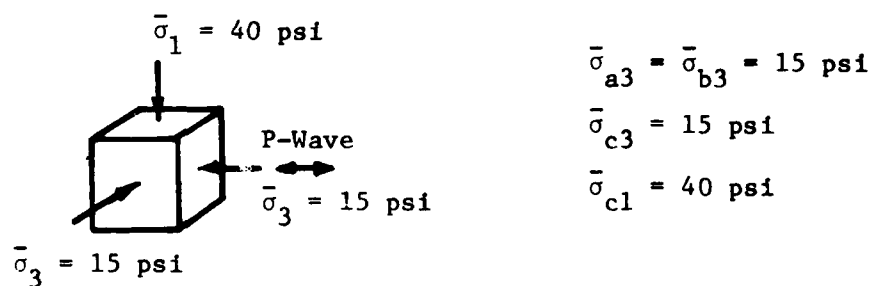
### 7.2.2 Effect of Principal Stress in Direction of Wave Propagation

The variation of P-wave velocity with variation in principal stress in the direction of wave propagation is shown in Figs. 7.2, 7.3, and 7.4. Figure 7.2a shows the variation in P-wave velocity upon increasing  $\bar{\sigma}_1$  ( $\bar{\sigma}_{a1}$ ) while  $\bar{\sigma}_3$  was held constant, whereas, Figs. 7.3a and 7.4a show the variation in P-wave velocity upon increasing  $\bar{\sigma}_3$  ( $\bar{\sigma}_{a3}$ ) while  $\bar{\sigma}_1$  was held constant. Also shown in each figure (Figs. 7.2b, 7.3b, and 7.4b) is the  $\log V_p - \log \bar{\sigma}_a$  relationship for the corresponding unloading sequence. A least-squares straight line was fit to the data in each figure and is shown by a solid line in the figures. The lines show that the  $\log V_p - \log \bar{\sigma}_a$  relationship can be approximated by a linear relationship with a slope between 0.20 and 0.25.

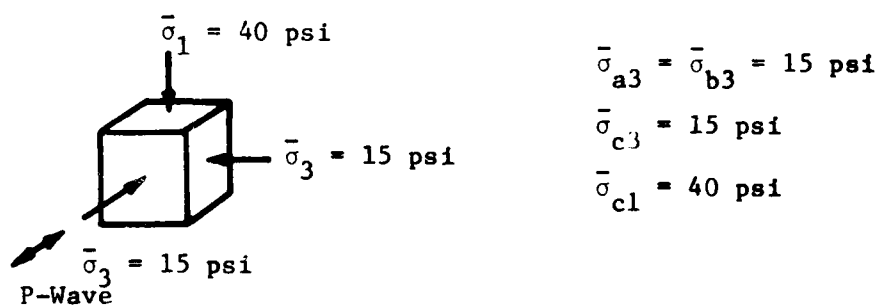
The variation in P-wave velocity with isotropic confining pressure is also shown in Figs. 7.2, 7.3, and 7.4 by the dashed lines. In these figures, the isotropic confining pressure,  $\bar{\sigma}_o$ , was set equal to  $\bar{\sigma}_a$  to determine the corresponding velocities along the correct axis of wave propagation (as found in Chapter 6) to try to account for any structural anisotropy (discussed in Section 7.2.5). In all cases, the variation in  $V_p$  with  $\bar{\sigma}_a$  shown



a) Vertical Axis

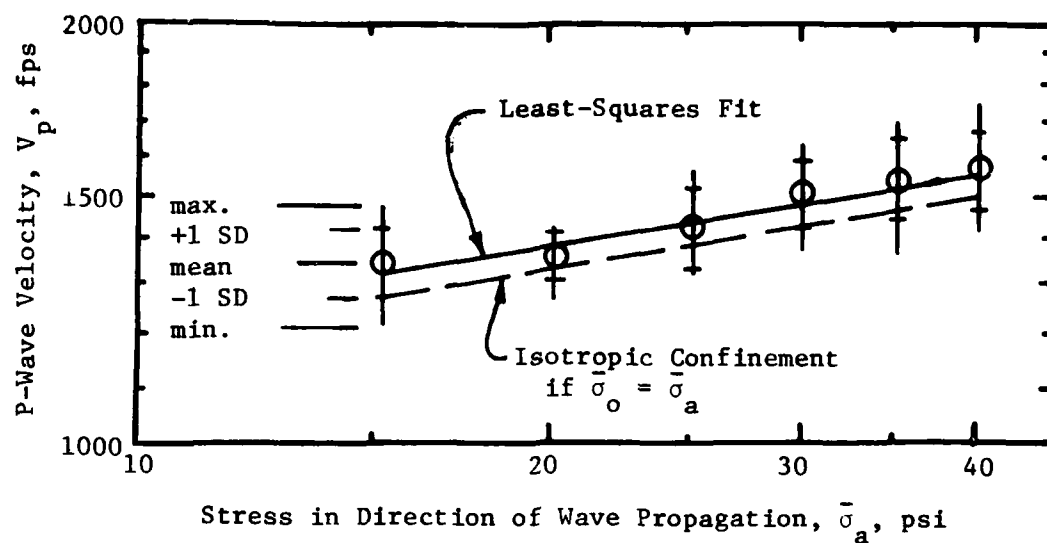


b) East-West Axis

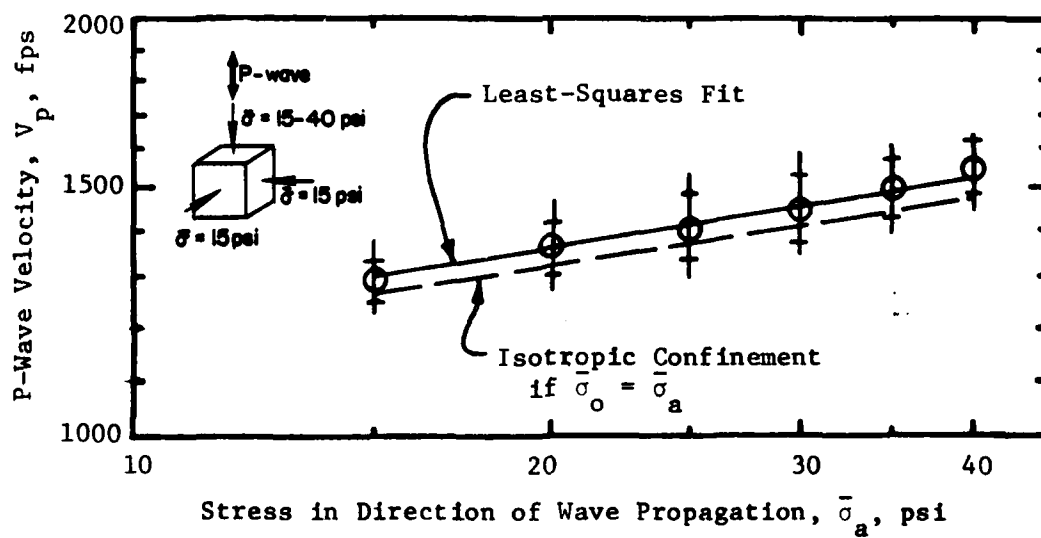


c) North-South Axis

Fig. 7.1 - Illustration of Notation Used to Describe State of Stress Relative to Wave Motions

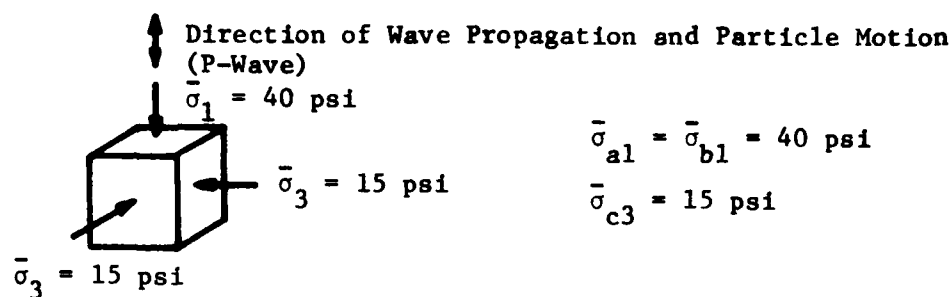


a) Loading

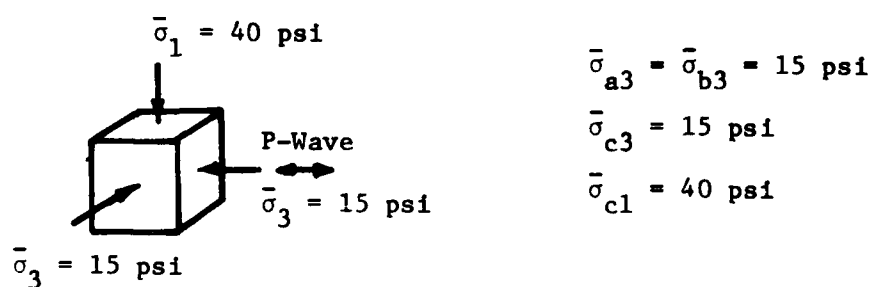


b) Unloading

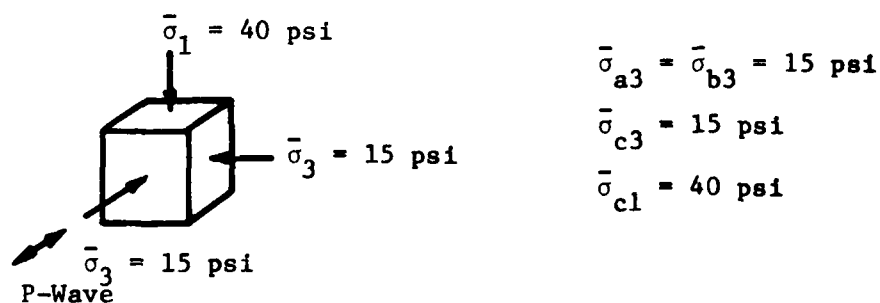
Fig. 7.2 - Effect of Major Principal Stress in Direction of Wave Propagation on Compression Wave Velocity for Biaxial Confinement



a) Vertical Axis

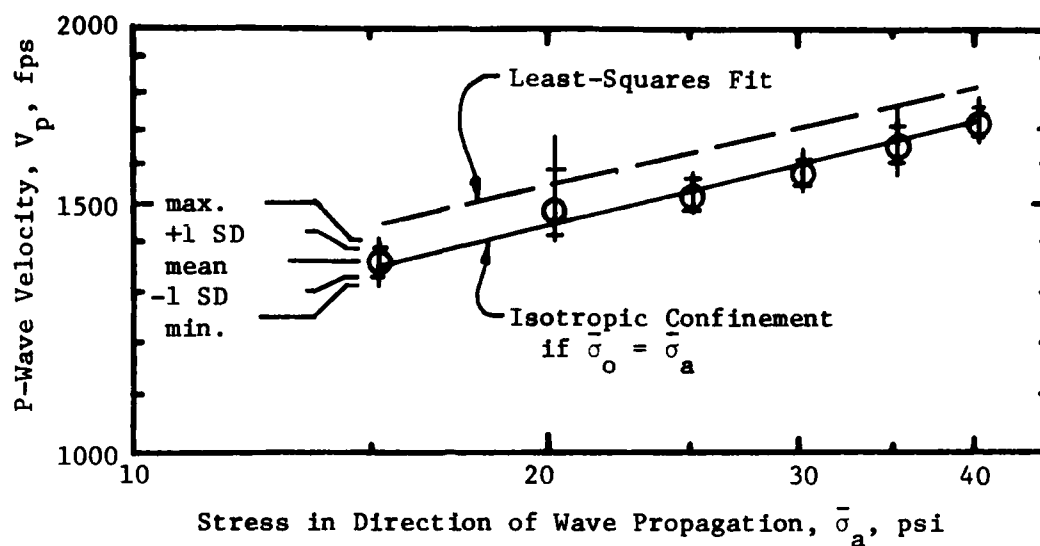


b) East-West Axis

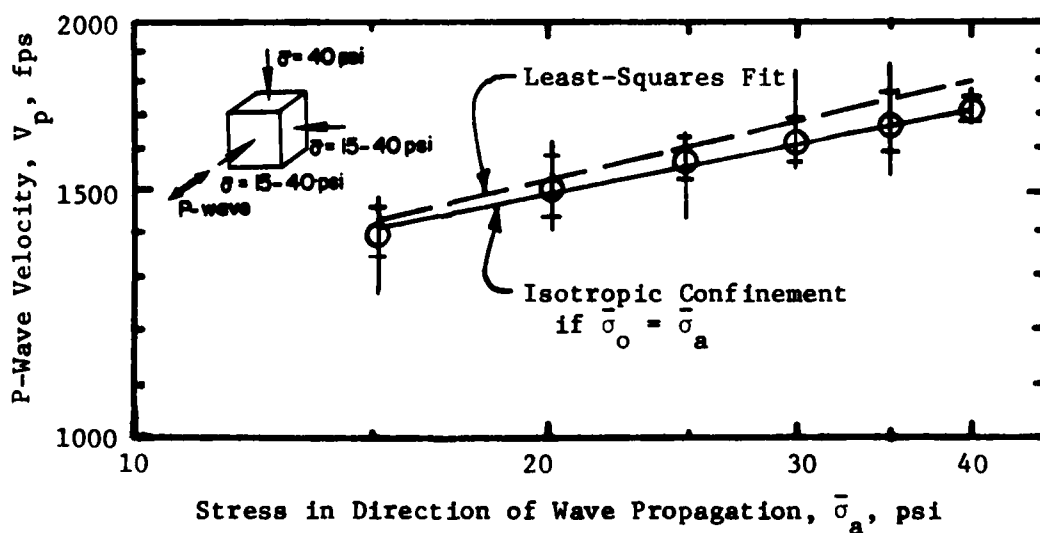


c) North-South Axis

Fig. 7.1 - Illustration of Notation Used to Describe  
State of Stress Relative to Wave Motions

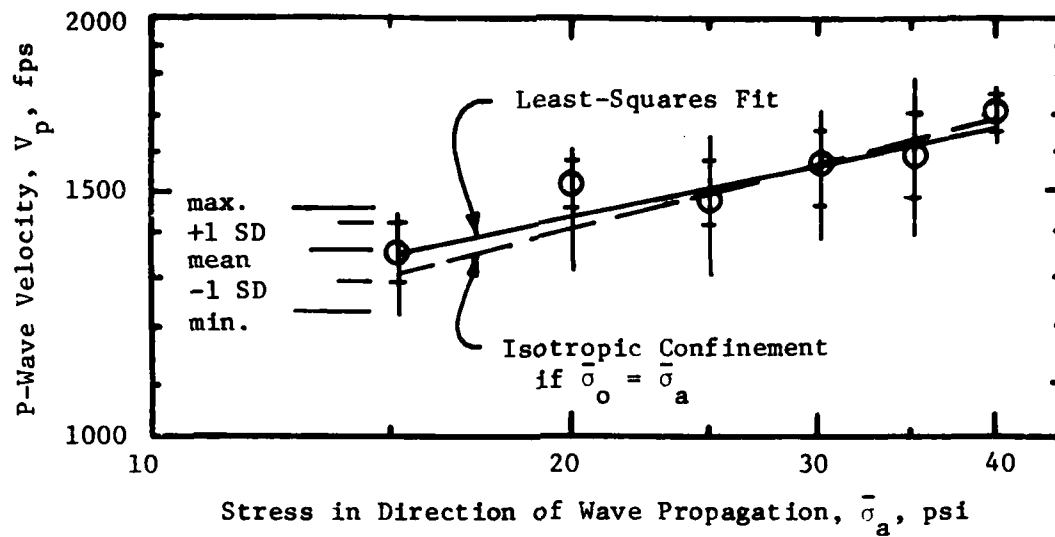


a) Loading

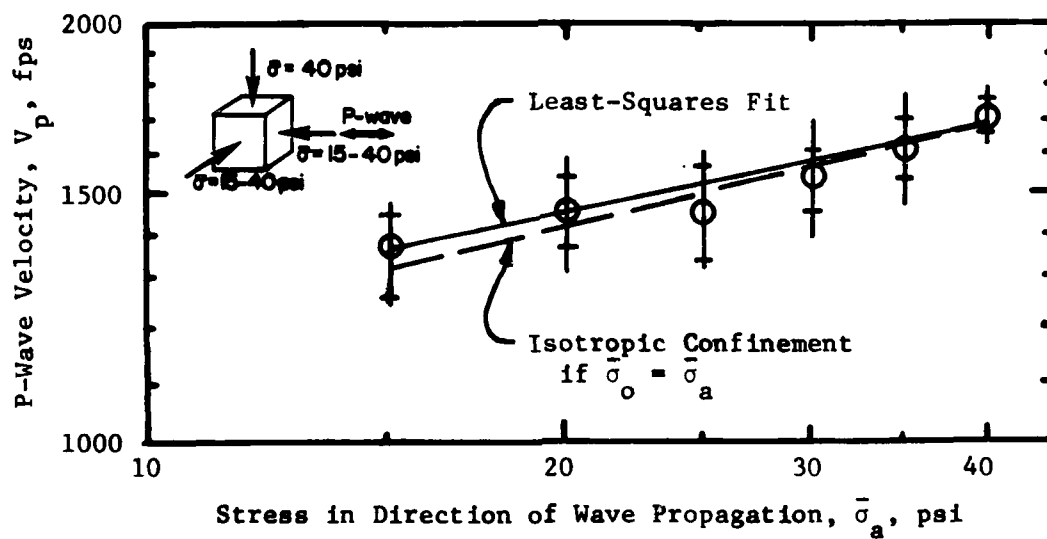


b) Unloading

Fig. 7.3 - Effect of Minor Principal Stress in Direction of Wave Propagation on Compression Wave Velocity for Biaxial Confinement



a) Loading



b) Unloading

Fig. 7.4 - Effect of Minor Principal Stress in Direction of Wave Propagation on Compression Wave Velocity for Biaxial Confinement



by the solid line is almost the same as that predicted by the isotropic relationship if  $\bar{\sigma}_a$  is substituted for  $\bar{\sigma}_o$ .

To permit study of the variation in  $V_p$  with  $\bar{\sigma}_a$ , equations were patterned after those from Chapter 6 defining the isotropic relationship between  $V_p$  and  $\bar{\sigma}_o$ , with  $\bar{\sigma}_a$  used in place of  $\bar{\sigma}_o$ . It is then possible to compare the constants  $C_1$  and  $C$ , and slopes  $m$  and  $n$  from the isotropic equations in Chapter 6 to those from the biaxial equations defined below:

$$V_p = C_1 \bar{\sigma}_a^m \quad (7.3)$$

and

$$M = 2.00 C Pa^{1-n} \bar{\sigma}_a^n \quad (7.4)$$

where:  $V_p$  = P-wave velocity in fps,  
 $\bar{\sigma}_a$  = effective pressure in direction of wave propagation,  
 in psi for Eq. 7.3, and in the same units as  $M$  for  
 Eq. 7.4,

$M$  = constrained modulus in desired units, and

$Pa$  = atmospheric pressure in same units as  $M$ .

Table 7.1 lists the values of  $C_1$ ,  $C$ ,  $m$ , and  $n$  for Eqs. 7.3 and 7.4 (shown by the solid lines in Figs. 7.2, 7.3 and 7.4) together with the corresponding values for isotropic confinement (Eqs. 6.9 and 6.14) for the same axis of propagation. The smallest difference between the isotropic and biaxial relationships occurs in the vertical direction when  $\bar{\sigma}_1$  was varied. The resulting slopes

TABLE 7.1

Comparison of Constants and Slopes for Equations Relating  
 $V_p$  or  $M$  to  $\bar{\sigma}_o$  for Isotropic Confinement\* and to  $\bar{\sigma}_a$  for Biaxial Confinement\*\*

Axis of Propagation	Biaxial Confinement			Isotropic Confinement			Percent Change					
	C <sub>1</sub>	m	C	n	C <sub>1</sub>	m	C	n	C <sub>1</sub>	m	C	n
(1)	(2)	(3)	(4)	(5)	(6)	(7)	(8)	(9)	(10)	(11)	(12)	(13)
Vertical +	281	0.20	1221	0.40	271	0.20	1136	0.40	3.7	0.0	1.3	0.0
Vertical -	276	0.20	1156	0.40	271	0.20	1136	0.40	1.9	0.0	1.7	0.0
North-South +	218	0.24	1354	0.48	250	0.23	1529	0.46	12.8	4.3	11.5	4.3
North-South -	253	0.22	1344	0.44	250	0.23	1529	0.46	1.2	4.3	13.8	4.3
East-West +	293	0.20	1329	0.40	210	0.24	1255	0.48	28.4	16.7	5.8	16.7
East-West -	274	0.21	1353	0.42	210	0.24	1255	0.48	23.4	12.5	7.8	12.5

+ = loading

- = unloading

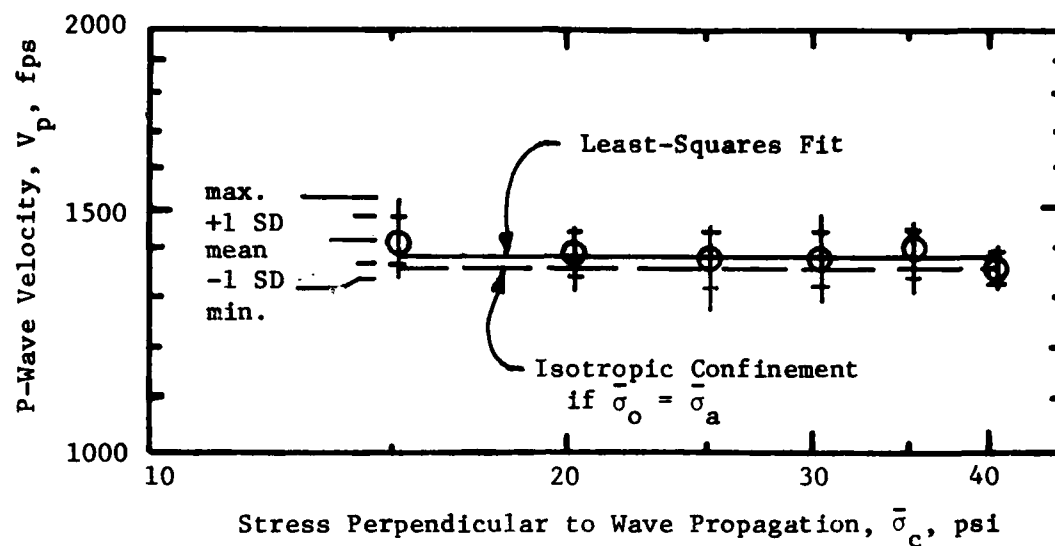
$$* V_p = C_1 \bar{\sigma}_o^m \quad (6.9) \quad M = 2.00 C Pa^{1-n} \bar{\sigma}_o^n \quad (6.14)$$

$$** V_p = C_1 \bar{\sigma}_a^m \quad (7.3) \quad M = 2.00 C Pa^{1-n} \bar{\sigma}_a^n \quad (7.4)$$

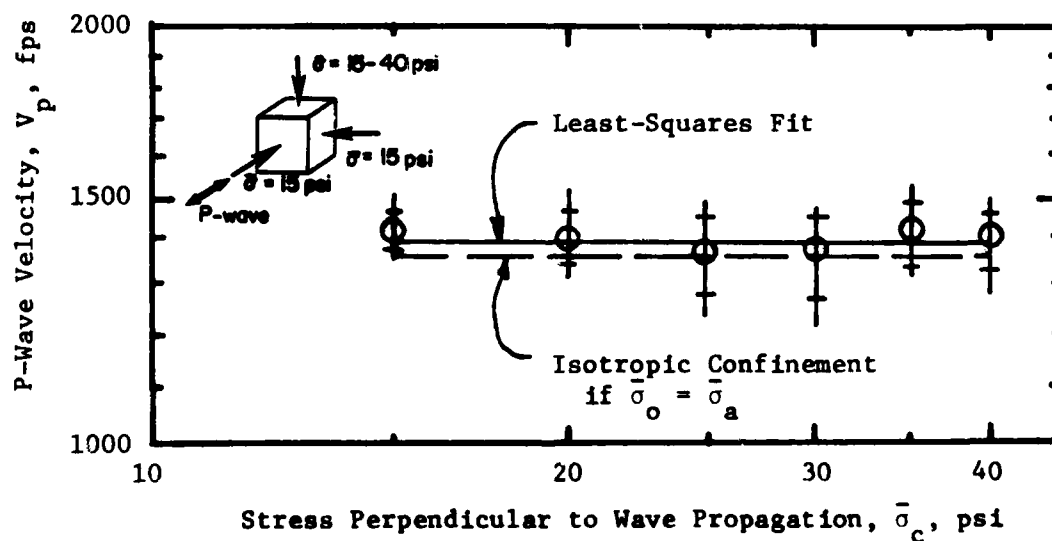
(m and n) are identical and the constants ( $C_1$  and C) vary by less than four percent. When  $\bar{\sigma}_3$  was varied along the north-south and east-west axes, slightly larger differences were found for the slopes and constants between the isotropic and biaxial relationships. The slopes varied from 4.3 to 16.7 percent, although the maximum change in slope was only 0.08. The variation in constants ranged from 1.2 to 28.4 percent; however, most differences were less than fifteen percent. It is apparent from the relatively small percent differences between the values for isotropic confinement and biaxial confinement with varying mean effective principal stress that the stress along the direction of propagation controls the behavior of the P-wave velocity for a body wave, independent of whether that is the major or minor principal stress axis.

### 7.2.3 Effect of Principal Stresses in Direction Perpendicular to Wave Propagation

If Eqs. 7.3 and 7.4 are correct, then stresses perpendicular to the direction of wave propagation should not affect P-wave velocity measured under biaxial loading. The variation of  $V_p$  with  $\bar{\sigma}_c$  is shown by the solid lines in Figs. 7.5, 7.6, and 7.7. These lines are essentially horizontal, with all slopes less than 0.03 and an average for all tests of -0.01. These flat slopes mean that the P-wave velocity can be considered constant and independent of  $\bar{\sigma}_c$ .

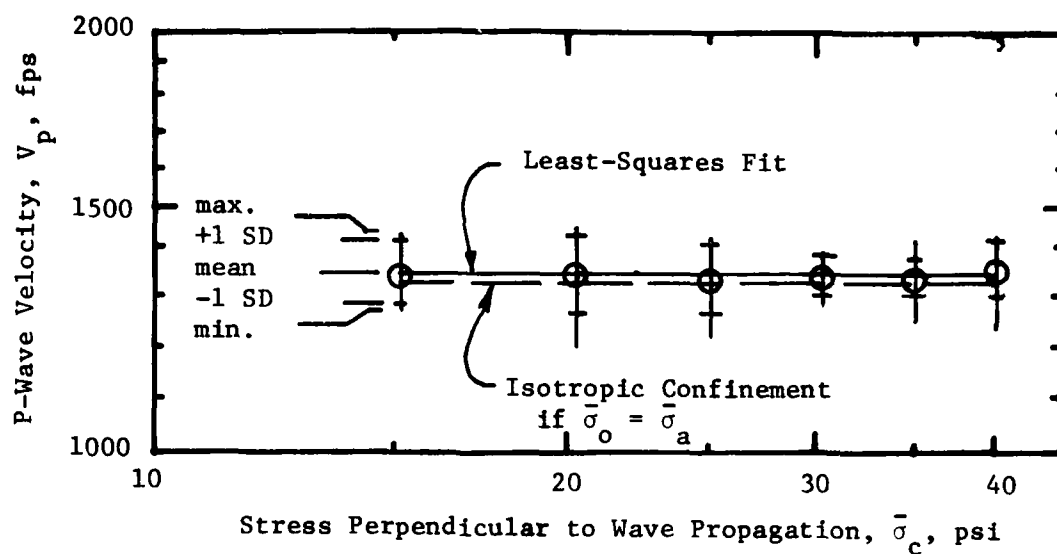


a) Loading

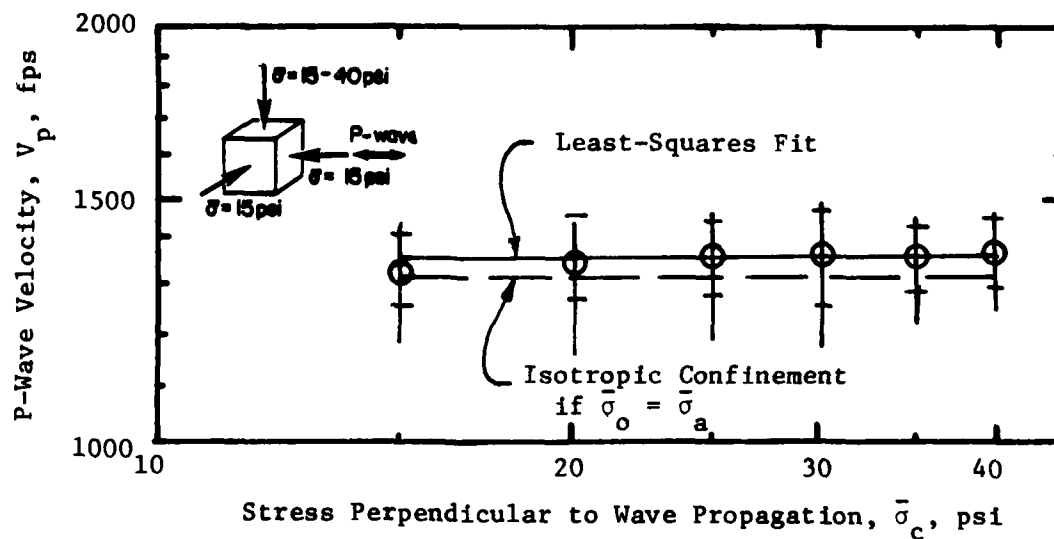


b) Unloading

Fig. 7.5 - Effect of Major Principal Stress Perpendicular to Wave Propagation on Compression Wave Velocity for Biaxial Confinement

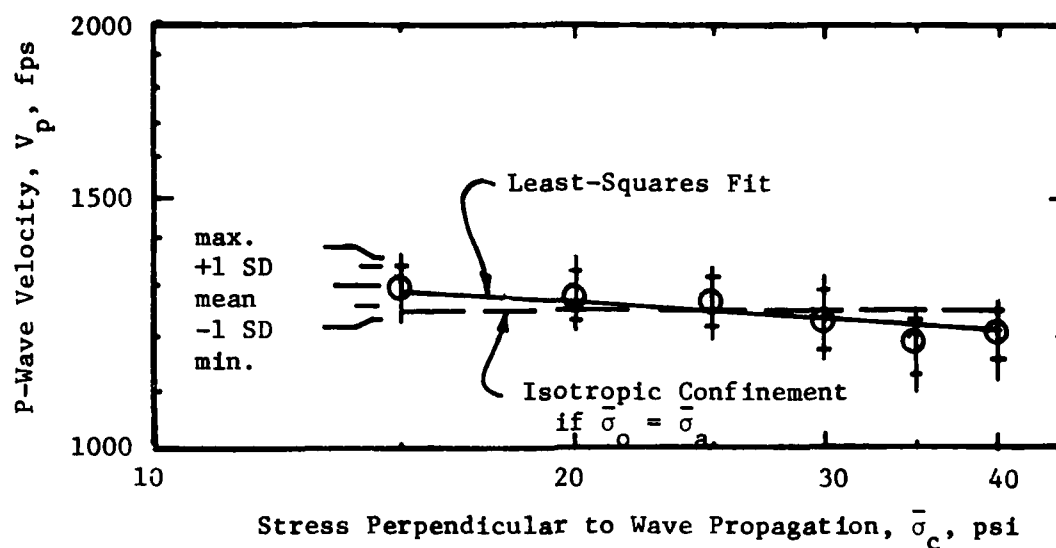


a) Loading

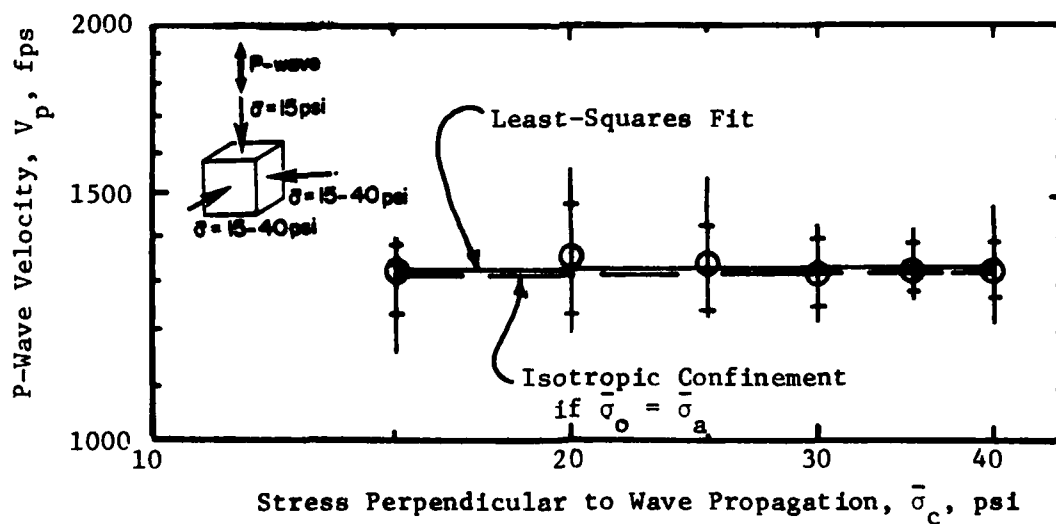


b) Unloading

Fig. 7.6 - Effect of Major Principal Stress Perpendicular to Wave Propagation on Compression Wave Velocity for Biaxial Confinement



a) Loading



b) Unloading

Fig. 7.7 - Effect of Minor Principal Stress Perpendicular to Wave Propagation on Compression Wave Velocity for Biaxial Confinement

For comparison with isotropic confinement, dashed lines were drawn in Figs. 7.5 through 7.7 which correspond to the P-wave velocity calculated for the particular axis of propagation if  $\bar{\sigma}_0$  is set equal to  $\bar{\sigma}_a$  in the relationship derived for isotropic confinement in Chapter 6. The velocity based on isotropic confinement is constant since  $\bar{\sigma}_a$  was constant for these tests.

Table 7.2 shows a comparison of velocities computed for biaxial confinement with those computed for isotropic confinement. The percent difference between velocities for biaxial and isotropic confinement ranges from 0.4 to 3.4 percent, and averages less than two percent. These very small differences between velocities for the different confinement states means that the P-wave velocity is not affected by a variation in principal stress perpendicular to the direction of wave propagation, i.e.  $\bar{\sigma}_{c1}$  or  $\bar{\sigma}_{c3}$ .

#### 7.2.4 Effect of Stress History

Biaxial tests with the vertical axis as the major principal axis were repeated in an unloading sequence to study the effect of stress history. The unloading sequence is presented in Figs. 7.2b through 7.7b. The constants reflecting the variation in P-wave velocity with pressure for the solid lines shown in these figures are presented in Table 7.1 and 7.2. Of interest here are those pairs of tests which compare loading and unloading sequences along the same axis over the same pressure range. The least-squares lines from Figs. 7.2 through 7.7 are summarized for ease in

TABLE 7.2

Comparison of  $V_p$  for Isotropic and Biaxial Confinement  
States When  $\bar{\sigma}_a$  was Constant and  $\bar{\sigma}_c$  Varied

Axis of Propagation	Biaxial Confinement			Calculated Isotropic $V_p^{**}$ (fps)	Percent Change $\frac{(5)-(4)}{(4)} \times 100\%$ (%)
	$\bar{\sigma}_a$ (psi)	Slope	Mean $V_p$ (fps)		
(1)	(2)	(3)	(4)	(5)	(6)
Vertical +	40	-0.006	1585	1531	3.4
Vertical -	40	-0.03	1580	1531	3.1
North-South +	15	-0.03	1441	1462	1.4
North-South -	15	-0.01	1428	1462	2.3
East-West +	15	0.01	1339	1326	1.0
East-West -	15	0.03	1331	1326	0.4

+ = loading

- = unloading

\* In each case  $\bar{\sigma}_c$  ranges from 15 to 40 psi.

$$** V_p = C_1 \bar{\sigma}_o^m$$



comparison in Fig. 7.8. The constants are also repeated in Table 7.3 for easy comparison. The differences between pairs of test results in the table ranges from zero to 13.8 percent, with all but three comparisons under five percent. Therefore, there is no noticeable effect of stress history in the biaxial test series.

#### 7.2.5 Effect of Structural Anisotropy

To observe the effect of structural anisotropy, P-wave velocities were determined with the north-south axis of the cube as the major principal axis. In this sequence, only  $\bar{\sigma}_1$  was increased, and there was no unloading. The resulting variations in P-wave velocity with confining pressure are shown in Fig. 7.9 following the same procedure that was used to present the data in Sections 7.2.2 and 7.2.3 when  $\bar{\sigma}_1$  was along the vertical axis. Dashed lines are also included in the figure to show the variation in  $V_p$  calculated from Eq. 6.9 (for isotropic confinement) by setting  $\bar{\sigma}_0$  equal to  $\bar{\sigma}_a$ . The constants and slopes ( $C_1$ ,  $C$ ,  $m$ , and  $n$ ) of Eqs. 6.9, 6.14, 7.3, and 7.4 or constant velocities for these tests are presented in Table 7.4.

The relationship between P-wave velocity and stress for the wave propagating along the major principal axis for this orientation of  $\bar{\sigma}_1$  is the same as for the orientation with  $\bar{\sigma}_1$  along the vertical axis. Similarly, the relationship between  $V_p$  and  $\bar{\sigma}_c$  for this orientation of  $\bar{\sigma}_1$  is the same as for the orientation with  $\bar{\sigma}_1$  along the vertical axis. Therefore, structural anisotropy has

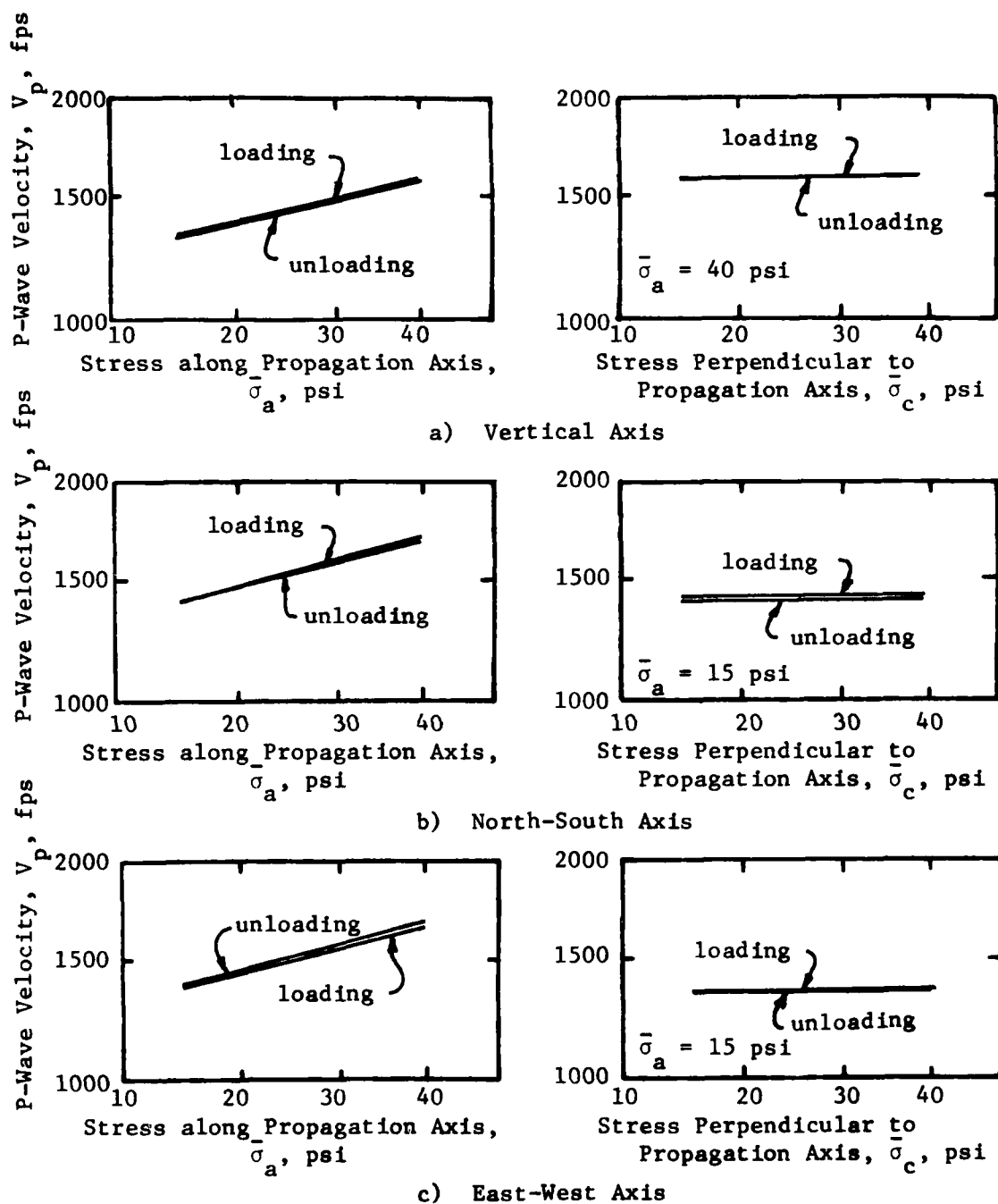


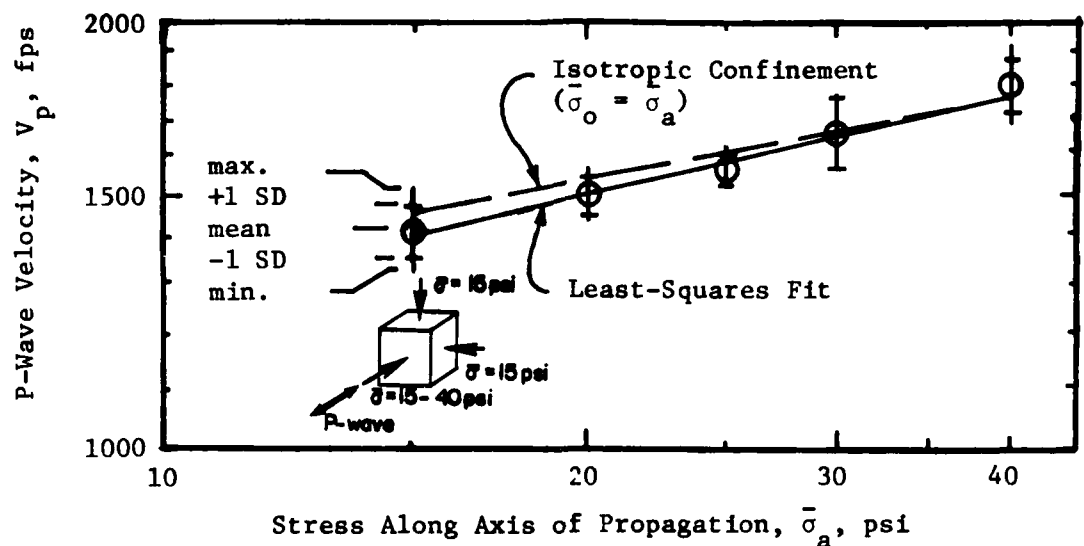
Fig. 7.8 - Summary of Effect of Stress History on P-Wave Velocity

TABLE 7.3

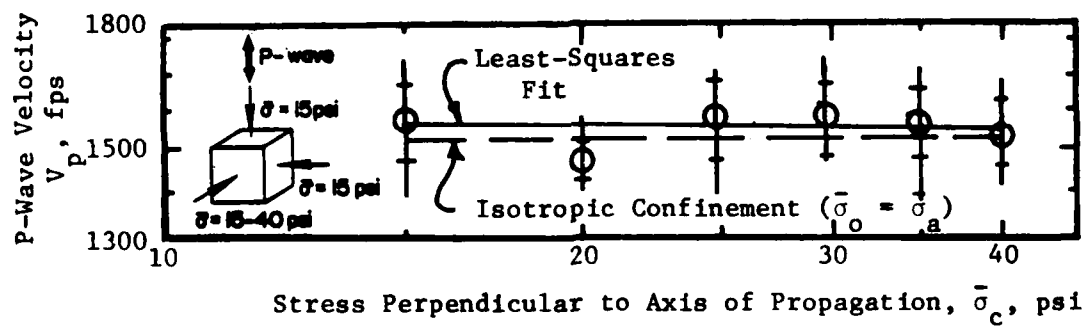
Comparison of Constants of Eq. 7.3\* or  
Mean P-wave Velocity During Loading and Unloading  
Sequences in Biaxial Confinement

Axis of Propagation		$C_1$	$m$	Mean $V_p$	Percent Change		
					$m$	$C_1$	$V_p$
(1)		(2)	(3)	(4)	(5)	(6)	(7)
Vertical	loading	287	.20	-	0.0	1.8	-
	unloading	276	.20	-			
North-South	loading	218	.24	-	8.3	13.8	-
	unloading	253	.22	-			
East-West	loading	293	.20	-	4.7	6.5	-
	unloading	274	.21	-			
Vertical	loading	-	-	1585	-	-	0.3
	unloading	-	-	1580			
North-South	loading	-	-	1441	-	-	0.9
	unloading	-	-	1428			
East-West	loading	-	-	1339	-	-	0.6
	unloading	-	-	1331			

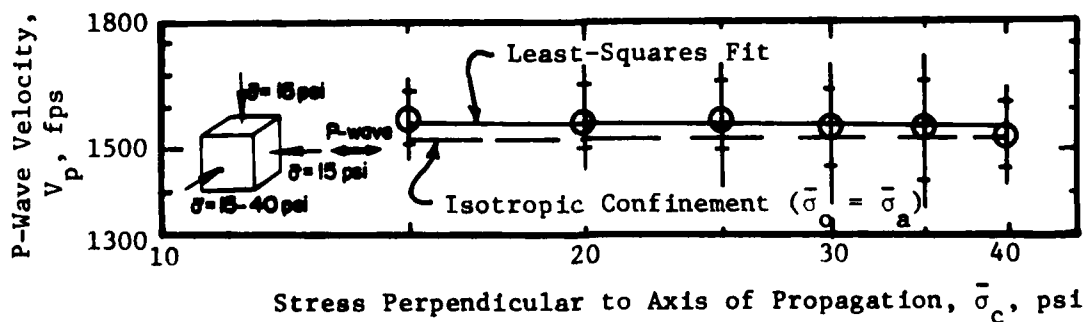
$$* V_p = C_1 \bar{\sigma}_a^m$$



a) North-South Axis



b) Vertical Axis



c) East-West Axis

Fig. 7.9 - Effect of Structural Anisotropy on Compression Wave Velocity for Biaxial Confinement

TABLE 7.4  
Comparison of Constants for Equations\* or Mean  $V_p$  for  
Isotropic and Biaxial Confinement with  $\sigma_1$  along the North-South Axis

Axis of Propagation	Biaxial Confinement					Isotropic Confinement					Percent Difference
	Constants				Mean V <sub>p</sub> (fps)	Constants				Mean V <sub>p</sub> (fps)	
	C <sub>1</sub>	m	C	n		C <sub>1</sub>	m	C	n		
(1)	(2)	(3)	(4)	(5)	(6)	(7)	(8)	(9)	(10)	(11)	(12)
North-South	225	-	-	-	-	250	-	-	-	-	10.0
	-	0.24	-	-	-	-	0.23	-	-	-	4.3
	-	-	1354	-	-	-	-	1529	-	-	11.5
	-	-	-	0.48	-	-	-	-	0.46	-	4.3
Vertical	-	-	-	-	1257	-	-	-	-	1259	0.1
East-West	-	-	-	-	1338	-	-	-	-	1326	0.9

$$* V_p = C_1 \bar{\sigma}_a^m \quad (7.3)$$

$$M = 2.00 C Pa^{1-n} \bar{\sigma}_a^n \quad (7.4)$$

no effect on the relationship between P-wave velocity and confining pressure. Rather, structural anisotropy affects only the constants in Eqs. 7.3 and 7.4, with the differences less than eleven percent.

#### 7.2.6 Effect of Lateral Pressure Coefficient on P-wave Velocity

The variation of  $V_p$  with the variation in the lateral pressure coefficient,  $K$ , is shown in Figs. 7.10 and 7.11. This type presentation is simply another way of presenting the results shown earlier except that it indirectly shows the effect of shearing stress on  $V_p$  because as  $K$  varies from unity, shear stress in the sample increases.

The lateral pressure coefficient,  $K$ , can be defined in two ways: either as  $K_{13}$  using Eq. 6.2 or as  $K_{ac}$  as follows:

$$K_{ac} = \frac{\bar{\sigma}_a}{\bar{\sigma}_c} \quad (7.5)$$

where  $\bar{\sigma}_a$  = stress in direction of wave propagation, and  
 $\bar{\sigma}_c$  = stress perpendicular to wave propagation.

The first definition,  $K_{13}$ , is the more classical soil mechanics definition of the earth pressure coefficient (although usually it would be written as  $K_{31}$  or simply  $K$  and equated to  $\bar{\sigma}_3$  divided by  $\bar{\sigma}_1$ ). The variation in  $V_p$  with  $K_{13}$  is presented in Fig. 7.10. To permit values of  $K$  less than one to indicate that the direction of wave propagation was not in the direction of the major principal stress, the second definition,  $K_{ac}$ , was chosen, and these results are presented in Fig. 7.11.

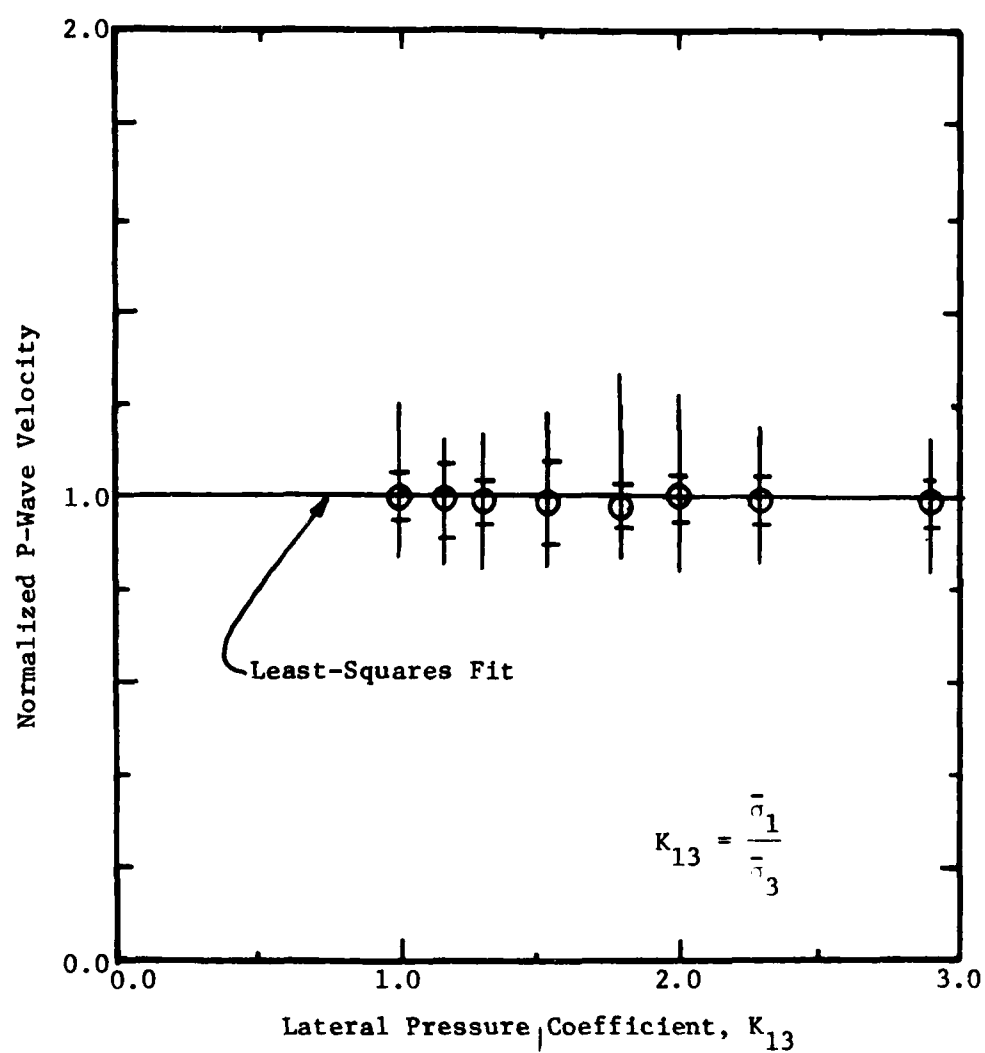


Fig. 7.10 - Variation in Normalized P-Wave Velocity with Lateral Pressure Coefficient,  $K_{13}$ , for Biaxial Loading

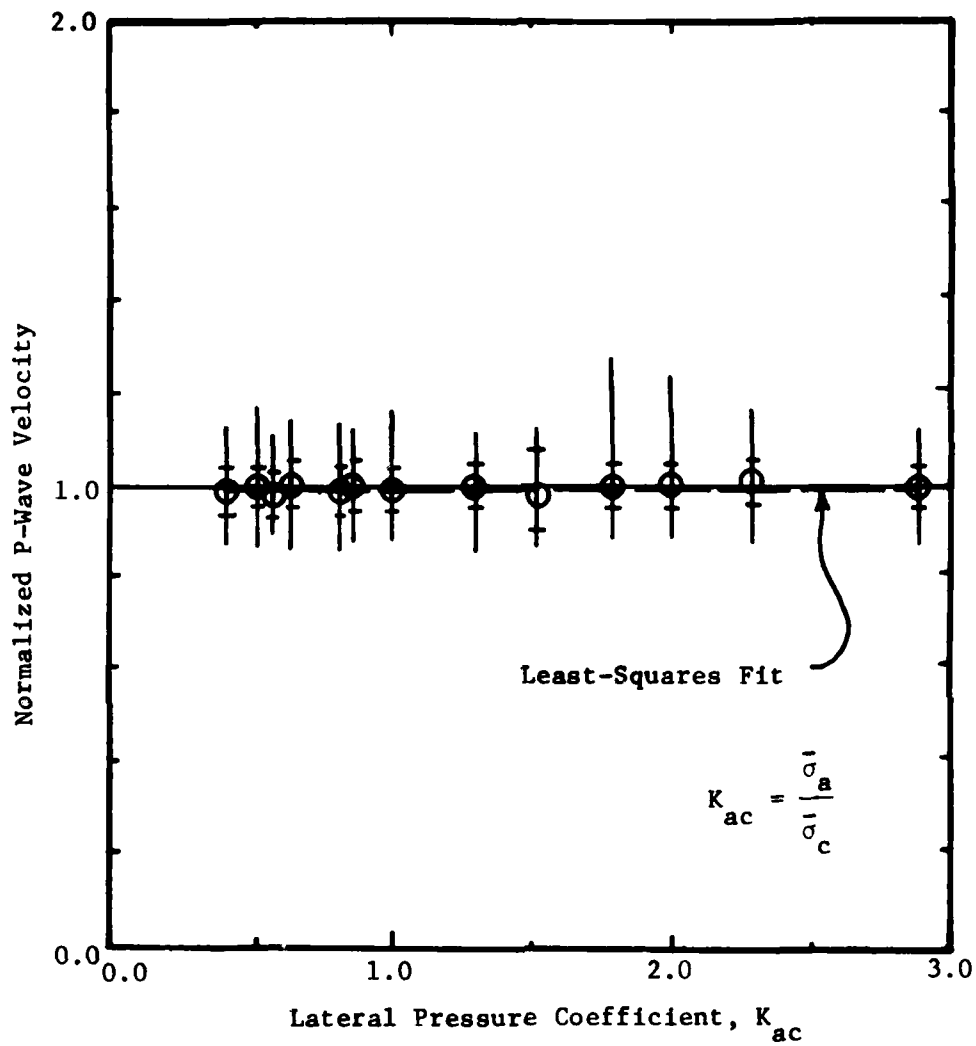


Fig. 7.11 - Variation in Normalized P-Wave Velocity with Lateral Pressure Coefficient,  $K_{ac}$ , for Biaxial Loading



The ordinate of both Figs. 7.10 and 7.11 is the normalized P-wave velocity. Normalized values of  $V_p$  were computed by taking the values of  $V_p$  determined for biaxial confinement and dividing them by the P-wave velocities determined from the isotropic relationship setting  $\bar{\sigma}_o$  equal to  $\bar{\sigma}_a$  along the proper axis of wave propagation. By normalizing  $V_p$ , any effect of structural anisotropy is eliminated, and all data may be plotted together. Since the equations of P-wave velocity discussed in Sections 7.2.2 and 7.2.3 are so close to the corresponding isotropic equations along the axes in question, it appears that the effect of structural anisotropy under biaxial loading is the same as under isotropic loading.

The data presented in Figs. 7.10 and 7.11 are evenly banded about unity. A value of one for the normalized velocity means that the P-wave velocity under biaxial confinement is the same as  $V_p$  determined for isotropic confinement, if  $\bar{\sigma}_a$  is substituted for  $\bar{\sigma}_o$ . Therefore, the same conclusion as in Sections 7.2.2 and 7.2.3 is reached: P-wave velocity for a body wave under isotropic or biaxial loading depends solely on the stress in the direction of wave propagation.

### 7.3 TESTING WITH A CONSTANT MEAN EFFECTIVE PRINCIPAL STRESS

Hardin and Black (1966) stated that the shear modulus, and therefore S-wave velocity, was constant along lines of constant mean effective principal stress. To determine if this relationship could be extended to P-waves (which the profession has simply

assumed to be true), a series of biaxial tests was run with a constant value of  $\bar{\sigma}_0$ . The value of  $\bar{\sigma}_0$  chosen was 20 psi (138 kPa) since it was about the mid-value of the range of confining pressures possible in the cube. Therefore, a reasonable range in  $\bar{\sigma}_1$  values was possible without exceeding the limit of the cube and reasonable range in  $\bar{\sigma}_3$  values was possible without resulting in a shear failure of the sample.

This test series began with an isotropic state of stress at 20 psi (138 kPa). The vertical stress ( $\bar{\sigma}_1$ ) was then increased in 2-psi (14 kPa) increments while the horizontal stresses ( $\bar{\sigma}_3$ ) were each reduced in 1-psi (7 kPa) increments, thus keeping  $\bar{\sigma}_0$  constant. This was continued until the value of the lateral pressure coefficient,  $K_{13}$ , reached 2.29. The sequence was reversed using larger stress increments this time until isotropic confinement with 20 psi (138 kPa) was again achieved. In addition, at several times during the triaxial testing series presented in Chapter 8, a biaxial state of stress with  $\bar{\sigma}_0 = 20$  psi (138 kPa) was achieved, and this data was included in this analysis. The complete biaxial testing series included tests 4A through 13, 15, 20 and 27 from Table 5.1 which can be seen on Fig. 5.1 between the dates of July 7, 1981, and August 6, 1981.

Figure 7.12 shows, for each principal stress axis, the variation in P-wave velocity with pressure along that axis. A least-squares straight line fit to the data is shown along each axis as a solid line. Dashed lines are also included in Fig. 7.12

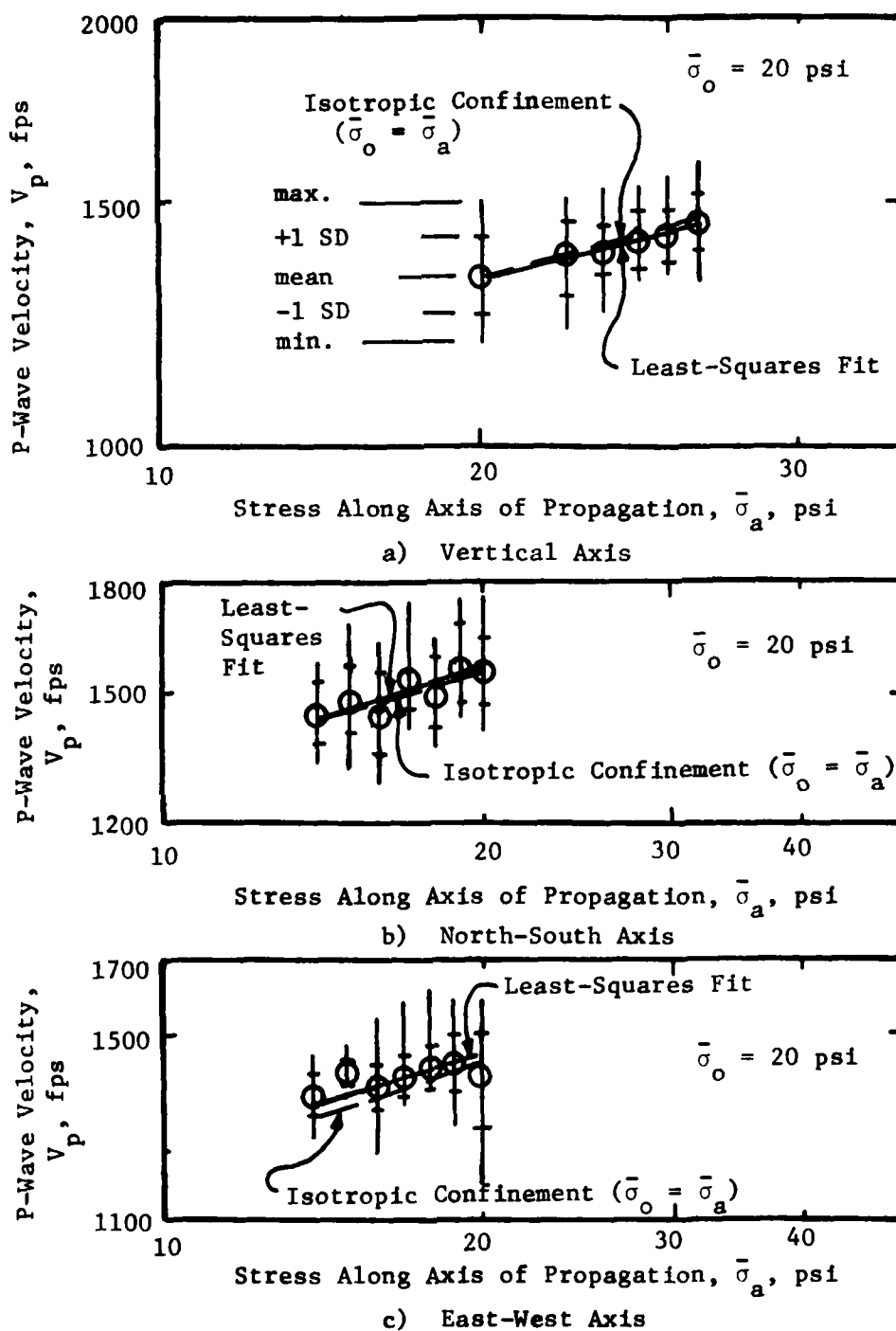


Fig. 7.12 - Effect of Principal Stress in Direction of Wave Propagation on Compression Wave Velocity for Biaxial Confinement with Constant Mean Effective Principal Stress

showing the variation in P-wave velocity based on isotropic confinement as determined by Eq. 6.9 if  $\bar{\sigma}_o$  is set equal to  $\bar{\sigma}_a$ . In all cases, the least squares solid line for biaxial confinement is almost identical to the relationship based on isotropic confinement with  $\bar{\sigma}_o$  equal to  $\bar{\sigma}_a$ .

From the preceeding figures, it is apparent that the P-wave velocity is not constant under constant  $\bar{\sigma}_o$ . Also, since the biaxial P-wave velocity in these tests is the same as the isotropic velocity at the stress in the direction of propagation, it again follows that the P-wave velocity for a body wave under biaxial loading depends solely on the stress in the direction of propagation.

As another method of presentation, all data is presented together in the normalized form explained in Section 7.2.6 in Fig. 7.13. Again, the data is evenly banded about unity. This time the scatter is less with only a few points outside a  $\pm 10$  percent range.

#### 7.4 SUMMARY AND CONCLUSIONS

Two series of tests were performed in which  $V_p$  was measured under biaxial confinement. The first series employed a varying mean effective principal stress, but only  $\bar{\sigma}_1$  or  $\bar{\sigma}_3$  (not both) were varied at one time. In the second series, both  $\bar{\sigma}_1$  and  $\bar{\sigma}_3$  were varied together in such a way as to maintain a constant mean effective principal stress of 20 psi (138 kPa). All data for this sand over the stress range in these tests lead to the

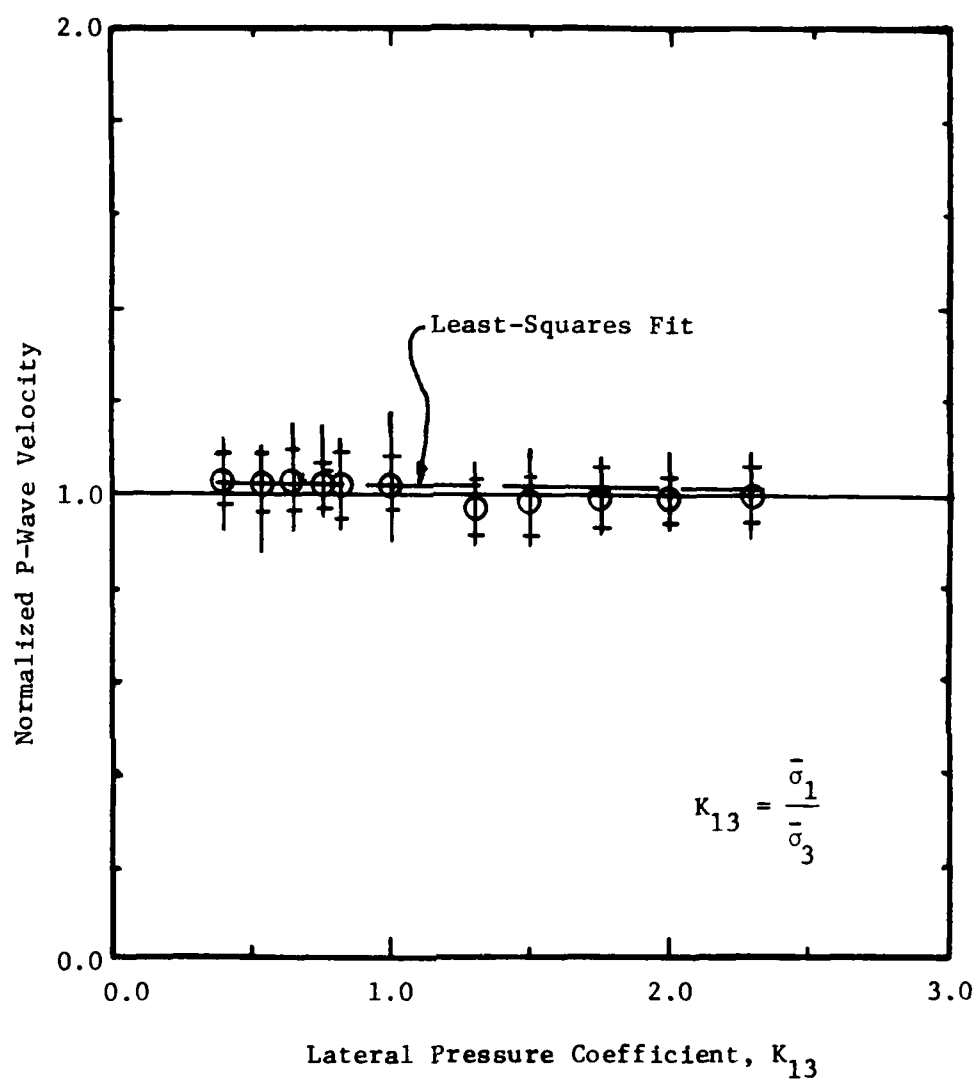


Fig. 7.13 - Variation in Normalized P-Wave Velocity with Lateral Pressure Coefficient,  $K_{13}$ , for Biaxial Loading with Constant  $\bar{\sigma}_0$

conclusion that for biaxial confinement the velocity of compression waves propagating as body waves varies solely with the stress along the axis of wave propagation according to Eq. 7.3.

The values of the constant,  $C_1$ , and slope,  $m$ , in Eq. 7.3 for biaxial confinement are the same as those in Eq. 6.9 for isotropic confinement. However, the values of  $C_1$  and  $m$  vary with the axis of propagation because of structural anisotropy as in the case of isotropic confinement.

## CHAPTER EIGHT

### TRIAXIAL CONFINEMENT

#### 8.1 INTRODUCTION

After studying the effect of the isotropic and biaxial states of stress on P-wave velocity, the final step in this initial study was to investigate the effect of the triaxial state of stress on  $V_p$ . To obtain triaxial loading, confining pressures were applied such that the major principal stress,  $\bar{\sigma}_1$ , was applied along one axis of the cube, the intermediate principal stress,  $\bar{\sigma}_2$ , along another axis, and the minor principal stress,  $\bar{\sigma}_3$ , along the third axis. For the majority of these tests, the major principal stress was oriented along the vertical axis and the minor principal stress was oriented along the east-west axis of the cube. However, a final series of tests was run with  $\bar{\sigma}_1$  oriented along the north-south axis of the cube to study any effect of structural anisotropy.

As in the biaxial test series, two series of triaxial tests were performed. In the first series, the intermediate principal stress,  $\bar{\sigma}_2$ , was varied while the major and minor principal stresses,  $\bar{\sigma}_1$  and  $\bar{\sigma}_3$ , were kept constant at 40 psi (276 kPa) and 15 psi (103 kPa), respectively. The object was to observe the effect of  $\bar{\sigma}_2$  on P-wave velocity. This test series is referred to as triaxial confinement with a variable mean effective principal

stress. In the second test series, all three principal stresses were varied simultaneously in such a manner that the mean effective principal stress was kept constant. This test series is referred to as triaxial confinement with a constant mean effective principal stress.

Throughout both test series the compression wave velocities were measured along each axis of the cube at the various triaxial states of stress. For triaxial loading, two forms of the lateral pressure coefficient are required to describe the state of stress. The first,  $K_{13}$ , relates the minor principal stress,  $\bar{\sigma}_3$ , to the major principal stress,  $\bar{\sigma}_1$  (also used to describe biaxial loading in Chapter 7) as:

$$K_{13} = \frac{\bar{\sigma}_1}{\bar{\sigma}_3} \quad (8.1)$$

The second,  $K_{23}$ , relates the intermediate principal stress,  $\bar{\sigma}_2$ , to the minor principal stress:

$$K_{23} = \frac{\bar{\sigma}_2}{\bar{\sigma}_3} \quad (8.2)$$

The coefficient  $K_{13}$  varied from 1.00 to 3.00 and was constant at 2.67 for triaxial confinement with a variable mean effective principal stress, as listed in Table 5.1. The coefficient  $K_{23}$  varied from 1.00 to 2.67 as also shown in Table 5.1.

The method of data analysis and presentation for the triaxial confinement tests is the same as that presented in



Chapter 6 for the isotropic confinement tests. Typical travel time records can be seen in Appendix E. The variation in  $V_p$  for triaxial confinement with a variable effective mean principal stress is presented first because it most easily shows the effect of triaxial loading on  $V_p$ . The effect of structural anisotropy and stress history is also incorporated into this section. The effect on  $V_p$  of triaxial loading with a constant mean effective principal stress is then presented in Section 8.3.

## 8.2 TESTING WITH A VARIABLE MEAN EFFECTIVE PRINCIPAL STRESS

The triaxial testing series with a variable mean effective principal stress began with the soil sample under a biaxial loading condition with  $\bar{\sigma}_1$  equal to 40 psi (276 kPa) along the vertical axis and  $\bar{\sigma}_3$  equal to 15 psi (103 kPa) along the two horizontal axes. This relationship between  $\bar{\sigma}_1$  and  $\bar{\sigma}_3$  ( $K_{13} = 2.67$ ) did not vary during testing. The north-south stress was chosen to be the intermediate principal stress,  $\bar{\sigma}_2$ , and was increased in 5-psi (34 kPa) increments to 40 psi (276 kPa) while the other stresses were kept constant. Table 5.1 shows these tests as numbers 45 through 50, and the load history can be seen in Fig. 5.1 during the time of August 11 through August 14, 1981. The entire series was then reversed to evaluate any effect of stress history as discussed in Section 8.2.3. Table 5.1 shows these tests as numbers 50 through 55, and the load history can be seen in Fig. 5.1 during the time of August 14 through August 17, 1981.

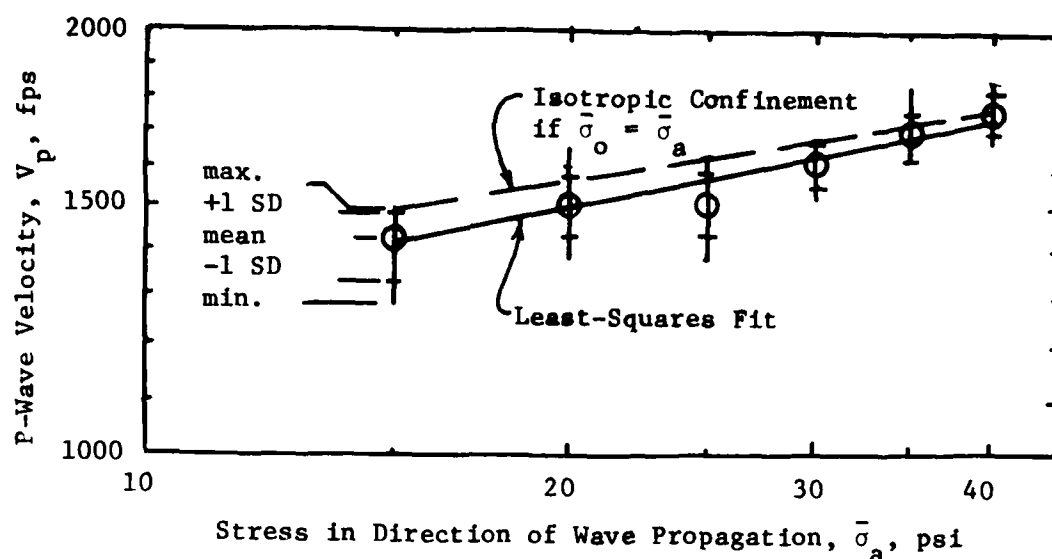
The tests to evaluate the effect of structural anisotropy on P-wave velocity under triaxial confinement were performed by using the north-south axis to replace the vertical axis of the cube as the major principal stress axis and then using the vertical axis as the intermediate principal stress axis. Table 5.1 lists these tests as numbers 61 through 66, and the load history can be seen in Fig. 5.1 during the time of August 18 and August 19, 1981. Results from this testing are presented and discussed in Section 8.2.4.

The stress notation used for presentation of the triaxial tests is the same as that used for the biaxial confinement tests as described in Section 7.2.1.

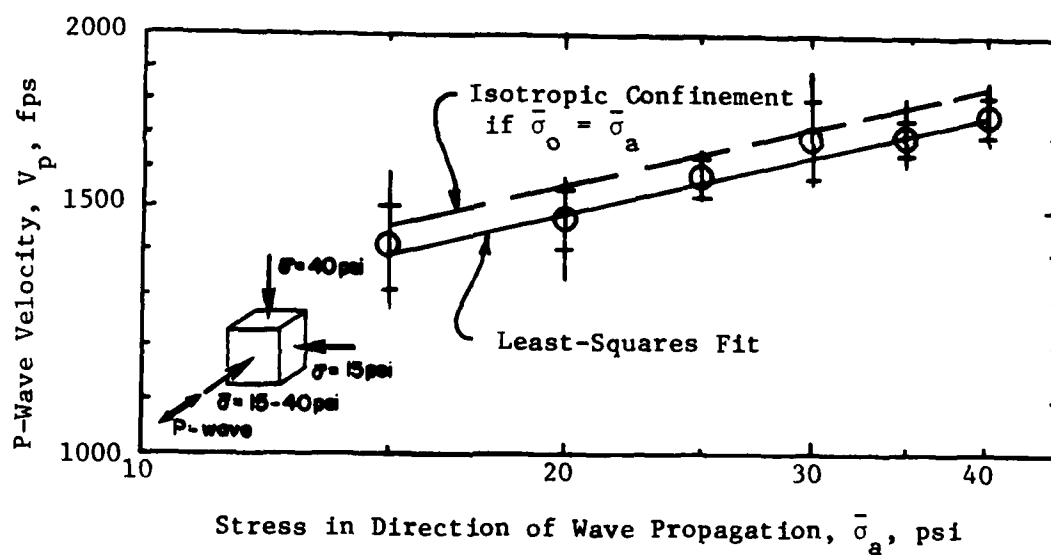
#### 8.2.1 Effect of Principal Stress in Direction of Wave Propagation

The variation of P-wave velocity with the variation in the intermediate principal stress in the direction of wave propagation is shown in Fig. 8.1a for the loading sequence and in Fig. 8.1b for the unloading sequence. Least-squares straight lines were fit to the data in Fig. 8.1 and are shown by the solid lines. The lines show that the  $\log V_p - \log \bar{\sigma}_a$  relationship can be approximated by a linear relationship with a slope slightly less than 0.25 for both the loading and unloading sequences.

The dashed lines in Fig. 8.1 show the variation in P-wave velocity with isotropic confining pressure. The dashed lines were determined by setting  $\bar{\sigma}_o$  equal to  $\bar{\sigma}_a$  in the equations derived



a) Loading



b) Unloading

Fig. 8.1 - Effect of Intermediate Principal Stress in Direction of Wave Propagation on Compression Wave Velocity for Triaxial Confinement

in Chapter 6, which relate  $V_p$  to isotropic confining pressure for each axis of wave propagation to try to account for structural anisotropy (see Section 8.2.4). The variation in  $V_p$  with  $\bar{\sigma}_a$ , shown by the solid line in Fig. 8.1, is almost the same as that predicted by the isotropic relationship and  $\bar{\sigma}_a$ .

The equations derived in Chapter 6 for the relationship between  $V_p$  and isotropic confining pressure and which were used in Chapter 7 for the biaxial tests were again used to study the results of the triaxial tests. In this way, it was possible to compare the constants,  $C_1$  and  $C$  (dimensionless), and slopes,  $m$  and  $n$ , from the equations:

$$V_p = C_1 \bar{\sigma}_a^m \quad (8.3)$$

and

$$M = 2.00 C Pa^{1-n} \bar{\sigma}_a^n \quad (8.4)$$

where:  $V_p$  = P-wave velocity in fps,  
 $\bar{\sigma}_a$  = effective pressure in the direction of wave propagation, in psi for Eq. 8.3, in the units of  $M$  in Eq. 8.4,  
 $M$  = constrained modulus in desired units, and  
 $Pa$  = atmospheric pressure in the same units as  $M$ .

Table 8.1 lists the values of the constants for the lines shown in Fig. 8.1 together with the corresponding values for the isotropic relationship along the axis of wave propagation. The differences between constants for isotropic and triaxial confinements range

TABLE 8.1

Comparison of Constants and Slopes for Equations Relating  $V_p$  or  $M$   
to  $\bar{\sigma}_o$  for Isotropic\* Confinement and to  $\bar{\sigma}_a$  for Triaxial\*\* Confinement

Axis of Propagation	Triaxial Confinement				Isotropic Confinement				Percent Change			
	$C_1$	m	C	n	$C_1$	m	C	n	$C_1$	m	C	n
(1)	(2)	(3)	(4)	(5)	(6)	(7)	(8)	(9)	(10)	(11)	(12)	(13)
North-South +	256	0.22	1375	0.44	250	0.23	1529	0.46	2.3	4.3	10.0	4.3
North-South -	239	0.23	1397	0.46	250	0.23	1529	0.46	4.0	0.0	8.6	0.0

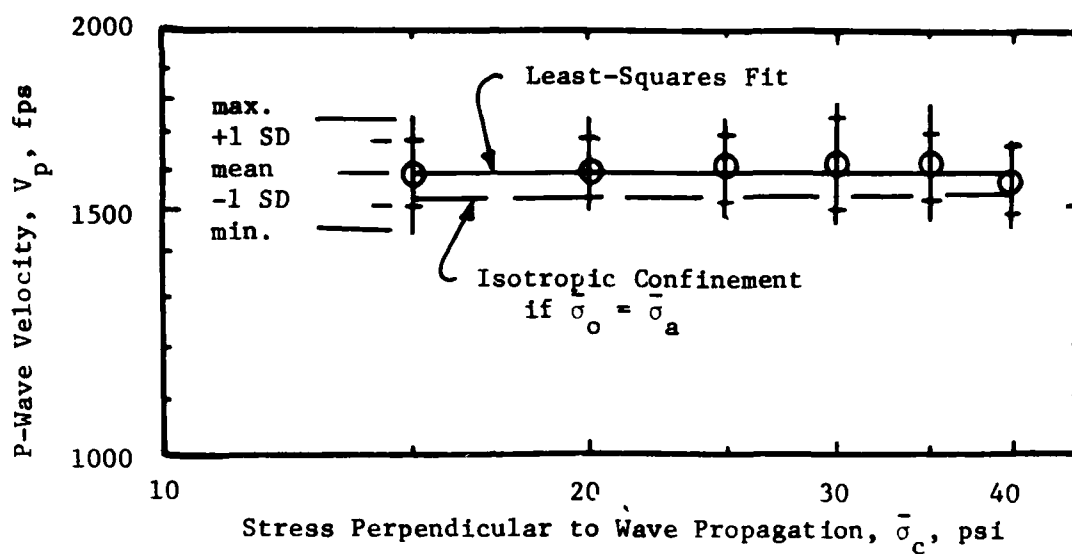
+ = loading      \*  $V_p = C_1 \bar{\sigma}_o^m$  (6.9)       $M = 2.00C Pa^{1-n} \bar{\sigma}_o^n$  (6.14)

- = unloading      \*\*  $V_p = C_1 \bar{\sigma}_a^m$  (8.3)       $M = 2.00C Pa^{1-n} \bar{\sigma}_a^n$  (8.4)

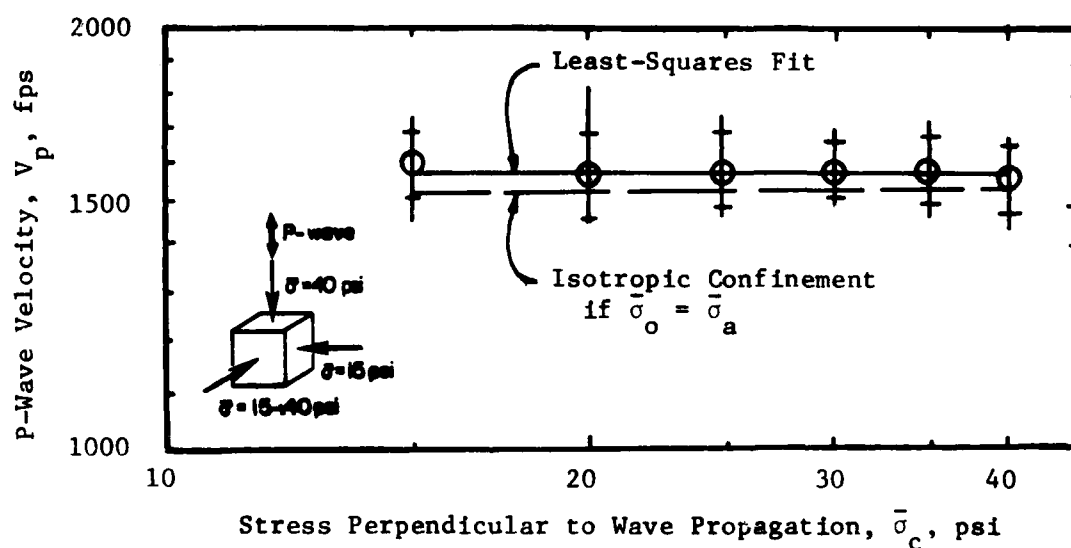
from zero to ten percent with most differences below five percent. From these low percent differences, it is apparent that the stress along the direction of wave propagation controls the P-wave velocity under triaxial confinement.

### 8.2.2 Effect of Principal Stresses in Direction Perpendicular to Wave Propagation

If Eqs. 8.3 and 8.4 are correct from triaxial loading, as they are for biaxial loading, then stresses perpendicular to the direction of wave propagation should not affect P-wave velocity. The variation in  $V_p$  with variation in  $\bar{\sigma}_{c2}$  (where  $\bar{\sigma}_c$  was  $\bar{\sigma}_2$ ) is shown in Fig. 8.2 from propagation in the  $\bar{\sigma}_1$  direction and in Fig. 8.3 for propagation in the  $\bar{\sigma}_3$  direction. Parts a and b of Figs. 8.2 and 8.3 correspond to loading and unloading sequences, respectively. The least-squares lines shown in the figures as solid lines are essentially horizontal, with slopes less than 0.02, which means that the P-wave velocity can be considered constant along the direction represented. As in the biaxial tests, a dashed line was drawn on the figures corresponding to the velocity calculated for the axis of propagation by setting  $\bar{\sigma}_o$  equal to  $\bar{\sigma}_a$  (constant in these tests) in the isotropic relationships derived in Chapter 6. Table 8.2 compares the mean P-wave velocity found in the triaxial confinement tests with that computed from the relationship for isotropic confinement. The percent differences between the velocities range from 3.2 to 4.2 percent. These small

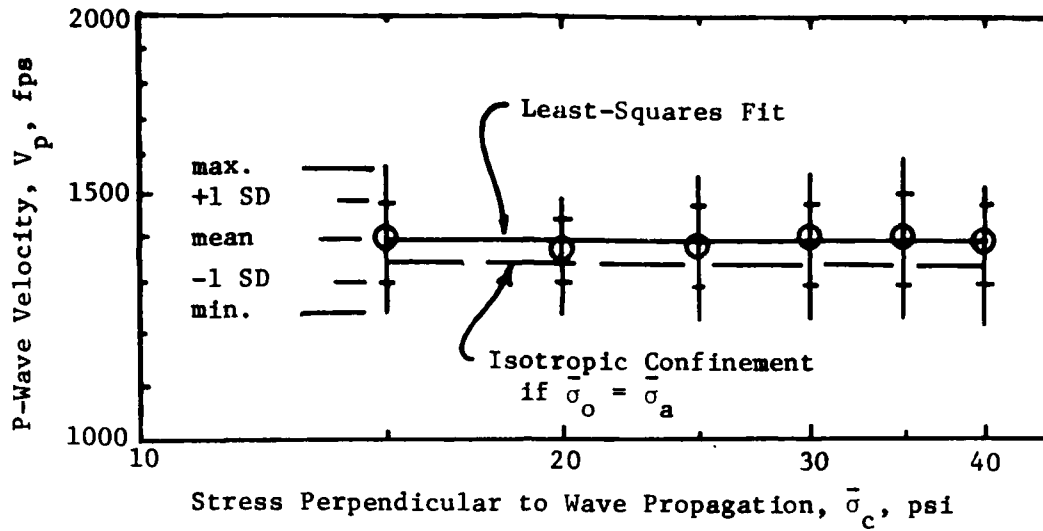


a) Loading

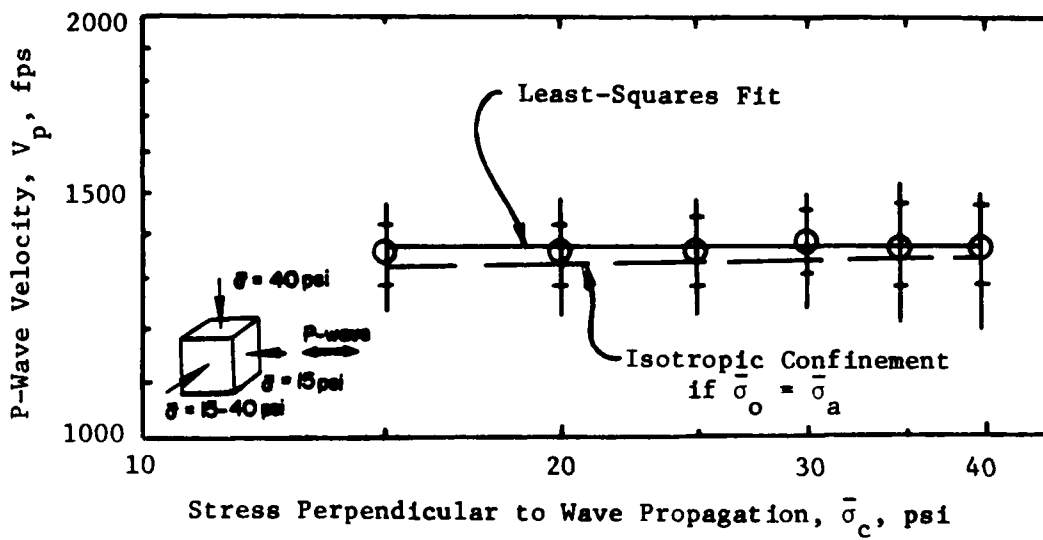


b) Unloading

Fig. 8.2 - Effect of Intermediate Principal Stress Perpendicular to Wave Propagation on Compression Wave Velocity for Triaxial Confinement



a) Loading



b) Unloading

Fig. 8.3 - Effect of Intermediate Principal Stress Perpendicular to Wave Propagation on Compression Wave Velocity for Triaxial Confinement



TABLE 8.2

Comparison of  $V_p$  for Isotropic and Triaxial Confinement States  
When  $\bar{\sigma}_a$  was Constant and  $\bar{\sigma}_{c2}$  Varied

Axis of Propagation*	$\bar{\sigma}_a$ (psi)	Triaxial Confinement		Calculated Isotropic** $V_p$ (fps)	Percent Change $\frac{(5)-(4)}{(4)} \times 100\%$ (%)
		Slope	Mean $V_p$ (fps)		
(1)	(2)	(3)	(4)	(5)	(6)
Vertical +	40	0.00	1595	1531	4.2
Vertical -	40	0.02	1584	1531	3.5
East-West +	15	0.01	1379	1326	4.0
East-West -	15	0.02	1369	1326	3.2

+ = loading  
- = unloading

\* In each case  $\bar{\sigma}_{c2}$  ranged from 15 to 40 psi.

\*\*  $V_p = C_1 \bar{\sigma}_o^m$

differences suggest that P-wave velocity is not affected by a variation in the intermediate principal stress when it is perpendicular to the direction of P-wave propagation.

### 8.2.3 Effect of Stress History

Those tests discussed in Sections 8.2.1 and 8.2.2 and shown in Figs. 8.1, 8.2 and 8.3 were performed under loading and unloading stress conditions to study the effect of stress history. The unloading sequence is shown as part b in each of the figures. The constants and slopes used to describe the variation in  $V_p$  with triaxial confinement are given in Table 8.3 so that pairs of tests corresponding to loading and unloading can be compared. The percent difference in constants from the loading and unloading sequences ranges from -6.6 to 4.3 percent, averaging only -0.9 percent. Therefore, it may be assumed that there is no noticeable effect of stress history in the triaxial test sequence.

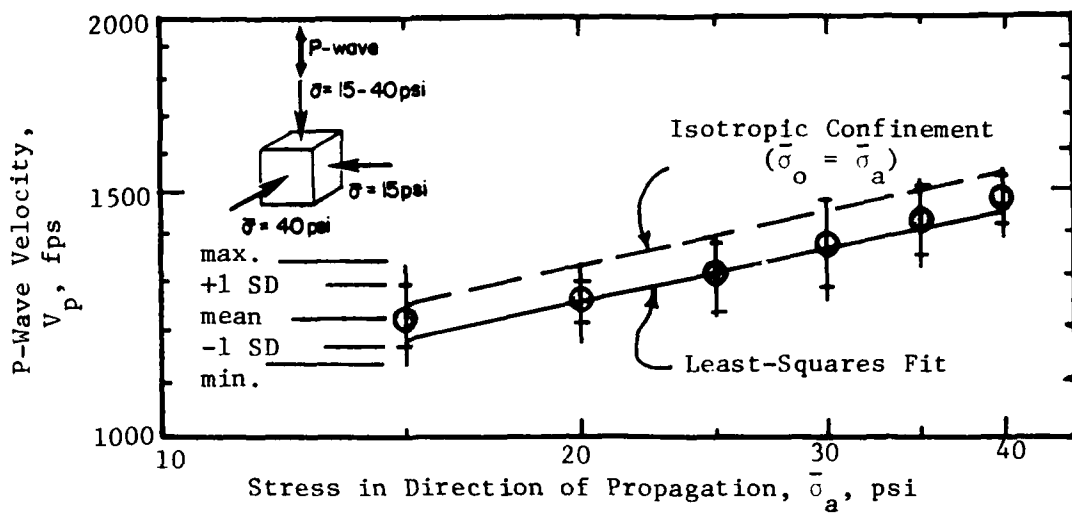
### 8.2.4 Effect of Structural Anisotropy

As in testing under biaxial confinement, P-wave velocities were also determined with the major stress axis reoriented to the north-south axis of the cube to observe the effect of structural anisotropy. The intermediate principal axis,  $\bar{\sigma}_2$ , was then reoriented along the vertical axis and was increased in the same manner as before (Section 8.1) but was not unloaded. Figure 8.4 shows the resulting variation in P-wave velocity with triaxial confining pressure along each axis of the cube. As before, the

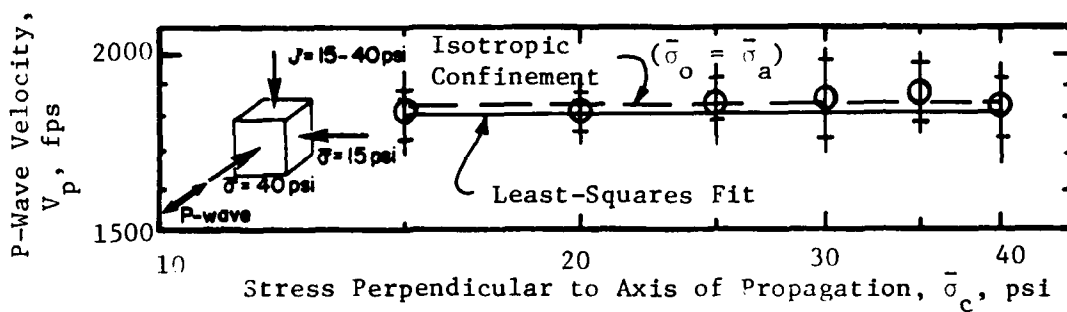
TABLE 8.3  
Comparison of Constants of Eq. 7.3\* or Mean P-wave Velocity  
during Loading and Unloading Sequences in Triaxial Confinement

Axis of Propagation (1)	$C_1$ (2)	m (3)	Mean $V_p$ (4)	Percent Change		
				$C_1$ (5)	m (6)	$V_p$ (7)
Vertical	loading	-	1595	-	-	0.7
	unloading	-	1584	-	-	-
North-South	loading	0.22				
	unloading	0.23		-6.6	4.3	-
East-West	loading	-	1379	-	-	0.7
	unloading	-	1369	-	-	-

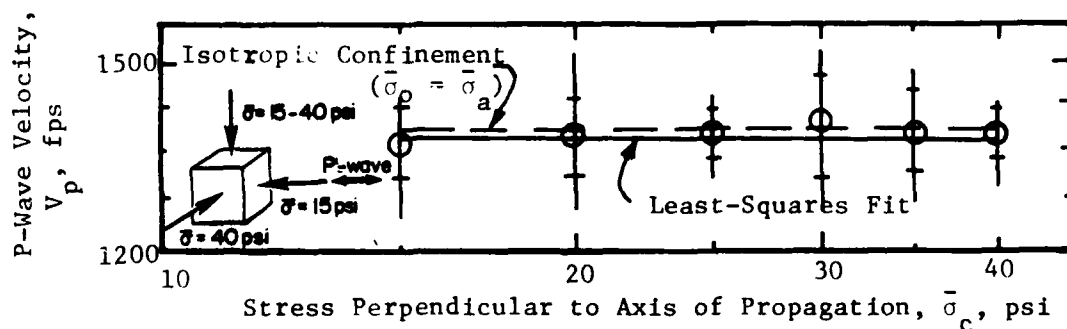
$$* V_p = C_1 \bar{\sigma}_a^m$$



a) Vertical Axis



b) North-South Axis



c) East-West Axis

Fig. 8.4 - Effect of Structural Anisotropy on Compression Wave Velocity for Triaxial Confinement

solid line represents a least-squares fit through the data, and the dashed line corresponds to the P-wave variation under isotropic confinement determined by setting  $\bar{\sigma}_o$  equal to  $\bar{\sigma}_a$  in the relationship derived in Chapter 6.

The constants for the equations used in Sections 8.2.1 and 8.2.2 to describe the P-wave variation are presented in Table 8.4 for the tests shown in Fig. 8.4. As before, the differences between the tests with triaxial and isotropic confinements are small, ranging from zero to 10.5 percent. Therefore, structural anisotropy does not effect the relationship between P-wave velocity and triaxial confinement. Structural anisotropy is only evident in the difference in values of the constants and slopes of the equations describing this relationship for the different axes of propagation.

#### 8.2.5 Effect of Lateral Pressure Coefficient on P-wave Velocity

Two definitions for the lateral pressure coefficient,  $K$ , were presented in Section 8.1. The first of these,  $K_{13}$  as defined by Eq. 8.1, was held constant at 2.67 in the series of triaxial tests with varying mean effective principal stress. The second coefficient,  $K_{23}$  as defined by Eq. 8.2, which relates the intermediate principal stress to the minor principal stress ranged from 1.00 to 2.67 in this test sequence.

Figure 8.5 shows the variation of  $V_p$  with the variation in  $K_{23}$  as simply another method of presenting the results shown earlier in this chapter. The ordinate in the figure is the



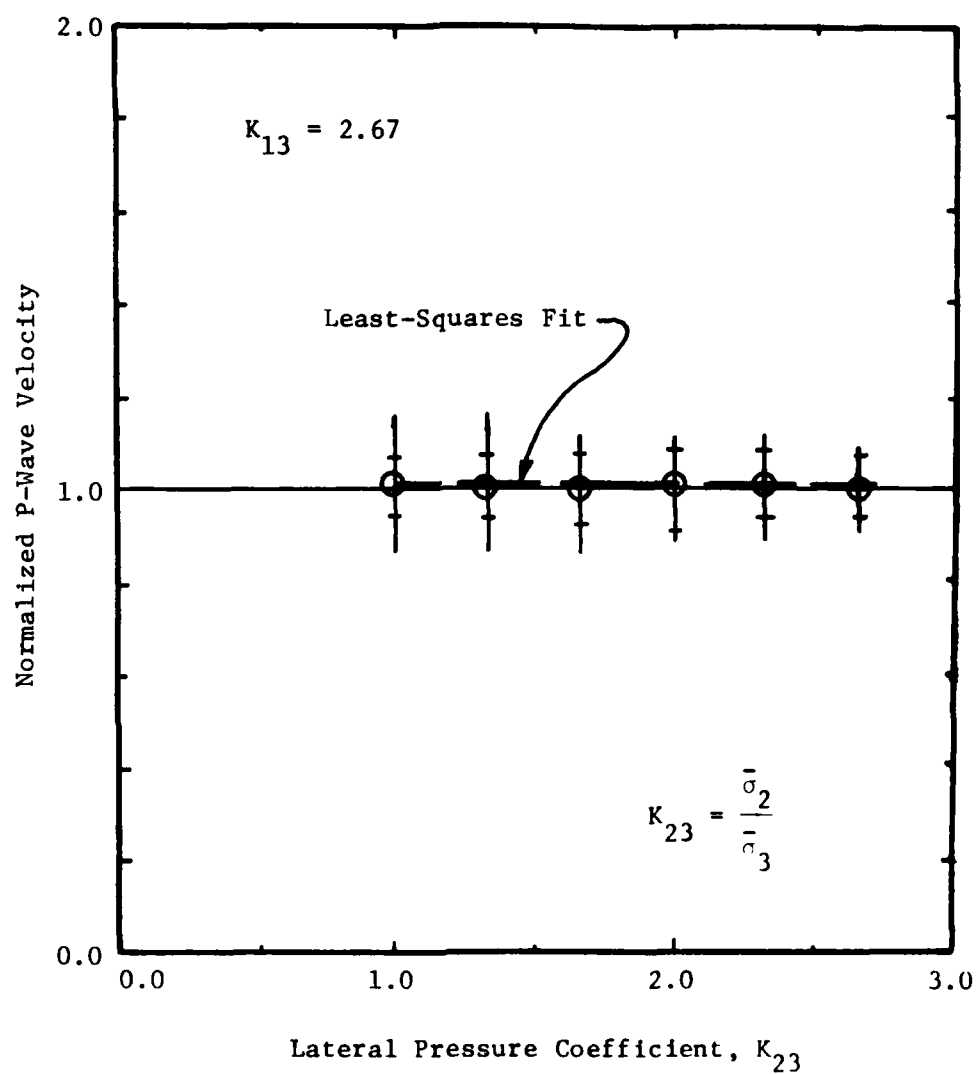


Fig. 8.5 - Variation in Normalized P-Wave Velocity with Lateral Pressure Coefficient,  $K_{23}$ , for Triaxial Loading

normalized P-wave velocity to try to account for structural anisotropy. Normalized values of  $V_p$  were computed by taking the values of  $V_p$  determined for triaxial confinement and dividing them by the P-wave velocities determined from the isotropic relationships by setting  $\bar{\sigma}_0$  equal to  $\bar{\sigma}_a$  along the proper axis of propagation.

The data presented in Fig. 8.5 are evenly banded about unity as was the case for testing under biaxial confinement. A value of one for the normalized velocity means that the P-wave velocity under triaxial confinement is the same as the velocity under isotropic confinement if the stress in the direction of wave propagation is the same in both cases. Therefore, the conclusion reached in Chapter 7 for biaxial confinement may be extended for triaxial confinement; that is, P-wave velocity for a body wave under any loading depends solely on the stress in the direction of wave propagation.

### 8.3 TESTING WITH A CONSTANT MEAN EFFECTIVE PRINCIPAL STRESS

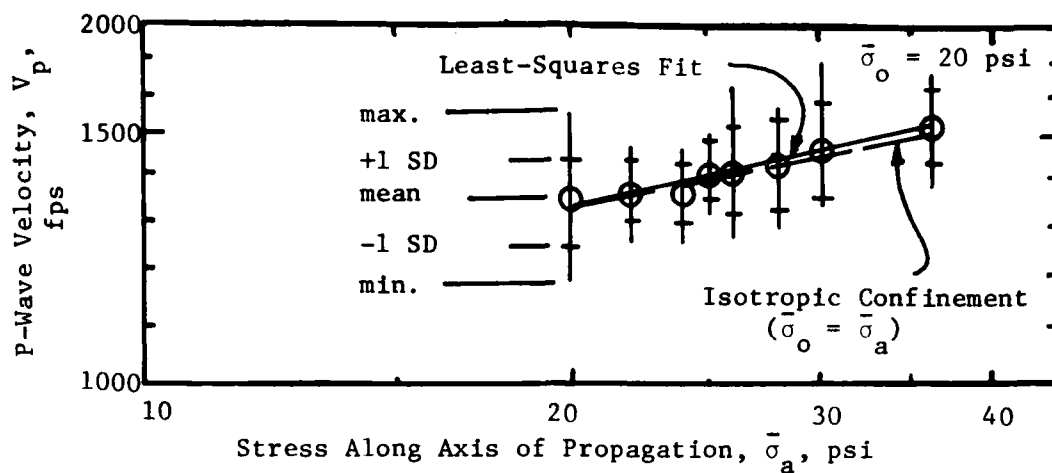
It was shown in Section 7.3 that under biaxial loading, the statement by Hardin and Black (1966) that S-wave velocity was constant along lines of constant mean effective principal stress,  $\bar{\sigma}_0$ , could not be extended to P-wave velocities when P-waves were acting as body waves. This relationship was again checked under triaxial loading. The value of  $\bar{\sigma}_0$  of 20 psi (138 kPa) was chosen since it was about the mid-value of the range of confining pressures possible in the cube and, therefore, a reasonable range in  $\bar{\sigma}_1$



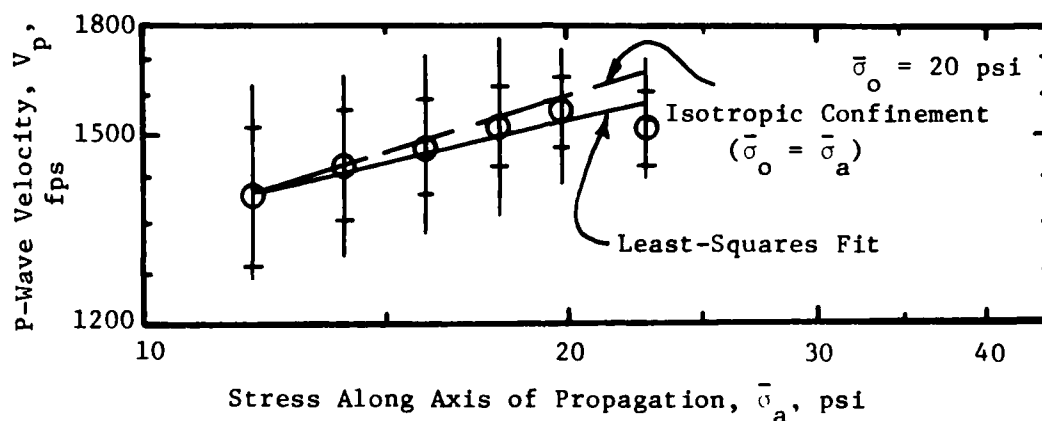
values was possible without exceeding the limit of the cube, and reasonable ranges in  $\bar{\sigma}_2$  and  $\bar{\sigma}_3$  values were possible without resulting in a shear failure in the sample.

This test series began with an isotropic state of stress at 20 psi (138 kPa). The vertical stress ( $\bar{\sigma}_1$ ) was then increased in 2-psi (14 kPa) increments (except for a final 6-psi (42 kPa) increment) while  $\bar{\sigma}_2$  and/or  $\bar{\sigma}_3$  were varied in 2-psi (14 kPa) increments, thus keeping  $\bar{\sigma}_0$  constant while increasing both  $K_{13}$  and  $K_{23}$ . This was continued until a biaxial state of stress was reached where  $K_{13}$  was at a value of 3.00. The sequence was reversed using larger increments this time until a value of  $K_{13}$  of 2.08 and  $K_{23}$  of 1.92 were reached. The testing series included tests 13 through 23 from Table 5.1 which can be seen on Fig. 5.1 between the dates of July 23 and August 5, 1981.

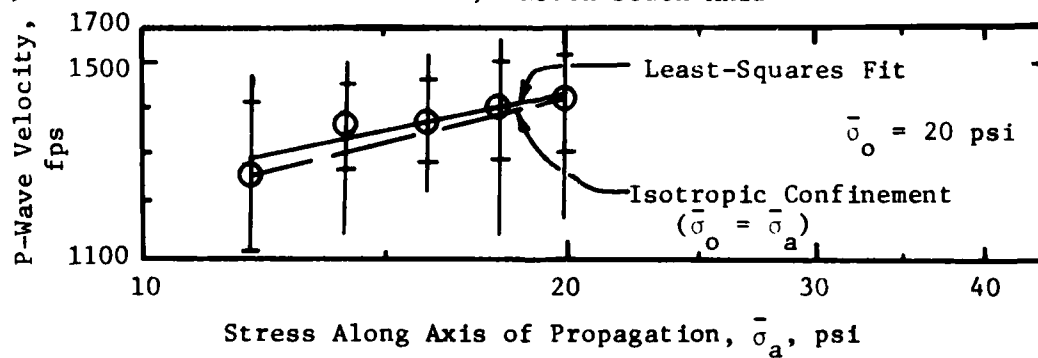
Figure 8.6 shows, for each axis of the cube, the variation in P-wave velocity with pressure along that axis. The solid line on each plot represents the least-squares fit of the data, and the dashed line represents the variation in P-wave velocity with isotropic confining pressure as determined by the relationship presented in Chapter 6 by setting  $\bar{\sigma}_0$  equal to  $\bar{\sigma}_a$ . In all cases the two lines are nearly identical. The constants derived from this data for the equations presented in Section 8.2 are tabulated together with the corresponding constants for isotropic confinement in Table 8.5. The percent difference between the constants under



a) Vertical Axis



b) North-South Axis



c) East-West Axis

Fig. 8.6 - Effect of Principal Stress in Direction of Wave Propagation on Compression Wave Velocity for Triaxial Confinement with Constant Mean Effective Principal Stress

TABLE 8.5

Comparison of Constants and Slopes for Equations\* Relating  $V_p$  or  $M$   
to  $\bar{\sigma}_o$  for Isotropic Confinement and to  $\bar{\sigma}_a$  for Triaxial Confinement  
with a Constant Mean Effective Principal Stress

Axis of Propagation	Triaxial Confinement				Isotropic Confinement				Percent Change			
	$C_1$	m	C	n	$C_1$	m	C	n	$C_1$	m	C	n
(1)	(2)	(3)	(4)	(5)	(6)	(7)	(8)	(9)	(10)	(11)	(12)	(13)
Vertical	252	0.21	1145	0.42	271	0.20	1136	0.40	7.0	5.0	0.8	5.0
North-South	311	0.20	1501	0.40	250	0.23	1529	0.46	19.6	13.0	1.8	13.0
East-West	249	0.22	1305	0.44	210	0.24	1255	0.48	18.6	10.0	4.0	10.0

$$* V_p = C_1 \bar{\sigma}_a^m \quad (8.3) \quad M = 2.00C Pa^{1-n} \bar{\sigma}_a^n \quad (8.4)$$

triaxial and isotropic confinement ranges from 0.8 to 19.6 percent, with two-thirds of the results showing differences of ten percent or less.

As used in Section 7.2.6 for the biaxial tests, graphs of normalized velocity versus lateral pressure coefficients have been made for the triaxial tests. However, in the triaxial series, both  $K_{13}$  and  $K_{23}$  were varied. Therefore, two figures, Figs. 8.7 and 8.8, have been drawn to show the data. Again the data is evenly banded about unity with only a few points outside the  $\pm 10$  percent range.

From the preceding figures, it is apparent that the P-wave velocity under triaxial confinement is not constant when  $\bar{\sigma}_0$  is held constant. Also, since the P-wave velocity in these triaxial tests is essentially the same as the velocity measured for an isotropic state of stress when  $\bar{\sigma}_0$  equals the stress in the direction of propagation, it again follows that the P-wave velocity depends solely on the stress in the direction of propagation when the compression wave is acting as a body wave (in contrast to a compression wave in a rod).

#### 8.4 SUMMARY AND CONCLUSIONS

Two series of tests were performed in which P-wave velocity was measured under triaxial confinement. The first series had a varying mean effective principal stress and only  $\bar{\sigma}_2$  was varied. In the second series, all three principal stresses were varied together so that a constant mean effective principal stress of

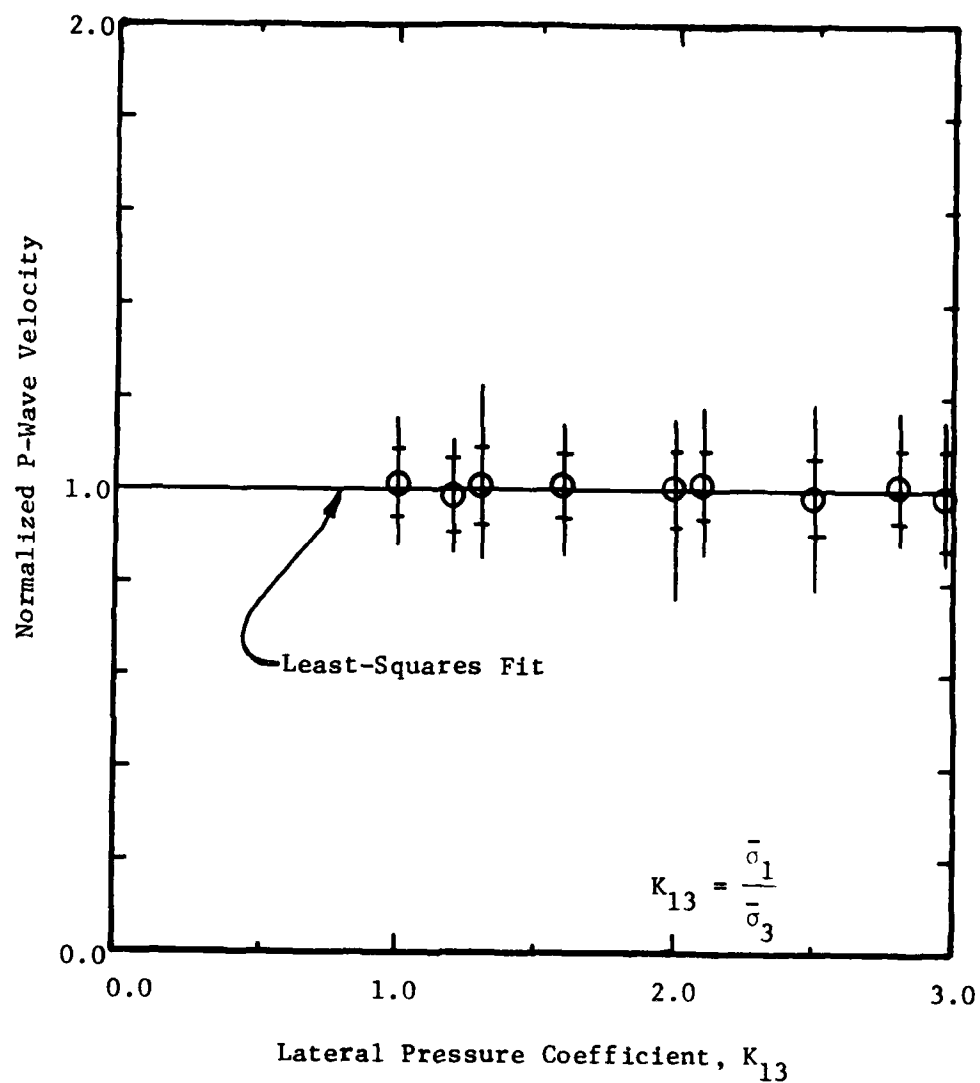


Fig. 8.7 - Variation in Normalized P-Wave Velocity with Lateral Pressure Coefficient,  $K_{13}$ , for Triaxial Loading

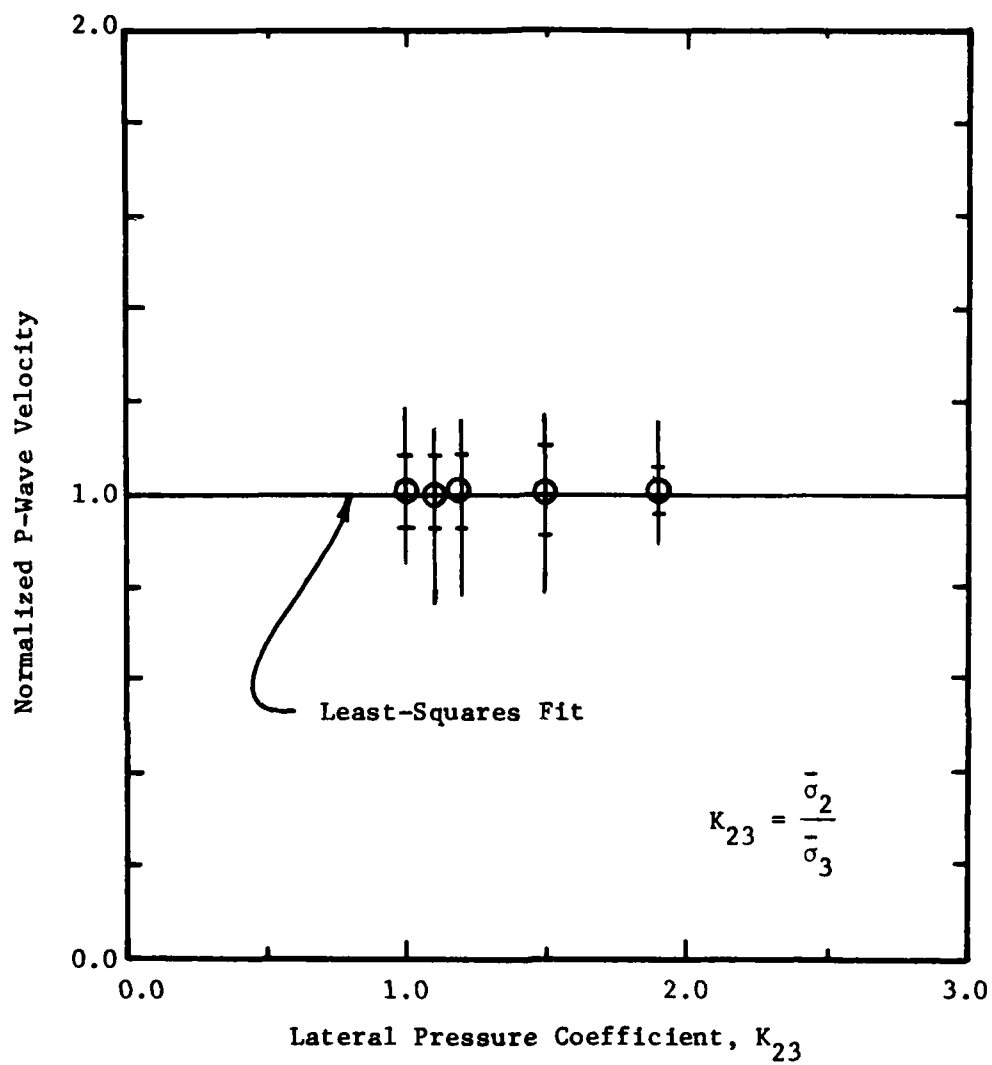


Fig. 8.8 - Variation in Normalized P-wave Velocity with Lateral Pressure Coefficient,  $K_{23}$ , for Triaxial Loading

20 psi (138 kPa) was maintained. All of the data for this sand over the stress range of the tests leads to a conclusion similar to that reached for the biaxial tests: under triaxial (or biaxial) confinement, the compression wave velocity for a body wave varies solely with the stress along the axis of wave propagation according to Eq. 8.3. The values of the constant,  $C_1$ , and slope,  $m$ , are the same for isotropic, biaxial, or triaxial confinement, but they vary with the axis of propagation because of structural anisotropy.

CHAPTER NINE  
SUMMARY, CONCLUSIONS AND RECOMMENDATIONS FOR  
FUTURE WORK

9.1 SUMMARY AND CONCLUSIONS

The overall objective of this research project is to study the effect of state of stress on the dynamic properties of soil. This initial segment of the research dealt with the design and construction of a testing apparatus and investigation of the effect of state of stress on velocities of compression waves propagating along principal stress directions in a dry sand.

9.1.1 Triaxial Testing Device

Much of the effort of this part of the research was spent constructing a viable triaxial testing device. Such a device was built of reinforced steel to hold a cube of soil measuring 7 ft (2.1 m) on a side. Rubber membranes were placed between the sand and walls of the steel cube on three mutually perpendicular sides which correspond to the three principal stress axes of the soil sample. The membranes were hydraulically loaded to apply a stress to the soil ranging from zero to 40 psi (zero to 276 kPa). Compression and shear waves were generated along each axis of the cube by striking a source along the desired axis and in the appropriate direction. The sources directly contacted the soil and



protruded through ports in side walls of the cube. Wave motions were monitored by a series of accelerometers embedded in the sand. A pair of digital oscilloscopes were used to record the output of the accelerometers for later recall and evaluation.

From the waveforms recorded by the oscilloscopes, direct and interval velocities, frequency, and attenuation characteristics of the waves were determined at the various states of stress. Stress and strain data were also collected from instrumentation embedded in the sand. The data pertaining to compression waves has been analyzed in this thesis. Shear wave analysis was done by Knox (1981), and the attenuation characteristics will be analyzed in the future. The conclusions reached based on the compression wave data are summarized below.

#### 9.1.2 Effect of the State of Stress on $V_p$

Compression wave velocities were measured under various isotropic, biaxial, and triaxial states of stress. The following conclusions were reached for P-waves propagating as body waves in the dry sand.

1. The velocity of the P-wave depends upon only the stress in the direction of wave propagation. This relationship may be expressed in a form similar to that used by Hardin and Richart (1963):

$$V_p = C_1 \bar{\sigma}_a^m \quad (9.1)$$

where:  $V_p$  = P-wave velocity in fps,  
 $C_1$  = constant,  
 $\bar{\sigma}_a$  = stress in direction of wave propagation in psf, and  
 $m$  = slope of the curve.

The velocity of a P-wave propagating as a body wave is proportional to the constrained modulus,  $M$ . Therefore, the above relationship may also be expressed in a non-dimensional form similar to Hardin (1978) for cohesionless material:

$$M = \frac{(1-\nu) S_1}{(1+\nu)(1-2\nu)F(e)} P_a^{1-n} \bar{\sigma}_a^n \quad (9.2)$$

where:  $\nu$  = Poisson's ratio,  
 $S_1$  = dimensionless constant,  
 $F(e)$  = function of void ratio,  $e$ , ( $F(e)=0.3+0.7e^2$ ),  
 $P_a$  = atmospheric pressure, in units of  $M$ , and  
 $n$  = slope of the curve.

2. The constants for the above equations were found to be the same under isotropic, biaxial, and triaxial confinement for the same axis of propagation. The range and average values determined for these constants are as follows:

$C_1$  ranged from 210 to 311 and averaged 243,  
 $m$  ranged from 0.20 to 0.24 and averaged 0.22,  
 $C$  ranged from 1136 to 1529 and averaged 1299, and  
 $n$  ranged from 0.40 to 0.48 and averaged 0.44.

3. Structural anisotropy of the sample did not affect the relationship between  $V_p$  and  $\bar{\sigma}_a$ . However, it did cause a variation in the constants depending on the axis of propagation. The variation in constants for Eqs. 9.1 and 9.2 between the different axes ranged from zero to 11.5 percent and averaged 5.8 percent. This variation in constants is less than the range of 6 to 15 percent variation in  $V_p$  due to structural anisotropy in sand found by Schmertmann (1978).

4. Stress history did not affect the P-wave velocity over the stress range used in these tests. The maximum percent difference in velocities or constants between loading and unloading was only 13.8 percent (averaging 4.3 percent) and, therefore, was neglected.

#### 9.1.3 Stress-Strain Measurements

Because of problems with both the stress and strain instrumentation, no accurate stress-strain data were collected. An approximate relationship was derived from monitoring the amount of water going into or coming out of the membranes during loading. The pressure read by the gage on the panel board was plotted against this approximate strain to reach the following conclusions.

1. There is an initial seating strain probably caused by the rubber membranes expanding to fill the voids between the wall of the cube and the soil. This effect is most pronounced between zero and 20 psi (zero and 138 kPa) but can still be observed up to the maximum stress of 40 psi (276 kPa).

2. After initial seating, the stress-strain relationship is approximately linear, with the strain returning to approximately the same initial value after a loading-unloading sequence.

#### 9.1.4 Importance to Laboratory Testing and Constitutive Modeling

The conclusion that the velocity of a P-wave propagating as a body wave through sand depends only on the stress along the axis of wave propagation is important in attempting to correlate laboratory and field testing. Compression wave velocity along principal stress directions may be predicted for any state of stress in the field based on isotropic dynamic laboratory testing as long as the isotropic confining pressure equals the effective principal stress in the field in the direction of the P-wave propagation.

Since Knox (1981) found that shear wave velocity is influenced by both the stress in the direction of wave propagation and the stress in the direction of particle motion (which are in perpendicular directions for shear waves), the assumption that properties based on compression waves acting as body waves can be used to predict shear-wave derived properties is invalid for other than isotropic confinement. Therefore, new methods must be developed to include the effect of non-isotropic states of stress in correlations between shear-wave derived properties and compression-wave derived properties.

#### 9.2 RECOMMENDATIONS FOR FUTURE WORK

The triaxial testing device which was built for this research has significant experimental use in the future. Static as

well as dynamic testing is possible. However, the following recommendations deal only with improving the device and suggestions for continuing and extending the present research.

1. The present source was somewhat difficult to use because of its configuration. There were also cases of sand leakage. Therefore, the design of a new source would be useful to future researchers.

2. A drain line should be added to the panel board so that emptying of the accumulators is an easy process during unloading.

3. A new raining device for dry sand should be designed and built to try to improve the uniformity of deposition of sand. This may also decrease the structural anisotropy observed in the sand sample.

4. The stress and strain cells should be individually calibrated in the laboratory before any future use in a soil sample. The poor results and problems associated with this equipment shows a need for calibration. Although there are inherent problems with these devices, careful placement can reduce many of the problems.

5. Another sample of dry sand should be tested for two reasons. First, additional results should be generated by different researchers to confirm the conclusions reached in this phase of the research. Second, the effect of an improvement to the device, such as a new rainer, may be observed when compared to that presented in this thesis.

6. Additional types of soils should be tested to see if the relationship between P-wave velocity and confining pressure determined for dry sand is applicable to other soils. Some suggested samples include sands with varying moisture content, sands with embedded cobbles or rocks, sands with embedded silt or clay seams, and cohesive soils. Cohesive soils will present problems in placement and consolidation at each confinement step.

7. Waves should be propagated at oblique angles to the principal stress axes to investigate the interaction between the principal stresses and the three-dimensional effect of structural anisotropy and stress anisotropy.

## APPENDIX A

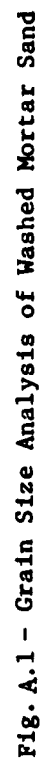
ENGINEERING PROPERTIES OF SAND  
(Taken Directly from Knox, 1982)

## A.1 INTRODUCTION

The sand used in the initial wave propagation testing was selected in June, 1980 and was delivered to the Ferguson Structural Engineering Laboratory at the Balcones Research Center in August, 1980. The sand was selected because it is available locally in large quantities and because it fulfills several requirements as discussed in Section A.2. Enough sand was initially ordered to form at least two separate cube samples. Since delivery to the Ferguson Laboratory, the sand has been located in an outdoor storage bin adjacent to the laboratory. The outdoor bin is not covered but has 3-ft (0.91 m) high concrete walls and a concrete floor.

## A.2 SAND CLASSIFICATION

The sand is a medium to fine, washed mortar sand with a specific gravity of 2.67. The sand classifies as SP in the Unified Soil Classification System. The results of grain size analyses performed on five different sand samples are shown in Fig. A.1. Based on the average grain size curve, the sand has an effective grain size,  $D_{10}$ , of 0.28 mm and a uniformity coefficient,  $C_u$ , of 1.71. A soil with a uniformity coefficient smaller than 2.0 is considered uniform. Therefore, the average grain size curve shows





the uniform grading of this mortar sand which makes the sand well-suited for the planned testing. Because of the relatively uniform size of the sand grains, the sand can be rained into the triaxial cube without significant segregation, an important consideration in this test series. The ability to rain the sand into the cube without significant segregation coupled with raining the sand from a minimum height of 3 ft (0.91 m) (Marcuson and Bieganousky, 1977) ensures not only uniform samples but also reproducible samples for each test.

Sand samples were taken from the storage bin from the time the sand was first delivered in August 1980 until the time the sand was used to fill the cube in June 1981. Since there is little scatter in the grain size curve, it can be concluded that there was no significant alteration of the original sand material with time. Therefore, the amount of fines can be expected to remain reasonably constant from one sample to the next. Sand fines are important to the quality of waves generated in the sand mass and to the density of the sand sample.

In the initial testing, the sand was tested in a dry state. The sand was dried in the sun to a water content of less than 0.5 percent. At this water content the sand did not tend to clump due to surface water on the sand grains. Small portions of sand were raked out in one-inch (2.54 cm) layers over a large area to dry in the heat of the sun. The sand was constantly raked and turned over to ensure complete drying. Dried sand was then placed

in piles and protected from moisture in the air by covering the piles with plastic sheets.

### A.3 DRAINED SHEARING STRENGTH

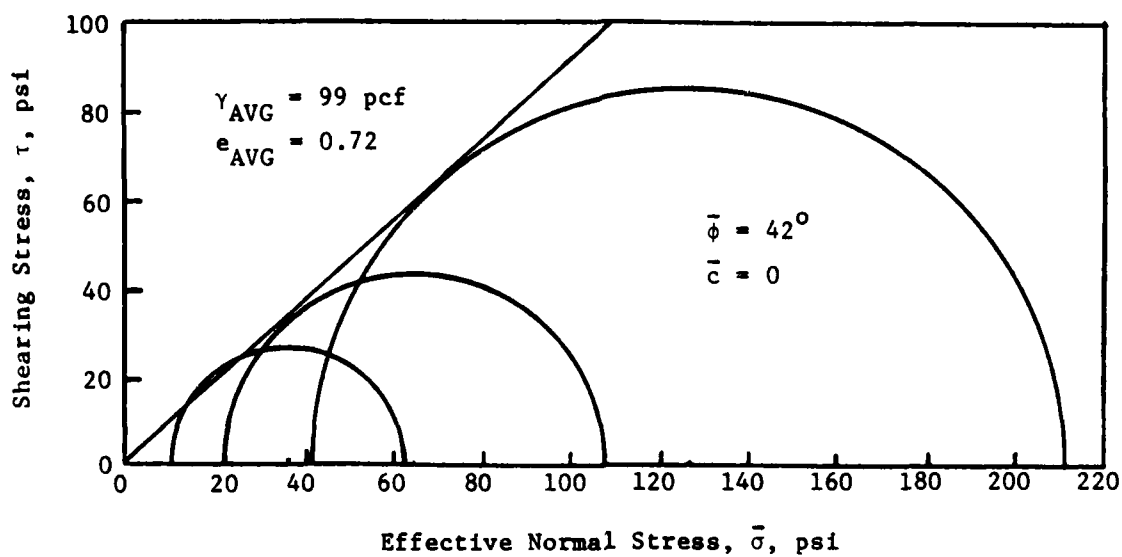
A series of consolidated drained (S-type) triaxial tests was performed with the sand to determine the effective strength parameters: friction angle,  $\bar{\phi}$ , and apparent cohesion,  $\bar{c}$ . The tests were performed with 1.5-in. (3.81-cm) diameter samples which had heights of 3 in. (7.62 cm). The sand was air dried prior to testing and had an average water content of 0.4 percent.

To determine the variation in  $\bar{\phi}$  and  $\bar{c}$  with density, the sand was tested at two different average dry densities, 83 and 99 pcf (1343 and 1602 kg/m<sup>3</sup>) which represents loose and dense states for the sand, respectively. To obtain a dense sample, sand was rained into the sample mold (on the base pedestal of the triaxial device) from a height of 3 ft (0.91 m). This was done by permitting the sand to fall freely through a 3-ft (0.91 m) long tube into the mold. Loose sand samples were constructed by pouring the sand through a funnel with the spout kept just above the top of the sample in the mold. The sand was poured slowly but continuously into the mold to minimize any tendency to segregate and layer. None of the samples were compacted after the sand was placed in the mold since the sand mass in the cube was not going to be compacted after it was placed. In fact, it was felt that the dense sand samples would most closely represent the sand after it was placed (by raining) in the cube.

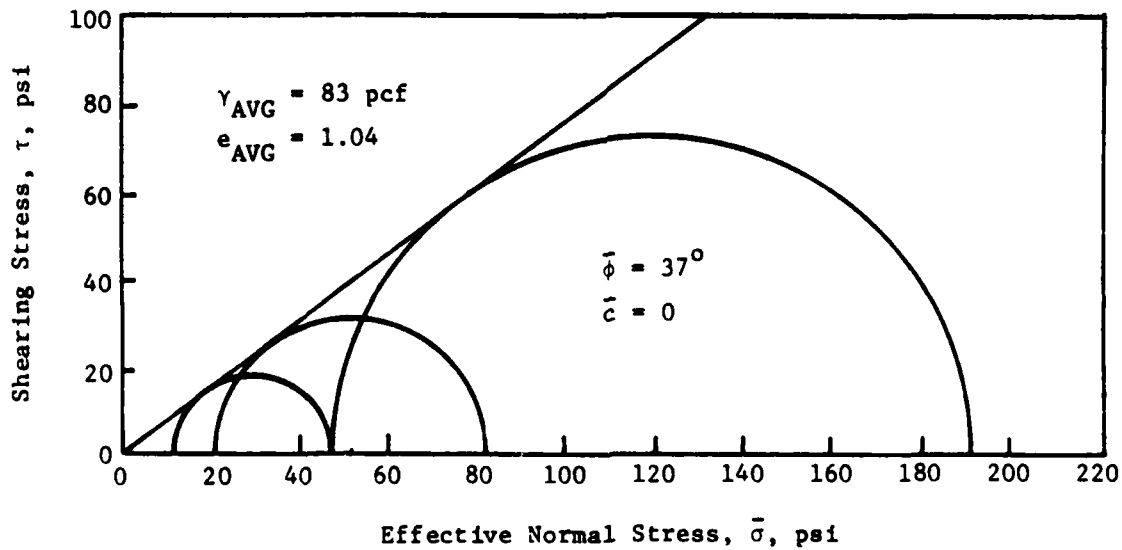
Failure envelopes for the loose and dense sand samples are shown in Fig. A.2. Based on the failure envelopes,  $\bar{\phi}$  increases as density increases, ranging from 37 degrees for the loose samples to 42 degrees for the dense samples. The value of  $\bar{c}$  can be considered essentially zero for both the loose and dense states.

Once the failure envelopes were determined, the stress difference between the three principal stress axes was studied to determine if any combination of triaxial stresses would cause the sand to fail in the cube while being loaded. From this study (using a conservative value of 40 degrees for  $\bar{\phi}$ ) it was concluded that with a major and minor principal stress combination of 40 and 5 psi (275.6 and 34.5 kPa) respectively, the sand sample would fail. Therefore, this combination of principal stresses was excluded from testing.

The principal stress combination was limited further by the nonuniform vertical stresses in the sand. There is a variation of vertical stress with depth acting on the sand because of body forces within the cube. These body forces are due to the increase in total weight of sand with depth and the increase in total weight of water with depth in the loading membranes. The variation of vertical geostatic stress ranges from zero at the top of the sample to 4.52 psi (31.1 kPa) at the bottom with an average value of 2.3 psi (15.8 kPa) in the middle. It was desired to reduce the significance of body forces on wave propagation and so it was decided to test only at confining pressures where the body forces



a. Dense Sand Sample



b. Loose Sand Sample

Fig. A.2 - Failure Envelopes for Loose and Dense Sand Samples from Consolidated, Drained Triaxial Tests

at the middle of the sample were less than 25 percent of the applied pressure. With this approach, 10 psi (68.9 kPa) was selected as the minimum pressure at which any wave testing would be conducted. As a result, 10 psi and 40 psi (68.9 and 275.6 kPa) represent the minimum and maximum principal stresses in this study, with  $\bar{\sigma}_3$  being large enough to overshadow the body forces and with  $\bar{\sigma}_1 - \bar{\sigma}_3$  satisfying the stress difference requirements based on  $\bar{\phi}$ .

#### A.4 ISOTROPIC DYNAMIC TESTING

Dynamic soil property tests were performed on the sand at the Soil Dynamic Laboratory at the University of Texas at Austin. Resonant column equipment was used to evaluate the shear modulus,  $G$ , shear wave velocity,  $V_s$ , and material damping ratio,  $D$ , of the sand, which are defined as,

$$G = \rho V_s^2 \quad (\text{A.1})$$

$$D = \frac{\delta^2}{4\pi^2 + \delta^2} \quad (\text{A.2})$$

where:  $\rho$  = mass density of the sand, and

$\delta$  = log decrement determined from the free-vibration-decay-curve.

Isotropic confining pressures were maintained through resonant column testing with hydrostatic confining pressures ranging from 2.5 to 80 psi (17.2 to 551.2 kPa). Sand samples experienced

two-way cyclic loading, undergoing complete stress reversal. Both low-amplitude and intermediate-amplitude tests were used to evaluate  $V_s$ ,  $G$  and  $D$ . Low-amplitude tests are defined as those tests in which the single-amplitude shearing strain,  $\gamma$ , did not exceed 0.001 percent. Intermediate-amplitude tests are those tests in which shearing strains were in the range of 0.001 to about 0.01 percent.

The significance of low-amplitude testing is that dynamic soil properties are essentially constant in this strain range (Hardin and Drnevich, 1972a and b), and it is the strain range expected in the initial tests in the triaxial cube. At shearing strains above 0.001 percent, dynamic soil properties may be influenced by strain amplitude depending on several variables such as the soil type, strain amplitude, and confining pressure.

#### A.4.1 Low-Amplitude Dynamic Properties

Three series of low-amplitude tests were performed to determine the effect of the effective mean principal stress,  $\bar{\sigma}_o$ , on  $V_s$ ,  $G$  and  $D$ . Different initial void ratios of 0.59, 0.70 and 0.76 were achieved in the different test series. In addition, the second and third test series included unloading pressure sequences to study the effect of overconsolidation and stress history on the dynamic properties. The second test series had one cycle of loading and unloading while the third test series included 2.5 load cycles (load-unload-reload-unload-reload).

The variation in the low-amplitude  $G$  with effective hydrostatic confining pressure is shown in Fig. A.3. A linear relationship between  $\log G$  and  $\log \bar{\sigma}_0$  exists with the shear modulus increasing as confining pressure increases. In addition, the shear modulus decreases as void ratio increases at any confining pressure. However, the decrease in shear modulus with increasing void ratio does not significantly change the slope of the  $\log G - \log \bar{\sigma}_0$  relationship.

Based on low-amplitude resonant column tests, the shear modulus can be expressed in the form of (Hardin, 1978):

$$G_{\max} = \frac{A \text{OCR}^K}{0.3 + 0.7e^2} P_a^{1-n} \bar{\sigma}_0^n \quad (\text{A.3})$$

where:  $G_{\max}$  = shear modulus in psi,  
 $A$  = constant (dimensionless),  
 $\text{OCR}$  = overconsolidation ratio (dimensionless),  
 $K$  = factor based on Plasticity Index of soil (for sand,  $K = 0$ ),  
 $e$  = void ratio,  
 $P_a$  = atmospheric pressure in psi,  
 $\bar{\sigma}_0$  = effective confining pressure in psi, and  
 $n$  = slope of the  $\log G - \log \bar{\sigma}_0$  relationship.

Average values for  $A$  and  $n$  were determined for these tests and found to be 705 and 0.48, respectively. These values of  $A$  and  $n$  result in an average ratio of calculated shear modulus divided by

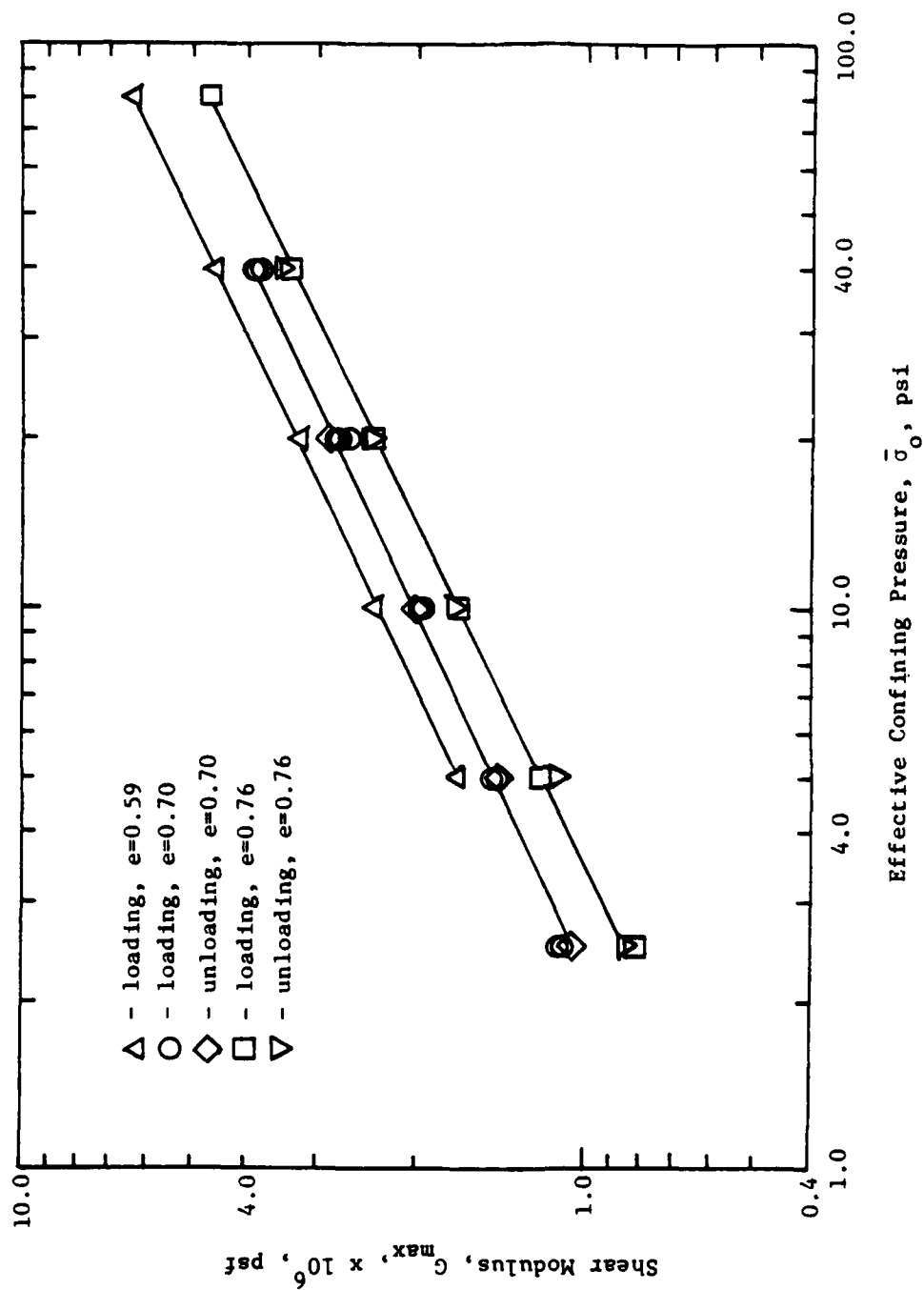


Fig. A.3 - Variation in Low-Amplitude Shear Modulus with Effective Confining Pressure



measured shear modulus from the resonant column test for all the tests equal to 0.99 with a standard deviation of 0.05. A maximum deviation of  $\pm 11$  percent was found between the calculated and measured shear moduli. Therefore, Eq. A.3 can be used to predict the shear modulus (and hence shear wave velocity) of the sand in the triaxial cube when the loading is hydrostatic.

The unloading pressure sequence shown in Fig. A.3 indicates that previous stress history (for stress-controlled boundaries) has little effect on the shear modulus and shear wave velocity of this sand and, for practical purposes, can be neglected. This behavior represents an important consideration in conducting the tests in the cube because it means that stress history can be ignored in performing the low-amplitude tests.

Shear wave velocity is related to shear modulus, as indicated by Eq. A.1, by the one half power. The variation in  $V_s$  with effective hydrostatic confining pressure is shown in Fig. A.4. A linear relationship also exists between  $\log V_s$  and  $\log \bar{\sigma}_0$  with the shear wave velocity increasing as confining pressure increases. Also, shear wave velocity decreases as void ratio increases at any confining pressure. As with the shear modulus, the decrease in shear wave velocity with increasing void ratio does not significantly change the slope of the  $\log V_s - \log \bar{\sigma}_0$  relationship.

The variation in low-amplitude material damping ratio with confining pressure is shown in Fig. A.5 for the sand tested at all three void ratios. The results show that  $D$  tends to decrease

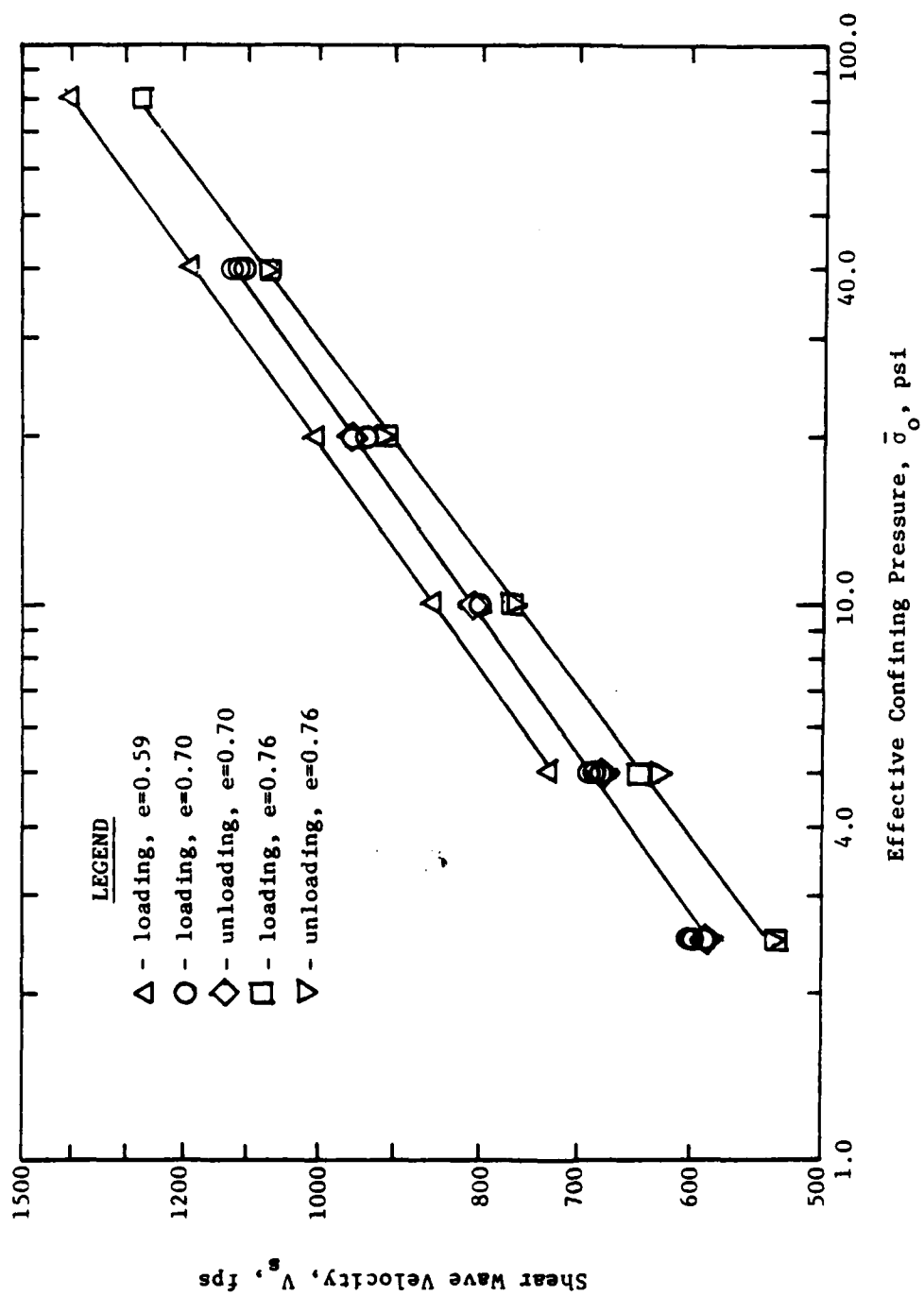


Fig. A.4 - Variation in Low-Amplitude Shear Wave Velocity with Effective Confining Pressure

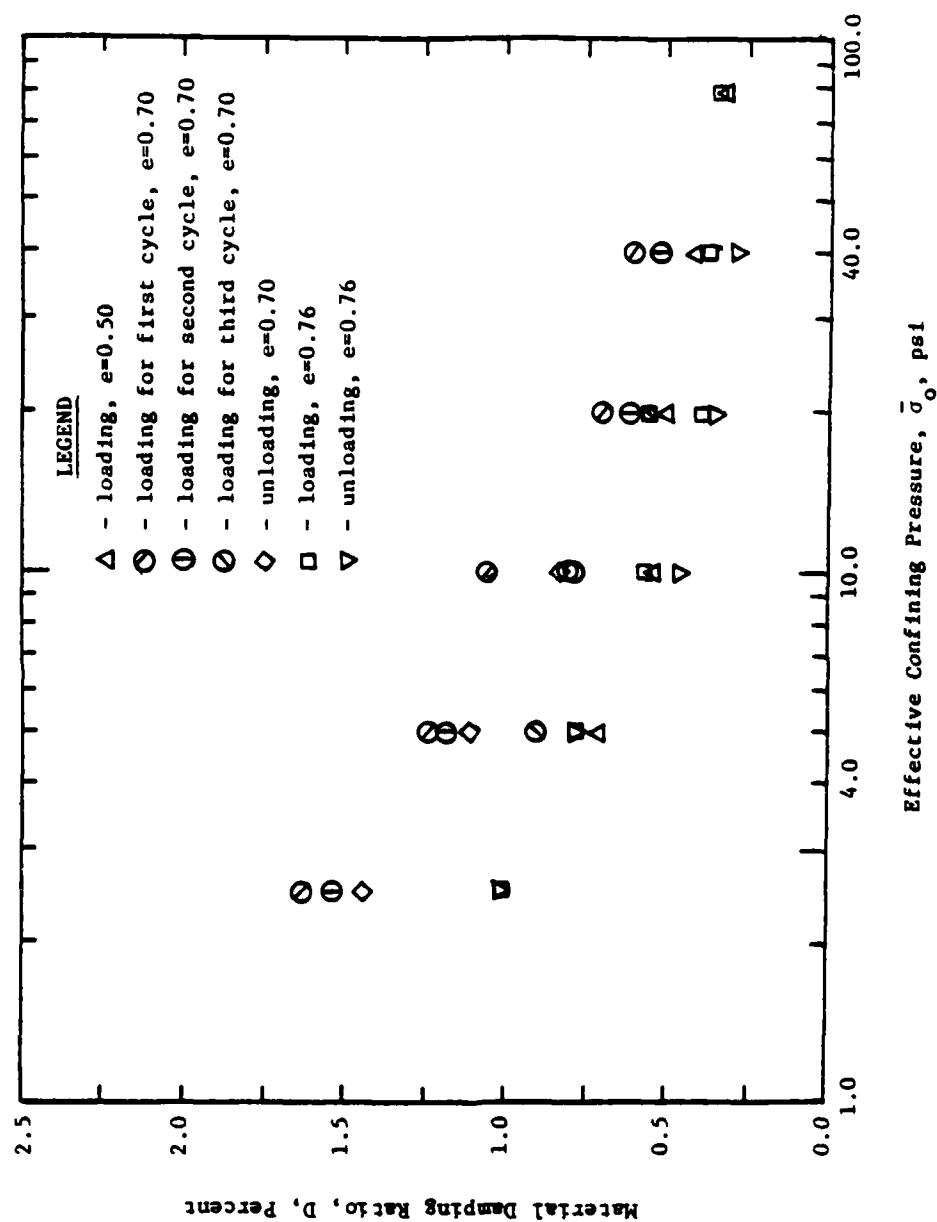


Fig. A.5 - Variation in Low-Amplitude Material Damping Ratio with Effective Confining Pressure

as confining pressure increases, with the rate of decrease becoming less significant as confining pressure increases. Significant scatter in the damping data exists, and because of this scatter, the effect of void ratio upon damping of the sand at any confining pressure is not obvious. Hardin and Drnevich (1972a) indicate that damping ratio decreases as void ratio increases for undisturbed natural soils. However this trend is not shown by this sand. As a result, only a range for  $D$  can be given to compare with the results from the cube. Attention may also have to be paid to the effect of stress history on material damping of the sand. Although the value of  $D$  at any void ratio is similar for both loading and unloading, as shown in Fig. A.5, the large scatter in the data ( $\pm 30$  percent typical  $\pm 40$  percent maximum) masks any lesser variation of  $D$  with stress history. Nevertheless, the resonant column data indicate that  $D$  varies, on the average, from 1.3 percent at low effective confining pressure to 0.3 percent at higher effective confining pressures.

#### A.4.2 Intermediate-Amplitude Dynamic Properties

One intermediate-strain-amplitude test series was performed to determine the effect of shearing strain amplitude on the shear modulus and material damping of the sand in this strain range. This test series was performed at the same set of confining pressures as the low-amplitude tests for the sample with an initial void ratio of 0.76 and was performed on the loading sequence with this sample.

The variation in shear modulus with shearing strain amplitude at each confining pressure is shown in Fig. A.6. As seen in the figure, shear modulus decreases slightly with increasing shearing strains for confining pressures less than about 40 psi (275.6 kPa). For confining pressures of 40 psi (275.6 kPa) or above, shear modulus is essentially constant over the magnitude of shearing strains tested. However, for testing purposes in the triaxial cube, shear modulus can be considered constant unless  $\gamma$  exceeds 0.003 percent. As a result, shear wave velocity can also be considered constant up to this strain amplitude.

The variation in material damping ratio with shearing strain amplitude is shown in Fig. A.7 at each of the confining pressures tested. The figure shows that damping ratio increases with increasing strain amplitude and for shearing strains above about 0.001 percent. This variation is largest at the lowest confining pressure. These results show that for testing in the cube above a strain of 0.001 percent, care must be taken in analyzing the data to account properly for the effect of strain amplitude.

#### A.5 SUMMARY

The sand used in this stage of wave propagation testing is a uniform, medium to fine, washed mortar sand which classifies as SP in the Unified Soil Classification System. Because of the uniformity of the sand, no segregation should occur as the sand is rained into the cube, and, as such, a more uniform and reproducible

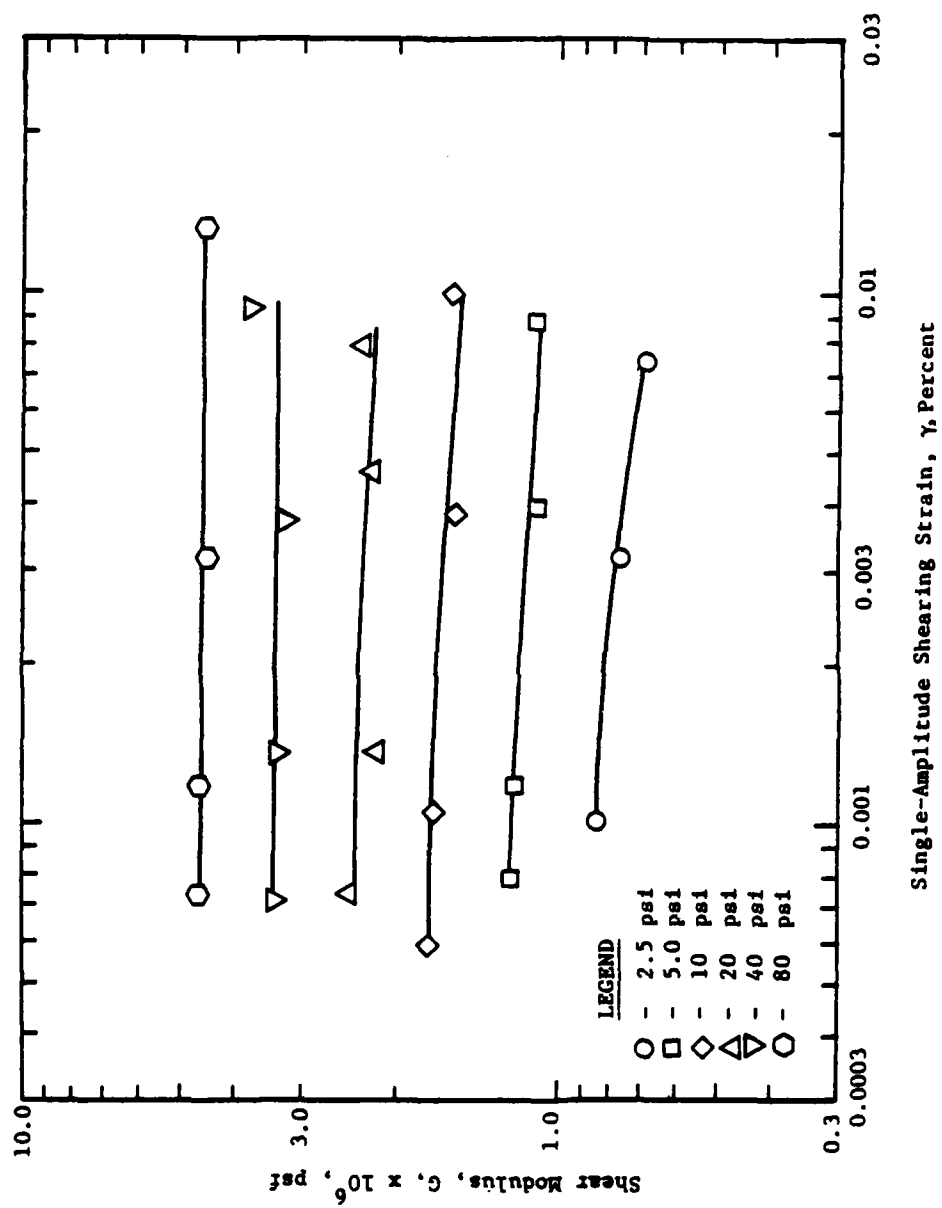


Fig. A.5 - Variation in Shear Modulus with Shearing Strain

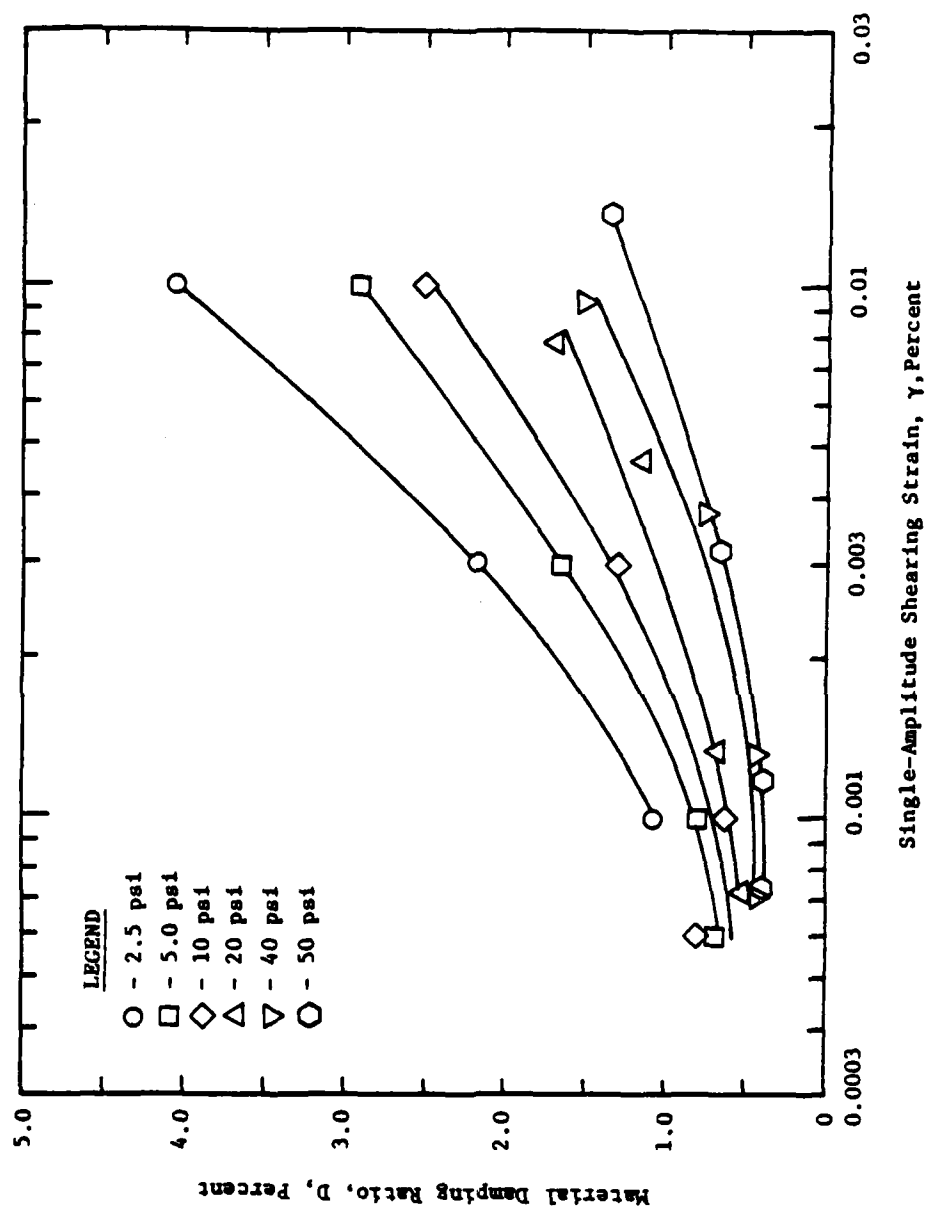


Fig. A.7 - Variation in Material Damping Ratio with Shearing Strain

sand sample is possible from test to test. The sand was tested in an air-dried state with a water content of less than 0.5 percent.

Results from consolidated drained triaxial tests show that  $\bar{\phi}$  for the sand varies with the density, ranging from 37 degrees in a loose state (83 pcf, 1343 kg/m<sup>3</sup>) to 42 degrees in a dense state (99 pcf, 1602 kg/m<sup>3</sup>). The value of  $\bar{c}$  was essentially zero for any density. Because of the limitation of the maximum allowable stress difference (based on the failure envelope with a  $\bar{\phi}$  of 40 degrees) and to reduce the mathematical significance of body forces acting on the sample, the applied pressures within the cube were selected to range from 10 to 40 psi (68.9 to 275.6 kPa).

Both low-amplitude and intermediate-amplitude resonant column tests were performed on sand samples with an effective hydrostatic pressure varying from 2.5 to 80 psi (17.2 to 551.2 kPa). Low-amplitude tests with shearing strains less than 0.001 percent were performed at three different void ratios. Results from the low-amplitude tests show that a linear relationship exists for  $\log G$  (and therefore  $\log V_s$ ) and  $\log \bar{\sigma}_o$ , with the shear modulus (and shear wave velocity) increasing as the confining pressure increases. Shear modulus (and shear wave velocity) decreases as void ratio increases, although this decrease does not change the slope of the  $\log G - \log \bar{\sigma}_o$  (or  $\log V_s - \log \bar{\sigma}_o$ ) relationship. Previous stress history had no significant effect on the value of shear modulus (or shear wave velocity) for these tests. Material damping ratio decreases as effective confining pressure increases. The range of



average D varies from 1.3 percent at low confining pressures to 0.3 percent at high confining pressures, with  $\pm$  30 percent scatter typical.

An intermediate-amplitude resonant column test was performed on one sample for a pressure range of from 2.5 to 80 psi (17.2 to 551.2 kPa). Results show that the shear modulus decreases slightly with increasing shearing strains above 0.003 percent for confining pressures less than 40 psi (275.6 kPa). For testing purposes in the triaxial cube, the shear modulus (and shear wave velocity) can be considered constant at any pressure unless the shearing strain exceeds 0.003 percent. Material damping ratio decreases as shearing strain increases for strains above 0.001 percent, with the variation largest at the lower confining pressures. For shearing strains greater than 0.001 percent, care must be taken to account for strain amplitude effects on D.

APPENDIX B

Computer Listing of Program CUBE

```

PROGRAM CUBE (INPUT,TAPE2,TAPE1=INPUT)

THIS PROGRAM TAKES TRAVEL TIME AND AMPLITUDE DATA FROM
THREE TRAVEL TIME RECORDS AND COMPUTES DIRECT AND INTERVAL
VELOCITIES, FREQUENCIES, AND ALL DAMPING COEFFICIENTS.

TAPE2 IS A FILE TO BE USED AS PART OF THE DATA FOR A
PLOTING PROGRAM WRITTEN BY THE AUTHOR OF THIS PROGRAM
INTERVAL VELOCITIES AND SIGMA(IMIT) ARE LISTED.

DEVELOPED SPECIFICALLY FOR USE ON THE MODEL CUBE PROJECT
BY STUART KUPPERMAN, JUNE 9, 1981.

INPUT SET-UP
NOTE: ALL INPUT IS FREE FORMAT. THEREFORE, ZEROS MUST BE
USED WHERE APPROPRIATE AND F OR I BELOW SIGNIFIES FLOATING
(DECIMAL POINT REQUIRED) OR INTEGER (NO DECIMAL POINT).

NOTE: TIME SHOULD BE INPUT IN SECONDS

CARD A
  SIGMA1(F),SIGMA2(F),SIGMA3(F),NUMBER OF B CARDS TO FOLLOW(I)

CARD B
  SOURCE NO.(I),HIT DIRECTION(I),TRACE 1-T1(F),T2(F),T3(F),A1(F),
  A2(F),TRACE2-T1(F),T2(F),T3(F),A1(F),A2(F),TRACE 3-T1(F),T2(F),
  T3(F),A1(F),A2(F)

CARD B IS REPEATED FOR EACH RECORD TO BE REDUCED
CARDS A AND B ARE REPEATED FOR EACH PRESSURE LEVEL

CARD C (FINAL CARD ON DECK)
  .,.,.,.,.

NOTE: VALUES OF DISTANCE (DIST(I,J,K)) MUST BE SET EQUAL TO
THE CORRECT DISTANCES OF THE ACTUAL SOURCE-RECEIVER
SPACING IN THE CUBE. (LINES 89 TO 91 IN
THE SOURCE LISTING.) DISTANCE MUST BE IN FEET FOR
VELOCITIES TO BE IN FT/SEC.

VARIABLES USED IN THIS PROGRAM

A(I,J)    AMPLITUDE OF TRACE I
           J=1 HALF AMPLITUDE
           J=2 FULL AMPLITUDE
ALPHA(I)  OUTPUT COEFFICIENT OF ATTENUATION
AAVG      AVERAGE COEF. OF ATTENUATION
D(I)      OUTPUT DAMPING RATIO
DELTA(I)  LOG DECREMENT
DIST(I,J,K) DISTANCE BETWEEN SOURCE AND RECEIVER
           I=SOURCE NUMBER
           J=RECEIVER NUMBER
           K=HIT DIRECTION
F(I)      OUTPUT FREQUENCY
FAVG      AVERAGE FREQUENCY
FTOT      TOTAL USED IN COMPUTING AVERAGE
I,J,K     LOOP AND OTHER PARAMETERS
IMIT      HIT DIRECTION
IP        #P
IS        #S

```



```

      K=9+(I-1)*3+J
      IF ((T(J,I).GT.0.) .AND. (T(J+1,I).GT.0.)) GO TO 140
      V(K)=0.
      GO TO 150
140  V(K)=(DIST(ISRC,J+1,INIT)-DIST(ISRC,J,INIT))/(T(J+1,I)-T(J,I))
      READING=READING+1.
150  VTOT=VTOT+V(K)
      IF ((T(3,I).GT.0.) .AND. (T(1,I).GT.0.)) GO TO 160
      V(12+(I-1)*3)=0
      GO TO 170
160  V(12+(I-1)*3)=(DIST(ISRC,3,INIT)-DIST(ISRC,1,INIT))/(T(3,I)-T(1,I))
      VTOT=VTOT+V(12+(I-1)*3)
      READING=READING+1.
170  CONTINUE
      VAVG=VTOT/READING

      FREQUENCY
      READING=0.
      FTOT=0.
      DO 210 I=1,3
        DO 190 J=1,2
          K=(I-1)*3+J
          IF ((T(I,J).GT.0.) .AND. (T(I,J+1).GT.0.)) GO TO 180
          F(K)=0.
          GO TO 190
180  F(K)=(0.25*J)/(T(I,J+1)-T(I,J))
          FTOT=FTOT+F(K)
          READING=READING+1.
190  CONTINUE
          K=1+3
          IF ((T(I,3).GT.0.) .AND. (T(I,1).GT.0.)) GO TO 200
          F(K)=0.
          GO TO 210
200  F(K)=0.75/(T(I,3)-T(I,1))
          FTOT=FTOT+F(K)
          READING=READING+1.
210  CONTINUE
          FAVG=FTOT/READING

      COEFF. OF ATTENUATION
      READING=0.
      AAVG=0.
      DO 250 I=1,2
        DO 230 J=1,2
          K=(I-1)*3+J
          IF ((A(J,I).GT.0.) .AND. (A(J+1,I).GT.0.)) GO TO 220
          ALPHA(K)=0.
          GO TO 230
220  ALPHA(K)=ALOG((DIST(ISRC,J,INIT)/DIST(ISRC,J+1,INIT)))/(A(J,I)/A(J+1,I))/(DIST(ISRC,J+1,INIT)-DIST(ISRC,J,INIT))
          READING=READING+1.
          AAVG=AAVG+ALPHA(K)
230  CONTINUE
          IF ((A(1,I).GT.0.) .AND. (A(3,I).GT.0.)) GO TO 240
          ALPHA(I+3)=0.
          GO TO 250
240  ALPHA(I+3)=ALOG((DIST(ISRC,1,INIT)/DIST(ISRC,3,INIT)))/(A(1,I)/A(3,I))/(DIST(ISRC,3,INIT)-DIST(ISRC,1,INIT))

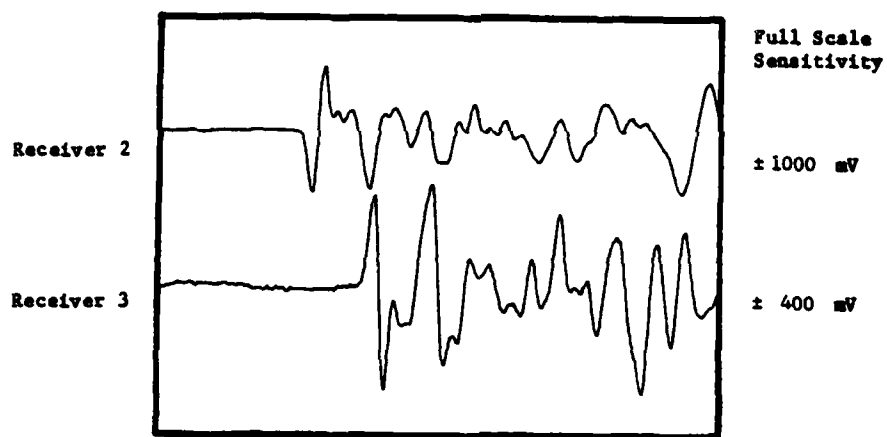
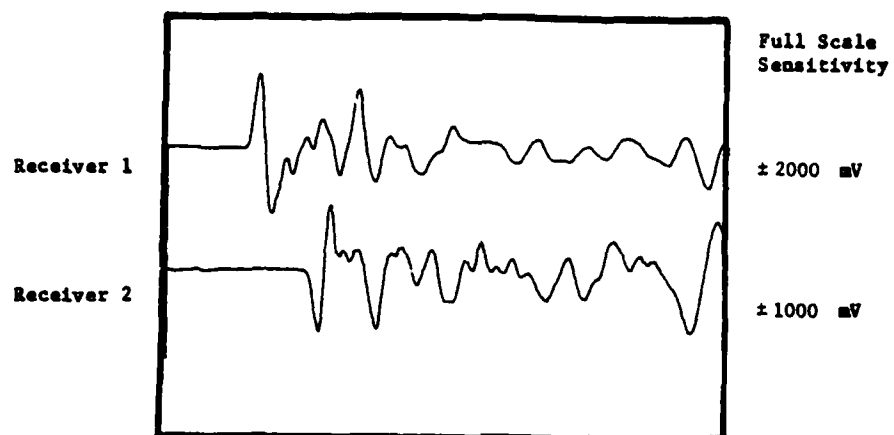
```

```

      READING=READING+1.
      AAVG=AAVG+ALPHA(I*3)
25.) CONTINUE
      AAVG=AAVG/READING
      LOG DECREMENT,DAMPING RATIO, AND Q
      TERM=VIAVG/FAVG
      DO 274 I=1,6
      IF (ALPHA(I).LE.0.) GO TO 264
      DELTA(I)=ALPHA(I)*TERM
      Q(I)=0.2931/(1.-EXP(-2.*DELTA(I)))
      R(I)=SQRT(DELTA(I)*DELTA(I)/(39.4784*DELTA(I)+DELTA(I)))
      GO TO 274
26.) D(I)=0.
      DELTA(I)=0.
      Q(I)=0.
27.) CONTINUE
      OUTPUT
      ITYPE=IS
      IF (ISRC.EQ.INIT) ITYPE=IP
      PRINT 280, ISRC,INIT,ITYPE,(((T(I,J),J=1,3),A(I,1),A(I,2)),I=1,C)800209
1 3), (V(I),I=1,3),VDAVG,(V(I),I=10,18),VIAVG,F,FAVG,ALPHA,AAVG,DFC)800210
2 LTA,D,Q C)800211
28.) FORMAT (1X,10H4SOURCE NO.,12,14H HIT DIRECTION,12,24 (,41,6H=HAVF),C)800212
13(/1X,6HINPUT,3(F6,5,1X),2(F6,4,1X))/5X,11HDIRECT VEL.,4X,3F6,0,C)800213
26X,F6,0/5X,13HINTERVAL VEL.,2X,10F6,0/5X,9HFREQUENCY,4X,10F6,0/5X,C)800214
31HCOEF OF ATTEN.,2X,6F6,3,18X,F6,3/5X,10HLOG DECR.,5X,6F6,3/5X,7HNC)800215
DAMPING,4X,6F6,3/5X,10H,14X,6F6,0/1X) C)800216
WRITE (2,290) ((SIGMA(INIT),V(I)),I=10,18) C)800217
290 FORMAT (2X,F10.2,F10.2) C)800218
GO TO 324 C)800219
320 PRINT 310, ISRC,INIT C)800220
31.) FORMAT (24H *ERROR*--SOURCE NO.,12,14H HIT DIRECTION,12,11H IMPNS,C)800221
174LE1 C)800222
32.) CONTINUE C)800223
GO TO 144 C)800224
33.) STOP C)800225
      END C)800226
      C)800227

```

APPENDIX C  
Sample Isotropic Data



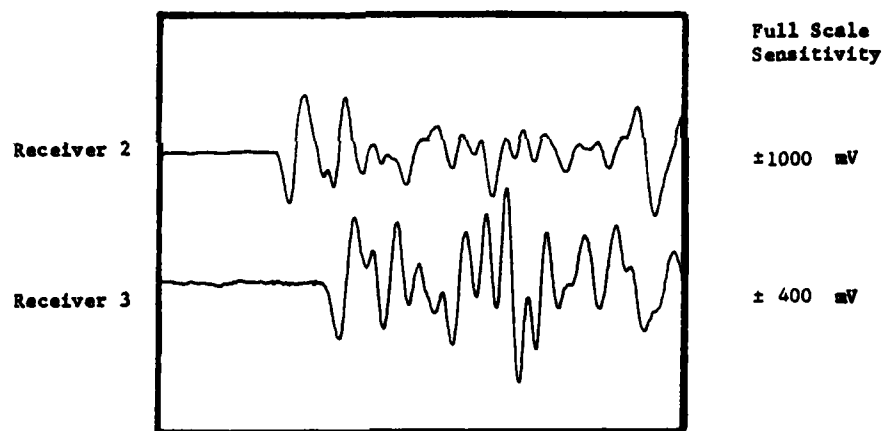
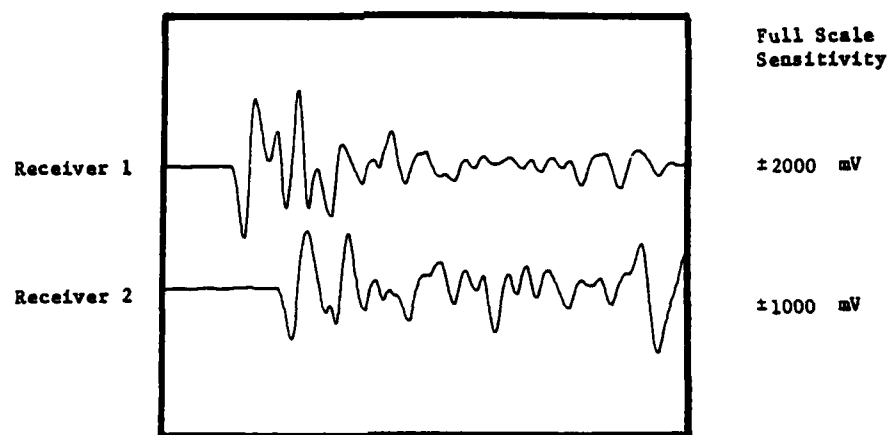
TEST NUMBER: 67 (isotropic)

PROPAGATION DIRECTION: Vertical

PRESSURE ALONG AXIS: 20 psi

Fig. C.1 - Accelerometer Records for Sample Isotropic Data



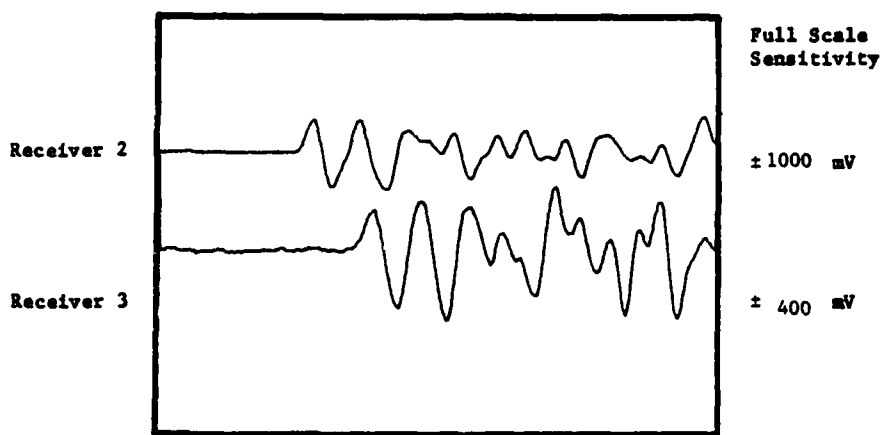
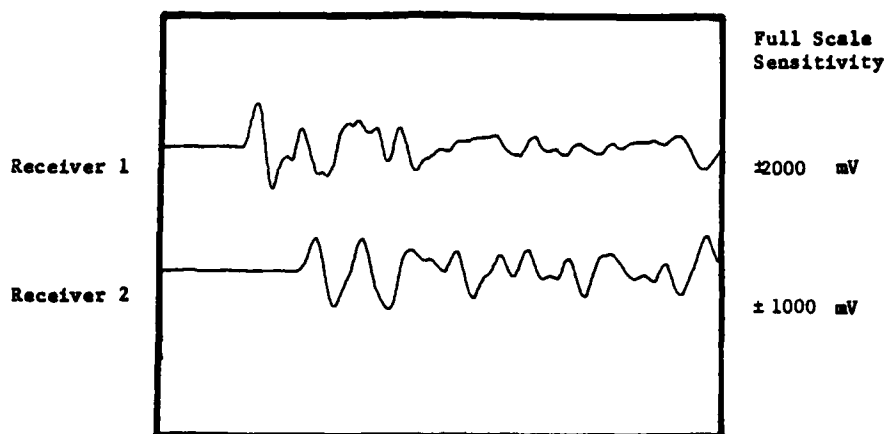


TEST NUMBER: 67 (isotropic)

PROPAGATION DIRECTION: North-South

PRESSURE ALONG AXIS: 20 psi

Fig. C.2 - Accelerometer Records for Sample  
Isotropic Data



TEST NUMBER: 67 (isotropic)

PROPAGATION DIRECTION: East-West

PRESSURE ALONG AXIS: 20 psi

Fig. C.3 - Accelerometer Records for Sample Isotropic Data

## TRAVEL TIME DATA SHEET

TEST NO.: 67 (ISOTROPIC)      DIRECTION OF AXIS      PRESSURE AT CENTER      PRESSURE AT GAGE  
 DATE: 8/19/81      1-1 Top-bottom      psi      psi  
 P-DATA BY: SEK      20.0      20.9  
 S-DATA BY: ---      20.0      20.9

DISK	TRACK	DIRECTION OF PROPAGATION	DIRECTION OF PARTICLE MOTION	P or S	TRACE 1						TRACE 2						TRACE 3					
					t <sub>1</sub>	t <sub>2</sub>	t <sub>3</sub>	A <sub>1</sub>	A <sub>2</sub>	t <sub>1</sub>	t <sub>2</sub>	t <sub>3</sub>	A <sub>1</sub>	A <sub>2</sub>	t <sub>1</sub>	t <sub>2</sub>	t <sub>3</sub>	A <sub>1</sub>	A <sub>2</sub>	t <sub>1</sub>	t <sub>2</sub>	t <sub>3</sub>
16-9	8	1-1	1-1	P	1.450	1.680	1.930	0.716	1.362	2.530	2.785	2.995	0.305	0.625	3.670	3.940	4.150	0.187	0.386			
16-10	8																					
16-9	4	2-2	2-2	P	1.390	1.645	1.855	0.704	1.371	2.305	2.545	2.865	0.256	0.539	3.195	3.535	3.815	0.114	0.243			
16-10	4																					
16-7	8	3-3	3-3	P	1.485	1.750	2.035	4.240	8.390	2.460	2.816	3.165	1.625	3.355	3.535	3.910	4.350	0.772	1.950			
16-8	8																					

t in msec      A in volts

Table C.1 - Travel Time Data Sheet Determined From Sample Isotropic Data

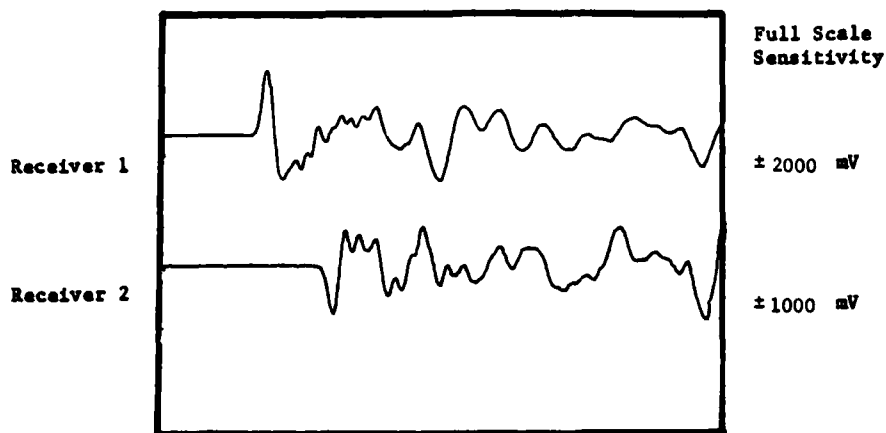
DATA REDUCTION FOR SIGMA(1)= 20.0 SIGMA(2)= 20.0 SIGMA(3)= 20.0

(FREQ.) (DAMPING) DIRECT (INTERVAL)	FIRST ARRIVAL (TRACE 1) (HALF AMPL)			FIRST TROUGH (TRACE 2) (FULL AMPL)			FIRST PEAK (TRACE 3)			AVG
	1	2	3	1	2	3	1	2	3	
	1-2	2-3	1-3	1-2	2-3	1-3	1-2	2-3	1-3	
SOURCE NO. 1 HIT DIRECTION 1 (P-WAVE)										
INPUT .00145 .00148 .00193	.7140	1.3610								
INPUT .00253 .00278 .00299	.3345	.6245								
INPUT .00367 .00394 .00415	.1472	.3864								
DIRECT VEL.	1372.	1320.	1334.							1343.
INTERVAL VEL.	1250.	1377.	1315.	1222.	1359.	1292.	1268.	1359.	1315.	1306.
FREQUENCY	1047.	2070.	1562.	940.	2381.	1613.	926.	2381.	1563.	1610.
COEF OF ATTN	.250	.064	.150	.193	.060	.122				.140
LOG DECR.	.203	.052	.122	.157	.040	.099				
DAMPING	.032	.048	.019	.025	.008	.016				
Q	19.	63.	29.	23.	67.	35.				
SOURCE NO. 2 HIT DIRECTION 2 (P-WAVE)										
INPUT .00139 .00145 .00186	.7042	1.3710								
INPUT .00231 .00255 .00287	.2555	.5385								
INPUT .00324 .00353 .00381	.1144	.2434								
DIRECT VEL.	1396.	1492.	1540.							1478.
INTERVAL VEL.	1639.	1695.	1662.	1667.	1515.	1587.	1485.	1579.	1531.	1505.
FREQUENCY	940.	2381.	1613.	1042.	1562.	1339.	735.	1786.	1210.	1405.
COEF OF ATTN	.204	.204	.204	.241	.200	.265				.270
LOG DECR.	.333	.334	.334	.274	.327	.300				
DAMPING	.053	.053	.053	.044	.052	.048				
Q	13.	13.	13.	15.	13.	14.				
SOURCE NO. 3 HIT DIRECTION 3 (P-WAVE)										
INPUT .00149 .00175 .00293	4.2400	4.3940								
INPUT .00246 .00281 .00317	1.6250	3.3950								
INPUT .00353 .00391 .00435	.7720	1.0900								
DIRECT VEL.	1347.	1423.	1414.							1305.
INTERVAL VEL.	1538.	1399.	1463.	1408.	1370.	1389.	1327.	1286.	1296.	1344.
FREQUENCY	943.	1754.	1364.	704.	1020.	1064.	667.	1136.	920.	1109.
COEF OF ATTN	.264	.258	.262	.238	.124	.181				.222
LOG DECR.	.332	.322	.327	.297	.155	.226				
DAMPING	.053	.051	.052	.047	.025	.036				
Q	13.	13.	13.	14.	24.	17.				

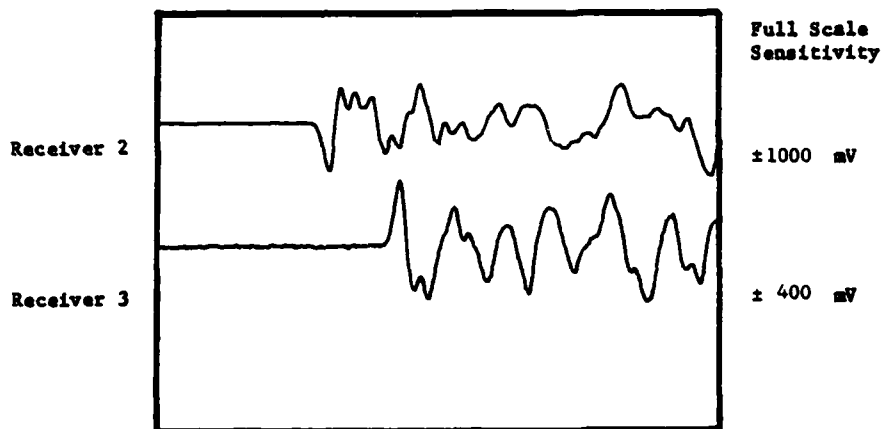
Fig. C.4 - Output from Program CUBE for Isotropic Data

## APPENDIX D

## Sample Biaxial Data



Disk/Track Number: 15-3/1  
Record Length: 10.2 msec



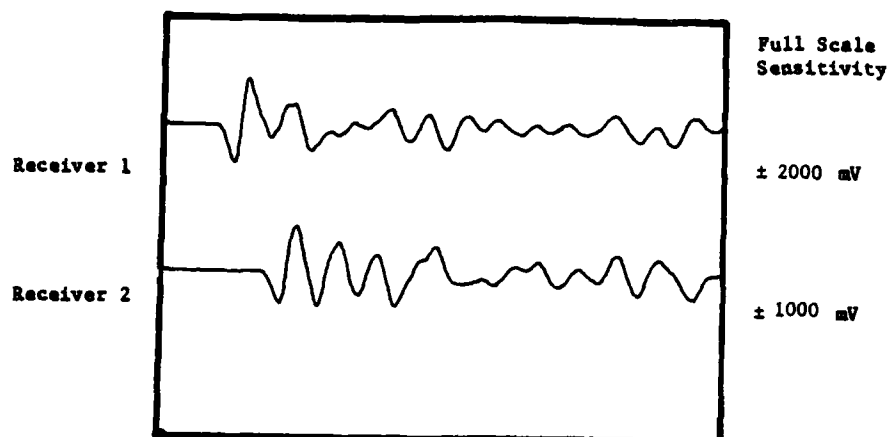
Disk/Track Number: 15-4/1  
Record Length: 10.2 msec

TEST NUMBER: 60 (biaxial)

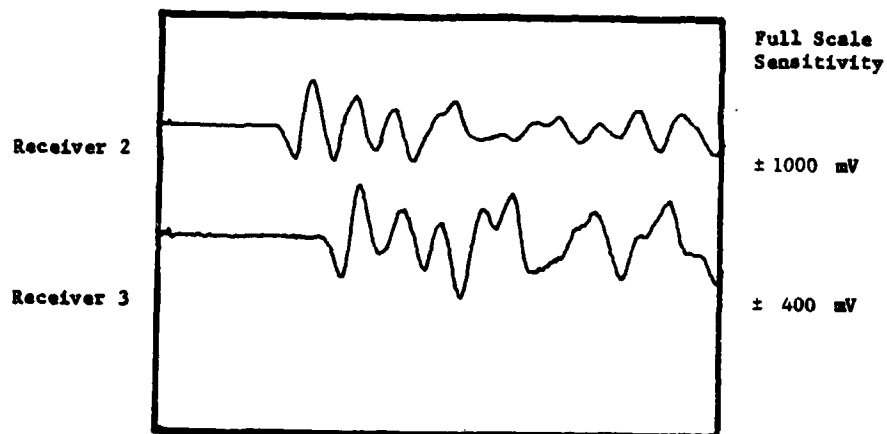
PROPAGATION DIRECTION: Vertical

PRESSURE ALONG AXIS: 15 psi

Fig. D.1 - Accelerometer Records for Sample  
Biaxial Data



Disk/Track Number: 15-3/5  
Record Length: 10.2 msec



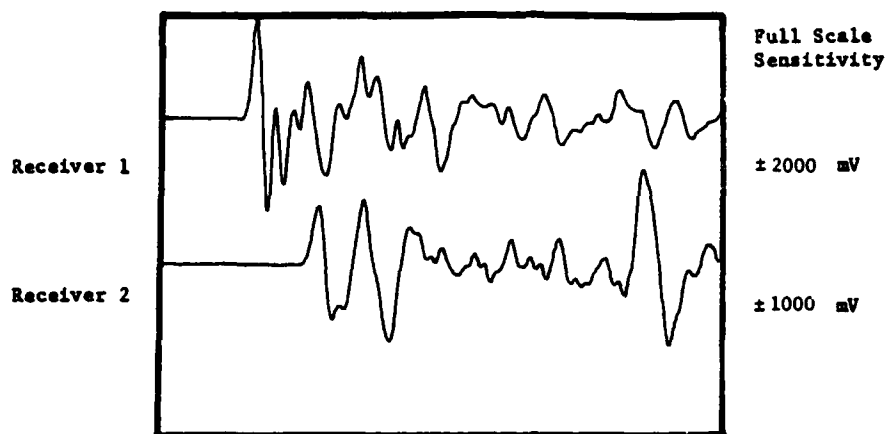
Disk/Track Number: 15-4/5  
Record Length: 10.2 msec

TEST NUMBER: 60 (Biaxial)

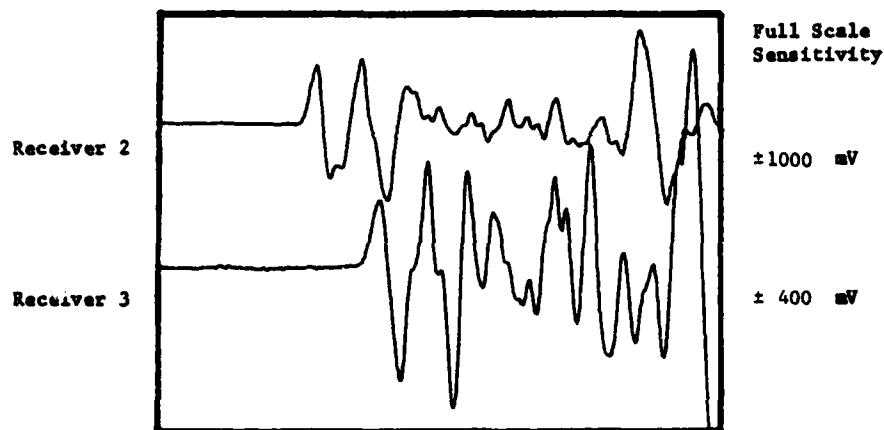
PROPAGATION DIRECTION: North-South

PRESSURE ALONG AXIS: 35 psi

Fig. D.2 - Accelerometer Records for Sample  
Biaxial Data



Disk/Track Number: 15-5/1  
Record Length: 10.2 msec



Disk/Track Number: 15-6/1  
Record Length: 10.2 msec

TEST NUMBER: 60 (biaxial)

PROPAGATION DIRECTION: East-West

PRESSURE ALONG AXIS: 15 psi

Fig. D.3 - Accelerometer Records for Sample  
Biaxial Data



## TRAVEL TIME DATA SHEET

TEST NO.: 60 (BIAXIAL) \_\_\_\_\_

DATE: 8/18/81 \_\_\_\_\_

P-DATA BY: SEK \_\_\_\_\_

S-DATA BY: --- \_\_\_\_\_

DIRECTION OF AXIS

1-1 Top-bottom \_\_\_\_\_

2-2 North-South \_\_\_\_\_

3-3 East-West \_\_\_\_\_

PRESSURE AT CENTER  
psi

15.0 \_\_\_\_\_

35.0 \_\_\_\_\_

15.0 \_\_\_\_\_

PRESSURE AT GAGE  
psi

14.8 \_\_\_\_\_

35.9 \_\_\_\_\_

15.9 \_\_\_\_\_

DISK	TRACK	DIRECTION OF PROPAGATION	DIRECTION OF PARTICLE MOTION	P or S	TRACE 1			TRACE 2			TRACE 3								
					t <sub>1</sub>	t <sub>2</sub>	t <sub>3</sub>	A <sub>1</sub>	A <sub>2</sub>	t <sub>1</sub>	t <sub>2</sub>	t <sub>3</sub>	A <sub>1</sub>	A <sub>2</sub>	t <sub>1</sub>	t <sub>2</sub>	t <sub>3</sub>	A <sub>1</sub>	A <sub>2</sub>
15-3	1	1-1	1-1	P	1.600	1.910	2.190	0.573	0.973	2.825	3.100	3.310	0.221	0.380	4.085	4.355	4.615	0.120	0.200
15-4	1																		
15-3	5	2-2	2-2	P	1.055	1.370	1.620	0.334	0.757	1.915	2.225	2.520	0.147	0.353	3.060	3.375	3.695	0.122	0.170
15-4	5																		
15-5	1	3-3	3-3	P	1.555	1.815	2.005	0.911	1.737	2.615	2.930	3.155	0.265	0.515	3.745	4.040	4.435	0.121	0.37
15-6	1																		

t in msec      A in volts

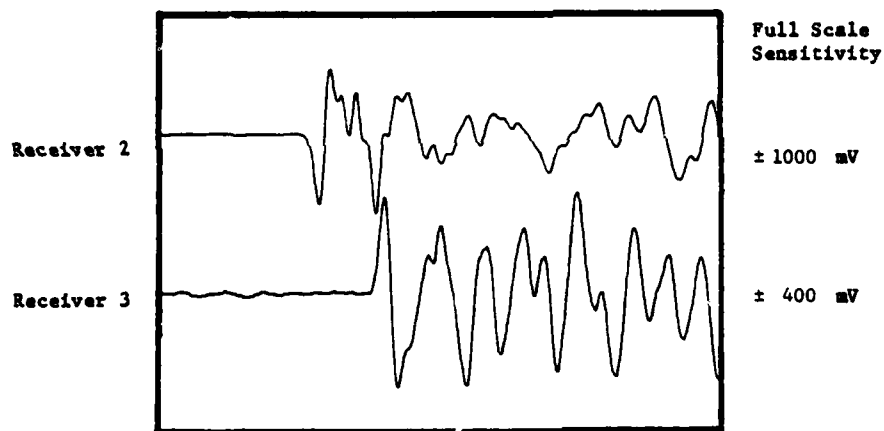
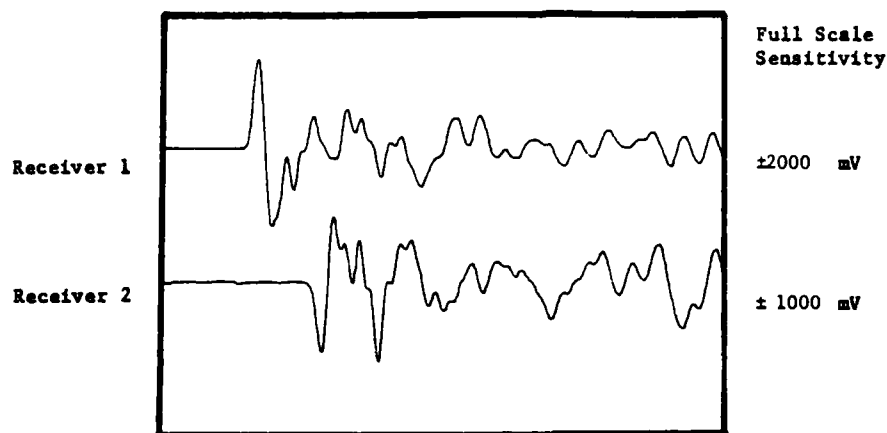
Table D.1 - Travel Time Data Sheet Determined From Sample Biaxial Data

DATA REDUCTION FOR SIGMA(1)= 15.0 SIGMA(2)= 35.0 SIGMA(3)= 15.0

FREQCY (DAMPING) DIFFCT (INTERVAL)	FIRST ARRIVAL (TRACE 1) (HALF AMPL)			FIRST TROUGH (TRACE 2) (FULL AMPL)			FIRST PEAK (TRACE 3)			AVG
	1	2	3	1	2	3	1	2	3	
	1-2	2-3	1-3	1-2	2-3	1-3	1-2	2-3	1-3	
SOURCE NO. 1 HIT DIRECTION 1 (P-WAVE)										
INPUT .00140 .00191 .00219	.5730	.9730								
INPUT .00240 .00317 .00331	.2205	.3705								
INPUT .00400 .00445 .00462	.1204	.2004								
DIRECT VEL.	1240.	1142.	1202.							1209.
INTERVAL VEL.	1112.	1244.	1175.	1134.	1251.	1144.	1205.	1203.	1204.	1191.
FREQUENCY	806.	1746.	1271.	909.	2381.	1546.	926.	1923.	1415.	1448.
COEF OF ATTEN	.324	.140	.225	.314	.161	.232				.233
LOG DEPR.	.264	.116	.186	.250	.133	.192				
DAMPING	.041	.010	.030	.041	.021	.030				
Q	15.	30.	20.	16.	27.	20.				
SOURCE NO. 2 HIT DIRECTION 2 (P-WAVE)										
INPUT .00104 .00137 .00162	.3300	.7570								
INPUT .00192 .00227 .00252	.1465	.3530								
INPUT .00306 .00334 .00370	.1220	.1600								
DIRECT VEL.	1830.	1706.	1614.							1750.
INTERVAL VEL.	1700.	1310.	1406.	1754.	1304.	1400.	1667.	1277.	1446.	1400.
FREQUENCY	704.	2008.	1327.	806.	1605.	1200.	794.	1562.	1181.	1247.
COEF OF ATTEN	.168	.119	.024	.127	.247	.187				.105
LOG DEPR.	.108	0.000	.029	.159	.292	.221				
DAMPING	.032	0.000	.005	.024	.046	.035				
Q	19.	2.	113.	20.	14.	18.				
SOURCE NO. 3 HIT DIRECTION 3 (P-WAVE)										
INPUT .00184 .00211 .00205	.9110	1.7370								
INPUT .00240 .00293 .00316	.2645	.5105								
INPUT .00374 .00440 .00447	.1206	.3268								
DIRECT VEL.	1244.	1334.	1334.							1320.
INTERVAL VEL.	1415.	1327.	1370.	1345.	1351.	1348.	1357.	1172.	1258.	1327.
FREQUENCY	962.	2124.	151.	794.	2222.	1349.	847.	1246.	1067.	1357.
COEF OF ATTEN	.451	.284	.369	.438	.065	.251				.310
LOG DEPR.	.442	.280	.361	.420	.063	.246				
DAMPING	.070	.044	.057	.068	.010	.039				
Q	11.	15.	12.	11.	53.	16.				

Fig. D.4 - Output from Program CUBE for Biaxial Data

APPENDIX E  
Sample Triaxial Data

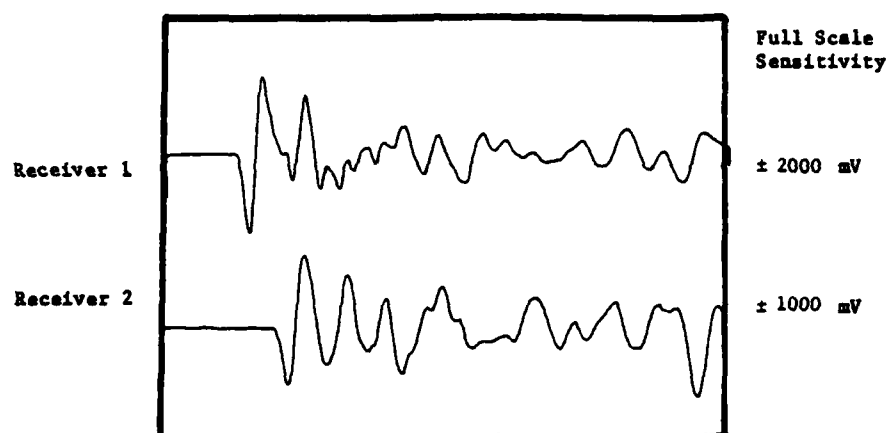


TEST NUMBER: 62 (triaxial)

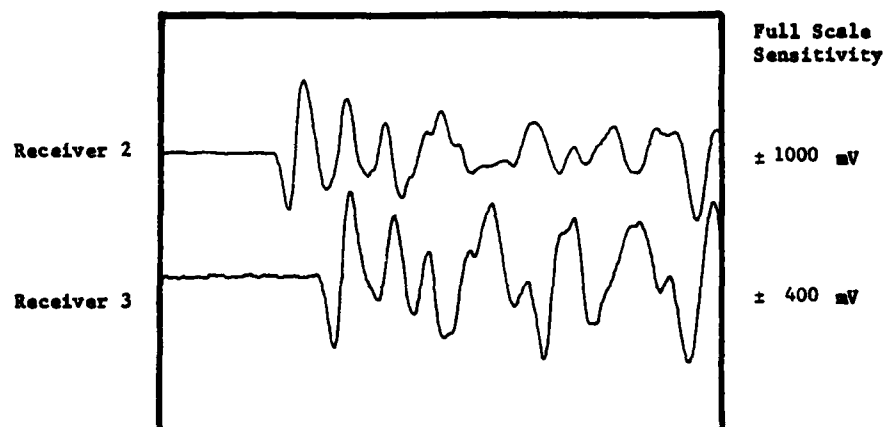
PROPAGATION DIRECTION: Vertical

PRESSURE ALONG AXIS: 20 psi

Fig. E.1 - Accelerometer Records for Sample  
Triaxial Data



Disk/Track Number: 15-7/7  
Record Length: 10.2 msec



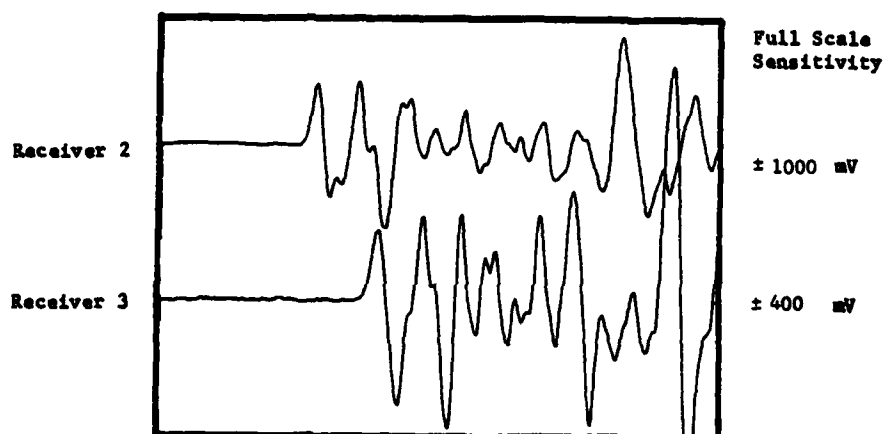
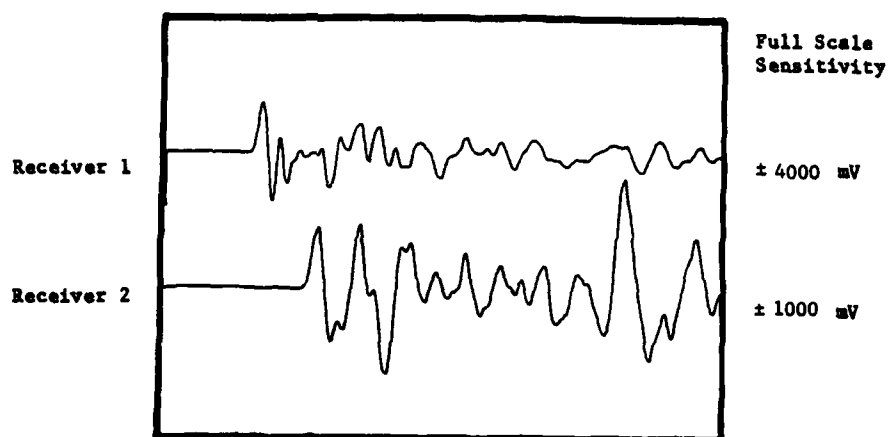
Disk/Track Number: 15-8/7  
Record Length: 10.2 msec

TEST NUMBER: 62 (triaxial)

PROPAGATION DIRECTION: North-South

PRESSURE ALONG AXIS: 40 psi

Fig. E.2 - Accelerometer Records for Sample  
Triaxial Data



TEST NUMBER: 62 (triaxial)

PROPAGATION DIRECTION: East-West

PRESSURE ALONG AXIS: 15 psi

Fig. E.3 - Accelerometer Records for Sample Triaxial Data

## TRAVEL TIME DATA SHEET

TEST NO.: 62 (TRIAXIAL)      DIRECTION OF AXIS      PRESSURE AT CENTER      PRESSURE AT GAGE  
 DATE: 8/18/81      1-1 Top-bottom      20.0      19.8  
 P-DATA BY: SEK      2-2 North-South      40.0      40.9  
 S-DATA BY: ---      3-3 East-West      15.0      15.9

DISK	TRACE	DIRECTION OF PROPAGATION	DIRECTION OF PARTICLE MOTION	P or S	TRACE 1						TRACE 2						TRACE 3					
					t <sub>1</sub>	t <sub>2</sub>	t <sub>3</sub>	A <sub>1</sub>	A <sub>2</sub>	t <sub>1</sub>	t <sub>2</sub>	t <sub>3</sub>	A <sub>1</sub>	A <sub>2</sub>	t <sub>1</sub>	t <sub>2</sub>	t <sub>3</sub>	A <sub>1</sub>	A <sub>2</sub>	t <sub>1</sub>	t <sub>2</sub>	t <sub>3</sub>
15-7 3	3	1-1	1-1	P	1.485	1.760	1.995	0.860	1.622	2.600	2.895	3.115	0.345	0.667	3.835	4.085	4.325	0.188	0.375			
15-8 3	3																					
15-7 7	7	2-2	2-2	P	1.300	1.520	1.770	0.763	1.520	2.085	2.340	2.635	0.282	0.640	2.885	3.165	3.450	0.145	0.310			
15-8 7	7																					
15-9 3	3	3-3	3-3	P	1.555	1.780	1.965	0.970	1.918	2.545	2.885	3.100	0.301	0.564	3.690	4.010	4.380	0.139	0.345			
15-10 3	3																					

t in msec      A in volts

Table E.1 - Travel Time Data Sheet Determined from Sample Triaxial Data

DATA REDUCTION FOR SIGMA(1)= 20.2 SIGMA(2)= 40.4 SIGMA(3)= 15.0

PERCENT DAMPING PIPECT (INTERVAL)	FIRST ARRIVAL (TRACE 1) (HALF AMPL)			FIRST TROUGH (TRACE 2) (FULL AMPL)			FIRST PEAK (TRACE 3)			AVG
	1	2	3	1	2	3	1	2	3	
	1-2	2-3	1-3	1-2	2-3	1-3	1-2	2-3	1-3	
SOURCE NO. 1 HIT DIRECTION 1 (P-WAVE)										
INPUT .00140 .00176 .00199 .0600 1.0220										
INPUT .00260 .00406 .00312 .3450 .0665										
INPUT .00344 .00400 .00432 .1670 .3745										
DIRECT VEL.	1340.	1205.	1200.							1302.
INTERVAL VEL.	1211.	1271.	1203.	1169.	1319.	1256.	1205.	1290.	1253.	1249.
FREQUENCY	.009.	.0120.	.0171.	.047.	.0273.	.0456.	.0000.	.0003.	.0531.	.0522.
COEF OF ATTN	.293	.142	.212	.275	.122	.193				.206
LOG DECP.	.201	.117	.174	.226	.100	.150				
DAMPING	.030	.010	.020	.036	.016	.025				
Q	10.	30.	21.	17.	35.	23.				
SOURCE NO. 2 HIT DIRECTION 2 (P-WAVE)										
INPUT .00130 .00152 .00177 .0630 1.5200										
INPUT .00200 .00214 .00263 .2915 .0400										
INPUT .00200 .00317 .00345 .1450 .3104										
DIRECT VEL.	1492.	1450.	1712.							1610.
INTERVAL VEL.	1211.	1475.	1403.	1020.	1010.	1020.	1734.	1040.	1700.	1034.
FREQUENCY	.130.	.0000.	.1506.	.000.	.1695.	.1364.	.003.	.1754.	.1327.	.1416.
COEF OF ATTN	.243	.201	.242	.105	.241	.210				.230
LOG DECP.	.300	.260	.313	.252	.312	.202				
DAMPING	.050	.001	.050	.040	.050	.005				
Q	12.	15.	13.	10.	10.	15.				
SOURCE NO. 3 HIT DIRECTION 3 (P-WAVE)										
INPUT .00150 .00170 .00196 .0720 1.0100										
INPUT .00200 .00200 .00310 .3010 .5635										
INPUT .00340 .00401 .00430 .1300 .3050										
DIRECT VEL.	1200.	1375.	1355.							1330.
INTERVAL VEL.	1015.	1310.	1400.	1357.	1333.	1345.	1322.	1172.	1242.	1330.
FREQUENCY	.111.	.0703.	.1000.	.730.	.0300.	.1351.	.701.	.1351.	.1007.	.1475.
COEF OF ATTN	.007	.277	.342	.404	.000	.200				.300
LOG DECP.	.300	.291	.300	.001	.000	.201				
DAMPING	.050	.000	.000	.000	.013	.030				
Q	12.	10.	10.	11.	42.	10.				

Fig. E.4 - Output from Program CUBE for Triaxial Data



## REFERENCES

1. Arthur, J. R. F. and Menzies, B. K. (1972), "Inherent Anisotropy in a Sand," Geotechnique, Vol. 22, No. 1, pp. 115-128.
2. Beiganousky, W. A., and Marcusson, W. F., III (1976), "Uniform Placement of Sand," Journal of the Geotechnical Engineering Division, ASCE, Vol. 102, No. GT3, March, pp. 229-233.
3. Bishop, A. W. and Green, G. E. (1965), "The Influence of End Restraint on the Compression Strength of a Cohesionless Soil," Geotechnique, Vol. 15, No. 3, pp. 423-266.
4. Hadala, P. F. (1967), "The Effect of Placement Method on the Response of Soil Stress Gages," Proceedings, International Symposium on Wave Propagation and Dynamic Properties of Earth Materials, Albuquerque, N.M.
5. Hardin, B. O. (1978), "The Nature of Stress-Strain Behavior of Soils," Proceedings of the Earthquake Engineering and Soil Dynamics Conference, ASCE, Pasadena, CA, June 19-21, 1978, Vol. I, pp. 3-90.
6. Hardin, B. O. and Black, W. L. (1966), "Sand Stiffness Under Various Triaxial Stresses," Journal of the Soil Mechanics and Foundations Division, ASCE, Vol. 92, No. SM2, March, pp. 27-43.
7. Hardin, B. O. and Drnevich, V. P. (1970), Shear Modulus and Damping in Soils: I. Measurement and Parameter Effects, University of Kentucky Technical Report, UKY 26-70-CE2, Soil Mechanics Series No. 1, July, 45 pp.
8. Hardin, B. O. and Drnevich, V. P. (1972a), "Shear Modulus and Damping in Soils: Measurement and Parameter Effects," Journal of the Soil Mechanics and Foundations Division, ASCE, Vol. 98, SM6, June, pp. 603-624.
9. Hardin, B. O. and Drnevich, V. P. (1972b), "Shear Modulus and Damping in Soils: Design Equations and Curves," Journal of the Soil Mechanics and Foundations Division, ASCE, Vol. 98, No. SM7, July, pp. 667-692.

10. Hardin, B. O. and Richart, F. E., Jr. (1963), "Elastic Wave Velocities in Granular Soils," Journal of the Soil Mechanics and Foundations Division, ASCE, Vol. 89, No. SM1, February, pp. 33-65.
11. Hoar, R. J. and Stokoe, K. H., II (1978), "Generation and Measurement of Shear Waves in Situ," Dynamic Geotechnical Testing, ASTM STP 654, pp. 3-29.
12. Kilbuszewski, J. J. (1948), "General Investigation of the Fundamental Factors Controlling Loose Packing of Sands," Proceedings of the Second International Conference on Soil Mechanics, Rotterdam, Vol. 7, pp. 47-49.
13. Knox, D. P. (1982), "Effect of State of Stress on Velocity of Low-Amplitude Shear Waves Propagating Along Principal Stress Directions in Dry Sand," M.S. Thesis, University of Texas at Austin, 1982. (See Reference 14)
14. Knox, D. P., Stokoe, K. H., II, and Kopperman, S. E. (1982), "Effect of State of Stress on Velocity of Low-Amplitude Shear Waves Propagating Along Principal Stress Directions in Dry Sand," Geotechnical Engineering Report GR82-23, Civil Engineering Department, The University of Texas at Austin.
15. Ko, H. Y. and Scott, R. F. (1967), "A New Soil Testing Apparatus," Geotechnique, Vol. 17, No. 1, pp. 40-57.
16. Ko, H. Y. and Sture, S. (1974), "Three-Dimensional Mechanical Characterization of Anisotropic Composites," Journal of Composite Materials, Vol. 8, April, pp. 173-190.
17. Laier, J. E., Schmertmann, J. H., and Schaub, J. H. (1975), "Effect of Finite Pressuremeter Length in Dry Sand," Proceedings of Specialty Conference on In-Situ Measurement of Soil Properties, ASCE, Vol. 1, pp. 241-259.
18. Lawrence, F. V. (1963), The Response of Soils to Dynamic Loadings, Report 14: Propagation Velocity of Ultrasonic Waves through Sand, Massachusetts Institute of Technology, Department of Civil Engineering, Research Report R63-8, March, 54 pp.
19. Lawrence, F. V. (1965), Ultrasonic Shear Wave Velocities in Sand and Clay, Massachusetts Institute of Technology, Department of Civil Engineering, Research Report R65-05, January, 24 pp.
20. Marcusson, W.F., III and Beiganousky, W. A. (1977), "Laboratory Standard Penetration Tests on Fine Sands," Journal of the Geotechnical Engineering Division, ASCE, Vol. 103, No. GT6, June, pp. 565-588.

- 2 . Richart, F. E., Jr., Hall, J. R., Jr., and Woods, R. D. (1970), Vibrations of Soils and Foundations, Prentice Hall, 414 pp.
- 2 . Roesler, S. K. (1979), "Anisotropic Shear Modulus Due to Stress Anisotropy," Journal of the Geotechnical Engineering Division, ASCE, Vol. 105, No. GT5, July, pp. 871-880.
- 2 . Roscoe, K. H. (1953), "An Apparatus for the Application of Simple Shear to Soil Samples," Proceedings, Third International Conference on Soil Mechanics and Foundations, Zurich, Vol. 1.
- 2 . Rowe, P. W. and Barden, L. (1964), "Importance of Free Ends in Triaxial Testing," Journal of Soil Mechanics and Foundation Division, ASCE, Vol. 90, No. SM1, January, pp. 1-27.
- 2 . Schmertmann, J. H. (1978), Effect of Shear Stress on Dynamic Bulk Modulus of Sand, U.S. Army Engineering Waterways Experiment Station, Technical Report S-78-16, October, 92 pp.
- 2 . Silver, M. L. and Park, T. K. (1975), "Testing Procedure Effects on Dynamic Soil Behavior," Journal of the Geotechnical Engineering Division, ASCE, Vol. 101, No. GT10, pp. 1061-1083.
- 2 . Sutherland, H. B. and Mesdary, M. S. (1969), "The Influence of the Intermediate Principal Stress on the Strength of Sand," Proceedings of the Seventh International Conference on Soil Mechanics, Mexico City, Vol. 1, pp. 391-399.
- 2 . Truesdale, W. B. and Schwab, R. B. (1967), "Soil Strain Gage Instrumentation," Proceedings, International Symposium on Wave Propagation and Dynamic Properties of Earth Materials, Albuquerque, N.M.
- 2 . Wetzal, R. A. and Vey, E. (1970), "Axisymmetric Stress Wave Propagation in Sand," Journal of the Soil Mechanics and Foundations Division, ASCE, Vol. 96, No. SM5, September, pp. 1763-1786.
- 2 . Wilson, S. D. and Miller, R. P. (1962), Discussion of "Foundation Vibrations," Transactions, ASCE, Vol. 127, Part I, pp. 913-917.
- 3 . Woods, R. D. (1978), "Measurement of Dynamic Soil Properties," Proceedings of the Earthquake Engineering and Soil Dynamics Conference, ASCE, Pasadena, CA, June 19-21, 1978, Vol. I, pp. 91-178.

**SUPPLEMENTARY**

**INFORMATION**

A120425 UNCLASSIFIED

Change

SECURITY CLASSIFICATION OF THIS PAGE (When Data Entered)

REPORT DOCUMENTATION PAGE		READ INSTRUCTIONS BEFORE COMPLETING FORM
1. REPORT NUMBER <b>AFOSR-TR- 82-0907</b>	2. GOVT ACCESSION NO. <b>ADA120425</b>	3. RECIPIENT'S CATALOG NUMBER
4. TITLE (and Subtitle) <b>EFFECT OF STATE OF STRESS ON VELOCITY OF LOW-AMPLITUDE COMPRESSION WAVES PROPAGATING ALONG PRINCIPAL STRESS DIRECTIONS IN DRY SAND</b>		5. TYPE OF REPORT & PERIOD COVERED <b>ANNUAL Final</b> <b>1 Oct 79 - 31 Dec 81</b>
7. AUTHOR(s) <b>STEWART E. KOPPERMAN, KENNETH H. STOKOE, II, and DAVID P. KNOX</b>		6. PERFORMING ORG. REPORT NUMBER
9. PERFORMING ORGANIZATION NAME AND ADDRESS <b>UNIVERSITY OF TEXAS AT AUSTIN DEPARTMENT OF CIVIL ENGINEERING AUSTIN, TX 78712</b>		8. CONTRACT OR GRANT NUMBER(s) <b>AFOSR-80-0031</b>
11. CONTROLLING OFFICE NAME AND ADDRESS <b>AIR FORCE OFFICE OF SCIENTIFIC RESEARCH/NA BOLLING AFB, DC 20332</b>		10. PROGRAM ELEMENT, PROJECT, TASK AREA & WORK UNIT NUMBERS <b>61102F 2307/C1</b>
14. MONITORING AGENCY NAME & ADDRESS (if different from Controlling Office)		12. REPORT DATE <b>February 1982</b>
		13. NUMBER OF PAGES <b>288</b>
		15. SECURITY CLASS. (of this report) <b>UNCLASSIFIED</b>
16. DISTRIBUTION STATEMENT (of this Report) <b>Approved for Public Release; Distribution Unlimited.</b>		15a. DECLASSIFICATION/DOWNGRADING SCHEDULE
17. DISTRIBUTION STATEMENT (of the abstract entered in Block 20, if different from Report)		
18. SUPPLEMENTARY NOTES		
19. KEY WORDS (Continue on reverse side if necessary and identify by block number) <div style="display: flex; justify-content: space-between;"> <div> <b>COMPRESSION WAVES</b>  <b>SEISMIC VELOCITY</b>  <b>CONSTRAINED MODULUS</b>  <b>DAMPING</b>  <b>TRIAxIAL TESTING</b> </div> <div> <b>BIAXIAL TESTING</b>  <b>LOW AMPLITUDE BODY WAVES</b>  <b>STRESS HISTORY</b>  <b>STRUCTURAL ANISOTROPY</b> </div> </div>		
20. ABSTRACT (Continue on reverse side if necessary and identify by block number) <p>Little research has been performed in which the effect of biaxial and triaxial states of stress on the propagation velocity of compression and shear waves has been investigated. Therefore, a triaxial testing device was constructed, and an initial test series was performed to determine the relationship between propagation velocities and state of stress in a dry sand. The testing device was constructed of reinforced steel and was designed to hold a cubic soil sample measuring 7 ft (2.1 m) on a side. Rubber membranes</p>		

**UNCLASSIFIED**

SECURITY CLASSIFICATION OF THIS PAGE (When Data Entered)

were placed between the soil and three mutually perpendicular walls of the cube, corresponding to the three principal planes. The membranes were filled with water and pressurized to achieve the desired state of stress, either isotropic, biaxial, or triaxial. Waves were generated at sources contacting the soil surface and extending outside the cube. The waves were monitored by accelerometers placed in the soil sample. The accelerometer records were recorded on digital oscilloscopes for determination of velocities. Stress and strain measuring devices were also placed in the soil. The effects on compression of the sample were determined. Structural anisotropy caused a variation between principal stress axes of about ten percent in velocity at a given pressure. Stress history resulted in no noticeable variation in P-wave velocity and, therefore, was neglected. Biaxial and triaxial loading results lead to the same conclusion, namely that the velocity of compression waves propagating along principal stress directions in dry sand as low-amplitude body waves depends only on the stress in the direction of wave propagation. This conclusion is important in that compression wave velocity has been assumed to depend primarily on the mean effective principal stress in the past.